Doctoral theses at NTNU, 2013:226

Tor Olav Løveng Sunde

Aqueous sol-gel processing of transparent conducting rare earth doped indium tin oxide

Doctoral Thesis

Tor Olav Løveng Sunde

ISBN 978-82-471-4570-8 (printed version)
ISBN 978-82-471-4571-5 (electronic version)
ISSN 1503-8181

NTNU – Trondheim
Norwegian University of
Science and Technology

NTNU
Norwegian University of Science and Technology
Thesis for the degree of Philosophiae Doctor
Faculty of Natural Sciences and Technology
Department of Materials Science and Engineering

Doctoral theses at NTNU, 2013:226

NTNU

NTNU – Trondheim
Norwegian University of
Science and Technology

Tor Olav Løveng Sunde

Aqueous sol-gel processing of transparent conducting rare earth doped indium tin oxide

Thesis for the degree of Philosophiae Doctor

Trondheim, June 2013

Norwegian University of Science and Technology
Faculty of Natural Sciences and Technology
Department of Materials Science and Engineering

NTNU – Trondheim
Norwegian University of
Science and Technology

NTNU
Norwegian University of Science and Technology

Thesis for the degree of Philosophiae Doctor

Faculty of Natural Sciences and Technology
Department of Materials Science and Engineering

ISBN 978-82-471-4570-8 (printed version)
ISBN 978-82-471-4571-5 (electronic version)
ISSN 1503-8181

IMT-Report 2013:180

Doctoral theses at NTNU, 2013:226

Printed by Skipnes Kommunikasjon as

This thesis has been submitted to

Department of Materials Science and Engineering
Norwegian University of Science and Technology

in partial fulfilment of the requirements for
the academic degree

Philosophiae doctor

June 2013

Acknowledgments

First and foremost I would like to express my sincere gratitude to my main supervisor, Professor Tor Grande. His vast knowledge, enthusiasm and feedback have been vital for this work. I could truly not have asked for a better supervisor, and I am grateful for the excellent guidance I received through our weekly meetings. He gave me freedom to work independently, yet always knew when to give me a push in the right direction. I would also like to thank my co-supervisor, Professor Mari-Ann Einarsrud. Her knowledge has been of great importance, especially regarding the chemistry and sintering aspects of my work. Particularly her excellent feedback and comments during the writing of papers and the final thesis was invaluable.

I am also grateful towards Professor Thomas O. Mason at Northwestern University, Evanston, Il, USA for welcoming me to visit his group for four months during the fall of 2012. His vast knowledge in electroceramics, particularly TCOs, interest in my work and enthusiasm was greatly appreciated. I would also like to thank all of the members of his group, Arpun Nagaraja, Ted Yeh, Patrick Duffy, Alex Dolgonos, Qimin Zhu, Stephanie Morffit and particularly Alex Adler for their warm welcome and all their help in the lab. It will be a pleasure to come back and join their group again.

I would also like to thank my collaborators at the Department of Physics, NTNU: Dr. Ragnhild Sæterli for performing the TEM experiments, Lars Martin Sandvik Aas, Dr. Zahra Ghadyani and Professor Morten Kildemo for the ellipsometry characterisation, and Professor Mikael Lindgren and Jerome Maria for helping me with different spectroscopy experiments.

I have to thank my office mates, Vegar Øygarden, Astri Bjørnetun Haugen and Ørjan Fossmark Lohne, for the great time we shared during the past four year. Together with Carl Erik Foss, Morten Tjelta and Astrid Bakken we have been class mates for nine years now, and it has truly been a pleasure. I have many great memories from the games of Zatacka, the coffee breaks and all our trivial conversations. I have also been fortunate to be a part of the Inorganic materials and ceramics group, who, together with the rest of the people at KII, contributes to a great, social working environment. Dr. Julian Tolchard, Eli-Beate Larsen, Kjell Røkke, Gunn Torill Wikdahl, Dr. Yingda Yu and Associate Professor Sverre Magnus Selbach deserve to be mentioned for all their help. It has also been a pleasure to co-supervise the master students Helle Ervik Fossheim, Benjamin Otter and Sandra H. Skjærvø. I learnt a lot from their contributions. I also would like to thank all of my fellow team members in our department football team, PolyCrystal

Palace. I am proud of many of my accomplishments in Trondheim, but perhaps none more so than what we have achieved together.

I also want to thank my family for their help, support, care and encouragement, not only for the past four years!

Last but not least, I would like to thank my dear Torunn! You have always been there for me and the time I spend with you is always my favourite part of the day. Every day with you is special and you truly bring out the best in me!

Preface

The present dissertation is based on work carried out from August 2009 until June 2013, including one year of teaching duties. The main supervisor has been Professor Tor Grande with Professor Mari-Ann Einarsrud as co-supervisor. The experiments were mainly performed at the Department of Materials Science and Engineering at the Norwegian University of Science and Technology (NTNU), with the majority of the characterisation of the functional properties of REE-doped materials being performed at Northwestern University, Evanston, Il, USA.

The work has been funded by NTNU and the strategic research area MATERIALS at NTNU.

All of the experiments have been conducted by the author, except for TEM characterisation by Dr. Ragnhild Sæterli and ellipsometry characterisation by Dr. Zahra Ghadyani and Lars Martin Sandvik Aas, all from the Department of Physics, NTNU. The transmission spectroscopy in Figure 7.4 was carried out by Dr. Jerome Maria and the XRD and FTIR spectroscopy in Figure 5.3 and Figure 5.5 was performed by Helle Ervik Fossheim. Initial sintering studies of nano-crystalline In_2O_3 and ITO were performed by the author as a master student at the Department of Materials Science and Engineering in spring 2009. All the experimental work presented in Chapter 6 was performed after August 2009, with the exception of Figure 6.6 and Figure 6.13.

Parts of this dissertation have been published in the Following Papers:

> T. O. L. Sunde, E. Garskaite, B. Otter, H. E. Fossheim, R. Saeterli, R. Holmestad, M.-A. Einarsrud and T. Grande, "Transparent and conducting ITO thin films by spin coating of an aqueous precursor solution." *Journal of Materials Chemistry,* **22** 31 (2012) p. 15740-15749.
>
> T. O. L. Sunde, M.-A. Einarsrud and T. Grande, "Solid state sintering of nano-crystalline indium tin oxide." *Journal of the European Ceramic Society*, **33** 3 (2013) p. 565-574.

Tor Olav Løveng Sunde

Trondheim, 20th of June 2013

Summary

Transparent conducting oxides (TCOs) demonstrate optical transparency in the visible region of the electromagnetic spectrum combined with near-metallic electrical conductivity. Owing to this unique combination of properties, TCOs have found numerous technological applications. Among the TCOs, indium tin oxide (ITO) is widely recognised as having the best combination of transparency and conductivity. The aim of this work was to develop an aqueous sol-gel process to prepare ITO and also doped ITO materials. The motivation was to make a simple, inexpensive and environmentally friendly process, while retaining the ability to prepare excellent materials. Wet chemical deposition techniques have many advantages compared to commercial physical deposition techniques, like sputtering, such as cost, simplicity and readily control of homogeneity and composition. Moreover, by using water instead of organic solvents, the process has the potential to be environmentally friendly and less expensive and thereby more relevant for up-scaling to industrial levels. The challenges related to the frequently used In- or Sn-chloride precursors in soft chemistry synthesis were circumvented by using indium nitrate and tin acetate as precursors.

The aqueous sol-gel process developed in this work was demonstrated to give phase-pure In_2O_3 and ITO thin films as well as nano-crystalline powders. A gel was formed after evaporation of the solvent, and the amorphous nature of the gel demonstrated homogeneous cation distribution. Calcination of the gel caused decomposition and crystallisation to the desired oxide material. The chemistry of the sol-gel process was investigated by varying the initial cation concentration and the organic complexing agents. These parameters were demonstrated to influence on the decomposition/crystallisation of the gel during thermal treatment and the phase purity of the final oxide materials. The presence of hydroxyl groups appeared to be important regarding complexing and immobilisation of the cations, and the possible formation of the metastable rhombohedral polymorph of In_2O_3 could be controlled by the choice of the organic additives.

ITO thin films were successfully deposited on substrates by spin coating using the aqueous sol-gel route. The ITO thin films were demonstrated to have excellent optical properties, such as a high transmittance in the visible region and band gap similar to reported values. The electrical properties of the as-deposited films were also quite promising. Particularly after heat treatment at high temperatures and annealing in reducing atmospheres, the specific resistance was excellent compared to ITO thin films prepared by other sol-gel methods and comparable to the best

reported values for ITO. In situ conductivity measurements confirmed the effect of the annealing atmosphere on the conductivity of the films.

It has been known for decades that it is difficult to fabricate polycrystalline In_2O_3 and ITO with high density. Nevertheless, the sintering of ITO is industrially important due to an industrial demand for dense ITO-targets used in sputtering. A comprehensive sintering study of the nano-crystalline, phase-pure powders of In_2O_3 and ITO was performed. Particularly the phase purity of the powder was important with respect to previous similar sintering studies. The mechanisms governing the sintering, with particular focus on the mass transport mechanisms, the effect of the tin doping and the sintering atmosphere were investigated. Mass transport below 1200 °C was given particular consideration since this temperature region has received very little attention in the literature. Hence, the present findings are also relevant for mass transport during heat treatment of ITO thin films, which is performed at significantly lower temperatures than the sintering of sputtering targets.

One of the main motivations for working with ITO was the possibility to dope ITO with rare earth elements (REEs), thereby enabling the combination of the excellent properties of the ITO host with the characteristic luminescence of the REEs. A thorough investigation of the equilibrium phase composition and solid solubility of neodymium, europium and terbium in In_2O_3 and ITO at 1400 °C was performed. It was confirmed that the cubic In_2O_3 crystal structure is a promising host for REEs, as expected from the crystal structure of the pure rare earth oxides. The solubility was shown to decrease with increasing size mismatch between the ionic size of the dopant and the host. Phase-pure materials of In_2O_3 and ITO doped with REEs were successfully prepared in form of nano-crystalline powders and thin films. In this form the solubility limit for the REEs could be circumvented by synthesis of metastable materials. The effect of the REE-doping on the optical and electrical properties of the two host materials was investigated by various spectroscopic techniques and electrical conductivity and thermopower measurements. Neither the conductivity nor the transparency of ITO thin films was significantly deteriorated by the REE-doping. Finally, strong emissions at around 611 nm were observed for Eu-doped In_2O_3, demonstrating the possibility of obtaining photoluminescence in a TCO host material.

Table of contents

Scientific papers

1. Background

Transparent conducting oxides (TCOs) are a unique class of materials, combining the properties of near-metallic conductivity, high optical transmittance in the visible region of electromagnetic radiation and high reflectance in the near-infrared region [1-6]. Due to this remarkable combination of properties TCO materials have numerous technological applications, such as flat panel displays, energy efficient windows, photovoltaic devices, thin film transistors, organic light emitting diodes (OLEDs), gas sensors, etc [4]. In order for a material to be transparent in the visible region of the electromagnetic spectrum, the band gap of the semiconductor must be larger than approximately 3 eV. However, oxides with a fundamental band gap of 3 eV or more are insulators at room temperature. In order for these materials to become conducting, free carriers must be donated into the conduction band either by non-stoichiometry, such as oxygen vacancies, or by doping [5]. However, the possible donors must have their ionisation energy close to the conduction band, in order to retain the large band gap and thus the optical transparency in the visible region. This condition severely restricts the possible materials that can be used as TCOs. Though the combination of transparency and conductivity in the same material is highly unusual and remarkable, it can be found in the oxides of In, Zn, Sn, Cd and Ga and also various mixtures between them, as shown in Figure 1.1 [1]. Over the past years the field has had a dramatic increase in interest and activity, both with respect to the scientific and technological aspects, and is notable for its current vitality with thousands of papers published over the last few years [3, 7, 8].

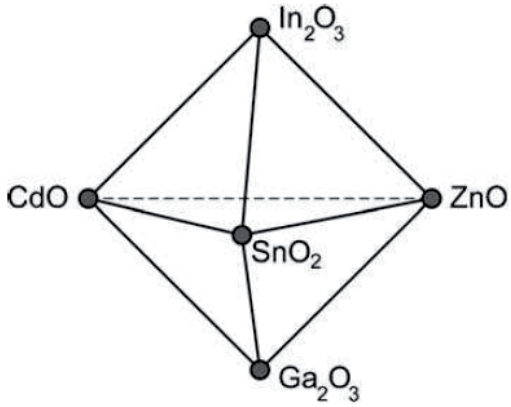

Figure 1.1. Composition space of conventional TCO materials [1].

The two largest industrial applications of TCOs are flat panel displays and energy-efficient windows, followed closely by the rapidly growing photovoltaic (PV) industry [7]. The market for flat screen high definition televisions, along with portable electronics and new hand-held devices, all with smart displays, has grown significantly over the past decade. In fact, the flat panel display market earned revenues of $65.25 billion in 2005 and was estimated to almost double to $125.32 billion by 2012 [7]. All of these devices require an electrical field to control the pixels, and are thus dependent on TCOs to function as transparent electrodes [4].

The growing awareness of energy efficiency makes energy efficient windows into a market in considerable growth. Because the TCO layer on such windows is transparent in the visible region, it allows the sunlight to pass from the outside to the inside. But as TCOs additionally are highly reflective in the infrared region it prevents the heat radiation from indoors from escaping [6]. This combination of properties makes these low thermal emittance-, or "low-e"-windows, very attractive for cold or moderate climates. In Europe alone, the demand for TCO-coated glass was 60×10^6 m^2 in 2007 and is estimated to grow to about 100×10^6 m^2 in a few years [7]. Additionally, TCO layers are also necessary as transparent electrodes for electrochromic or smart windows, which can be tuned to how much light they transmit [9, 10].

Application in PV devices is the third largest and fastest growing segment of the TCO market [7]. In order for solar cells to significantly contribute to the ever-increasing global energy demands, both the cost of the solar cells must be reduced and the efficiency increased. There are multitudes of emerging approaches, strategies and designs in order to achieve this, and TCOs are an integral part of the solar cell device in nearly all of them [11]. Typical designs of high efficiency solar cells where TCO layers are important components are given in Figure 1.2.

Indium oxide doped with tin oxide, also known as Indium Tin Oxide (ITO), is recognised as the TCO with the best combination of visible transmittance and electrical conductivity [8, 12-14]. There are different requirements for TCO materials depending on the specific application [15]. However, the excellent properties of ITO make it the material of choice especially for applications where the TCO is used as a transparent electrode, in which ITO is estimated to have a large market share [7, 16]. Undoped In_2O_3 can also be a TCO, with the donated electrons coming from oxygen vacancies [17], but n-type tin doping is normally used in order to prepare materials with superior conductivity. Indium is a limited resource, which, combined with its increasing usage, makes ITO an expensive material. Several alternative materials have been investigated in order to replace ITO, but none of them are yet able to match the excellent combination of

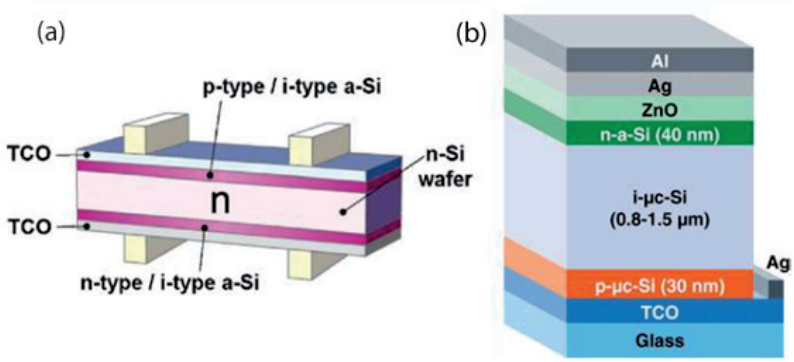

Figure 1.2. Typical configurations of novel PV devices where TCO layers are important components, a) Sanyo HIT cell (Heterojunction with Intrinsic Thin-layer) and b) amorphous-Si nip cell [7, 11].

transparency and conductivity [18, 19]. Hence, it is estimated that ITO will continue to be important for the transparent electrode market for many years, especially for applications where performance matters more than price [20].

ITO thin films can be deposited by a wide range of techniques, such as rf and dc sputtering [21-23], chemical vapour deposition [24-26], vacuum evaporation [27-29], pulsed laser deposition [30-32] and sol-gel methods [33-35], among which sputtering appears to be most widely used industrially [4, 12, 14]. Though sputtering can produce films with excellent properties, there are some disadvantages, such as high costs, low utilisation of target materials and that it produces rather brittle films [14]. The latter is especially crucial for the deposition of TCOs on flexible substrates, which has recently emerged as a hot research topic [36]. Aqueous based deposition techniques have several advantages both with respect to costs and being environmentally friendly [34]. The first part of this thesis work was devoted to the development of a water-based sol-gel process to ITO powders and thin films.

It has recently become attractive to dope wide band gap semiconductors with luminescent rare earth elements (REEs) [37]. Luminescent materials, also known as phosphors, usually consist of a host material and an activator. The latter is usually a REE or a transition metal which is added to the host as a dopant and is the species which is responsible for the luminescence [38]. The activators are usually efficient emitters of light once they are in the excited state, yet often ineffective at absorbing energy in the first place, due to forbidden 4f-4f transitions, which can severely limit the efficiency of the phosphor [39]. It is therefore, in many cases, attractive to co-dope the host with a sensitiser, a material that is good at absorbing

energy and can transfer this energy to the activator [38, 40]. An interesting feature of phosphors with wide band gap hosts, however, is that the luminescence can be sensitised by the host material itself, not from a co-dopant. In this case, UV light is absorbed and used to excite electrons across the band gap of the host, upon which the energy of the electrons in the conduction band can be transferred to the activator, thereby making the luminescence more efficient [37, 41, 42]. An illustration of such possible energy transfer mechanisms is given in Figure 1.3. It is not clear whether this energy transfer is occurring directly from the electrons in the conduction band or through defect states in the band gap.

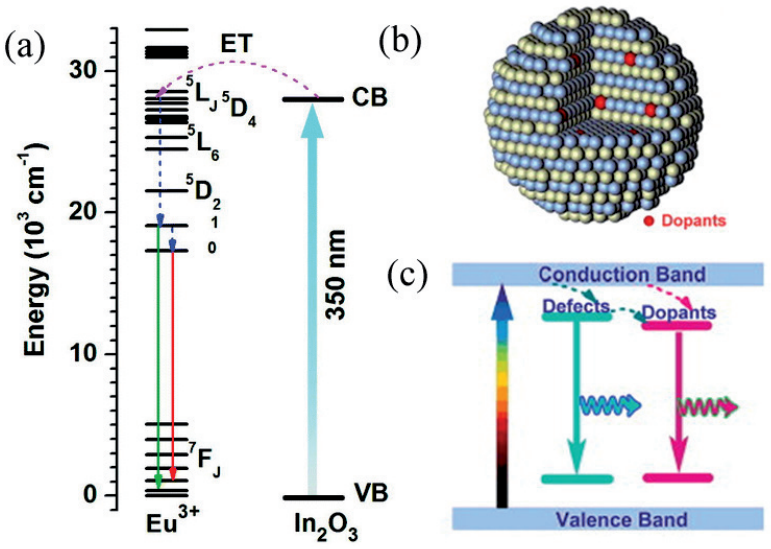

Figure 1.3. a) Schematic illustration of a direct transfer from the conduction band of In_2O_3 to Eu^{3+} after absorption of UV light [43]. b) Schematic illustration of a wide band gap semiconductor doped with luminescent rare earth elements [37]. c) The energy transfer leading to the sensitisation is proposed to either occur directly from the conduction band to the dopant or through defect states in the band gap [37].

Furthermore, the host materials in phosphors are traditionally dielectric materials, which are electrical insulators [38]. However, if it would be possible to create a phosphor that is conducting, by using for example a TCO as the host, it would potentially open up for new possibilities. An attractive way of utilising such a material is by applying electroluminescence, i.e. luminescence that is activated by en electric field or a current passing through the material [44]. As this field of

science is fairly immature it is not necessarily directed against a specific application. However, it is proposed that these novel materials, with a very interesting combination of properties, can find new applications, such as upconversion phosphors with potential use in solar cells, diodes or displays, lasing, bioimaging, optoelectronics or others [37, 42, 43, 45-47]. From a fundamental point of view it is of interest to investigate both how a TCO host affects the luminescence of the activators as well as how the dopant affects the transmittance and conductivity of the host. The latter was the motivation for investigating the effect of doping ITO with rare earth elements, utilising the aqueous sol-gel processing of ITO developed in this study.

2. Aim of the work

The first part of the thesis work was dedicated to the development of a wet chemical aqueous sol-gel route for the synthesis of ITO. The motivation was to develop a simple, inexpensive and environmentally friendly process, while retaining the ability to prepare excellent materials. Wet chemical methods have many advantages compared to physical methods, including cost, simplicity and readily control of homogeneity and composition. Furthermore, using water, as opposed to organic solvents, makes the synthesis more environmentally friendly and less expensive. The developed aqueous synthesis route was used to prepare ITO thin films with excellent properties by spin coating, but was also used to prepare nano-crystalline, phase-pure ITO powders.

During the synthesis of nano-crystalline ITO powders and further processing into ceramic monoliths it became apparent that sintering of ITO was challenging. Sintering of ITO is industrially important due to the need to fabricate dense targets for sputtering. The fundamentals of ITO sintering is also highly relevant for the heat treatment of ITO thin films, especially in cases where slurries containing ITO nano-particles are used to deposit the films, which is proposed as a promising technique for deposition on flexible substrates [14]. The second part of the study was therefore devoted to the sintering mechanism of nano-crystalline and phase-pure In_2O_3 and ITO powders.

The initial motivation for the interest in TCOs was their importance in the development of the next generation of solar cells. During the course of the work it became intriguing to explore the possiblities of utilising the TCO-layers in solar cells in a more active manner than just as transparent electrodes. More specifically, it was interesting to investigate the effect of doping a TCO with luminescent REEs. This could potentially enable upconversion, meaning the absorption of two or more low-energy photons with subsequent emission of a high-energy photon, in a layer which can also be used as an electrical contact. The chosen TCO was ITO because of its state of the art properties and also because indium oxide has the same crystal structure as the rare earth oxides [48, 49]. This indicated that the solid solubility of REEs was not too low for practical applications. The chosen REEs were neodymium, Nd, europium, Eu and terbium, Tb, because they are known to be attractive activator dopants [39], have their characteristic luminescence emissions in different regions of the electromagnetic spectrum [50] and also because of their considerable different ionic radii [49]. The initial emphasis was on the solid solubility and phase contents, including establishing the relevant phase equilbria and solubility limits in the respective phase diagrams. The subsequent focus was on

how the REE doping affected the TCO properties of the host, and to a lesser degree directly on the actual luminescence of the activator dopant. The former is of fundamental interest and has received significantly less attention in the literature. The novelty of these doped ITO materials lies in the new combination of properties, not only in the luminescence itself, but also how the inherent properties of the host become affected by the REE doping.

3. Introduction

3.1. Transparent conducting oxides

The ability of a material to be both transparent and electrically conductive at the same time is quite unique. The first report of a TCO was made by Bädeker in 1907, when it was published that an evaporated cadmium metal film could be oxidised to become transparent while retaining its electrical conductivity [51]. About half a century later more reports started emerging for CdO [52], but also for In_2O_3 and SnO_2 [53]. After a significant scientific effort, TCO materials such as doped SnO_2 and ITO with excellent properties were reported about a decade later [8, 54, 55]. An early application was to reduce the heat losses in sodium lamps [54], but the films were also used for transparent heating elements for aircraft and automobile windows [2]. Though the history of the TCO field is long and diverse the TCO industry is still dominated by only a few materials, most notably ITO, fluorine-doped SnO_2 and aluminium-doped ZnO. Furthermore, there is still not a complete theoretical understanding of the materials nor an ability to reliably predict the properties of new materials [7]. A recent example is amorphous In-Zn-O where even the basic transport physics is not understood [56]. Moreover, the industrial demand for better TCO materials it is continuously increasing. It is gradually becoming clear that the limits for todays materials are being reached and that existing materials may not be sufficient to meet future demands. There is therefore a need for a deeper understanding in order to improve the properties of excisting materials or predicting new potentially better materials.

The oxides of indium, tin, zinc, cadmium and gallium make up the conventional TCO composition space. Common for all of them is that they are post-transition metals with a full d-band and a relatively large band gap because of the strong metal-oxygen bond. Except for ZnO, this bond is predominantly ionic. The dispersion of the conduction band gives a high electron mobility, whereas the valence band is fairly flat making the hole mobility low. Hence, practically all TCOs are n-type conductors while it is significantly more challenging to produce p-type TCOs [57]. The general opto-electronic properties of TCOs can be summarised as near-metallic conductivity ($> 10^3$ S/cm), high transparency in the visible region (> 80 %) and high reflectivity in the infrared (IR) region of the electromagnetic spectrum. These general properties are illustrated if Figure 3.1.

The electrical and optical properties of TCO thin films are heavily linked to each other and are both influenced by parameters such as film thickness and charge

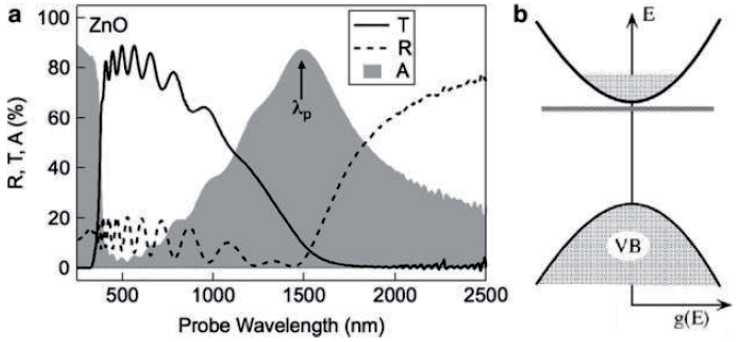

Figure 3.1. Optical spectra, transmittance, T, reflectance, R, and absorptance, A (a) and schematic electronic structure (b) of a typical ZnO-based thin film TCO material [7]. The plasma wavelength, λ_p, is indicated by an arrow.

carrier concentration. In the visible region of the spectrum, from about 380 to 740 nm, the transmittance is high while the reflectance and absorption are low. Here, interference due to the thickness of the films can be seen both in the transmittance and the reflectance curves in Figure 3.1 (a). The transparency window is restricted on the UV-side by the band gap of the material. Light with higher energy than the band gap will be absorbed by the material and used to excite electrons from the valence band to the conduction band, illustrated in Figure 3.1 (b). On the lower-energy side the transparency window is limited by the free electron properties of the material, where the plasma edge causes reflection and absorption.

The average transmittance in the visible region is generally a function of the film thickness, but can also be decreased by inhomogeneities in the film [2]. As the transmittance declines with film thickness, the sheet resistance, on the other hand, improves, which illustrates the link between the optical and electrical properties. A certain trade-off is thus necessary in order to optimise the properties of the film for the specific application. A TCO film should generally be thinner than approximately 150 nm in order to be suffuciently transparent [4]. The dependence of transmittance and sheet resistance on film thickness is given in Figure 3.2.

The frequency where the UV absorptions start is mainly dependent on the intrinsic band gap of the oxide, but is also linked with the free carrier concentration through the Burstein-Moss shift [58]. When the conduction band is empty the band gap is intrinsic. However, when the carrier concentration is increased the bottommost states in the conduction band become filled, which means that an increased energy

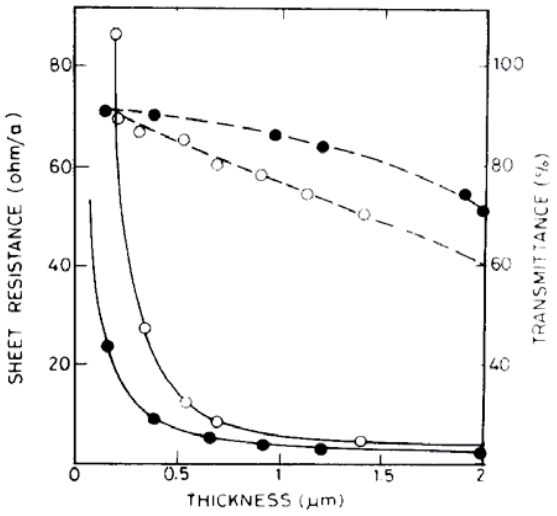

Figure 3.2. The dependence of the sheet resistance (solid lines, left axis) and average visible transmittance (broken lines, right axis) on the film thickness for fluorine-doped SnO_2 (○) and ITO (●) [2].

is necessary in order to excite electrons from the valence to the conduction band, as illustrated in Figure 3.3. This effect is well known for TCO-materials, and can increase the apparent band gap with as much as 0.8 eV [59]. Figure 3.4 shows how the absorption is shifted towards higher energies as the carrier concentration is increased. However, another effect is also illustrated in Figure 3.3. The increased carrier concentration will also cause many-body effects, like electron-electron and electron-impurity scattering, which will actually cause the top of the valence band and the bottom of the conduction band to come closer. Of these two effects the Burstein-Moss effect will dominate, causing a net increase in the observed band gaps with increased carrier concentration. However, the second effect, though smaller, can be very important in order to reconcile experiments with theory [59].

Though the link between the optical and electrical properties is evident on the UV-side, the influence of the carrier concentration is perhaps even more pronounced in the lower-energy IR-region. The transmittance in the IR-region will be reduced by collective oscillations of the conduction band electrons, known as plasma oscillations, causing both reflection and absorption through intraband transitions within the conduction band. These processes are quite complex, yet simplified models based on the classical Drude free electron theory gives an excellent agreement with experiments [1, 6]. At which frequecies the transmittance

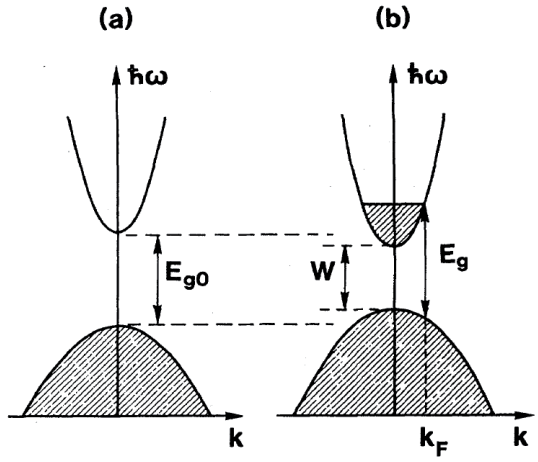

Figure 3.3. Schematic illustration of the band structure of a TCO with empty conduction band (a) and with electrons filling the bottom states in the conduction band (b). The filling of the bottommost states causes the apparent band gap to increase ($E_g > E_{g0}$). Modified from [59].

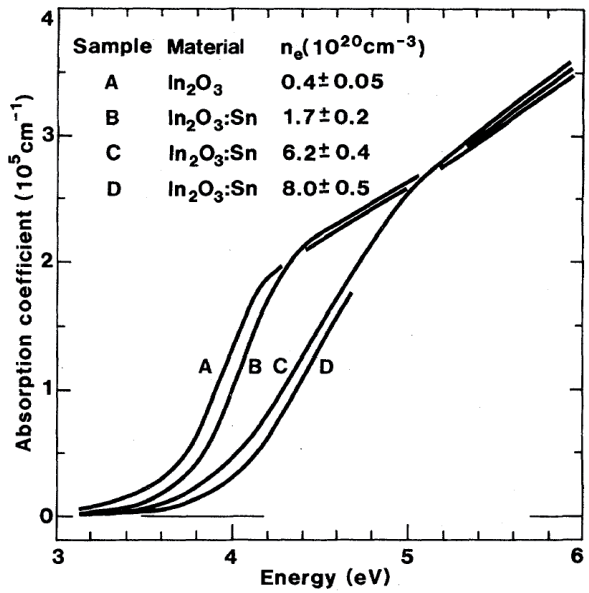

Figure 3.4. Absorption coefficient for four different In_2O_3-based samples with different carrier concentrations, n_e [59].

decreases is related to the plasma wavelength of the material, λ_p, which varies with the carrier concentration, n, according to the Equation 3.1:

$$\lambda_p \propto \frac{1}{\sqrt{n}} \tag{3.1}$$

Figure 3.5 illustrates how the onset of the reflection and the maximum absorption is shifted to higher wavelengths as the carrier concentration is increased, thereby reducing the region where the TCO is transparent. For the two curves with lowest carrier concentration the reflection and absorption starts at longer wavelengths than the figure depicts.

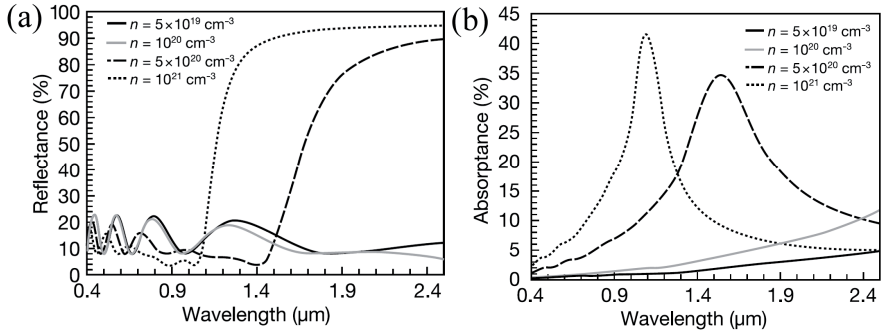

Figure 3.5. Calculated reflectance (a) and absorptance (b) of a general TCO thin film material as a function of wavelength. The carrier concentration, n, was varied between 5×10^{19} and 10^{21} cm^{-3}. Other parameters, such as mobility, film thickness and effective mass of the carriers were kept constant [1].

As the intrinsic conductivity of TCOs is fairly limited due to their large band gaps, either doping or introducing a non-stoichiometry in the material is important in order for the conductivity to become near-metallic [5]. The oxygen stoichiometry is therefore important, as oxygen vacancies in the lattice can donate electrons. However, doping is usually necessary in order to get materials with sufficient conductivity for most applications. For doping of TCO materials to be succesful, three criteria must be fulfilled; the dopant must be soluble in the host lattice, the donor level must be shallow in order to retain the large band gap and the dopant must not be compensated by an intrinsic defect [60]. Furthermore, the conductivity of a material is a function of the product of the carrier concentration and mobility. However, these two properties are also linked to each other making it impossible to increase the conductivity above a certain limit. The mobility of electrons can be limited by scattering from different sources, such as phonons, grain boundaries and

neutral and ionised point defects. The activated dopants which donate electrons also produce ionised impurities in the host lattice. A high carrier concentration therefore also leads to a high concentration of these ionised impurities [4]. In fact, in order to produce TCO material with a satisfactory conductivity to be useful for most applications, the carrier concentration is so high that the ionised impurity scattering is limiting the mobility [15]. This behaviour is illustrated in Figure 3.6 for ZnO materials with different carrier concentrations. For low carrier concentrations the mobility is limited by grain-boundary scattering, but as the carrier concentration is increased ionised impurity scattering becomes limiting. Furthermore, if the doping level is increased above a certain point the dopants will simply produce neutral dopants that do not contribute with electrons, but still decrease the mobility [15]. From the previous discussion it is evident that both the optical and electrical properties are diminished by a too high carrier concentration. In order to produce TCO-materials with improved conductivity it is therefore proposed that it is the mobility of the electrons that must be improved [7].

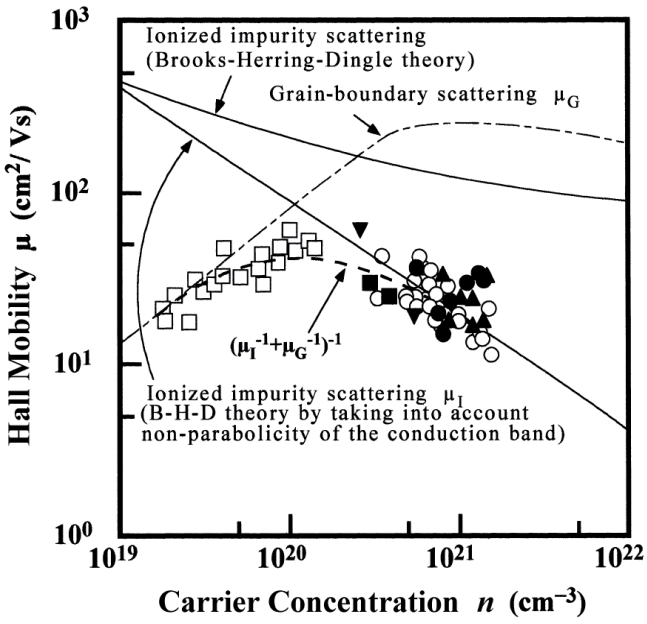

Figure 3.6. The electron mobility in ZnO materials as a function of the carrier concentration. For low carrier concentration the mobility is limited by grain boundary scattering but at higher concentrations ionised impurity scattering dominates [18].

3.2. Indium tin oxide

Indium tin oxide, i.e. indium oxide doped with tin oxide, is recognised as the state of the art TCO [6, 8, 12]. In_2O_3 crystallises in the cubic bixbyite structure, also known as the C-type rare earth structure, with space group $Ia\bar{3}$, nr 206 [48]. This structure is similar to that of fluorite, but differs in that only three quarters of the anion sites in fluorite are occupied, in accordance with the In_2O_3 stoichiometry. The bixbyite unit cell contains 16 formula units which correspond to 80 atoms and the cubic lattice parameter is 10.117 Å. The 32 cations in the unit cell occupy two different sites, the Wyckoff positions 8b and 24d [13]. A bixbyite unit cell is shown in Figure 3.7 (a) and the two different cation positions are illustrated in Figure 3.7 (b).

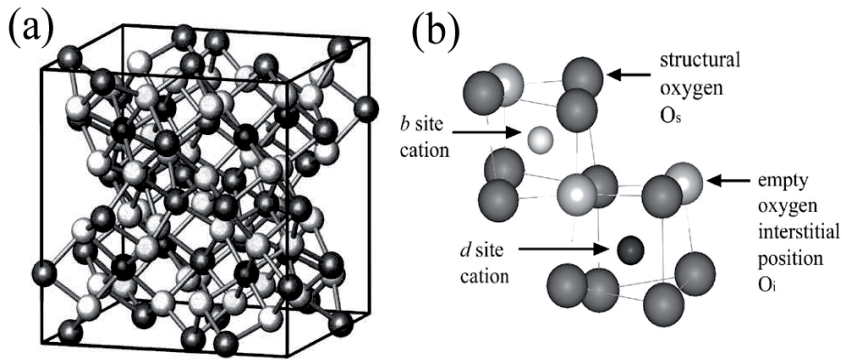

Figure 3.7. Illustration of the bixbyite crystal structure (a). Black spheres are indium atoms in the 8b position, grey spheres indium in the 24d position while the white spheres are oxygen atoms [61]. (b) Illustration of the two non-equivalent cation positions in the bixbyite lattice [13].

Both of the cation positions are in the center of distorted cubes where six of the corners in the cube are occupied by oxygen atoms and the two remaining corners, which are in the 16c position, are empty lattice sites. These sites are particularly important for the defect structure of ITO, as this is the sites for the interstitial oxygen ions [13, 62]. The difference between the two cation positions is that in the 8b position the two empty sites are along the body diagonal of the cube while they are along a side diagonal for the 24d position. The 8b position is more symetrical with all six oxygen anions at a distance of 2.18 Å, while the less symmetrical 24d positions has the oxygen atoms at three different distances, namely 2.13, 2.19 and 2.23 Å. The oxygen atoms are coordinated to four cations and occupy the 48e Wyckoff position. When tin doping is used, tin prefers to go into the higher

symmetry 8 b site [13, 63, 64]. The large and complex unit cell in the bixbyite structure is believed to be a major reason for why the theoretical understanding of ITO has been rather limited until recent years [8].

Indium oxide can also be found in a metastable rhombohedral corundum structure, with space group $R\bar{3}c$ and cell parameters a = 5.487 and c = 14.510 Å [65, 66]. This is a high pressure polymorph for In_2O_3. Sesquioxides with small cations, such as Al_2O_3, usually exist in the corundum crystal structure, wereas larger cation sesquioxides, among them In_2O_3, have the bixbyite structure. Most of the sesquioxides with the C type rare earth crystal structure as the stable polymorph will have the so-called A- or B-type rare earth crystal structures, with space group *P32/m* and *C2/m* respectively [49], as their high-pressure polymorphs [67]. Only In_2O_3 and Tl_2O_3 have the corundum structure as their high-pressure crystal structure, possibly because of their M-O bonds being more covalent than for many of the other sesquioxides [66, 67]. In both the bixbyite and the corundum structure the cations and anions have coordination numbers of 6 and 4 respectively, and the bond lengths are similar. However, the corundum polymorph is about 2.5 % denser because of a better packing of the anion sub-lattice. The polyhedra are also different; in the corundum the cations are in the center of regular octahedra, while the cations in bixbyite are coordinated to anions in six out of eight corners of a cube. The transition from bixbyite to corundum can be considered as a distorted ccp to hcp transition [68]. As the corundum structure is metastable for In_2O_3 at ambient conditions, once it is formed it will transform to the stable cubic bixbyite when heated to about 700 to 900 °C [68, 69]. Though the corundum structure is a high-pressure polymorph for In_2O_3, density functional theory (DFT) calculations have shown that this phase is actually metastable also at high pressures, with another phase, the ortorhombic Rh_2O_3(II) structure with space group *Pbna*, being stable at higher pressures [68, 70]. ITO generally has a bixbyite structure in all applications, but it has also been demonstrated that ITO with the corundum structure can be prepared with attractive properties [67, 71, 72], which has also been supported by DFT calculations [73]. Furthermore, though corundum In_2O_3 is a high-pressure phase, it has also been demostrated that the polymorph can be prepared at ambient pressures, when non-equilibrium conditions are applied [68, 71, 72]. More specifically, this has been reported when wet chemical methods have been used to produce 1D nanostructures [74, 75] or when InOOH is used as precursor [74, 76, 77].

The In_2O_3-SnO_2 phase diagram is depicted in Figure 3.8. The solubility of indium into tin oxide is limited to about 0.3 mol % [78], as In^{3+} is a larger cation than Sn^{4+} [79]. The most important technological phase, however, appears on the indium-rich

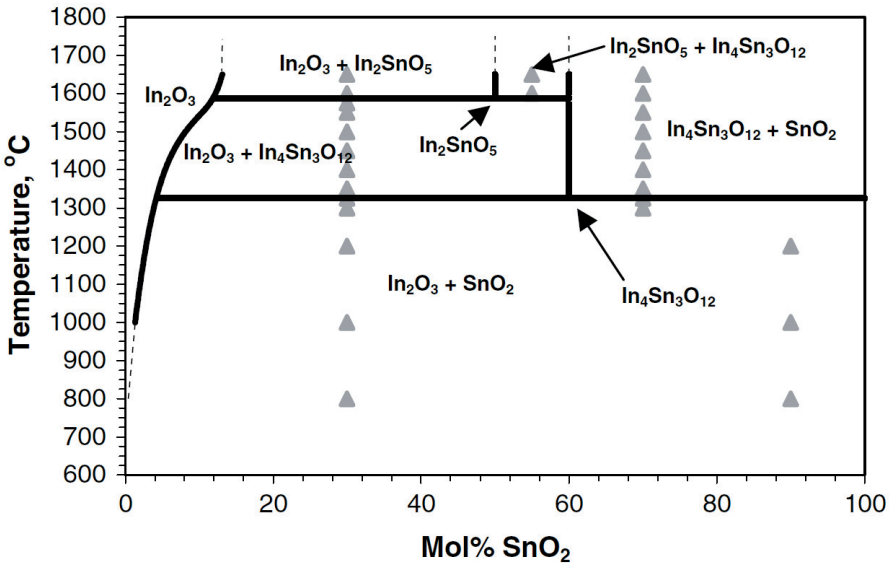

Figure 3.8 Phase diagram of the In_2O_3-SnO_2 system [78]. The grey triangles are the starting compositions that were used to obtain the compositional data.

side of the phase diagram. Though ITO is commonly used with tin doping amounts from 5 to 10 cat %, the thermodynamic solid solubility is only around 2 cat % when the temperature is below 1200 °C, and 3 cat % at 1375 °C [80]. This indicates that almost all ITO that is used in practical applications is actually not in equilibrium. The kinetics of the exsolution of excess tin compared to the solubility limit is relative slow at temperatures below 900 °C, suggesting why it is relatively easy to obtain ITO with high doping concentrations [80]. Furthermore, at higher temperatures an intermediate $In_4Sn_3O_{12}$-phase is formed [80]. This phase has space group $R\bar{3}$ and is, like bixbyite, a fluorite-related structure [63, 81]. There are some disagreements in the literature regarding at which temperature forms, but recent work indicates the formation temperature to be approximately 1340 °C [82]. Once the phase has formed, however, it is quite stable and not easily removed upon cooling to room temperature. Its structural similarities with bixbyite, makes this phase difficult to observe with XRD, as almost all reflections overlap [80]. This phase has also been reported to have good TCO properties [83]. At even higher temperatures, above 1650 °C, another intermediate phase, In_2SnO_5 has also been reported [78].

In the early 1980s Frank and Köstlin developed a model for the defect chemistry of ITO [84], of which its general features still appears to be valid [13, 85-87].

Undoped In_2O_3 is an n-type conductor [88-92], in which the free electrons are donated from oxygen vacancies according to Equation 3.2:

$$O_O^X \rightarrow V_O^{\bullet\bullet} + 2e' + \frac{1}{2}O_2(g) \qquad (3.2)$$

The removal of oxygen from the In_2O_3 lattice has been confirmed by thermogravimetrical analysis [90] and by electron probe microanalysis [93]. However, it is only possible to remove less than 1 % of the oxygen atoms, thereby restricting the carrier concentration of undoped In_2O_3 [84]. In order to further increase the conductivity doping is necessary. Doping with tin, thereby preparing ITO, is by far the most common choice, but also other dopants such as Mo^{6+} [94, 95], Zr^{4+} [96] and fluorine doping on the anion site [97] have been reported. When Sn^{4+} is incorporated into the bixbyite structure each tin atom theoretically donates one electron according to Equation 3.3:

$$2SnO_2 \rightarrow 2Sn_{In}^{\bullet} + 2e' + 3O_O^x + \frac{1}{2}O_2(g) \qquad (3.3)$$

Mössbauer experiments have only detected Sn^{4+}, not Sn^{2+}, which indicates that all tin dopants theoretically should be able to function as n-type donors [98-100]. However, the carrier concentration is only proportional to the amount of tin atoms at doping levels lower than about 1 cat % and at partial oxygen pressures below ~ 10^{-20} bar, indicating that the tin atoms are being compensated [84]. Frank and Köstlin suggested that this could theoretically be caused either by oxygen interstitials or by cation vacancies. Furthermore, they argued that the former was most likely due to observations of changes in film thickness after oxidation and reduction. This is also in agreement with the general trend of fluorite-related structures, being that the cation sub-lattice is left intact and it is the anion sub-lattice that is affected when the stoichiometry of the compound changes [84]. At high doping levels and high oxygen partial pressures the active tin dopants will thus be compensated by interstitial oxygen atoms which form clusters of the type of $(2Sn_{In}^{\bullet}O_i^{''})^X$. By postsynthesis reduction, these oxygen interstitals can be removed, thereby activating the tin donors again:

$$\left(2Sn_{In}^{\bullet}O_i''\right)^X \rightarrow \frac{1}{2}O_2(g) + 2Sn_{In}^{\bullet} + 2e' \qquad (3.4)$$

However, even though reduction of the clusters releases more charge carriers, the carrier concentration does not match the tin doping level even after post-reduction at pO_2-levels of ~ 10^{-20} bar. Frank and Köstlin proposed that some of the neutral defect clusters were reducable whereas in other clusters the interstitial oxygen was

so tightly bound that it was not possible to remove it by reduction [84]. It is generally still believed to be true that some of the dopant tin atoms can be activated by reduction whereas others remain compensated. However, there is some discrepancy in the literature regarding what makes the interstitial oxygen atoms so tightly bound in some clusters and not in others. It is proposed that the higher the amount of tin atoms surrounding an interstitial oxygen atom, the more tightly bound it is [13]. It has been demonstrated that oxygen deficiency can only occur for undoped In_2O_3, but never for ITO [87, 90, 93]. When tin is used as a dopant, Rietveld refinement has demonstrated that the interstitial oxygen positions will always be occupied to some extent, and that this occupation is reduced upon reduction, in agreement with the defect model [13, 64]. A calculated Brouwer diagram, i.e. a diagram showing the different defects in ITO as a function of the partial pressure of oxygen, is given in Figure 3.9 [87]. The diagram is divided into three regimes. In the first regime, at extremely low partial pressure of oxygen, the electron concentration, n, is given by the concentration of oxygen vacancies. At intermediate oxygen pressures practically none of the tin dopants are compensated and n follows the same curve as the amount of tin at indium sites, $Sn_{In}^{\bullet}$. As the oxygen partial pressure is increased, more $(2Sn_{In}^{\bullet}O_i^{''})^X$ clusters appears and at some point the amount of electrons are reduced by compensation of the tin donors. In this regime the amount of free electrons is proportional to $pO_2^{-1/8}$. In recent years,

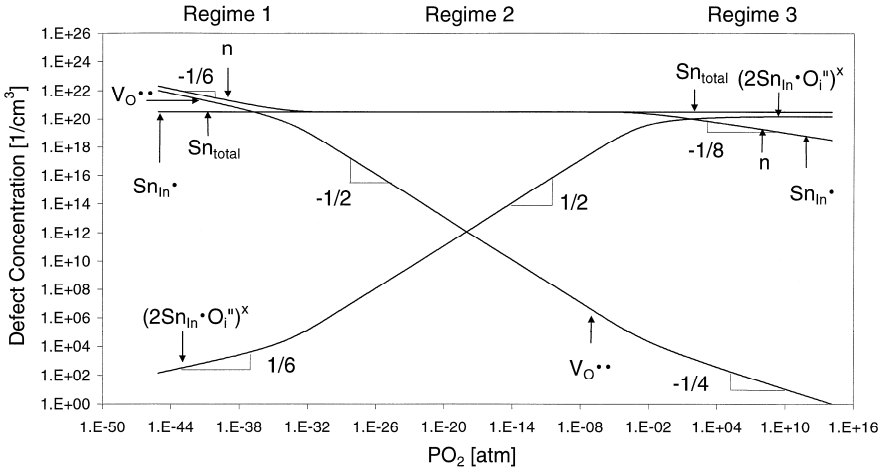

Figure 3.9. Calculated Brouwer diagram showing the defect concentration for different defects in ITO as a function of oxygen partial pressure. The values are calculated for ITO with 1 cat % Sn at 500 °C [101].

several DFT calculations have been made in order to investigate the possible point defects in ITO [70, 102]. These theoretical calculations tend to agree with the general features of the defect model proposed by Frank and Köstlin.

Even though Sn^{4+} is a smaller cation than In^{3+}, with the ionic radii being 0.71 and 0.81 Å respectively [79], the lattice parameter of the cubic unit cell of In_2O_3 actually expands with tin doping [63]. A typical figure illustrating how the lattice parameter of In_2O_3 varies with tin doping is given in Figure 3.10. The lattice parameter increases with doping until it saturates and reaches a plateau. This limit is related to the solubility limit and with higher tin content secondary phases will appear.

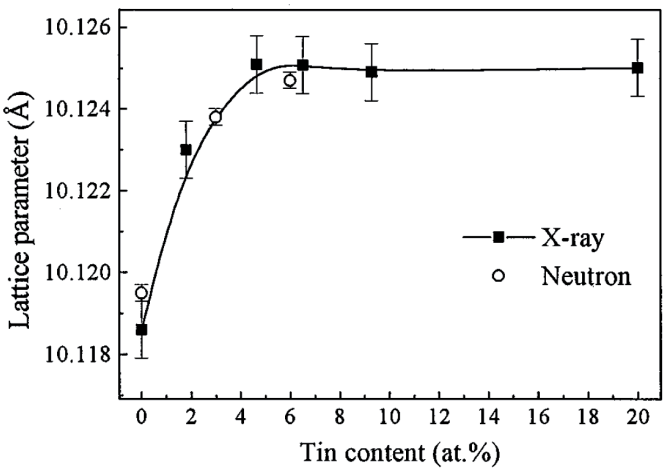

Figure 3.10. Variation of the cubic lattice parameter of In_2O_3 as a function of tin doping [63].

For undoped In_2O_3 the lattice parameter is not very dependent on the partial pressure of oxygen, although annealing in reducing atmospheres, appears to somewhat contract the lattice [13]. When In_2O_3 is doped with tin, on the other hand, the effect of annealing in reducing atmospheres is opposite. In this case removing interstitial oxygen atoms by reduction actually expands the lattice. This expansion is proposed to be due to incomplete shielding of the neighbouring positively charged Sn^{4+} atoms by the interstitial oxygen [13, 84]. Expansion due to reduction of metal cations is, however, well known in oxides, and is referred to as chemical expansion [103-105].

The conductivity of ITO increases with tin doping until it reaches a maximum at a certain dopant concentration and eventually decreasing upon further increase. This maximum is normally between 5 and 10 cat %, but depends on synthesis and deposition parameters [12]. Variations in the specific resistance and carrier concentrations of ITO as a function of tin doping amount are given in Figure 3.11 (a) and (b), respectively. The minimal resistance is located somewhere between 5 and 10 cat % Sn, but is also a function of the partial pressure of oxygen. It can clearly be seen that annealing in reducing atmospheres dramatically improves the conductivity by increasing the carrier concentration. It is also demonstrated in Figure 3.11 (b) that the carrier concentration is only proportional to the tin doping amount (parallell to the line marked $N = 3 \cdot 10^{20} \cdot c_{Sn}$) at low doping amounts and at low partial pressure of oxygen. The mobility of electrons in ITO is also affected by the tin doping. The mobility in undoped In_2O_3 single crystals has been reported to be 160 $cm^2 V^{-1} s^{-1}$ [106]. For ITO, on the other hand, the mobility drops down to about 30 $cm^2 V^{-1} s^{-1}$ [6]. The largest scattering source, which causes the drop in the mobility, is proposed to be ionised impurity scattering [4]. Thus, the tin dopant, which donates the electrons to get a high enough carrier concentration, is also limiting the mobility.

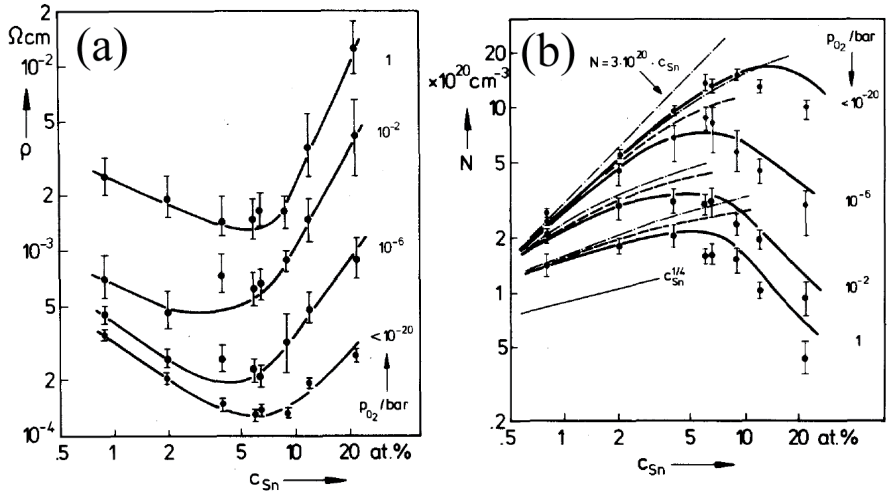

Figure 3.11. Variations in specific resistance (a) and carrier concentration (b) in ITO with varying tin doping amounts. The measurements were done at room temperature, but the samples were annealed at 500 °C in atmospheres with different pO_2. Modified from [84].

The optical properties of ITO is also heavily influenced by the carrier concentration, and thereby by the tin doping amount, as depicted in Figure 3.12 [8]. As the free charge carrier concentration is increased, the plasma wavelength is moved towards the visible region, according to Equation 3.1, which causes the reflection to begin at higher energies. Consequently, this shifts the wavelength at which the transmittance decreases similarly. Another interesting feature in Figure 3.12 is that for the curve with the lowest carrier concentration interactions with the lattice vibrations, or phonon absorptions, can be seen in the far infrared region. As the carrier concentration is increased, however, the free electron properties becomes so dominating that the phonon absorption cannot be observed anymore [6].

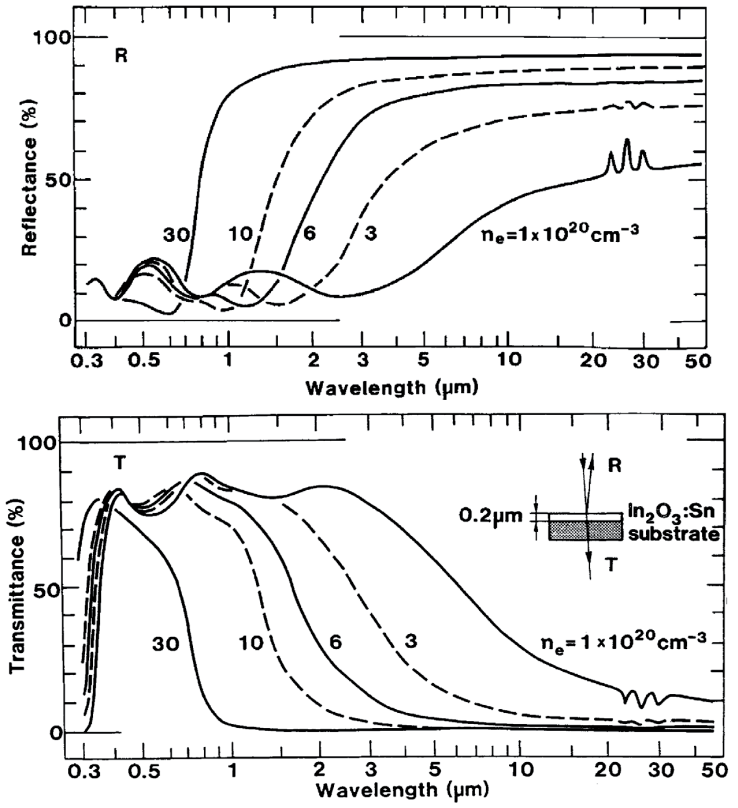

Figure 3.12. Calculated values for reflectance and transmittance for 200 nm thick ITO films with different charge carrier concentrations, n_e. From [8].

Already in 1977, Fan and Goodenough used X-ray photoemission spectroscopy (XPS) to propose a schematic band model for In_2O_3 and ITO [107], as depicted in Figure 3.13. More recently, as the computational capacity has improved, DFT calculations of both In_2O_3 [108, 109] and ITO [110, 111] has also appeared, and the calculated band structures correlates well with experimental photoemission spectra [112, 113]. Though the DFT calculations have demonstrated some discrepancies in the model from Fan and Goodenough [111], it still serves as an excellent model to describe some of the important features of ITO [5]. The top of the valence band consist mostly of oxygen 2p-states. Indium and tin 4d-states contributes more in the lower region of the valence band, and even further below comes oxygen 2s-states [60]. The bottom of the conduction band is dominated by indium 5s states, with indium 5p states being at higher energies. Oxygen vacancies, in the case of In_2O_3, or tin doping, in the case of ITO, will create shallow donor states just below the conduction band. When the carrier concentration is low, these states are separate. On the other hand, when the carrier concentration is increased the states

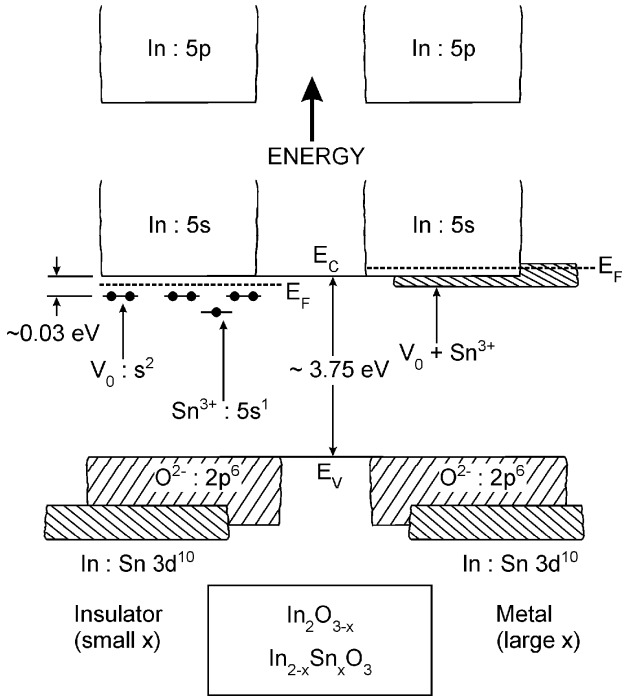

Figure 3.13. Schematic band structure model of In_2O_3 and ITO. From Edwards et al. [5], but modified from Fan and Goodenough [107]. The states at the bottom of the valence band should be In : Sn $4d^{10}$.

will create a contiunous donor band which overlaps with the conduction band, thereby creating a degenerate semiconductor. A further understanding of the electronic structure is gained from the DFT band calculations, where a typical example is given in Figure 3.14. The top of the valence band is rather flat, indicating a low mobility for holes, whereas the conduction band is higly dispersed. These features are common for all TCO-materials [60], and can explain why it is so difficult to obtain p-type TCOs with good conductivity [57, 114]. The band gap of materials are generally underestimated by DFT calculations [115, 116], which can be seen in the band gap in Figure 3.14 being only about 1 eV. Often a so-called scissor operator is used in order to shift the conduction bands higher in energy in order to match experimentally observed values. Though DFT-calculations have significantly increased the understanding of TCO-materials, there are still several issues that are being debated. At typical example is the inability to explain the intrinsic n-type conductivity of In_2O_3 [117]. Experimental results, more specifically the power-law dependence of the conductivity with $p_{O_2}^{-1/6}$, which has been well established [13, 84, 118] and can be seen in the left-hand side of Figure 3.9, indicates that the intrinsic conductivity is caused by oxygen vacancies donating

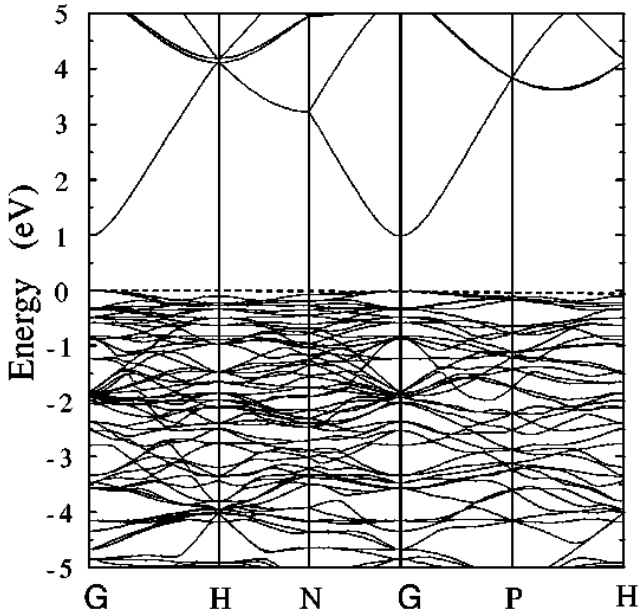

Figure 3.14. Calculated band structure of In_2O_3 [111].

two electrons each. However, it is not clear from DFT-calculations whether oxygen vacancies will create shallow donor levels which can actually donate delocalised electrons [119, 120]. This depends heavily on the choice of functionals and the operator used to correct the band gap values.

There has been a debate regarding the value and nature of the band gap in In_2O_3 and ITO. The band gap of ITO is widely quoted as being around 3.75 eV [59, 99]. However, weak absorptions starting from 2.62 eV have also been observed [121, 122] and X-ray photoemission spectra showed the top of the valence band to be less than 3 eV below the Fermi level (being just above the bottom of the conduction band) [112, 113, 123]. A hypothesis that In_2O_3 could have an indirect band gap at a lower energy than the direct band gap logically appeared. However, DFT band structure calculations could not demonstrate the possibility of an indirect band gap [73, 124, 125]. It has recently been demonstrated by Walsh et al. that the actual band gap is around 2.9 eV and direct [126]. The direct transition from the top of the valence band to the bottom of the conduction band is, however, parity forbidden and therefore weak. In order for strong transitions to occur, electrons must be excited from energy bands about 0.8 eV below the maximum of the valence band. This thereby explains why the observed band gap is usually in the order of 3.75 eV. An illustration of this phenomenon is given in Figure 3.15.

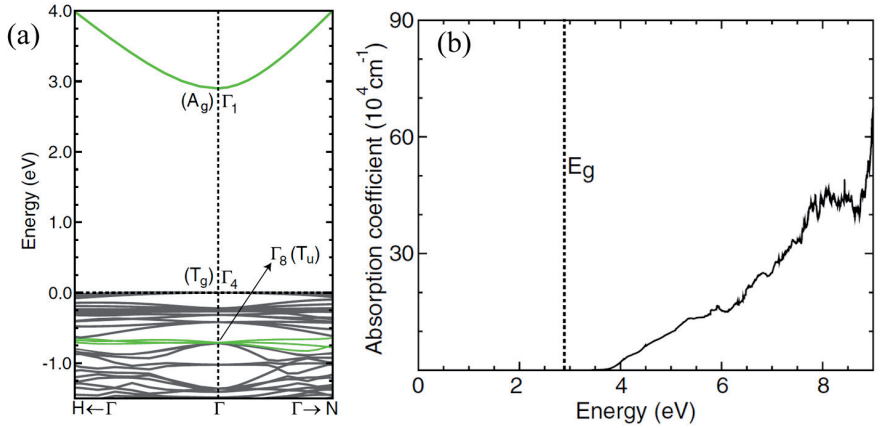

Figure 3.15. Calculated band structure of In_2O_3 (a). Strong excitations to the conduction band can only occur from below the green line labelled $\Gamma_8(T_u)$. Calculated absorption spectrum of In_2O_3 (b). From Walsh et al. [126].

3.3. Deposition of ITO thin films

Numerous thin film deposition techniques exist, all with different advantages and disadvantages [127]. Amongst the processes most widely used for ITO are rf and dc sputtering, chemical vapour deposition, vacuum evaporation, pulsed laser deposition and sol-gel methods [2, 3, 8]. The properties of the ITO thin films are known to vary and to be dependent on different deposition parameters [12]. The most widely used industrial technique for the deposition of ITO is sputtering [4, 14]. Sputtering is a physical vapour deposition process where high energy particles are bombarded onto a solid target material. Due to the high energy collisions atoms are then ejected from the target, travels through the sputter chamber and subsequently deposits on a chosen substrate [128]. Important parameters to control during the sputtering process are oxygen content in the sputtering gas, total gas pressure, the sputter power, the target to substrate distance, the substrate temperature, the post-deposition treatment and the target quality [4, 12]. When ITO first was sputtered onto glass for large-scale industrial purposes, some 40 years ago, metallic alloys of indium and tin was used as the target [4]. In this case the chamber was filled with oxygen in order to obtain the desired oxide final product. The properties of the materials deposited by this process was extremely sensitive to small changes in process parameters and the metallic target could also relatively easily be poisoned by impurities [129]. The industry therefore shifted to the use of ceramic oxide ITO targets instead. The properties of the target will greatly influence the sputtering process, and especially the density of the target has been shown to have an important effect, where high density targets lead to higher deposition rates and more homogeneous materials [129]. High density targets are, more specifically, less prone to black spots or nodule formation, i.e. the formation of large hillock-shaped defects on the target, which is illustrated in Figure 3.16. Once these are formed, some of the ejected material will deposit on the nodule, thereby making it grow. This causes severe instabilities in the sputtering process, as the nodule can explode, scatter and cause damage to the film, which is further explained in [130, 131].

Wet chemical methods can also be used to deposit ITO thin films [132, 133], generally by spin coating [134-139], spray coating [140-144] or dip coating [33, 35, 141, 145-153]. A subsequent heating and drying step is usually necessary in order to obtain the end product. Wet chemical deposition techniques generally have several advantages compared to sputtering or other physical deposition techniques [154]. The most significant advantage is the cost effectivenes, as the equipment used for wet chemical deposition is significantly simpler and less expensive. Furthermore, there is not a need for vacuum, meaning that there are no restrictions

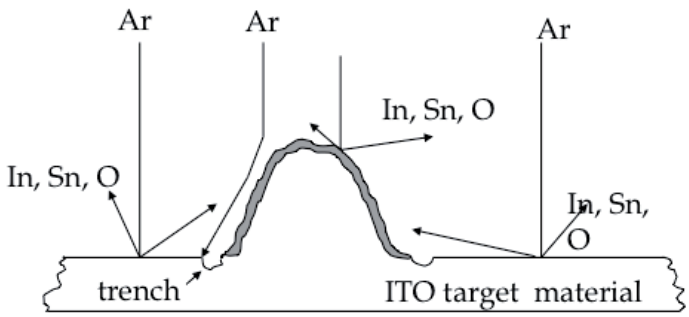

Figure 3.16. Cross section illustration of a nodule formed on the surface of an ITO sputtering target. From [130], but originally from [131]. Argon is used to bombard the ITO target with In, Sn and O atoms subsequently being ejected.

regarding the chamber size. It is therefore possible to coat larger substrates and substrates with different geometries compared to for instance sputtering [14]. Sputtering is also a wasteful process, as only about 15 to 30 % of the target is actually being deposited on the substrate. The rest ends up as waste on the chamber walls. In comparison solution based methods can have a better material utilisation [16]. Wet chemical methods also offer the possibility of controlling the homogeneity of the materials even down to the molecular scale. Additionally, the composition of the materials are readily controlled and trace amounts of dopant can easily be added [155]. The electrical conductivity of ITO thin films prepared by wet chemical or sol-gel methods are generally not as good as the best reported values for films deposited by other physical techniques [12, 154]. However, for some of the syntheses, especially where process parameters such as the post-synthesis annealing step in reducing atmospheres has been optimised [151], the reported conductivities are almost as good [135, 147, 156, 157]. Due to the popularity of ITO and the possible advantages of wet chemical methods, the literature on wet chemical techniques for the synthesis of ITO is vast. A brief review of the literature follows in the next paragraphs.

In the early 1980s Arfsten developed a classical sol-gel approach for the deposition of ITO thin films [33, 158]. This process was based on using indium and tin alcoxides, which upon chemical hydrolysis and condensation reactions form a polymer network based on M-O-M bonds between the metal cations and oxygen [159]. Typically, such reactions are given by Equation 3.5 and 3.6:

$$M(OR)_X + H_2O \rightleftharpoons M(OR)_{X-1}OH + ROH \quad (3.5)$$

$$M(OH)_X + M(OH)_X \rightleftharpoons (HO)_{X-1}M - O - M(OH)_{X-1} + H_2O \quad (3.6)$$

After this work other groups have also used similar sol-gel processes for deposition of ITO [137, 160]. Though this sol-gel process was demonstrated to be successful, it also has certain disadvantages, such as the cation alcoxides being expensive, difficult to obtain and sensitive to moisture. This approach gradually became less popular and techniques based on the dissolution of metal salts, which then later decompose to the oxide started to appear more frequently [34, 136, 147, 150, 154, 157]. Such processes are based on dissolving appropriately chosen metal salt precursors in a suitable solvent. As the salts are dissolved the cations are readily mixed at a molecular level. The challenge is then to maintain this molecular homogeneity as the solvent is evaporated and the material goes from a dissolved state to a solid state, i.e. preventing segregation or precipitation of unwanted secondary phases [161]. This is particularly important for complex multicomponent oxides [155].

Precursor solutions for wet chemical deposition techniques of ITO thin films can be sub-divided into two types depending on whether an organic solvent or water is used as the solvent. Proposed advantages of using organic solvents are that they lead to a better control of particle size, shape and crystallinity [162] and in some cases can dissolve higher concentrations of the metal salts, which in turn leads to thicker films during the deposition [151]. However, the disadvantage is that organic solvents are often flammable, expensive or harmful to the environment [34]. In comparison, using water as the solvent can be more environmentally friendly and thereby potentially more suitable for large-scale processes. In addition to the advantages related to so-called green chemistry, price and availability also points to water being a good candidate for a solvent in an industrial process [34, 136]. A large majority of the literature on wet chemical methods for preparation of ITO is based on organic solvents such as ethylene glycol [135, 154], acetylacetone [35, 153, 163], acetic acid [157], ethanol [147, 164], methanol [165], propanol [151] and benzene [166], although some water based processes have been reported [34, 134, 145]. Several metal salts have also been used as precursors. For indium, $In(NO_3)_3$ [134, 145, 154] and $InCl_3$ [135, 141, 157] are repeatedly used, although the use of metal-organic precursors such as indium acetoacetonate [35, 166] have also been reported. For tin, the choice of precursor is less diverse with a majority of the reported procedures using $SnCl_4$ [145, 167] as a precursor, although also in this case other alternatives have been reported [156, 166]. The use of tin nitrates has been reported [134], but pure tin nitrates, both based on Sn(II) and Sn(IV), are reported to be unstable under ambient conditions [163, 168, 169]. The choice of using chlorides is usually motivated by their high solubility. However, their use often complicates a synthesis with regard to safety and environmental concerns and subsequent washing steps can be necessary to remove residual chlorides formed during the process.

One of the most popular wet chemical methods for the preparation of complex functional materials is the Pechini method [170]. This process is based on the use of organic molecules in order to maintain the homogeneity as the solvent is evaporated. Salts of the desired cations are first dissolved in an apropriate solvent. An α-hydroxycarboxylic acid with two or more functional groups, typically citric acid, is used as a complexing agent. This acid complexes the cations, which increases their solubility and thereby prevents precipitations. A polyhydroxy alcohol, often ethylene glycol, is used in combination with the acid, functioning as a polymerisation agent. When the temperature is elevated, the acid and the alcohol will react and form esters, according to the reaction in Equation 3.7:

$$ROOH + R'OH \rightleftharpoons ROOR' + H_2O \tag{3.7}$$

A polymer network will be formed as the ester reaction continues to create new bonds between the acids and the alcohols. This rigid network will limit the movement of the cations, which contributes to maintaining the local homogeneity, thereby preventing the formation of undesirable phases [155]. A conceptual illustration of the mechanisms behind the Pechini process is given in Figure 3.17.

In addition to the conventional wet chemical methods to prepare ITO thin films, there is also an increasing trend the past decade to prepare ITO thin films from slurries of already crystalline nano-particles [162, 171-179]. The main motivation for this appears to be the deposition on flexible organic substrates, such as polyethylene terephthalate (PET) and polyethylene naphtalate (PEN) [16, 180]. The possibility of depositing electronics on such substrates can make it feasable to prepare devices which are lightweight, bendable, conformable, rugged and not easily breakable. An illustration of such a device is given in Figure 3.18. There has been a great interest for such devices, both from industry and consumers, and these properties cannot be obtained on hard inorganic substrates [181]. These flexible substrates could also be beneficial for the achievement of roll-to-roll processing, which would lead to substantial gains in manufacturing throughput and economy [180]. The challenge with these flexible substrates is that they cannot withstand elevated temperatures. A typical sputtering deposition of ITO takes place at about 300 °C, which is so high that the flexible organic substrates will decompose [16]. For a thin film deposited by a conventional wet chemical technique a subsequent heating step is also necessary in order to decompose and crystallise the film [35]. The motivation for using a slurry of nano-particles to deposit the thin film is that this heat treatment step can be done before the deposition on the substrates, as the nano-particles in the slurry are already decomposed and crystalline. The film consisting of nano-particles will, however, require a sintering step at elevated temperatures in order to get a good contact between the particles, thereby ensuring

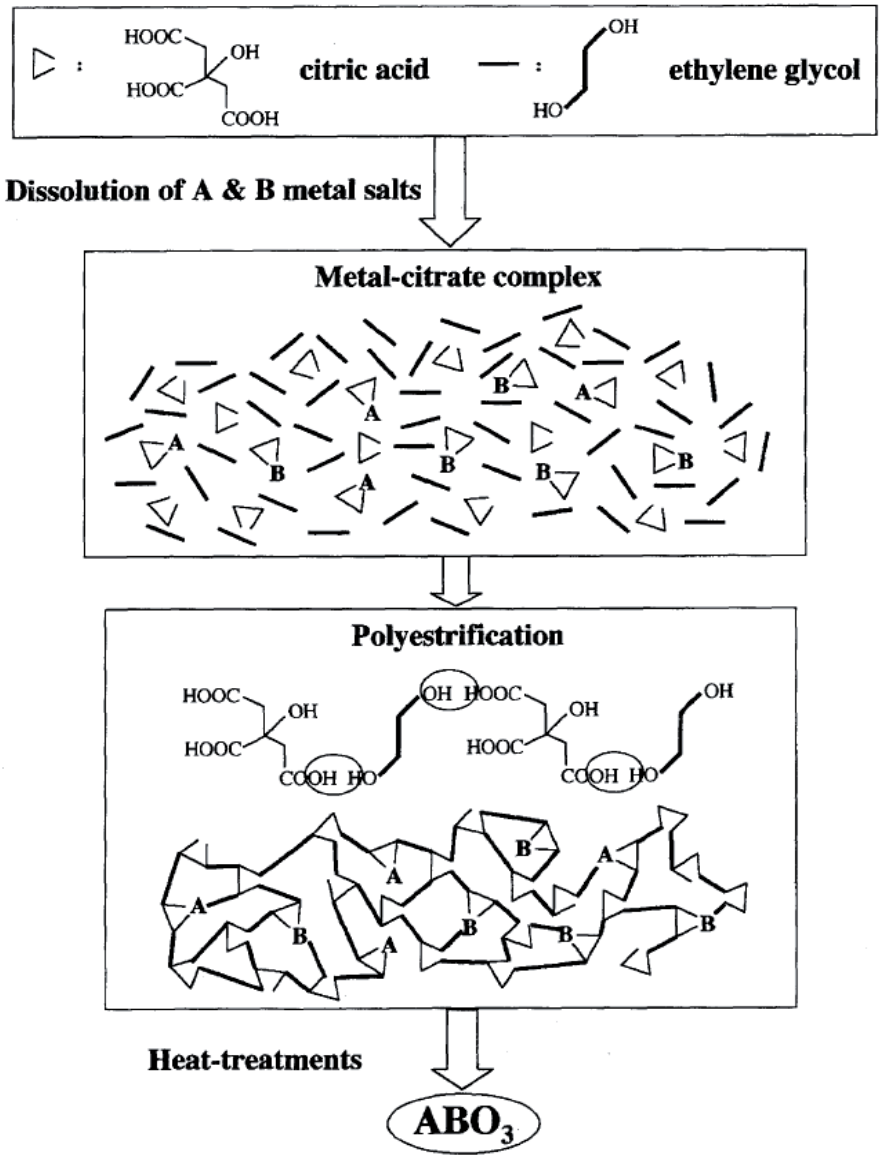

Figure 3.17. Conceptual illustration of the Pechini process for the preparation of a multicomponent ABO_3 oxide [155].

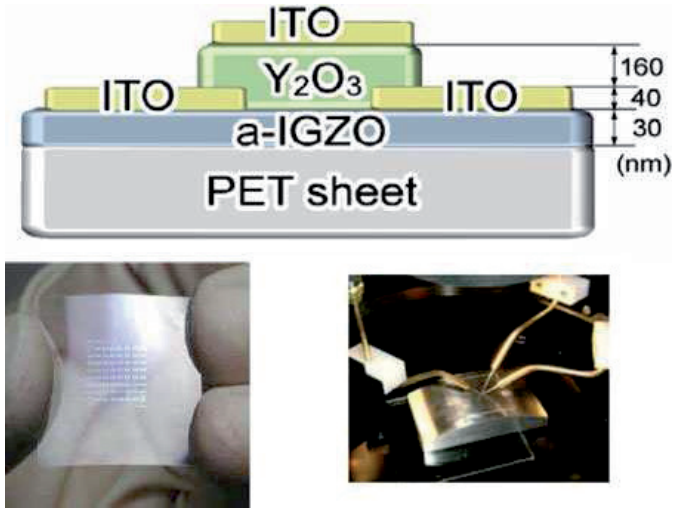

Figure 3.18. A transparent thin-film transistor (TTFT) on a flexible PET substrate, schematic model of the TTFT (top), a photograph illustrating how the flexible substrate with deposited electronic is fully transparent (bottom right) and a photograph of the TTFT in a bent position (bottom left). From [181], but originally from [36].

a sufficient conductivity [182]. There is thus a desire to prepare nano-particles with as small size as possible, in order to give a high driving force for sintering, meaning that the sintering step can take place at as low temperature as possible [177]. Furthermore, sputtered films of ITO are also quite brittle, which further indicates their low suitability for flexible devices. It is proposed that ITO thin films based on deposited layers of nano-particles could also have the potential to overcome this problem [16]. Another advantage of using slurries of nano-particles is the potential use of ink jet printing, which would make the patterning of the film easier [16, 138, 173, 183]. It is also proposed that such methods could give thicker deposited layers than conventional wet chemical deposition. This could avoid the use of multiple depositions in order to obtain sufficient conductivity, which is undesirable from an industrial point of view [174].

3.4. Sintering of ITO

Sintering can be defined as a thermal treatment used to convert a powder compact into a, most often preferrably dense, continuous solid [184]. In general, sintering processes can be divided into two types, solid-state and liquid phase sintering, depending on whether a liquid phase is formed during the heat treatment. For high-performance ceramic materials, where high purity is crucial, solid-state sintering is the most important [185], and only solid-state sintering is treated in the following text. The thermodynamic driving force for sintering is the reduction of free energy of the system by a decrease in surface area and also by aligning pressure differences that exist across the curved surfaces of the particles. Smaller particles will thereby have a larger driving force for sintering than larger particles [102]. Sintering is often thought of in stages according to which physical changes take place. During the first stage the particles bond together forming necks. In the second, the necks will grow, thereby forming grain boundaries, and some densification takes place. Finally, in the third stage, significant grain growth occurs and the remaining porosity between the grains is removed [186]. The final microstructure of the ceramic will depend on which mass transport processes that are present throughout the sintering. Mass transport from the surface of the particles to the neck will create a coarse and porous microstructure. Transport from the grain boundaries between the particles to the neck, on the other hand, will cause shrinkage and lead to a dense microstructure [185]. These mass transport mechanisms are illustrated in Figure 3.19.

Since sputtering is the most frequent industrial deposition technique for ITO thin films, and the importance of using highly dense ITO targets has been pointed out [12, 129, 187], the sintering of bulk ITO is highly industrially relevant. Furthermore, thin films prepared by deposition of suspensions containing ITO nano-particles on flexible substrates also require a subsequent heat treatment step [183]. Whereas the sintering of dense bulk ITO targets takes place at temperatures around 1400 °C, the heat treatment of films on flexible substrates takes place at significantly lower temperatures. However, the constrained sintering of thin films generally occurs through the same mechanisms as for bulk materials [188]. It has been known for decades that it is difficult to fabricate polycrystalline In_2O_3 and ITO with high density [88, 189, 190]. The challenges related to the densification have caused considerable interest in nano-crystalline In_2O_3 and ITO powders with enhanced sintering properties due to increased surface area [69, 191-198]. These powders have mostly been prepared by co-precipitation methods [69, 191-195, 197]. However, it is difficult to prepare single phase SnO_2-doped In_2O_3 by

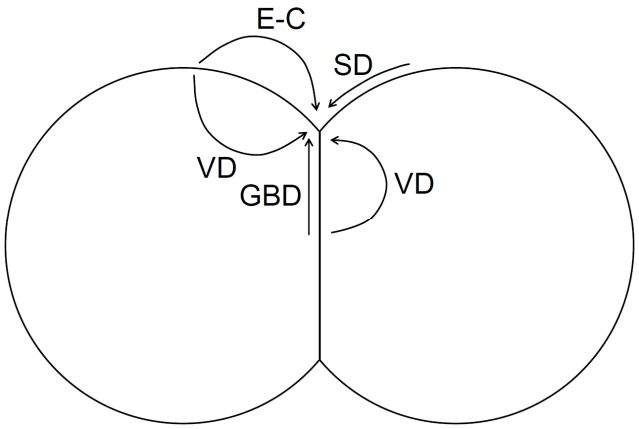

Figure 3.19. Mass transport mechanisms during sintering, including volume diffusion from surface and grain boundary (VD), grain boundary diffusion (GBD), surface diffusion (SD) and evaporation-condensation (E-C). Modified from [185].

co-precipitation due to the possibility of separate precipitations of In and Sn hydroxides, resulting in a heterogeneous cation distribution. Many interesting aspects regarding the sintering of ITO have been covered in the literature, including the use of sintering additives [199-202], the effect of the heating rate [191, 195], a phase transformation [69, 193], the tin doping concentration [194] and the pressure applied to compact the green body [192]. Reports on the sintering of dense ITO targest have also recently appeared in the litereture [203, 204]. However, a comprehensive understanding of the mass transport mechanisms taking place over a wide range of temperatures during the sintering of ITO appears to be lacking.

3.5 ITO doped with REEs

In 1888 the German physicist Eilhardt Wiedemann defined the word luminescense as all the emissions of light from a material that is not caused by it glowing due to high temperatures [205]. In order for this to occur the material must first absorb energy in some form, and the source of this energy adds different prefixes to the word. Photoluminescence is caused by the material absorbing energy in the form of photons, while cathodoluminescense and electroluminescense are caused by an electron beam hitting the material or by a current through the material, respectively [206]. Also other forms of luminescense, such as bioluminescense and chemoluminescense, exist. A luminescent material is often called a phosphor, and

the phosphors usually consist of a host and an activator [38]. The latter is normally an impurity, often added intentionally in small amounts, and is in fact the species which is responsible for the emission of light. In incandescence, where a material glows because of high temperatures, all of the atoms in the material are responsible for the emission. In luminescence, on the other hand, only a fraction of the atoms, the activators, are emitting light. The activator ions are normally rare earth elements or transition metals [38]. The REEs are characterised by partially filled 4f orbitals, and the emissions from these activators are due to energy transitions within this orbital. The 4f orbitals are shielded from external fields by the electrons in the 5s and 5p orbitals with higher energy. This means that 4f energy levels of the REEs are more or less not influenced by the crystal field from the host [207]. Furthermore, transitions within the 4f energy levels are generally parity forbidden, which leads to long lifetimes for phosphors based on REE activators [39]. Selected 4f energy levels of Nd, Eu and Tb are given in Figure 3.20.

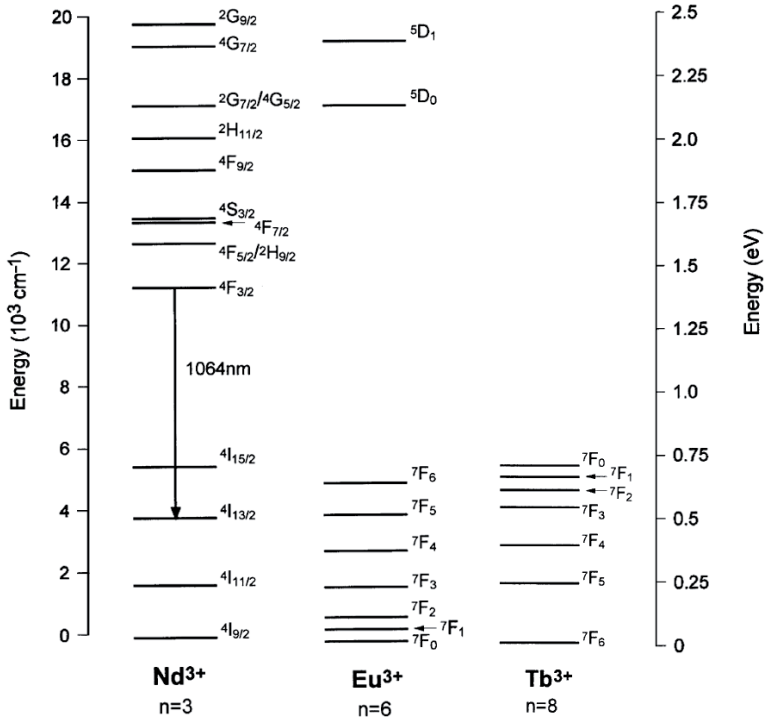

Figure 3.20. Selected 4f energy levels of Nd^{3+}, Eu^{3+} and Tb^{3+}, with 3, 6 and 8 electrons in the 4f orbitals respectively. A technologically important transition is marked for Nd^{3+}. Modified from [207].

The host material is not responsible for the emissions from phosphors, but the choice of an appropriate host is nevertheless important [208]. First and foremost, the activator should be soluble in the host. If the solubility is low, the activator will precipiate and form secondary phases, which will generally quench or significantly reduce the luminescence. This is either caused by increased ion-ion interactions due to the REE atoms coming closer or by the formation of a compound which is not optically active [207]. Furthermore, it is also important that the host does not have lattice vibrations or phonons that can interfere with the excited states of the REE [207]. If the energy of the excited state is in the same order of magnitude as the lattice vibrations, the excited electron can lose its energy to one or more phonons, and thereby relax in a non-emissive manner. Heavy halides, like chlorides, bromides and iodides, generally have very low phonon energies, but they are hygroscopic and therefore of low importance as host materials. Fluorides and oxides are chemically stable and more frequently used, though their phonons have higher energies [208]. In Figure 3.12 it can be seen that the lattice vibrations in In_2O_3 appear between 20 to 30 μm, or from 333 to 500 cm^{-1}, which should be low enough not to quench the most significant emissions in REEs [207].

Some of the properties of In_2O_3 or ITO indicate that they potentially can be a good host material for a phosphor. First of all the Re_2O_3 rare earth sesquioxides crystallises in the same bixbyite crystal structure as In_2O_3. Additionally, all of the REE are usually trivalent [49] and the size difference between In^{3+} and the REEs is not too large [79]. This indicates that the solid solubility of REEs in In_2O_3 could be sufficient to avoid quenching of the luminescence. Furthermore, the REEs are usually not good at absorbing energy because of the 4f transitions being forbidden. However, when a wide band gap semiconductor is used as a host it can absorb UV light with higher energy than the band gap. There is then a possibility of this energy being transferred to the activator, thereby sensitising the luminescence [37, 41, 42]. The possibility of this energy transfer has been a major driving force for the use of wide band gap host such as In_2O_3 [43], in addition to Al_2O_3 [209], ZnO [210-214], TiO_2 [50, 215-217], ZrO_2 [218] and SnO_2 [219, 220]. Excitation and emission spectra which indicate that this energy transfer has occurred in SnO_2 doped with europium and erbium are given in Figure 3.21. For both of the samples a broad excitation peak centered at 310 nm was observed, which corresponds to excitation over the band gap of the SnO_2 host. When the samples were excited at 310 nm the characteristic emissions from Eu^{3+} and Er^{3+} were observed, which indicates an energy transfer from the host to the activator.

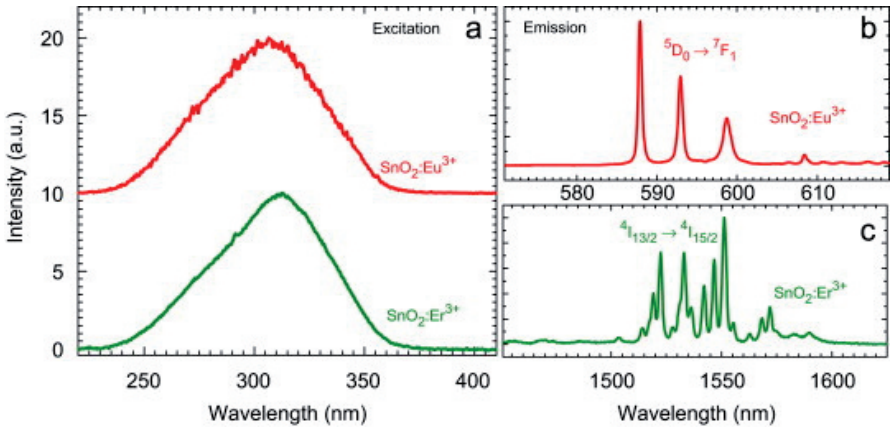

Figure 3.21. Excitation (a) and emission spectra (b and c) of nanoparticles of SnO_2 doped with Eu^{3+} and Er^{3+} [37]. All of the experiments were carried out at room temperature.

Furthermore, the traditional host materials used for REEs have been glasses and other insulators. Particularily erbium doped glasses have been thoroughly studied for the use as optical fiber waveguides [207, 221]. However, a material with the combination of being luminescent, while having a good conductivity, could be realised by chosing a TCO as a host. A material with this new combination of properties could potentially open ut for new applications. One way of utilising this combination of properties is through the use of electroluminescence, i.e. luminescence caused by a current of hot electrons travelling through the material and colliding with the optically active REE centres [207]. This has been stated as a motivation for studying ITO doped with REEs [45, 46, 222]. ITO is already used in electroluminescent devices such as OLED, but then only as a passive transparent electrode layer, not as the active emitting material [44].

The majority of the work concerning REE doping of indium oxide based hosts has used Eu^{3+} as the activator [42, 43, 209], although also Er^{3+} [45, 223] and Dy^{3+} [47] have also been applied. In most of the work undoped In_2O_3 has been used as the host, but in a few cases tin-doping to prepare ITO has been attempted [45, 46, 222]. The final state of the prepared samples is also quite varied, ranging from nano-crystalline [42] to sub-micron [43] powder to thin films on glass [45, 46] or even porous alumina substrates [209, 223]. In some cases a glass matrix has been used into which Eu^{3+} and In_2O_3 nanoparticles have been co-doped [41, 224].

It has been clearly demonstrated that it is possible to get strong emissions from these materials. However, in many of these cases the emission lines are fairly wide [42, 45], as can be seen in Figure 3.22, and it is therefore unclear whether the REE dopant is actually incorporated into the lattice of the host or is only located on the surface of a nano-particle [43]. For the thin film samples the annealing temperature has also been important parameter. The strongest emission signals are obtained from samples that have been exposed to temperatures as high as 1000 °C, though the exact mechanism causing this improvement is not understood [45, 223].

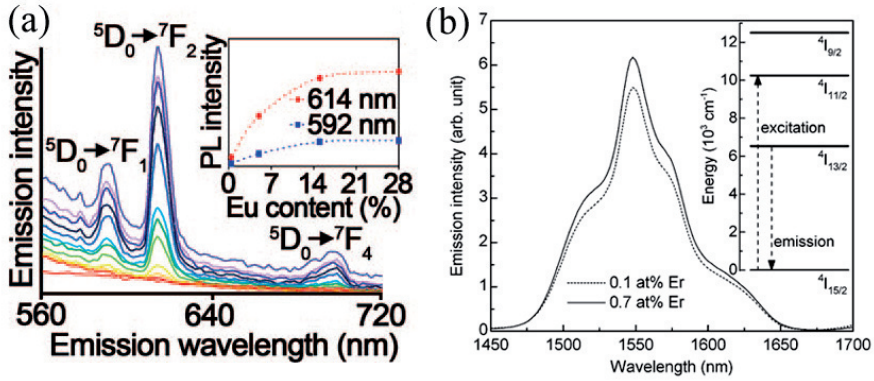

Figure 3.22. Emissions from Eu^{3+} in In_2O_3 quantum dots (a) [42] and Er in an ITO thin film (b) [45]. The different curves in (a) are for excitations at different wavelengths, ranging from 290 nm (uppermost curve) to 535 nm. The inset shows the intensity of two of the emissions as a function of the europium doping content. The samples in (b) were excited at 980 nm and the proposed energy transfers are given as an inset.

There is some degree of dicrepancy in the literature regarding the energy transfer from the host to the activator, called the host sensitisation. In fact, in some of the cases emission signals could only be obtained under direct excitation of the energy levels of the activator [45, 47], wereas in another case emissions were only observed upon excitation over the band gap of the host, and direct excitation was not possible [223]. However, it seems to be clear that an energy transfer from In_2O_3 to Eu^{3+} is achievable. Yu et al. prepared glass samples doped with europium, indium oxide nano-particles or both, of which the emission spectra are given in Figure 3.23. When the In_2O_3 nano-particles were excited across the band gap at 310 nm, they emitted light at 525 nm, probably from a shallow oxygen vacancy defect state. However, when europium doping was used simultaneously the emission

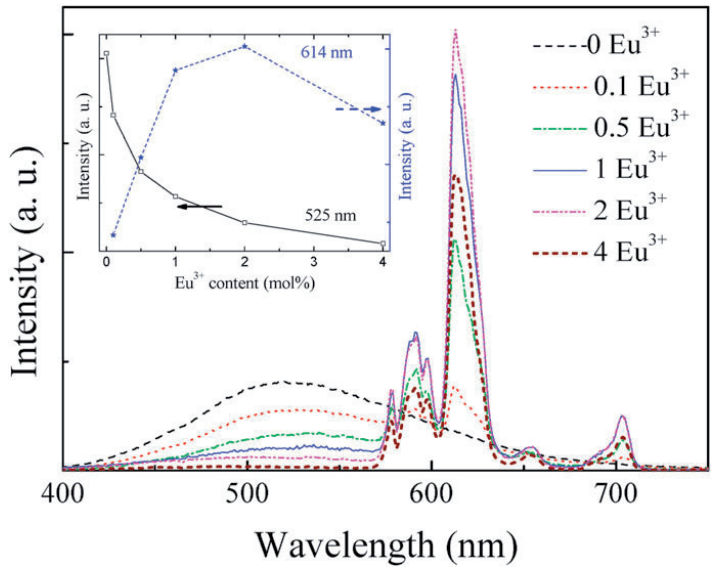

Figure 3.23. Emission spectra of glass samples co-doped with In_2O_3 nano-particles and a varying amount of Eu^{3+}. The inset shows the intensity of the emissions at 525 and 614 nm, related to In_2O_3 and Eu^{3+} respectively, as a function of the europium doping amount [41].

from In_2O_3 became weaker, while the characteristic europium emissions were enhanced compared to when europium was used alone [41].

Xiao et al. have also demonstrated this energy transfer for samples of In_2O_3 nanoparticles doped with Eu^{3+}, as can be seen in the excitation spectra given in Figure 3.24 [43]. The broad peak around 330 nm is believed to be excitation across the band gap of the host nano-particles. However, this excitation was strongest at 10 K, and almost completely quenched at room temperature. At higher wavelengths the sharp excitation peaks related to direct excitation of europium could be observed for all temperatures. Furthermore, the exact mechanism for this energy transfer is not known. Some models are proposed with a direct transfer from the conduction band of the host to the activator (Figure 1.3 (a)) [208], others where the energy is transferred from defect states, most likely oxygen vacancies, in the host (Figure 1.3 (c)) [41]. Other suggested models are based on the energy not being transferred directly to the activator, but to a Eu-O charge transfer band (CTB) [224]. The latter model is depicted in Figure 3.25. In this figure it is also demonstrated how the mismatch between the energy levels of the host and the activator will determine whether an energy transfer occurs or if the luminescence is quenched.

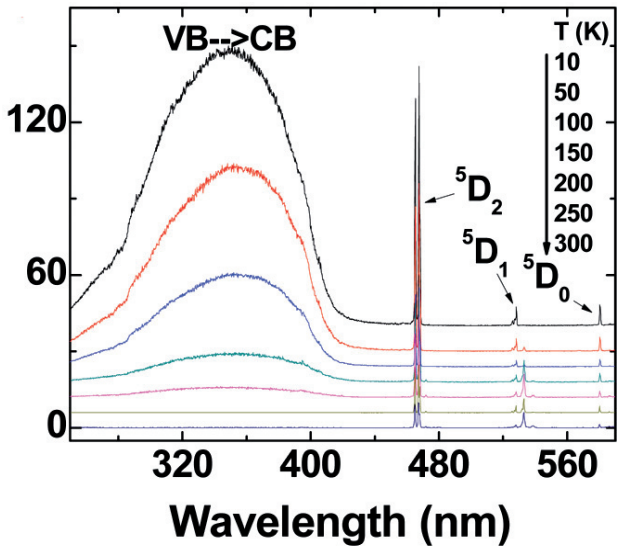

Figure 3.24. Excitation spectra monitoring the strongest emission peak at 611 nm for In_2O_3 nano-particles doped with Eu^{3+} at different temperatures [208].

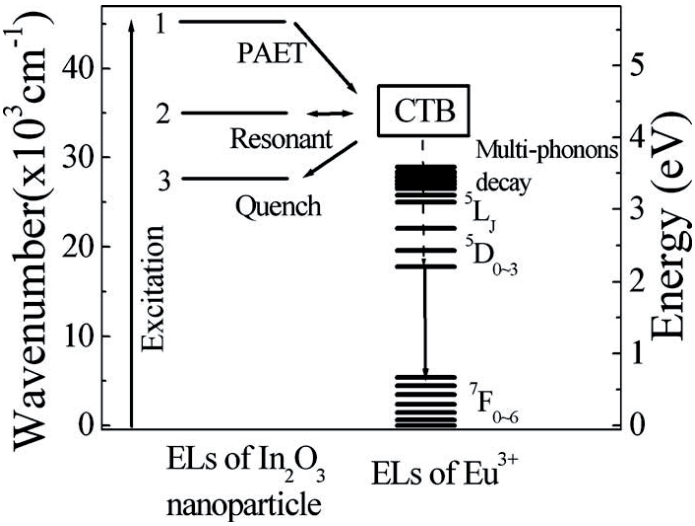

Figure 3.25. Schematic model of the energy transfer from the energy levels (ELs) of In_2O_3 nano-particles to Eu^{3+}. The three different energy levels for the In_2O_3 nano-particles are for different particle sizes giving three different band gaps, where the bottommost energy level is for bulk In_2O_3 [224].

A significant amount of the work has focused on nano-particles or quantum dot hosts. It is clear that by controlling the size of the nano-particles it could be possible to control their band gaps. This would affect where in the UV the nano-particles absorb light, and could also influence whether or not the energy levels of the host and activator are matched appropriately for the energy transfer to occur [224]. However, the exact effect of using nano-particles instead of larger sub-micron particles remains unclear and Xiao et al. observed a similar energy transfer in particles with sizes ranging from 14 to 110 nm [43].

The solubility limit of the REE activators in In_2O_3 and the amount of doping that can be used before concentration quenching of the emissions occurs remains unclear. When Er was added to ITO, no concentration quenching was observed up to at least 5 cat % [45], but a recent work by Ting et al. observed concentration quenching from Eu in ITO already above 0.1 cat % [222]. On the other hand, Vela et al. observed maximum emissions when 15 to 30 cat % Eu were doped into nano-particles of In_2O_3 (inset in Figure 3.22 a) [42]. There are clearly many phenomena regarding REE doping in In_2O_3 that remains unclear and there is a need for further work to clarify the potential of these materials. Finally, though emissions from the activators have been demonstrated, very little attention has been given in the literature to how the REE doping affects the conductivity and the transparency of the host. This effect would be very significant if the novel combination of materials properties, i.e. luminescence and conductivity at the same time, is to be utilised. For certain applications, such as solar cells, diodes or displays, it would also be crucial that the layer remains transparent.

4. Experimental

4.1. Powder preparation

A water-based modified Pechini sol-gel process was developed to prepare the materials studied in this work. A schematic flow chart for the process is given in Figure 4.1. Indium (III) nitrate hydrate ($In(NO)_3 \cdot xH_2O$), tin (II) acetate ($Sn(CH_3CO_2)_2$), neodymium (III) nitrate hexahydrate ($Nd(NO_3)_3 \cdot 6H_2O$), europium (III) nitrate pentahydrate ($Eu(NO_3)_3 \cdot 5H_2O$) and terbium (III) nitrate pentahydrate ($Tb(NO_3)_3 \cdot 5H_2O$) (all > 99.9 % trace metals basis, from Aldrich) were used as precursors. The stoichiometry of indium nitrate was determined by thermogravimetrical analysis prior to the syntheses. The indium nitrate was dissolved in de-ionised water, and a known weight of the solution was heated to 1100 °C to form indium oxide. From the weight of the formed oxide the cation concentration in the solution was determined.

The following materials were prepared: In_2O_3, In_2O_3 doped with 5, 10 and 15 cat% Sn (ITO, cat% = cation% Sn = $n_{Sn}/(n_{In}+n_{Sn})$), In_2O_3 doped with 0.5, 1, 2, 5 and 10 cat% RE (RE = Nd, Eu or Tb, cat% RE = $n_{RE}/(n_{In}+n_{RE})$) and ITO doped with 1, 5 and 10 cat% RE (RE = Nd, Eu or Tb, cation% RE = $n_{RE}/(n_{In}+n_{Sn}+n_{RE})$). The ratio between indium and tin was kept constant at 95:5 in the REE-doped ITO samples. The compositions of the materials are summarised in Table 4.1.

Stoichiometric amounts of the precursors were dissolved in de-ionised water and heated to about 80 °C on a hot plate with a magnetic stirrer. Acetic acid (AA, CH_3COOH, p.a. Acros Organics) and ethylene glycol (EG, $C_2H_4(OH)_2$, VWR) were added to the solution as complexing agents, in a molar ratio between the cations in the solution and each of the organics of 1:1.5. The sol was left on the hot plate overnight in order to evaporate the solvent and form a xerogel. The as-prepared gel was ground in a mortar and calcined at various temperatures for various times, typically for 3 h at 400 or 600 °C, in order to decompose the gel to a nano-crystalline oxide powder. Tartaric acid (TA, DL-tartaric acid, 99 %, Sigma-Aldrich) was used as complexing agent instead of acetic acid for the REE-doped samples, also with a ratio between the cations in the solution and the organic of 1:1.5. These samples were calcined at 600 °C for 15 h. The calcined oxide powder was then ball milled with 5 mm YSZ balls in absolute ethanol for 24 h. Plastic bottles of 500 mL were used for batches of about 30 grams of powder. The bottles were filled with grinding balls up to about 1/3 of their volume. The powder was added to the bottle and sufficient solvent to cover the powder and grinding media was added. The rotation speed was determined based on the diameter of the bottle

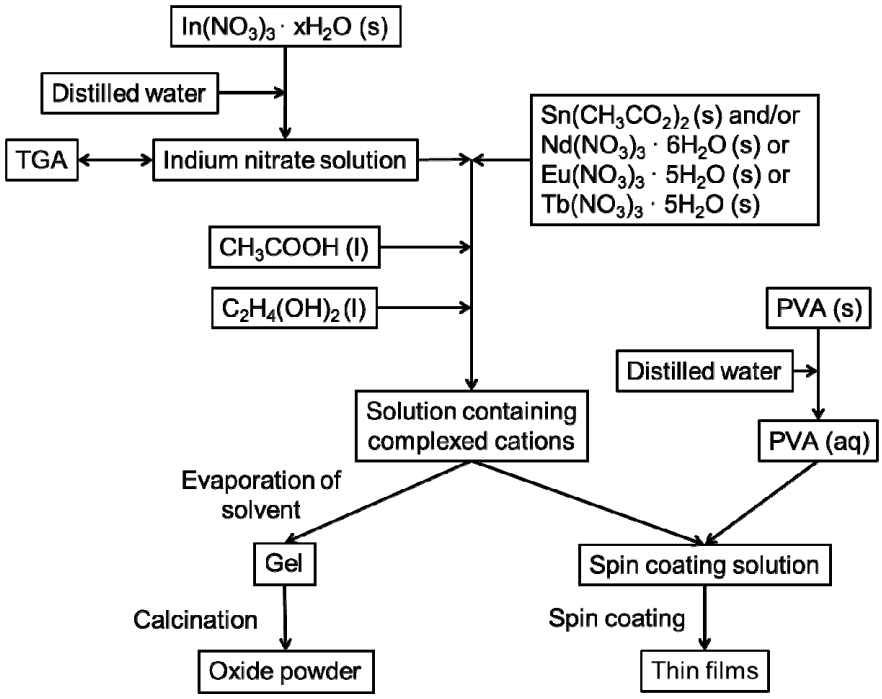

Figure 4.1. Flow chart for the developed aqueous sol-gel process.

and set to approximately 130 rpm. After the evaporation of the solvent, the powder was sieved through a 250 μm mesh and finally re-calcined at 400 °C. Pellets of the ball milled powders with 5 mm diameter and about 2.5 mm height were pressed in a uniaxial press at < 50 MPa, followed by subsequent cold isostatic pressing at 200 MPa. Green pellets were also prepared from un-milled powders to investigate the effect of ball milling on the final density. Stearic acid was used as a lubricant during the pressing of the pellets. The REE-doped samples were pressed to pellets of 15 mm diameter. The pressed pellets were sintered for 2 h in air at temperatures ranging from 600 to 1600 °C. The heating and cooling rates were 200 K/h.

The powder synthesis was also conducted using ethanol (EtOH), tartaric acid (TA), succinic acid (SA) (ReagentPlus ≥ 99 %, Sigma-Aldrich) and polyvinyl alcohol (PVA, VWR, average M_w ~ 88000 g/mol) as complexing agents. The molar ratio between the cations and the complexing agents was 1:3 when only one type of complexing agent was used and 1:1.5 for each of the complexing agents when two were used in combination. A solution similar to the one used for spin coating (described in the next paragraph) was used in the synthesis using PVA, but without

Table 4.1. The composition and label of the prepared materials in this work.

Material label	Nominal composition	cat% In	cat% Sn	cat% RE
In_2O_3	In_2O_3	100	-	-
ITO (5 cat% Sn)	$In_{1.9}Sn_{0.1}O_{3.05}$	95	5	-
ITO (10 cat% Sn)	$In_{1.8}Sn_{0.2}O_{3.10}$	90	10	-
ITO (15 cat% Sn)	$In_{1.7}Sn_{0.3}O_{3.15}$	85	15	-
In_2O_3:RE	$In_{1.99}RE_{0.01}O_3$	99.5	-	0.5
	$In_{1.98}RE_{0.02}O_3$	99	-	1
	$In_{1.96}RE_{0.04}O_3$	98	-	2
	$In_{1.9}RE_{0.1}O_3$	95	-	5
	$In_{1.8}RE_{0.2}O_3$	90	-	10
ITO:RE	$In_{1.881}Sn_{0.099}RE_{0.02}O_{3.0495}$	94.05	4.95	1
	$In_{1.805}Sn_{0.095}RE_{0.1}O_{3.0474}$	90.25	4.75	5
	$In_{1.71}Sn_{0.09}RE_{0.2}O_{3.045}$	85.5	4.5	10

the addition of AA and EG as designated complexing agents. In the synthesis where these different complexing agents were used, the cation concentration was 0.5 M (0.04 mol cations and 80 mL solution) and the Sn concentration was 5 cat%, while all other experimental parameters were kept the same. After the synthesis, the as-evaporated gels were ground in a mortar and calcined for 3 h at various temperatures.

4.2. Thin film deposition

The solution used for the spin coating was prepared from stoichiometric amounts of the cation precursors, AA and EG as described in the previous section. The cation concentration was 0.4 M. In order to successfully apply the solution for spinning, PVA was added as a wetting agent, in order to improve the wetting of the solution on the substrate. The first solution was therefore mixed in a 1:1 volume ratio with a solution of de-ionised water with 3 wt% PVA, so that the cation concentration of the final solution used for spin coating was 0.2 M. The prepared

ITO thin films had a tin concentration of 10 cat%. The thin films were deposited on square glass substrates (Menzel-Gläser, microscope slides) of 25 x 25 mm or single crystalline <100> YSZ, <0001> Al_2O_3 and <100> MgO square substrates of 15 x 15 mm (MolTech GmbH) by spin coating (Laurell WS-400B-6NPP-Lite Spinner) in a clean room ISO7 (NTNU NanoLab). The single crystalline substrates were polished on one side and the films were deposited on the polished side. The substrates were cleaned with soap water, rinsed in distilled water and ethanol and dried with an airbrush prior to the film deposition. A syringe with a 0.2 μm filter was used to apply the solution to the substrate prior to the spinning. Sufficient amount of solution to completely cover the substrate was used. The substrates were then spun at 3000 rpm for 45 seconds, although other rotation speeds were also attempted where this is noted. The films were calcinated under vacuum (10^{-2} mbar) in a rapid thermal process furnace (RTP, Jipelec JetFirst 200 Processor) at 530 °C for 1 h. At lower temperatures the transparency of the films were affected by carbon residues while higher temperatures would break or severely bend the glass substrate. ITO thin films on YSZ substrates were in some cases heat treated at 600 °C for 1 h or 700 or 800 °C for 30 min. The chamber was purged with nitrogen gas before the onset of the vacuum. This procedure was repeated in order to make films with multiple depositions.

In some cases the cation concentration and the amount of PVA added to the spin coating solution was altered. The labels, cation concentrations and PVA contents of these solutions are given in Table 4.2. The PVA content is the content of the PVA solution before the mixing while the cation concentration is the final concentration after mixing.

Table 4.2. Label, cation concentration and PVA content of different solutions used for spin coating

Solution label	PVA content [wt%]	Cation concentration [M]
Solution 1	3	0.2
Solution 2	3	0.5
Solution 3	5	0.2
Solution 4	5	0.5
Solution 5	5	1.0

Also thin films of In_2O_3 and ITO doped with 0.5, 1, 2, 5 and 10 cat% REE was prepared. For the REE-doped ITO samples the ratio between indium and tin was kept constant at 95:5, similarly as for the powder batches. Thin films of pure In_2O_3 and ITO with 5 cat% Sn was also prepared as references to the REE-doped films. The REE-doped thin films were prepared from Solution 2 and by three subsequent depositions.

4.3. Materials characterisation

Density

The density of the green pellets was calculated from their weight and dimensions. The density of sintered samples was measured by the Archimedes method in accordance with ISO-standard 5017 [225].

Thermogravimetry

Thermogravimetrical analyses (TGA, Netzsch, STA 449 C) of the gels were performed up to 1000 °C in air, with a heating rate of 2 K/min up to 400 °C and 10 K/min from 400 to 1000 °C. A Netzsch, QMS 403C Aëolos mass spectrometer was attached to analyse the evolved gases.

Viscosity

The viscosity of prepared solutions was measured by a Thermo Scientific HAAKE Mars III rheometer using the RheoWin 4 software. The experiments were performed at 25 °C. The reported values for the viscosity were obtained at a shear rate of 500 1/s.

Nitrogen gas adsorption

Nitrogen gas adsorption was carried out on the as-prepared powder and on samples after sintering at 600, 800 and 1000 °C (Micromeritics, Tristar 3000) to calculate the BET surface area and the BJH pore size distribution.

Dilatometry

The sintering of the pellets was monitored by dilatometry (Netzsch, Dil 402 C) in different atmospheres. The dilatometry was carried out in pure oxygen, air and nitrogen atmospheres with a heating rate of 2 K/min.

X-ray diffraction

The phase composition of the materials was studied by X-ray powder diffraction (XRD). All of the samples were analysed from 20 to 70 °2θ. The sintered pellets were crushed before the sample preparation. In cases where the amount of sample was small, a single crystal Si sample holder was used.

The In_2O_3 and ITO gels, powders and pellets were analysed by a Bruker AXS D8 Focus equipped with a LynxEye^{TM} detector and a Cu-radiation source ($CuK\alpha_{1,2}$) with Bragg Brentano geometry. The step size was 0.02 ° with 2 s per step counting time.

The REE-doped gels, powders and pellets were analysed by a Siemens D5005 instrument with an MBraun position sensitive detector, Cu-radiation source ($CuK\alpha_1$), primary monochromator and Bragg Brentano geometry. The step size was 0.03878 ° and the counting time was 7.3 s per step.

Thin film samples were analysed with a Siemens D5005 with a gracing incidence angle setup, Cu-radiation source ($CuK\alpha_{1,2}$), Göbel mirror, equatorial soller slits on the detector side and a Scintillation detector. The incident angle was set at 2 °, the incremental step was 0.08 ° and the counting time was 10 s per step.

Rietveld refinements of the diffractograms were carried out using the Topas software, v4.2 [226]. The crystal structure of the materials was refined using the space groups $Ia\bar{3}$ for cubic In_2O_3 [48], $R\bar{3}c$ for rhombohedral In_2O_3 [66], $P4_2/mnm$ for SnO_2 [227], $Fd\bar{3}m$ for the rare earth stannate pyrochlore phases $Re_2Sn_2O_7$ (Re = Nd, Eu and Tb) [228, 229], *Pnma* for $NdInO_3$ [230, 231] and $P6_3cm$ for $EuInO_3$ and $TbInO_3$ [232, 233]. The atomic positions used are listed in Table 4.3. A correction factor for sample displacement was included in the refinements. The diffraction patterns were fitted using fundamental parameters for the peak shape and Chebychev background model with a minimum order to account for the curvature, typically 4. The atomic positions were determined for each material refining from the heaviest element to the lightest. For the refinement of the diffractograms of the thin films, structure-less fits with Thompson-Cox-Hastings pseudo-Voigt peak models were used and the sample diplacement correction was not applied. Signals from the substrate could often be observed in the diffractograms of the thin films, as seen in Figure 7.1. In order to model the background, 6 orders were used in the Chebychev background model and a single peak was added to account for the substrate.

Table 4.3. Atomic positions used for the different space groups in the Rietveld refinement.

$Ia\bar{3}$		$R\bar{3}c$		$P4_2/mnm$	
In 1	(1/4, 1/4, 1/4)	In	(0, 0, z)	Sn	(0, 0, 0)
In 2	(x, 0, 1/4)	O	(x, 0, 1/4)	O	(x, y, 0)
O	(x, y, z)				

$Fd\bar{3}m$		$Pnma$		$P6_3cm$	
Sn	(0, 0, 0)	Nd	(x, 1/4, z)	Eu/Tb 1	(0, 0, z)
Re	(1/2, 1/2, 1/2)	In	(0, 0, 1/2)	Eu/Tb 2	(1/3, 2/3, z)
O 1	(x, 1/8, 1/8)	O 1	(x, 1/4, z)	In	(x, 0, 0)
O 2	(3/8, 3/8, 3/8)	O 2	(x, y, z)	O 1	(x, 0, z)
				O 2	(x, 0, z)
				O 3	(0, 0, z)
				O 4	(1/3, 2/3, z)

Electrical properties

The electrical conductivity of the thin films was measured using an in-house built van der Pauw apparatus with platinum contacts, the setup of which is given in Figure 4.2. The films on glass substrates were cut into squares of approximately 13 x 13 mm from the centre of the substrates, in order to fit with the equipment, while

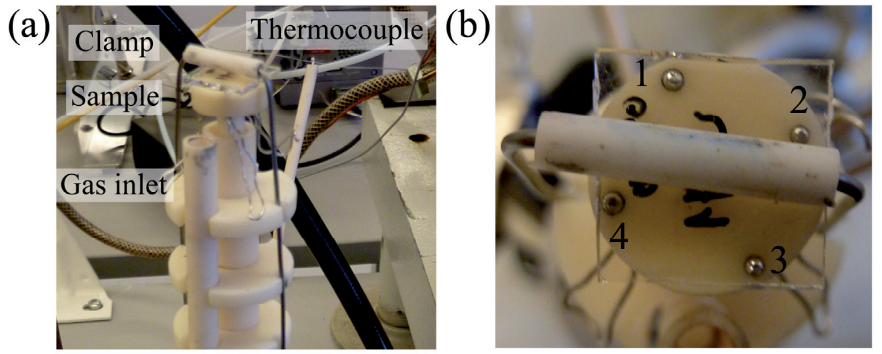

Figure 4.2. Setup of the van der Pauw apparatus (a). Top-view of the four electrodes (b). Modified from [234].

the films on the YSZ substrates were used with their original size. The samples were mounted on the equipment in a way to make the position of the electrodes close to the corners of the film and held down by a clamp. A current was forced between two adjacent electrodes along one side of the film and the voltage drop measured between the opposite two electrodes. Eight different measurements, where the current and voltage drop was measured along different sides of the films and in different directions were performed on each sample. The sheet resistance of the films, *Rs,* was calculated by the Equation 4.1 [235]:

$$R_s = \frac{\pi}{\ln 2} * \frac{R_{horizontal} + R_{vertical}}{2} * f \tag{4.1}$$

where the resistances, $R_{horizontal}$ and $R_{vertical}$, were determined as the average of the first and last four measurements respectively and f is a correction factor. The sheet resistance is the specific resistance of the material, ρ, divided by the thickness of the film, as shown in Equation 4.2.

$$R_s = \frac{\rho}{t} \tag{4.2}$$

The correction factor was obtained from Equation 4.3 [235].

$$\frac{R_{horizontal} - R_{vertical}}{R_{horizontal} + R_{vertical}} = \frac{f}{\ln 2} * \operatorname{arccosh} \frac{e^{\frac{\ln 2}{f}}}{2} \tag{4.3}$$

The resistivity measurements of the thin films were performed at ambient conditions, except where otherwise is noted. All of the thin film conductivity measurements were performed at a constant voltage of 2 V.

The equipment could be placed in a sealed quartz tube and placed in a furnace in order to measure in situ conductivity at elevated temperatures or in different atmospheres. A gas flow of about 50 mL/min was applied. The heating and cooling rates were 200 K/h. The sheet conductivity in the in situ measurements was calculated from the current and voltage drop in the van der Pauw set-up, which corresponds to the inverse of either $R_{horizontal}$ or $R_{vertical}$ in Equation 4.1. This value should not be mistaken for the real sheet conductivity of the film which generally would be about a factor of $\pi/\ln(2)$ lower. It was not attempted to measure the real conductivity during the in situ measurements, as this would have required reconnecting of the electrodes to measure the current and voltage drop along different sides of the film during the experiment.

Hall effect measurements were performed on the REE-doped thin films in a van der Pauw set-up (Ecopia HMS-3000). A 0.55 T magnet was used to provide the magnetic field. The experiments were performed at ambient conditions.

The conductivity of the bulk samples at ambient conditions were measured with a four point linear configuration, as depicted in Figure 4.3 (a). A current was forced between the outermost pins while the voltage drop was measured between the two innermost. The resistivity obtained from Ohms law was inverted and multiplied with the thickness of the pellet to obtain the conductivity of the sample. This value was then corrected for the geometry of the sample according to the equations in [236] and the references therein. The conductivity was also corrected for the porosity of the samples according to the Equation 4.4 [237]:

$$\sigma_{bulk} = \frac{\sigma_{composite}}{\left(1 - \frac{3}{2} * p\right)} \tag{4.4}$$

where $\sigma_{composite}$ is the measured conductivity of the whole sample, including the pores, p is the volume fraction of the porosity and σ_{bulk} is the corrected conductivity for the bulk of the sample alone.

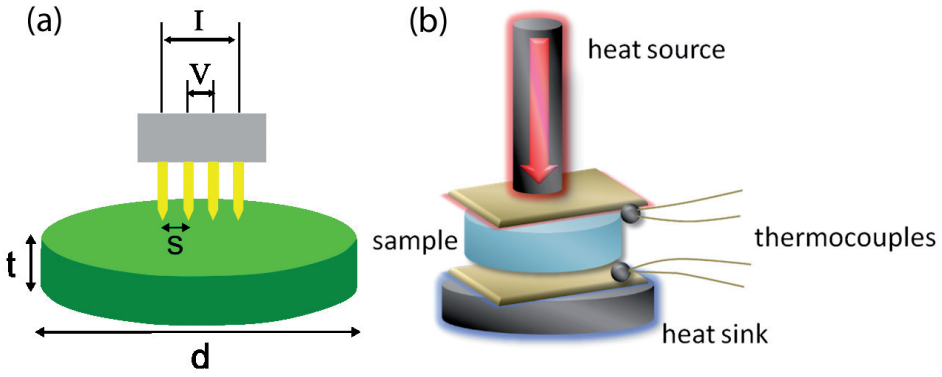

Figure 4.3. Schematic model of the four point linear conductivity (a) and the thermopower (b) set-up.

Thermopower

The thermopower or Seebeck coefficient, Q, of bulk samples was measured in a set-up as depicted in Figure 4.3 (b). The sample was placed between two gold foil sheets, attached to which were electrodes and thermocouples. The sample was then

pressed down between a heat source and a heat sink. The heat source was turned on until the temperature of the top of the sample was 100 °C and then turned off. The thermopower is obtained by plotting the voltage and temperature gradients across the sample during cooling, according to Equation 4.5:

$$Q = -\lim_{\Delta T \to 0}\left(\frac{\Delta V}{\Delta T}\right) \tag{4.5}$$

The most accurate value is obtained by only using data points from $\Delta T < 6$ K. This value was also corrected for the inherent thermopower of the platinum wires used as thermocouples [238, 239].

Optical properties

Optical transmission spectroscopy was carried out on the thin films in the UV-VIS-NIR region. The ITO thin films were analysed with a Shimadzu, UV-1601PC while the REE-doped thin films were analysed with a Perkin Elmer Lambda 1050. Diffuse reflectance spectroscopy was carried out on the REE-doped samples, both bulk pellets and thin films, on the Perkin Elmer spectrophotometer with an integrating sphere detector.

The absorption coefficient for the ITO thin films was calculated by neglecting the reflectance and using the simple relation:

$$\alpha = \frac{1}{t}\ln(T) \tag{4.6}$$

where T is the transmittance, α is the absorption coefficient and t is the thickness of the film.

When both the transmittance and the reflectance of the thin films were known, the absorption coefficient was calculated by the method developed by Cesaria et al. [240]. This method was developed for thin films on transparent substrates and is based on the comparison of the transmission and reflectance of the thin film on the substrate and the uncoated substrate. The band gap, E_g, was estimated by plotting $(\alpha h\upsilon)^2$ versus the photon energy, $h\upsilon$, according to the Equation 4.5:

$$\alpha = \frac{A\left(h\upsilon - E_g\right)^{\frac{1}{2}}}{h\upsilon} \tag{4.7}$$

where A is a proportionality constant.

For the bulk samples the band gaps were estimated by using the Kubelka-Munk method [241], which is based on the following relation:

$$F(R) = \frac{(1-R)^2}{2*R} \tag{4.8}$$

where R is the diffuse reflectance. The band gap was estimated by plotting $F(R)^2$ versus hv.

Infrared spectroscopy

Fourier transform infrared spectroscopy (FTIR, Bruker IFS 66v, OPUS 6.5 software) in transmission mode was performed on the powders calcinated at different temperatures embedded in KBr pellets (0.5 wt%).

Electron microscopy

Scanning electron microscopy (FEG-SEM, Zeiss Ultra 55 Limited Edition) was performed on fracture surfaces of the sintered pellets and on the thin films. Some of the thin film samples were cut in order to observe the cross section of the films. Transmission electron microscopy (TEM) specimens from the ITO powder with 5 cat% Sn after calcination at 600 °C were prepared by dispersing the powder in ethanol and dripping it onto a standard TEM Cu grid covered with holey C film. Additionally, specimens made from films with 10 subsequent depositions were prepared by Tripod wedge polishing using an Allied MultiPrep system. Plane-view specimens were prepared by polishing off the substrate using an angle of two degrees between the polishing plane and the film-substrate interface plane. Cross-section specimens were prepared by gluing two films together and polishing the material into a two degree wedge normal to the film-substrate plane, before Ar ion milling for a few minutes. TEM characterisation was performed at 200 kV using a JEOL2010F. Both electron microscopes were equipped with energy dispersive X-ray spectrometers (EDS) for elemental analysis (Oxford Instruments, X-Max^{TM}).

Particle size determination

The crystallite size of the powders was estimated by the line broadening of the (222) reflection of the bixbyite phase of In_2O_3 in the X-ray diffractograms using the Scherrer equation. An average particle size of the powders was also estimated from the BET surface area by assuming spherical particles. When SEM micrographs were used to estimate an average grain size, the given values are the average of 50 grains.

Ellipsometry

Thin films on glass substrates were analysed with an ellipsometer (RC2, J. A. Woollam Co.). The experiments were carried out with multiple angles of incidence, 55, 60, 65 and 70 °, in the range from 210 to 1700 nm. The output from the experiments was analysed with the CompletEase software. A model is constructed to describe the sample and is used to calculate its predicted response. The calculated values are compared to the experimental data and regression is used to improve the model in order to find the best match with the experimental results. This optimised model included data such as the thickness and the optical constants of the sample.

The second part of the complex dielectric function for the thin film, ε_2, was modelled with contributions from one Drude function and two Tauc-Lorentz functions, according to Equation 4.9:

$$\varepsilon_2 = \varepsilon_{Drude} + \varepsilon_{Tauc\text{-}Lorentz,1} + \varepsilon_{Tauc\text{-}Lorentz,2} \quad (4.9)$$

The complex dielectric function, $\tilde{\varepsilon}$, was found through a parametrisation of ε_2, and the first part of the complex dielectric function, ε_1, was found from the Kramers-Krönig relations. The glass substrate was modelled with a Cauchy function [242].

Photoluminescence

Time-resolved fluorescence decays were recorded using an IBH 5000 U fluorescence lifetime spectrometer system with 1 nm resolved excitation and emission monochromators (5000 M). An IBH 5000 XeF sub-microsecond xenon flashlamp was used for multi-channel scaling (MCS) measurements. The system was equipped with a TBX-04 picosecond photon detection module for detection in the UV/visible and a Hamamatsu NIR PMT module (H9170-5) for detection in the range 900–1700 nm. Melles Griot coloured glass filters were used to block scattered light from the excitation source as well as blocking unwanted light from the laser source. The luminescence decay times were measured and analysed using multi-channel scaling (MCS) along with the IBH Data Station v 2.1 software for operation of the spectrometer and analysis of the decay traces including reconvolution-fits. The lifetime was fitted according to Equation 4.10:

$$I(t)=Ae^{B\frac{t}{\tau}} \quad (4.10)$$

where $I(t)$ is the number of emitted photons as a function of time, A and B are constants and τ is the mean lifetime of the decay process. When more than one decay process was needed to model the lifetime, a sum of exponential terms was

used. Excitation and emission spectra were obtained by locking the emission and excitation wavelengths, respectively, monitoring the detector response while scanning the appropriate monochromator. Luminescence spectra were collected by a lens coupled to an optical fiber and analysed by a Hamamatsu Photonic Multichannel Analyzer (type C7473).

5. Sol-gel synthesis of In_2O_3-based materials

5.1. The sol-gel process and thermal decomposition of the gel

The developed sol-gel synthesis was succesfully applied to prepare phase-pure nano-crystalline powders of In_2O_3-based materials with composition as described in Table 4.1. All of the materials discussed in this chapter are ITO with 5 cat% Sn. This composition was selected as the ITO materials with best properties are known to be at a tin doping concentration between 5 and 10 cat% [12, 84]. In order to gain insight into the thermal decomposition of the gel, experimental techniques such as XRD, FTIR, TGA and DSC were applied. It also became desirable to further understand the chemistry of the sol-gel process. A series of syntheses with varying experimental parameters, most notably the initial cation concentration in the solution and different choices of the organic complexing agents, were performed and the obtained materials were characterised by XRD.

After the precursors and complexing agents had been dissolved and mixed in deionised water, according to the flow chart in Figure 4.1, the solutions appeared transparent, indicating that no precipitation had occurred. In some cases oxidation of the divalent tin precursor resulted in precipitation of a crystalline Sn(IV) hydroxide, as discussed in a later paragraph. White gels were formed in the bottom of the beaker after evaporation of the solvent. The gels appeared porous, powderlike and dry, but usually had a sticky and viscous skin layer on top. A photograph of a white gel after grinding with a pestle and mortar is given in Figure 5.1 (a). These general observations were common for all the different syntheses reported in this chapter.

Amorphous and homogeneous gels were obtained in the synthesis using AA and EG as shown by the X-ray diffraction patterns in Figure 5.2. No Bragg reflections due to crystalline phases were detected in the gels when using the optimised recipe. Precipitation of crystalline In-salts before the sol-gel transition and/or formation of the metastable rhombohedral In_2O_3-phase were, however, observed when other organic components were used or if the concentrations of the cations in the solution were altered. The chemistry of these experiments is reported in detail further below.

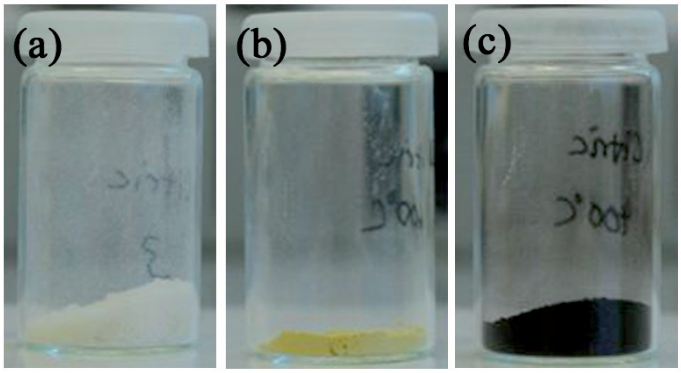

Figure 5.1. Photographs of a gel after grinding (a), ITO powder after calcination at 400 °C (b), ITO powder containing carbon residue after calcination at 400 °C (c). Modified from [243].

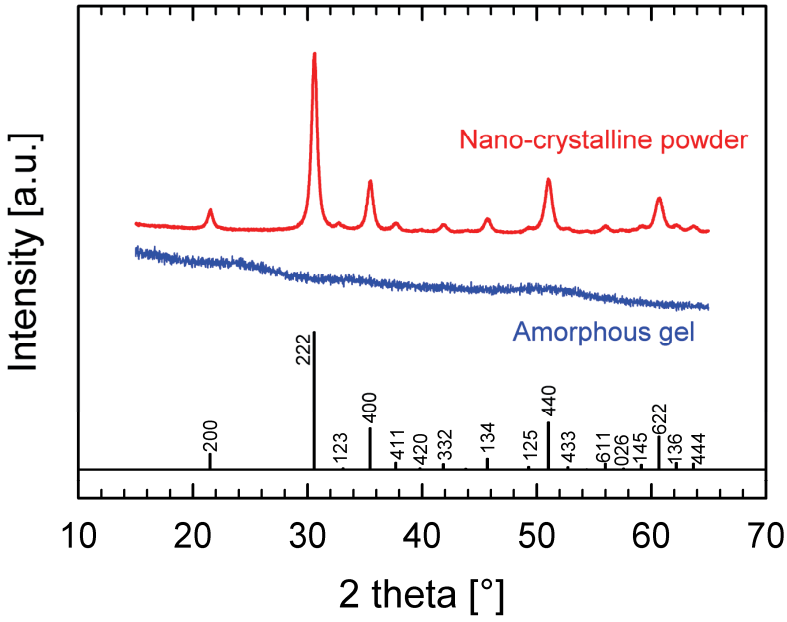

Figure 5.2. XRD patterns of an amorphous ITO gel after evaporation of the solvent and nano-crystalline ITO powder after calcination at 400 °C. The materials were prepared with acetic acid and ethylene glycol as complexing agents and an initial cation concentration of 0.125 M. The pattern for the powder could be indexed to the cubic In_2O_3 polymorph with space group $Ia\bar{3}$ given at the bottom.

The dried amorphous gel prepared with AA and EG as complexing agents decomposed and crystallised to cubic In_2O_3 (space group $Ia\bar{3}$) during heating, as evidenced by the diffractograms in Figure 5.2 and 5.3. The gels which were analysed in Figure 5.3 were prepared from the same batch. After grinding the gel in a morter, it was divided into smaller samples which were heat treated at different temperatures. The crystallisation was observed to take place between 250 and 300 ºC. Thermogravimetrical analysis of another dry gel prepared with an identical synthesis is shown in Figure 5.4 (blue curve, 1:1.5 AA + 1:1.5 EG). A significant weight loss is initiated below 250 ºC and the weight was stable from a few degrees below 300 ºC.

FTIR spectra of the powders calcinated at different temperatures are shown in Figure 5.5. These samples are the same as were analysed by XRD in Figure 5.3. Evidence of residual nitrate groups and organics in the gels is seen up to 250 ºC, while these characteristic bands are removed at 300 ºC, which correlates well with the results from TGA and XRD. The nano-crystalline ITO obtained after calcination at 300 ºC still contained some residual water from the solution, evidenced by the OH-stretching modes. The OH-content decreased by heat

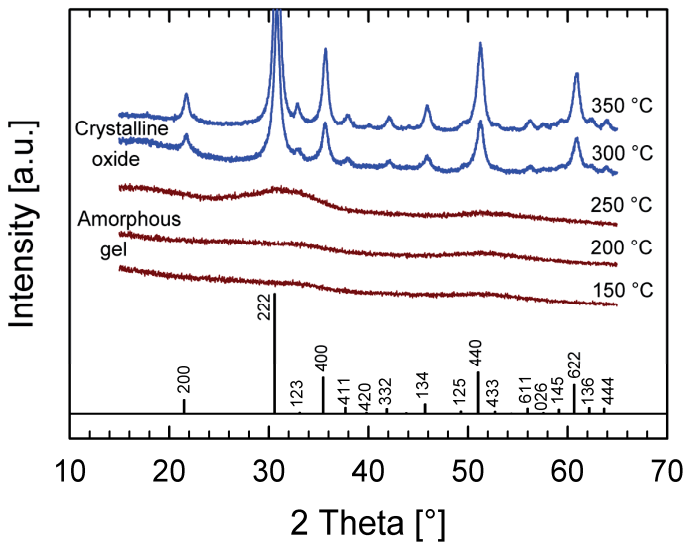

Figure 5.3. XRD of ITO gels prepared with acetic acid and ethylene glycol, an initial cation concentration of 0.125 M and a doping amount of 5 cat% Sn after calcination at different temperatures. A reference pattern of the cubic In_2O_3 crystal structure (space group $Ia\bar{3}$) is given at the bottom.

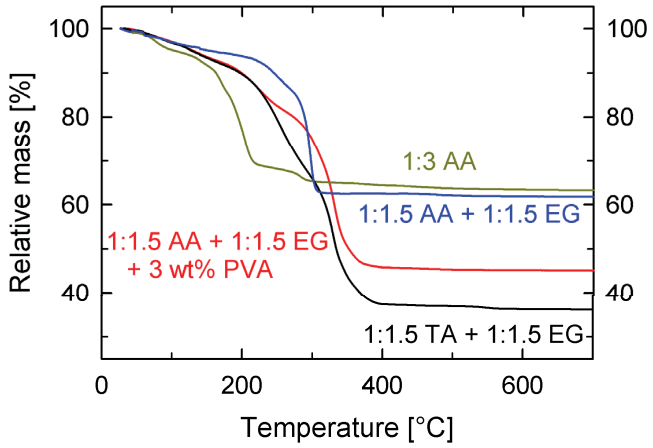

Figure 5.4. Thermogravimetrical analyses of as-evaporated gels synthesised with different complexing agent; acetic acid (AA), ethylene glycol (EG), tartaric acid (TA) and polyvinyl alcohol (PVA). The molar ratio between the cations and the complexing agents in the solution is indicated.

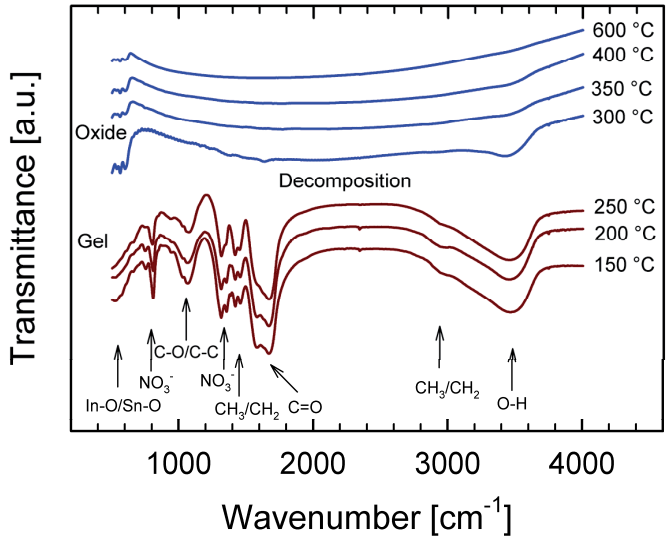

Figure 5.5. FTIR spectra of ITO gels prepared with acetic acid and ethylene glycol, an initial cation concentration of 0.125 M and 5 cat% Sn after calcination at different temperatures. The most characteristic vibrational modes in the samples are assigned.

treatment at higher temperatures, and no indication of OH-stretching modes could be observed after calcination at 600 ºC (Figure 5.5). From combining these results it is concluded that the crystallisation and decomposition of gels prepared with AA and EG occurred more or less simultaneously in the temperature interval between 250 and 300 ºC. During another TGA experiment of a gel prepared with TA and EG a mass spectrometer was attached in order to analyse the exhaust gases, the results of which can be seen in Figure 5.6. From about 100 °C evaporation of H_2O is evident. This signal drops after about 200 °C, but there are still signs of water being removed at temperatures up to 500 °C. The signals from CO_2 and NO and NO_2, respectively, given in Figure 5.6 (c) and (d), demonstrates the removal of organics and nitrates from the gel, in line with the FTIR results in Figure 5.5. Differential scanning calorimetry (DSC) was also performed in the same measurement and exothermic peaks are clearly visible in the same temperature region where the mass loss is evident. The exothermic nature is due to the oxidation and decomposition of the organic and nitrate components in the gel.

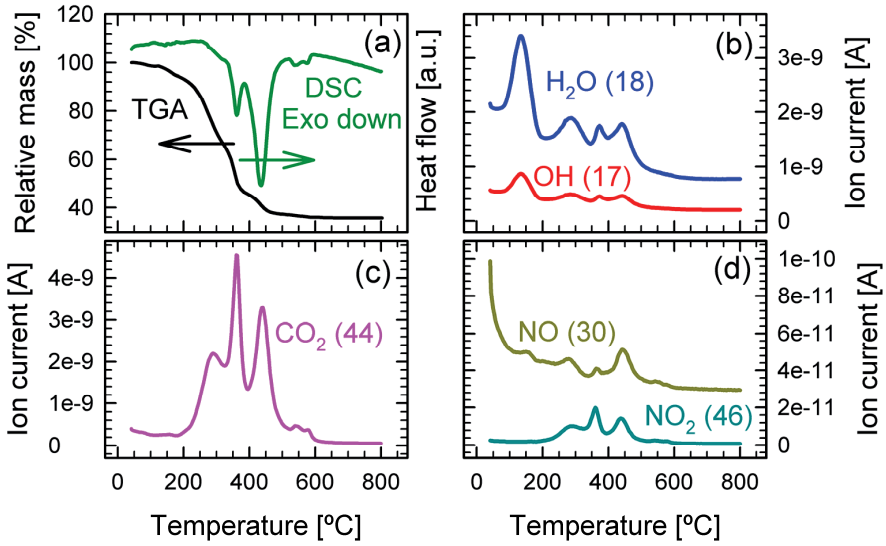

Figure 5.6. TGA and DSC of a gel prepared with TA and EG as complexing agents (a) were the exhaust gases were analysed with a mass spectrometer (b, c and d). The atomic mass of the gas species is indicated.

It was demonstrated that the synthesis with AA and EG could be used to prepare amorphous gels (Figure 5.2), but in certain initial experiments a crystalline phase was observed by XRD after drying (labelled In salt 5 in Figure 5.7). It was

confirmed that the crystalline phase was not a nitrate or an acetate and that the same salt was observed in syntheses both with and without tin. The phase had a similar structure to an indium hydroxide oxalate salt [244], but with a shift in the lattice parameter. It was concluded that the crystalline phase was an organometallic salt of indium and the organic additives. A series of three different syntheses were performed with an initial cation concentration of in the solution of 0.5, 0.125 and 0.05 M, with two parallells for each concentration. The two experiments with 0.5 M both yielded the organometallic salt, while the experiments with lower concentration all gave amorphous gels.

A series of ten experiments were carried out where the organic components in the recipe were alternated, all of which with an initial cation concentration of 0.5 M. The results from these experiments are summarised in Table 5.1. The synthesis yielded homogeneous and amorphous gels only when EG and the combination EG + TA was used. In all the other cases either precipitation of salts, presumably organometallic salts of indium and the respective organic additives, or crystallisation of In_2O_3 occurred during drying or before a gel was formed. The salts are labelled In salt X according to their appearance in Table 5.1. XRD of the different products, with the same labelling, is given in Figure 5.7. After calcination at 400 °C some of the samples were transformed to cubic In_2O_3 (labelled c-In_2O_3, space group $Ia\bar{3}$), however, in several of these materials rhombohedral In_2O_3 (labelled rh-In_2O_3, space group $R\bar{3}c$) was found in addition to the cubic phase. The phase composition and the crystallite size of the phases after calcination are also included in Table 5.1. No systematic trend could be observed regarding the crystallite sizes from the different experiments. Neither was there a trend in the lattice parameters of the two polymorphs as a function of the phase composition. The lattice parameter of the cubic polymorph is given in Figure 5.8, and in the same way no significant trend could be observed for the *a* and *c* lattice parameters of the rhombohedral phase. Furthermore, the completely decomposed gels were yellow, typical for indium oxide, seen in Figure 5.1 (b). In the case where larger organic molecules were used as complexing agents, the materials appeared black, as depicted in Figure 5.1 (c), which was due to carbon residues present in the materials. The carbon residual could be removed by oxidation during heat treatment at temperatures higher than 400 °C, thereby revealing the intrinsic yellow colour of the powder. TGA of gels, which resulted in yellow and black powders after calcination at 400 °C, are given in Figure 5.4 (yellow curve, 1:3 AA and black curve, 1:1.5 TA + 1:1.5 EG, respectively). The decomposition temperature interval is clearly dependent on the size of the organic complexing agent in the gels. After the TGA experiments the samples were yellow in line with expectations.

Table 5.1. Phase content, crystallite size and colour of gels and powders calcinated at 400 °C. The materials were prepared from sol-gel syntheses with different complexing agents, all with an initial cation concentration of 0.5 M.

Complexing agents	Cation:RCOOH ratio	Cation:ROH ratio	Gel/as evaporated	Powder calcinated at 400 °C						
				c-In_2O_3		rh-In_2O_3			Goodness of	
				wt%	crystallite size [nm]	wt%	crystallite size [nm]	Other phase	Rietveld fit R_{wp}	Colour
1:3 AA	1:3	-	c-In_2O_3 + In salt 1	85	19	15	43		10.9	yellow
1:3 EtOH	-	1:3	c-In_2O_3 + rh-In_2O_3	55	26	45	45		10.5	yellow
1:3 EG	-	1:6	Amorphous	90	21	10	13		7.0	black
1:3 SA	1:6	-	In salt 2	-	-	-	-	In salt 3[†]	-	black
1:3 TA	1:6	1:6	In salt 4	100	23	0	-		10.7	black
1:1.5 AA + 1:1.5 EG	1:1.5	1:3	In salt 5	93	13	7	7		6.9	yellow
1:1.5 EtOH + 1:1.5 SA	1:3	1:1.5	In salt 6	-	-	-	-	In salt 3[†]	-	black
1:1.5 TA + 1:1.5 EG	1:3	1:6	Amorphous	100	15	0	-		9.9	black
1:1.5 TA + 1:1.5 SA	1:6	1:3	In salt 7	100	12	0	-		10.6	black
PVA	-	~1:0.7	In salt 8	90	11	10	12		10.3	yellow

[†] An unknown organometallic salt was still present after the calcination at 400 °C of the sample prepared using SA and EtOH+SA, which made the Rietveld analysis of these samples difficult.

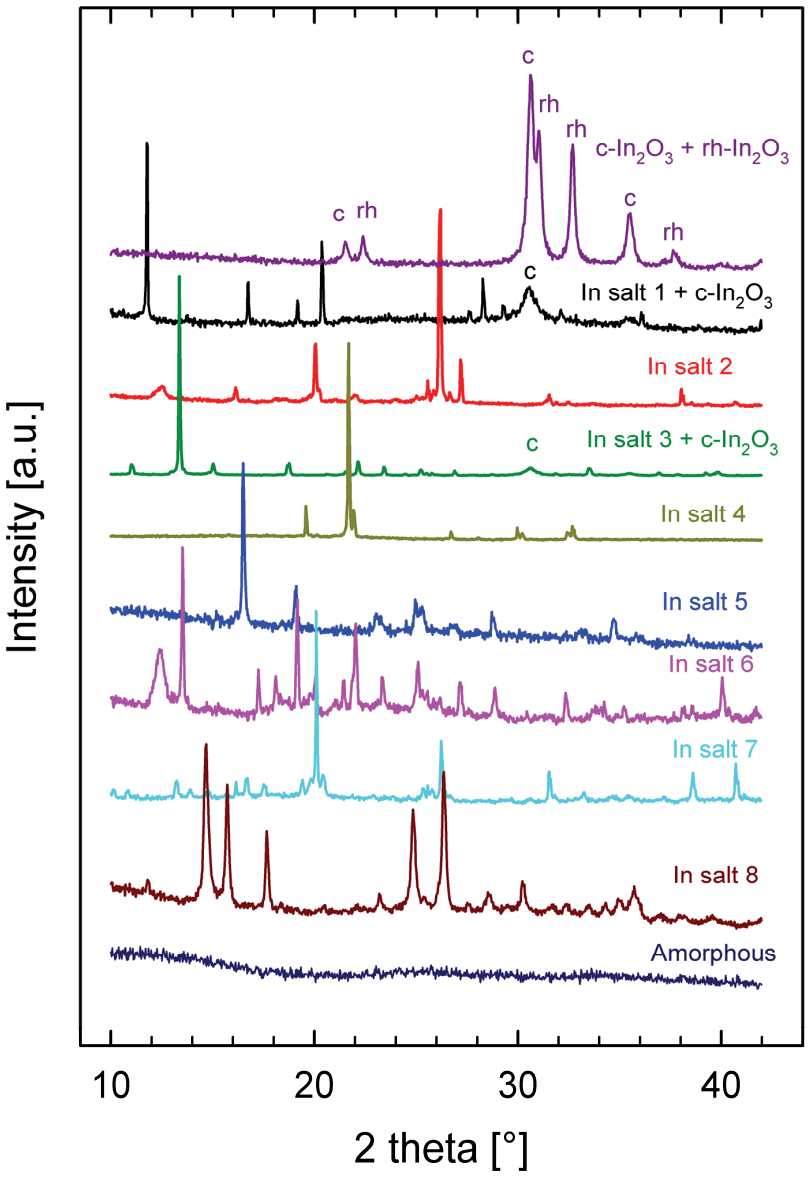

Figure 5.7. XRD of as-evaporated gels and powders calcinated at 400 °C after syntheses with different complexing agents. All the experiments were carried out with an initial cation concentration of 0.5 M. The diffraction lines from cubic In_2O_3 (space group $Ia\bar{3}$) and rhombohedral In_2O_3 (space group $R\bar{3}c$) are marked with *c* and *rh* respectively.

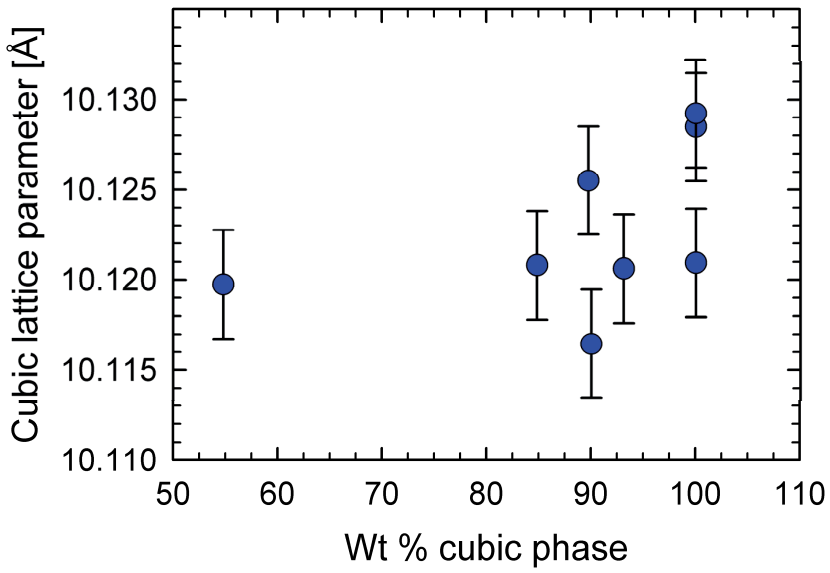

Figure 5.8. The lattice parameter of the cubic In_2O_3 polymorph as a function of the phase fraction of the cubic and rhombohedral polymorphs.

In solutions stored for longer periods of time, oxidation of the divalent tin precursor resulted in precipitation of crystalline Sn(IV) hydroxide. For the thin film deposition the solution was filtered before spin coating in order to remove the possible SnO_2 precipitates in the sol. Furthermore, the nominal tin content in the thin films was confirmed by EDS, as shown in Chapter 7, indicating that the amount of tin that was filtered away was small. Both electron and X-ray diffraction indicated no traces of tin hydroxides in either the powders or the thin films, as demonstrated in the next chapters.

5.2. Discussion

It was clearly demonstrated that homogeneous and nano-crystalline ITO can be prepared by the simple aqueous sol-gel process. The optimised precursor solution transformed to an amorphous gel during drying. The amorphous nature of the gel points to a homogenous distribution of the components and that segregation of In or Sn did not occur prior to the sol-gel transition. Moreover, the amorphous gel decomposed during calcination, which was accompanied by crystallisation to a single phase with the cubic In_2O_3 crystal structure. The decomposition and the crystallisation were clearly demonstrated to take place between 250 and 300 °C for syntheses with AA and EG, as evidenced by XRD, TGA and FTIR. These

observations suggest that the decomposition and crystallisation occurred simultaneously and could not be separated. The mobility of the atoms is fairly limited at the temperature region where the crystallisation takes place. However, the oxidation accompanying the decomposition of the gel is exothermic, as seen in Figure 5.6 (a), and this reaction can thereby release sufficient heat to thermally induce crystallisation of the amorphous oxide formed from the decomposed gel.

The synthesis used here resembles the Pechini method [155, 245]. This process utilises an α-hydroxycarboxylic acid, typically citric acid, as a complexing agent, and a polyhydroxy alcohol, like ethylene glycol, as a polymerisation agent, as described in Chapter 3.3. The intention is to avoid segregation and precipitation of unwanted phases as the solvent is evaporated by the complexing of the cations and the immobilisation caused by the rigid polyester network which forms due to reactions between the acid and the alcohol.

An amorphous gel was prepared using AA and EG when the initial cation concentration was 0.125 M or lower (Figure 5.2), while a precipitation of an organometallic salt with indium occurred when the concentration was 0.5 M (labelled In salt 5 in Table 5.1, and Figure 5.7). This observation can probably be explained by differences in the kinetics during the evaporation. If the initial cation concentration is higher, nucleation can occur before sufficient immobilisation of the cations takes place. When the cation concentration is lower, on the other hand, it takes longer time to reach supersaturation and the precipitation can be avoided by complexation of the cations. A similar observation was made by Fontaine et al. in the synthesis of $La_{2-x}NiO_{4+\delta}$ with an aqueous modified Pechini process, where phase-pure materials were only obtained when the cation concentration was below 0.15 M [246].

In order to investigate the chemistry related to the process, a series of experiments were carried out where different organic molecules with varying number and types of functional groups were applied. A cation concentration of 0.5 M was used in all of these experiments, because experiments with AA and EG demonstrated that it was difficult to prevent precipitation under these conditions. Only the experiments with EG and TA + EG gave amorphous gels (Table 5.1). Hence, EG clearly has an important effect on the complexing of the cations. Both of these experiments had a ratio between the cations and the ROH groups of 1:6, while the ratio between the cations and the RCOOH groups were 1:0 and 1:3, respectively (Table 5.1). Thus, it appears that for this material system the hydroxyl group is possibly more effective than the carboxyl group regarding the complexing of the cations. This observation is supported by the work of Kundu and Biswas, where PVA, and no carboxylic acids, was used to produce phase-pure ITO thin films [145]. However, the steric hindrance of the cation mobility is perhaps more important than complexing when

polymer chains like PVA are used [247]. Furthermore, for similar syntheses of $BiFeO_3$, Liu et al. observed that alcohol groups appeared to be vital, while the addition of carboxylic acid groups did not appear to be significant [248]. A possible explanation is that the ROH group is more important than the RCOOH group regarding complexing of the cations In^{3+}, Sn^{4+} and Bi^{3+}, which all form amphoteric oxides, while the carboxylic acid group is more important for the complexation of cations forming basic oxides.

The synthesis with TA and EG resembles the original Pechini process the most, with an α-hydroxy carboxylic acid and ethylene glycol, both with more than one functional group. The polyesterification will take place in the syntheses where these are used together. However, when only EG was used, the polyesterification reaction could not take place and a rigid polymer network could not be formed, though it is possible that some kind of bridging network was formed. When AA and EG were used in combination the ester reaction could occur. But as AA only has one functional group, a polymer network could again not be formed. However, also this synthesis route produced amorphous gels, when the solution was diluted (Figure 5.2). This implies that the polymer network is not necessarily critical for maintaining the homogeneity as the solvent is evaporated, as long as the cations are sufficiently immobilised by complexation.

Phase-pure cubic In_2O_3 was formed in the experiments where large organic molecules were used as complexing agents, such as TA, TA + EG and TA + SA. However, using smaller complexing agents such as AA, EtOH, EG and AA + EG, the metastable rhombohedral polymorph was also formed. Larger organic molecules, leading to a higher carbon to oxygen ratio, result in more reducing conditions during decomposition of the gel [249]. Thus, it appears that crystallisation of the rhombohedral polymorph is favoured kinetically by oxidising conditions. The absence of a trend in the lattice parameters of the two polymorphs as a function of the phase composition indicates that the tin dopant is not preferentially segregating into one of the phases. The rhombohedral polymorph is metastable and will transform to the cubic upon heat treatment to above 700 °C [68], and this phase transition has been observed to have a detrimental effect on densification [193]. However, DFT calculations have predicted that the rhombohedral polymorph should have good TCO properties, [73] and a composite film containing both rhombohedral and cubic In_2O_3 with good properties has recently been reported [71].

Several parameters must be considered when choosing the optimum complexing agents. Most important is the homogeneity of the gel, where it appears that EG is important. To stabilise the cubic polymorph of In_2O_3 relatively large organic molecules are desirable, while smaller organic molecules promote the formation of

rhombohedral In_2O_3. Furthermore, thermogravimetry (Figure 5.4, Table 5.1) demonstrated that the larger complexing agents require a higher temperature in order to fully decompose the gel. This might be undesirable, especially in cases where the substrate is temperature sensitive. A large amount of organic matter to be removed during the calcination might also cause problems during film formation, or even cause film cracking, especially for films above a critical thickness [132].

5.3. Conclusion

The environmentally friendly aqueous sol-gel process was demonstrated to produce amorphous gels after evaporation of the solvent, pointing to good homogeneity in the produced materials. Upon calcination the gel decomposed and crystallised to nanocrystalline particles with the cubic In_2O_3 structure, and XRD, TGA and FTIR analyses demonstrated that the two processes occurred simultaneously and could not be separated. The chemistry of the Pechini-related process was investigated and the functional groups of the organic additives, the size of the organic additives and the initial cation concentration in the solution were found to influence the homogeneity, phase composition and decomposition temperature of the prepared materials. The presence of hydroxyl groups in the process appears to be important regarding complexing and immobilisation of the cations, and the possible formation of the metastable rhombohedral In_2O_3-phase could be controlled by the choice of the organic additives.

6. Nano-crystalline phase-pure ITO powder

6.1. Characterisation of the powder

It was demonstrated that the developed sol-gel process could successfully be applied to prepare nano-crystalline ITO powders. All the powders discussed in this chapter were prepared with AA and EG as complexing agents and an initial cation concentration lower than 0.125 M in order to ensure that the powders were phase pure.

ITO powders with different Sn-concentrations were prepared and characterised with respect to phase purity and size in order to investigate the flexibility of the sol-gel process. Experimental techniques such as XRD, TEM and nitrogen gas adsorption were applied in this regard. The crystal structure, lattice parameter, crystallite size, BET surface area and particle size of the powders after calcination at 400 and 600 ºC are given in Table 6.1. The synthesis was found to be robust with respect to Sn-content in ITO as the amount of tin doping could be varied from 0 to 15 cat% without losing the phase purity. The diffractograms of the materials could be indexed exclusively to the cubic In_2O_3 crystal structure (space group $Ia\bar{3}$). The cubic lattice parameter, depicted in Figure 6.1, increased from 10.1207 ± 0.0014 to 10.1332 ± 0.0018 Å as the doping level increased from 0 to 15 cat% Sn, which is in good agreement with literature data [13, 63]. There was no significant difference between the lattice parameter of the powder calcinated at 400 and 600 ºC.

The crystallite size of the powders, as calculated from the line broadening in XRD, ranged from 11 to 26 nm. As expected, the crystallite size of the powder increased with increasing calcination temperature. Moreover, it also seems to be slightly reduced with increasing Sn-content, as reported for other synthesis methods [162, 250]. The particle size calculated from the BET surface area were consistent with the crystallite sizes, though slightly larger, in line with expectations.

Representative TEM images of the ITO powder with 5 cat% Sn after calcination at 600 °C are shown in Figure 6.2. Primary particles of approximately spherical shape and an average size of 15 ± 6 nm can be observed in the bright field image in Figure 6.2 (a). A high resolution image of such a particle is given in Figure 6.2 (b). The crystallite size inferred from XRD corresponds well with the observed particles sizes from the TEM images. Also larger agglomerates of the primary particles can be seen in the powder, which can explain why the particle size

Table 6.1. Crystal structure, lattice parameter, crystallite size, surface area and particle size of nano-crystalline ITO with different doping amount and calcination temperature.

Doping amount [cat% Sn]	Crystal structure	Calcination temperature [°C]	Lattice parameter [Å]	Crystallite size (XRD) [nm]	BET surface area [m^2/g]	Particle size (BET) [nm]	Goodness of Rietveld fit [R_{wp}]
0	cubic In_2O_3	400	10.1200 ± 0.0023	16 ± 3			5.4
		600	10.1207 ± 0.0014	26 ± 1	24.9 ± 0.8	34 ± 1	5.5
5	cubic In_2O_3	400	10.1231 ± 0.0020	11 ± 3			5.0
		600	10.1233 ± 0.0019	16 ± 2	39.4 ± 1.3	21 ± 1	4.0
10	cubic In_2O_3	400	10.1265 ± 0.0021	15 ± 1			3.8
		600	10.1300 ± 0.0023	18 ± 2			3.7
15	cubic In_2O_3	400	10.1311 ± 0.0016	15 ± 3			4.5
		600	10.1332 ± 0.0018	17 ± 3			5.2

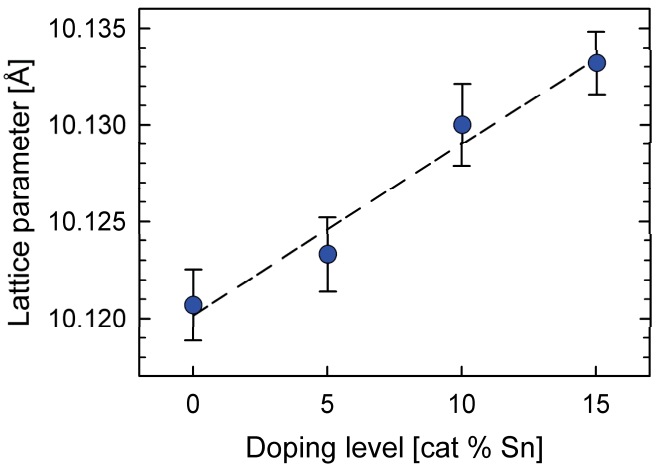

Figure 6.1. Cubic lattice parameter of the ITO powders calcinated at 600 ºC as a function of composition. The dashed line is a guide to the eye.

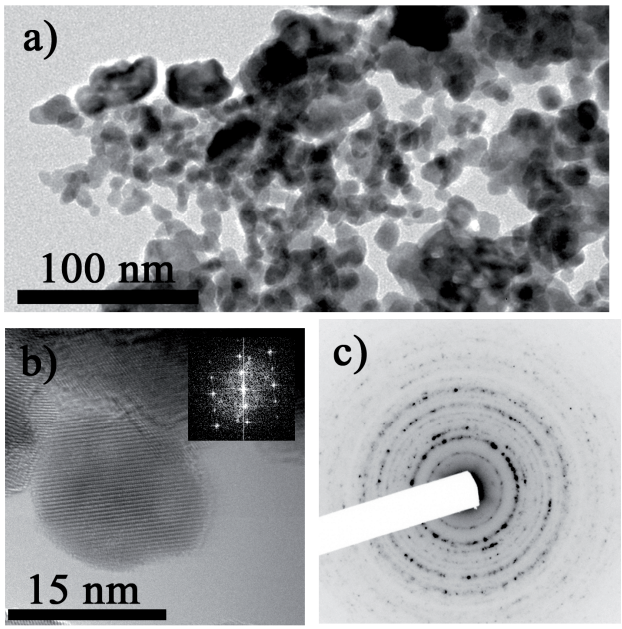

Figure 6.2. TEM images of ITO powder with 5 cat% Sn after calcination at 600 °C, bright field image (a), high resolution image with FFT image as inset (b) and diffraction pattern (c).

calculated from the BET surface area is slightly larger than the crystallite size. The diffraction pattern in Figure 6.2 (c) clearly demonstrates that the particles are crystalline. The pattern corresponds to the cubic In_2O_3 phase, and no reflections from any other crystalline phases were found, in agreement with XRD. The particles are single crystalline with little or no amorphous surface layer (Figure 6.2 (b)). The lattice fringes in the image corresponds to the [1-22] zone axis, with plane spacings of $d_{0\text{-}22}$=3.58Å and $d_{41\text{-}1}$=2.38Å, and the periodicity of the particle is clearly visualised in the Fast Fourier Transform (FFT) image. The concentration of tin, found by EDS, was 5 ± 1 cat%, confirming the nominal composition. The EDS spectrum of this powder is given in Figure 6.3, where signals from In, Sn and O can be seen. The signals from Cu comes from the copper grid the powder was dispersed on

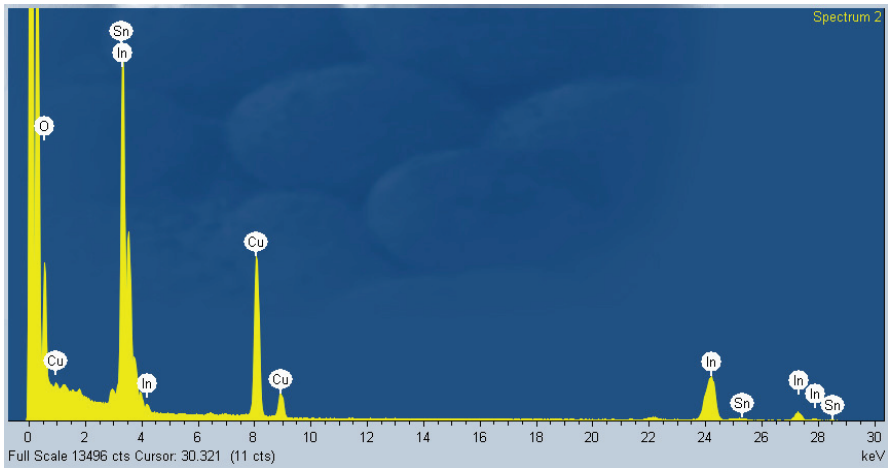

Figure 6.3. Typical EDS spectrum from ITO powder with 5 cat% Sn.

6.2. Sintering

Phase-pure and nano-crystalline powders of In_2O_3 and ITO with 5 cat% Sn after calcination at 600 °C were used in the sintering study. Particularly the phase purity was important, as the powders used in previous sintering studies of nano-crystalline ITO were prepared by co-precipitation [69, 191-197]. The ITO composition was selected based on the most frequently used doping levels of ITO being between 5 and 10 cat% Sn [61]. The undoped In_2O_3 material was used as a reference material in order to gain insight into how the tin doping affected the sintering process. One of the most important experimental tools to characterise sintering processes is dilatometry [185]. This technique was combined with other experiments such as density and weight loss measurements after isothermal sintering and SEM imaging in order to observe the microstructure throughout the different stages of sintering.

The linear shrinkage and differential linear shrinkage (densification rate) of In_2O_3 and ITO in air, measured by dilatometry, are shown in Figure 6.4. The final density of the samples after the experiment was 92.9 and 95.3 % for In_2O_3 and ITO, respectively. The corresponding green densities were 53.1 and 47.0 %. It is clear that tin doping deteriorates the densification of In_2O_3 at intermediate temperatures,

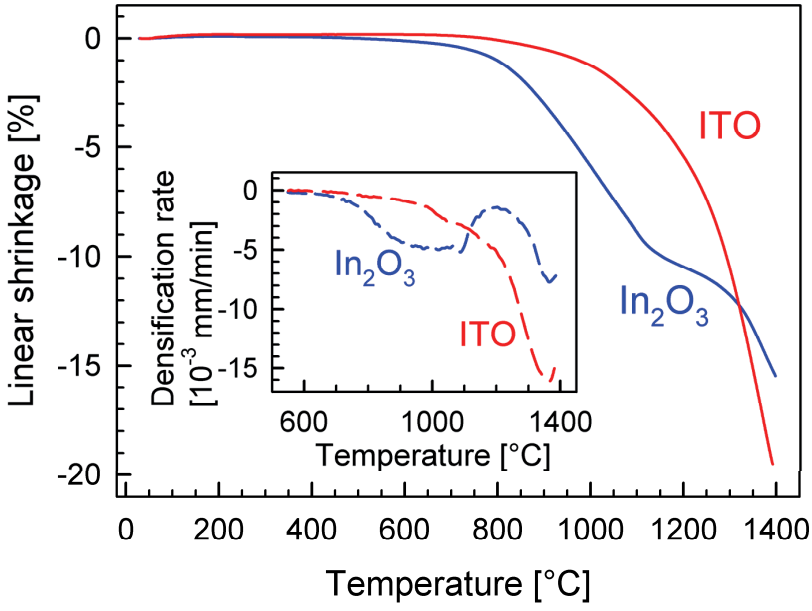

Figure 6.4. Linear shrinkage of In_2O_3 and ITO powder pellets in air with a heating rate of 2 K/min (solid lines). Inset: Densification rate of the samples (dashed lines).

which correlates well with previous reports [194, 196]. The onset of densification and the maximum densification rate for ITO were shifted towards higher temperatures relative to pure In_2O_3. However, above approximately 1200 °C the densification rate is higher for ITO, and the ITO samples actually obtained higher final densities in the dilatometer experiments. Similar conclusions could be drawn from the density of the pellets sintered for 2 h at isothermal conditions, shown in Figure 6.5. Pure In_2O_3 achieved higher densities at intermediate temperatures, while the density was approximately equal for the two materials at 1300 °C and higher. Both materials reached densities above 95 % after sintering at 1400 and 1450 °C, while the density decreased when the temperature was raised to 1500 and 1600 °C. The difference in density between the two materials after sintering at 600 and 800 °C is largely caused by the difference in green density. The ball milling procedure of the powder prior to the sintering was found to have a large impact on the sintering at high temperatures. For the samples prepared from non-ball milled powder the highest obtained density was approximately 88 % for In_2O_3 and only 70 % for ITO, as illustrated in Figure 6.6. Removal of hard agglomerates in the powders prior to the compaction was, thus, vital in order to obtain the high densities presented in Figure 6.5.

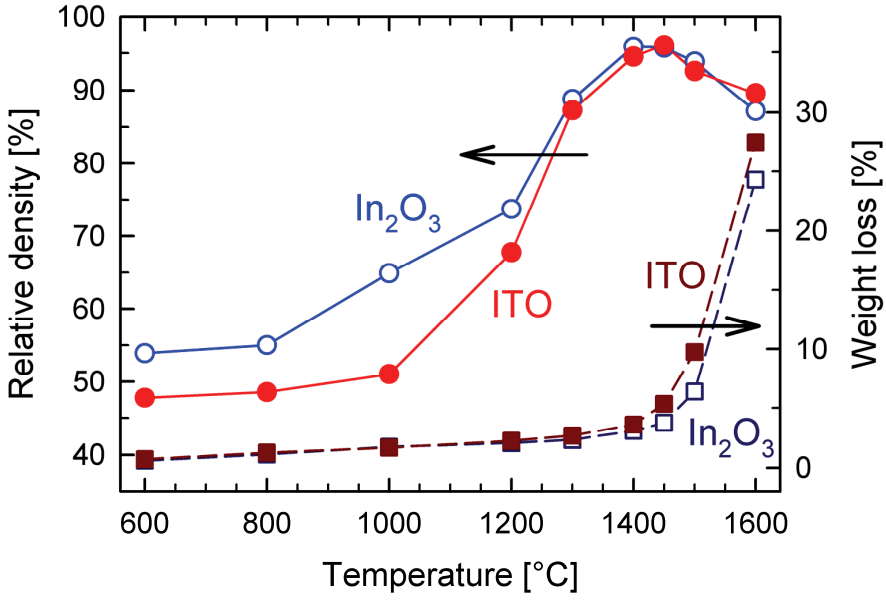

Figure 6.5. Final density of In_2O_3 (○) and ITO (●) and weight loss of In_2O_3 (□) and ITO (■) after isothermal sintering at different temperatures for 2 h.

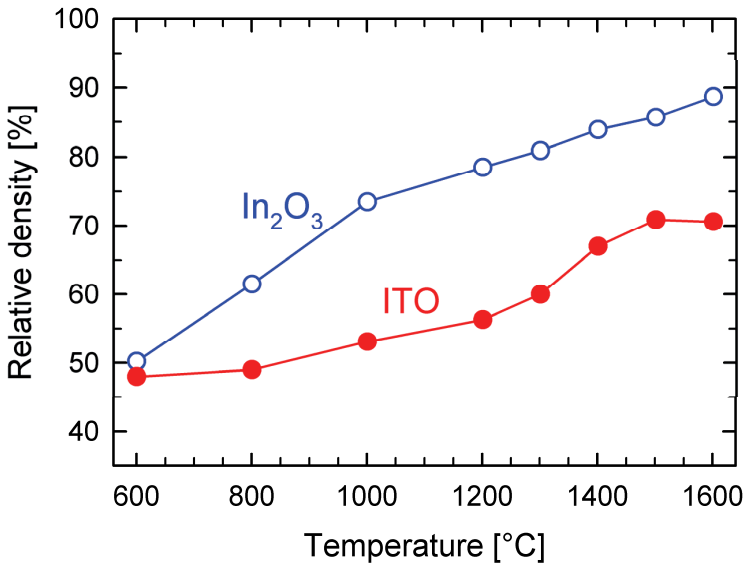

Figure 6.6. Final density of In_2O_3 (○) and ITO (●) prepared from non-ball milled powders after isothermal sintering at different temperatures for 2 h.

The weight loss observed after the isothermal sintering experiments is also included in Figure 6.5. The weight loss increased almost exponentially with sintering temperature above about 1300 °C, and the weight loss was notably higher for ITO compared to In_2O_3. The large weight losses at higher temperatures were found to be almost linearly proportional to the surface to volume ratio of the samples when pellets of different geometries were sintered. This shows that the weight loss could probably be significantly reduced by sintering in a suitable powder bed, though this was not further investigated. The observed weight loss below 1300 °C was attributed to the decomposition/evaporation of stearic acid, which was used as lubricant in the uniaxial pressing.

SEM micrographs of In_2O_3 and ITO after isothermal sintering at different temperatures are shown in Figure 6.7. The microstructure and the grain size are quite similar for both compositions after the heat treatment at 600 °C. The micrographs of the materials sintered at 1000 °C, on the other hand, demonstrated a significant difference in the microstructure of the In_2O_3 and ITO materials. A significant coarsening and grain growth have accompanied the densification of In_2O_3, while the microstructure of ITO demonstrates almost only coarsening in line with the observed lack of densification below 1000 ºC (Figure 6.4 and 6.5). The BET surface area, relative density and grain size of the two materials sintered at intermediate temperatures are given in Figure 6.8, while the pore size distributions

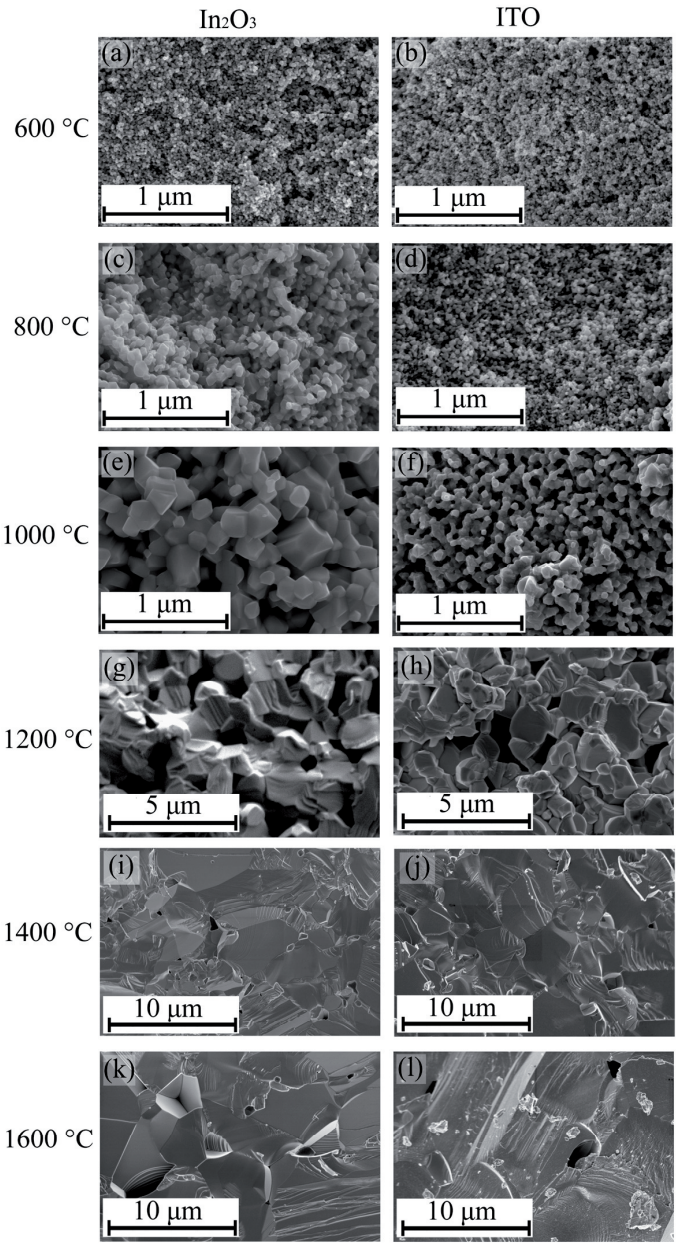

Figure 6.7. Microstructure of In_2O_3 and ITO after sintering at various temperatures. (a) In_2O_3 600 °C. (b) ITO 600 °C. (c) In_2O_3 800 °C. (d) ITO 800 °C. (e) In_2O_3 1000 °C. (f) ITO 1000 °C. (g) In_2O_3 1200 °C. (h) ITO 1200 °C. (i) In_2O_3 1400 °C. (j) ITO 1400 °C. (k) In_2O_3 1600 °C. (l) ITO 1600 °C.

calculated from nitrogen gas adsorption are shown in Figure 6.9. These results confirm the conclusions drawn from the micrographs in Figure 6.7. Both materials experience a substantial reduction of the surface area from 600 to 1000 °C, but the densification and the grain growth are significantly higher for In_2O_3 than for ITO. The pore size distribution is similar at 600 °C, but at 800 and 1000 °C the pore size is shifted towards larger pores for In_2O_3 and the total volume of pores is smaller for In_2O_3 compared to ITO. Both materials had densified considerably after sintering at 1200 °C, Figure 6.7 (g) and (h), though considerable porosity still remains. The

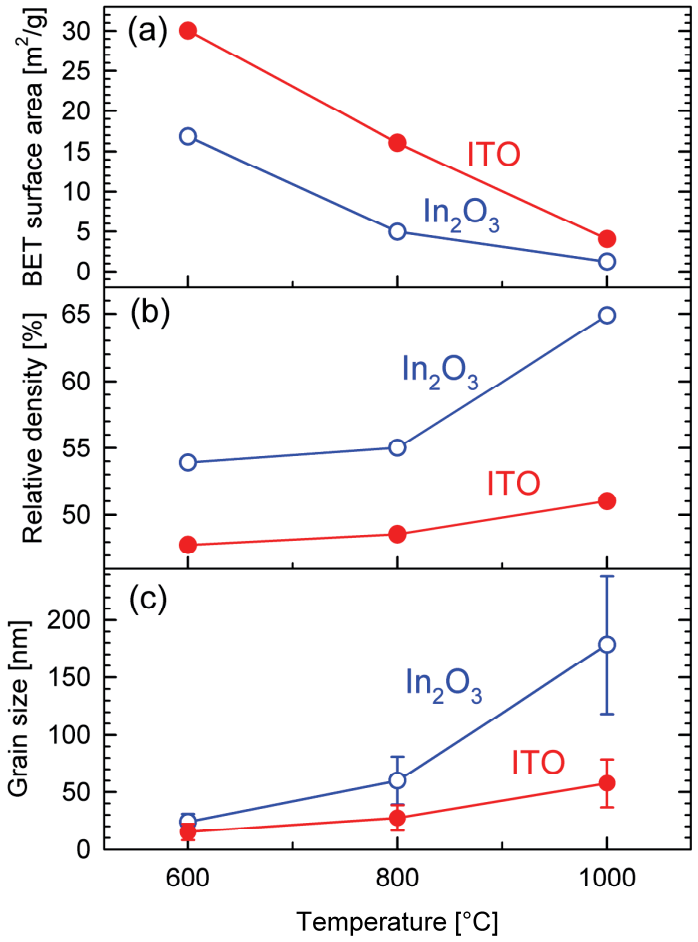

Figure 6.8. BET surface area (a), relative density (b) and grain size (c) of In_2O_3 (○) and ITO (●) as a function of temperature after isothermal sintering at 2 h at intermediate temperatures.

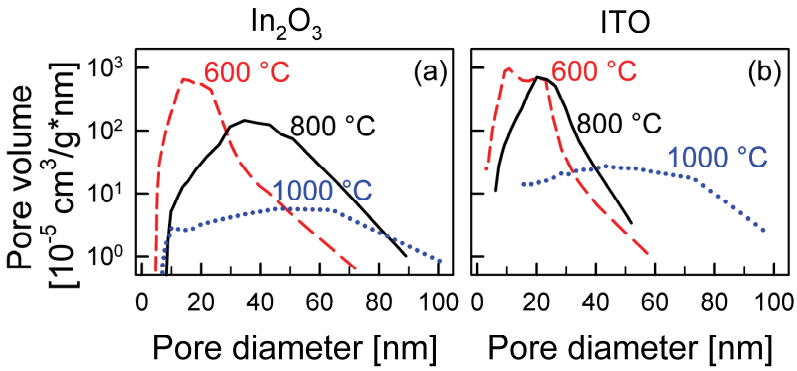

Figure 6.9. Pore size distributions for (a) In_2O_3 and (b) ITO after isothermal sintering at different temperatures obtained by nitrogen adsorption analysis.

grains had grown substantially for both compositions, but the grains of In_2O_3 still appear to be larger than for their ITO counterpart. The microstructures after sintering at higher temperatures, Figure 6.7 (i) - (l), are similar for both materials and clearly reflects the densities presented in Figure 6.5. At 1400 °C the microstructures are almost completely dense with only a few submicron pores, while larger pores are clearly seen at 1600 °C. The pores are mainly located at the grain boundaries, not within the grains.

The XRD patterns of ITO after sintering at different temperatures are given in Figure 6.10. The materials sintered at 800, 1400, 1500 and 1600 °C were single phase materials with only diffraction lines assigned to cubic indium oxide (space group $Ia\bar{3}$). On the other hand, for the materials sintered at 1000, 1200 and 1300 °C, three extra Bragg reflections were evident (marked * at 27, 34 and 52 °). These reflections could be indexed to SnO_2 (space group $P4_2/mnm$). The lattice parameter for the cubic In_2O_3 phase in ITO, determined by the Rietveld refinement of the diffractograms, is shown as a function of the sintering temperature in Figure 6.11. The lattice parameter decreased from 800 to 1000 °C, followed by an increase with increasing sintering temperature, before it eventually saturated at approximately 10.1260 Å, which is close to the lattice parameter previously reported for bulk ITO with 5 cat% Sn [63, 80]. The undoped In_2O_3 samples were phase pure and cubic throughout the sintering, without any reactions or phase transitions, and had a lattice parameter of 10.1195 Å.

The sintering kinetics was further investigated by dilatometry in three different atmospheres, synthetic air, oxygen and nitrogen, and the linear densification and the densification rate for the two materials are shown in Figure 6.12. The density and the weight loss observed after these experiments are given in Table 6.2. It has

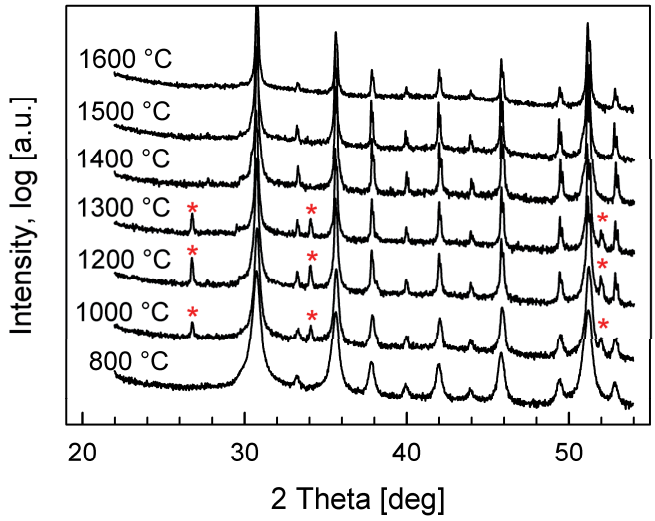

Figure 6.10. XRD patterns of ITO samples after isothermal sintering. Diffraction lines due to SnO_2 at 27, 34 and 52 ° are denoted by *.

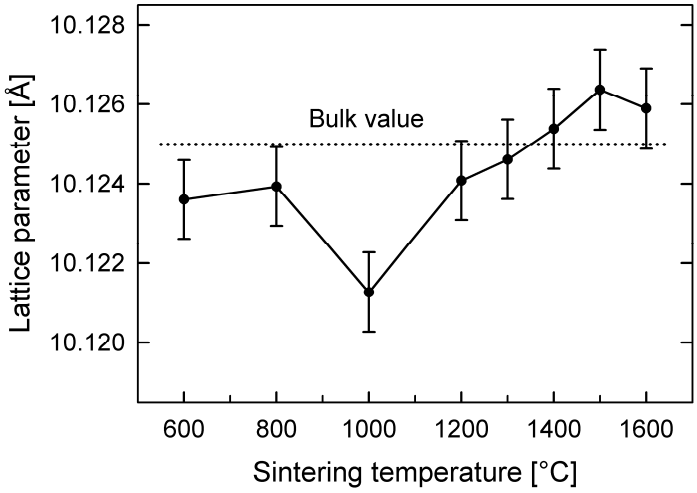

Figure 6.11. Cubic lattice parameter of In_2O_3 phase in the ITO material sintered at different temperatures. The data were obtained by Rietveld refinement of XRD patterns in Figure 6.10. The error was estimated to be 0.002 Å including the statistical error obtained from the Rietveld refinement. The reference value for bulk ITO with 5 cat% Sn is taken from [63].

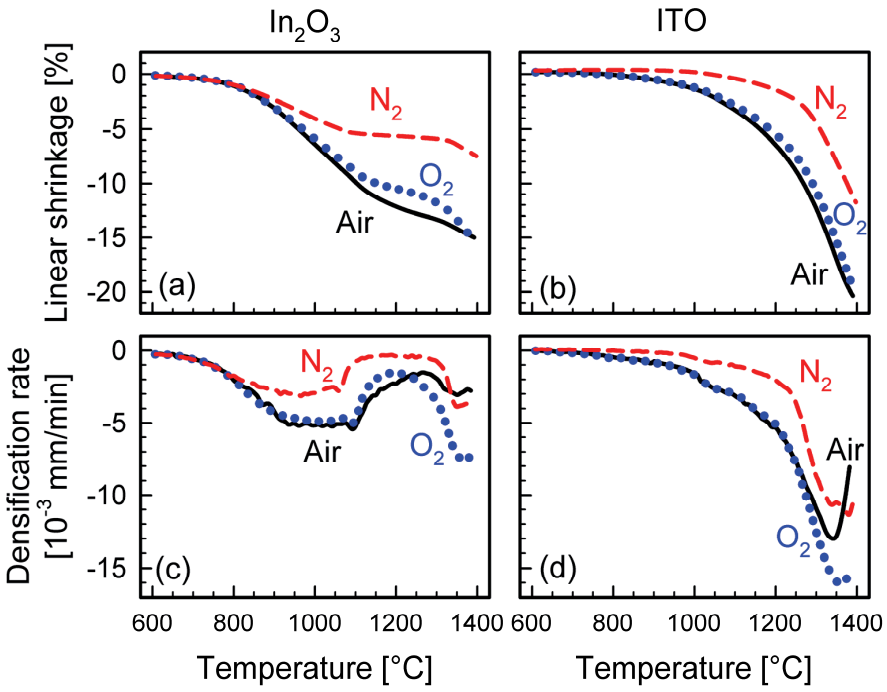

Figure 6.12. Linear shrinkage and densification rate of In_2O_3 and ITO in different atmospheres, synthetic air (solid lines), oxygen (dotted lines) and nitrogen (broken lines). (a) Linear shrinkage of In_2O_3. (b) Linear shrinkage of ITO. (c) Densification rate of In_2O_3. (d) Densification rate of ITO.

Table 6.2. Green density, final density and weight loss measured after dilatometry with different atmospheres.

Composition	Atmosphere	Green density [%]	Density [%]	Weight loss [%]
In_2O_3	Oxygen	52.6	88.9	2.1
In_2O_3	Synthetic air	53.1	92.9	2.0
In_2O_3	Nitrogen	53.0	68.9	2.2
ITO	Oxygen	47.4	95.5	2.5
ITO	Synthetic air	47.0	95.3	2.3
ITO	Nitrogen	48.9	71.5	3.9

been noted in several reports that it is advantageous to sinter ITO in oxygen [69, 191, 192, 251]. The difference in sintering behaviour in synthetic air and oxygen was minor, while there was a significant difference between the two oxygen-rich atmospheres and nitrogen (with an estimated oxygen partial pressure of 10^{-4}-10^{-5} bar). Below approximately 900 °C the sintering kinetics is not influenced by the atmosphere. Above this temperature, on the other hand, the densification is significantly retarded in nitrogen, and the final densities were almost 25 % lower than in air or oxygen. The weight loss also appears to be significantly higher in nitrogen, especially in the case of ITO.

6.3. Discussion

6.3.1. Properties of the powder

The average particle size of ITO powder with 5 cat% Sn was found to be 15 ± 6 nm after calcination at 600 °C, and the complementary data on the sizes from TEM, XRD and BET surface area were in very good agreement. The size coarsened with increasing calcination temperature and was somewhat smaller for the doped ITO powder compared to the undoped In_2O_3. The latter reflects that the cation mobility is reduced by doping In_2O_3 with a cation with a higher valance state. This is in line with similar information obtained by the investigation of sintering of nano-crystalline In_2O_3 and ITO as demonstrated by Kim et al. [194] and in this work.

The synthesised powders were highly crystalline as shown by both TEM and XRD. According to XRD the lattice parameter increased with increasing tin content, which is in line with previous reports [63]. Although Sn^{4+} is smaller than In^{3+} [79], it is known that the tin doping in ITO increases the lattice parameter due to interstitial oxygen atoms associated with the Sn-doping and incomplete shielding between the Sn^{4+}-ions [13]. The almost linear increase of the lattice parameter (Figure 6.1) indicates that as much as 15 cat% Sn has been successfully incorporated into the host lattice, which is significantly higher than the equilibrium solubility limit [78, 80]. The nano-crystalline ITO powders with high Sn-content are therefore metastable, and decomposition to ITO and SnO_2 will occur if the powders are heated above 800 ºC, as confirmed in Figure 6.10.

6.3.2 Sintering of In_2O_3

It is clear from the dilatometer data that the nano-crystalline In_2O_3 powder started to densify already at temperatures as low as 600 - 700 °C (Figure 6.4) in good agreement with previous reports [194, 196]. Solid state sintering (densification) can occur by either grain boundary diffusion or bulk (lattice) diffusion from the grain boundary. Lattice diffusion is not expected to take place when the absolute temperature is below 2/3 of the melting temperature of a material. The mass transport mechanism in the initial stage of densification of nano-crystalline In_2O_3 is therefore proposed to be grain boundary diffusion due to the high melting point of In_2O_3 (2183 K) [251]. In order for this mechanism to be active, grain boundaries must therefore have been formed by necking during heating to 600 °C. It is difficult to observe significant coarsening in the SEM-image of In_2O_3 at 600 °C (Figure 6.7 (a)), but there is a substantial drop in surface area from the powder to the sample sintered at 600 °C, showing that coarsening and neck formation has taken place. Surface diffusion contributes to the initial mass transport during heating of almost all systems [185], and is the only possible mass transport mechanism that may lead to coarsening at these low temperatures.

The densification rate of In_2O_3 increases from 700 to 1000 °C, where it goes through a maximum, and then decreases again as the temperature is further increased. It is common for many ceramic systems to go through regimes where surface diffusion, leading to coarsening, grain boundary diffusion, causing densification, and grain growth dominates sequentially as the temperature is elevated [184]. It was observed that the grain size of In_2O_3 began to increase substantially from about 800 and 1000 °C (Figure 6.7 and 6.8). A substantial amount of the driving force for densification is, thus, removed by the grain growth and coarsening.

The densification rate of In_2O_3 was observed to increase again above 1200 °C (Figure 6.4) and the densities after isothermal sintering increased significantly from 1200 to 1400 °C (Figure 6.5). Densification due to grain boundary diffusion is proposed to take place already at 700 °C, and it is unlikely that the same mass transport mechanism causes this re-entrance of densification at a temperature more than 500 °C higher. On the other hand, lattice diffusion will take place at a considerable rate at some point as the temperature is increased. It is therefore proposed that lattice diffusion causes the re-entrance of a higher densification rate from about 1200 °C, accompanied by grain growth and pore removal. An increasing weight loss is also starting to manifest itself in the same temperature region. This is an indication that evaporation-condensation, which is a mass transport mechanism leading to coarsening, starts to take place at a significant rate. There will be a competition between lattice diffusion and evaporation-condensation

regarding the use of the remaining driving force for sintering at high temperatures. However, the decreasing density above 1450 °C cannot solely be explained by an increasing influence of evaporation-condensation. In the dense microstructure of In_2O_3 obtained after sintering at 1400 °C for 2 h (Figure 6.7 (i)), no necks are present. The large weight loss demonstrates that significant evaporation from the sample is occurring, but at this stage the microstructure can no longer be influenced by evaporation-condensation, as there are no necks or areas with different curvature where the condensation can preferentially occur. On the other hand, a significant grain growth accompanied by pore growth and coarsening is observed when comparing the microstructure of the In_2O_3 material sintered at 1400 and 1600 °C. It is known that the coalescence and growth of gas filled pores due to grain growth can cause a decrease in density during prolonged sintering when an inert gas like nitrogen is filling the pores [185].

The sintering atmosphere starts to influence the sintering already below 900 °C (Figure 6.12). The effect of the atmosphere has been documented previously [69, 191], but the thermodynamics of the sublimation of these oxides has not been discussed regarding the sintering and will be presented here. According to thermodynamic data [252], the sublimation of In_2O_3 will mainly occur through the reaction given in Equation 6.1:

$$In_2O_3\,(s) \rightarrow In_2O\,(g) + O_2\,(g) \qquad (6.1)$$

Decreasing the partial pressure of oxygen would, therefore, enhance evaporation, which can explain why the sample sintered in nitrogen achieved a lower density (Table 6.2). The calculated partial pressure of In_2O (g) as a function of T and partial pressure of O_2 is shown in Figure 6.13 (a). The thermodynamic data for reaction (6.1) was taken from [253]. It has been shown by thermogravimetrical analyses that the sublimation of In_2O_3 starts to occur at noticeable rates at around 1200 °C [254, 255], which is in reasonably good agreement with the results in this work. At these high temperatures, the oxygen partial pressure will obviously influence on the sintering by affecting mass transport by evaporation-condensation. However, at 900 °C the vapour pressure of In_2O (g) is only about 10^{-15} bar even in the nitrogen atmosphere. Though the nano-size of the grains gives small diffusion lengths and large curvatures (driving force for mass transport), these very low vapour pressure suggests that mass transport by evaporation-condensation is not significant in this temperature region. Thus, it is likely that the partial pressure of oxygen may affect other mass transport mechanisms than evaporation-condensation, by introducing and removing oxygen vacancies and interstitials, either in bulk, at surfaces or grain boundaries as discussed further in Chapter 6.3.2. Finally, though it is clear that the In_2O (g) sub-oxide has a significantly higher

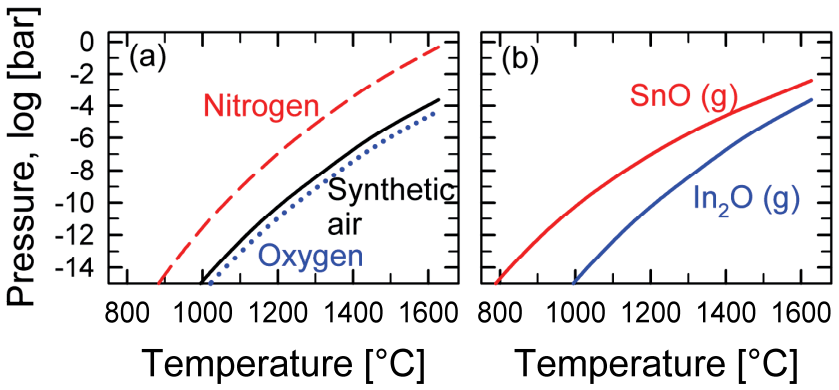

Figure 6.13. The partial pressure of the suboxides In_2O and SnO above the corresponding oxides as a function of temperature in different atmospheres. (a) Partial pressure of In_2O in nitrogen (dashed line), air (solid line) and oxygen (dotted line). Oxygen partial pressures of 10^{-4}, 0.2 and 1 were used for the respective atmospheres. (b) Comparison between the partial pressure of SnO and In_2O in air.

partial pressure in nitrogen than in air or oxygen, the difference between the two oxidising atmospheres is small. The dilatometer curves in Figure 6.12 and the densities and weight losses in Table 6.2 were similar for the materials sintered in air and oxygen. In a work by Kim et al. somewhat larger differences between samples sintered in air and oxygen was observed [191]. They argued that the effect was caused by reduced evaporation and also that in the final stage of sintering, where the porosity is mostly closed, the solubility of the gas in the solid lattice is vital for the elimination of the remaining pores. At this stage it is obvious that an oxygen atmosphere is a significant advantage, as air contains mostly nitrogen, which has a lower solubility in In_2O_3. Our results indicate that the advantage of choosing an oxygen atmosphere over air is mostly because of the final pore removal, while the reduction of the evaporation is less important in the final stage of sintering. However, in earlier stages of sintering, when concave curvature still remains in the microstructure, evaporation-condensation will contribute significantly to retard densification. A higher heating rate was used for the dilatometer experiments performed by Kim et al. [191]. This indicates that their samples could have more driving force for mass transport left when they reach temperatures where evaporation-condensation can occur, which could explain the larger influence from the oxygen atmosphere.

6.3.3. Sintering of ITO

It is evident from the present findings and previous reports [194, 196] that doping In_2O_3 with SnO_2 degrades the sintering properties at intermediate temperatures, even in the case of nano-sized powders. The poor sinterability of ITO compared to In_2O_3 can partly be explained by the higher valence of Sn^{4+} compared to In^{3+}. The cation with higher valence will cause a more covalent bond with oxygen and, thus, reduce the mobility of the cations in ITO. It is also known that Sn^{4+} is compensated by oxygen interstitials forming defect clusters [256], which also might influence on the bulk diffusion of cations. Furthermore, the fact that SnO_2 doping strongly influences the sintering denotes that the rate limiting step for the sintering process is cation diffusion. Reducing oxygen partial pressure would decrease the concentration of oxygen interstitials and expand the lattice, which suggest enhanced bulk diffusion of cations. The lower sintering rate in nitrogen (Figure 6.12) can therefore not be related to bulk diffusion of cations. This is also in line with the conclusion that the initial sintering is caused by grain boundary diffusion. To reveal the mechanism for the strong retardation of sintering under inert conditions further investigations are needed.

Only minor shrinkage was observed for ITO up to 1000 °C (Figure 6.4 and 6.5). The initial densification around 1000 °C, though significantly retarded compared to pure In_2O_3, can be ascribed to grain boundary diffusion due to the relatively moderate temperatures compared to the melting point of In_2O_3, as discussed above. The grain growth in ITO was also substantially lower than for In_2O_3 below 1000 °C. However, the significant reduction of surface area of the ITO material from 600 to 1000 °C clearly illustrates that coarsening has taken place (Figure 6.8). A highly porous and coarse microstructure, where the particles have grown together without significant densification, is evident in the SEM image of ITO after sintering at 1000 °C (Figure 6.7 (f)). Thus, it appears that the tin doping is hindering both grain boundary diffusion and grain growth, thereby opening for more coarsening in the ITO material compared to In_2O_3.

A secondary SnO_2-phase precipitated from the ITO solid solution between 800 and 1000 °C (Figure 6.10). The solid solution with 5 cat% Sn, prepared by the sol-gel route, is in a metastable state since 5 cat% Sn is significantly higher than the solubility limit of SnO_2 in ITO at 800 °C [78]. At low temperatures the cation mobility is not sufficient to acquire the stable two-phase equilibrium, but between 800 and 1000 °C the stable two phase mixture appeared, as shown by XRD. This exsolution of excess tin is in very good agreement with recent work by Gonzales et al. [80]. SnO_2(s) is most likely nucleated at the grain boundaries. This precipitation will, thus, lead to a temporarily higher concentration of Sn^{4+} at the grain boundaries, which can explain that grain boundary diffusion and grain growth are

hindered in ITO compared to In_2O_3 at these temperatures. The particle size of SnO_2 has been reported to be particularly important during sintering of initial mixtures of nano-crystalline In_2O_3 and SnO_2 [196]. The lattice parameter of cubic In_2O_3 is reported to increase with increasing amount of tin doping [63, 80]. Precipitation of SnO_2 reduced the tin content in the solid solution, which explains the observed reduction in the lattice parameter from 800 to 1000 °C. As the temperature was further increased the solubility of SnO_2 in In_2O_3 increases [78, 80], and SnO_2 re-dissolved in the ITO solid solution. The lattice parameter was observed to increase until it becomes close to constant (10.1260 Å) when the SnO_2-phase disappeared. This value is in good agreement with the previously reported lattice parameter for ITO with 5 cat% Sn [63, 80].

Other secondary phases in the In_2O_3-SnO_2 system, such as In_2SnO_5 and $In_4Sn_3O_{12}$, have also been reported to influence on the sintering of ITO [194, 196]. The presence of In_2SnO_5 has been reported to have a negative effect on the sintering, while the presence of $In_4Sn_3O_{12}$ has been reported to have a positive effect by hindering abnormal grain growth in the final stages of sintering. In_2SnO_5 is a metastable phase that appears when tin-doped $In(OH)_3$ prepared by co-precipitation decomposes [194], and was not observed in this work. $In_4Sn_3O_{12}$ is formed by In_2O_3 and SnO_2 at temperatures above 1345 °C [257]. According to the phase diagram [78, 80] this phase should appear when a tin doping amount of 5 cat% is used, but it was not possible to establish its presence in the ITO material used in this work. Small concentrations of this phase is difficult to detect by XRD because its strongest peaks have similar d-spacings to that of the cubic In_2O_3 bixbyite structure, as both of them are fluorite derived structures [257]. The weight loss of the samples shows that the Sn content could have been somewhat reduced by evaporation, however the lattice parameters give evidence that the actual tin content in the bulk remains at about 5 cat% even at higher temperatures (mainly loss from surface). The presence of secondary phases appears to be important [194], but the difference between the sintering of In_2O_3 and ITO cannot exclusively be explained by this factor. There is a significant difference between the densification of ITO and In_2O_3 before the appearance of SnO_2, and at 1300 °C the shrinkage rate of ITO is significantly higher than for In_2O_3, even though SnO_2 is still present (Figure 6.4 and 6.8). This indicates that the effect of other factors, such as the higher valency of Sn, should not be underestimated.

The densification rate of ITO increased significantly above 1100 - 1200 °C, which is also reflected in the SEM micrograph in Figure 6.7 (h). Densification in this temperature range is dominated by lattice diffusion based on the observations for pure In_2O_3. At higher temperatures than 1300 °C the weight loss observed for ITO becomes noticeable, and mass transport due to evaporation-condensation must take

place. SnO_2 has a relatively high vapour pressure and evaporates mainly according to the reaction given in Equation 6.2 [252]:

$$2\ SnO_2\ (s) \rightarrow 2\ SnO\ (g) + O_2\ (g) \qquad (6.2)$$

The calculated partial pressure of SnO (g) is significantly higher than for In_2O (g), as illustrated in Figure 6.13 (b), which explains the higher weight loss of ITO compared to In_2O_3 (Figure 6.5 and Table 6.2). However, even if the partial pressure of SnO (g) is high, it is only about 10^{-10} bar at 1000 °C. This partial pressure is not high enough to give a significant contribution from the evaporation-condensation mechanism. This implies that the mass transport mechanism leading to the considerable coarsening of ITO at intermediate temperatures most likely is surface diffusion (lattice diffusion from surface may also contribute to coarsening, but is not considered in this case). At temperatures above 1400 °C, there was a significant pore coarsening due to grain growth, also for ITO (Figure 6.7 (j) and (l)). This effect can explain the reduced density at higher temperatures, probably in combination with a higher influence from evaporation-condensation.

The presence of agglomerates has been reported to be important regarding the sintering of nano-crystalline ITO [192, 258]. The powder used in the present sintering study was prepared by a sol-gel method, and such Pechini-related syntheses are known to yield a certain degree of particle agglomeration [155]. Agglomerates can be seen in Figure 6.2 (a), though it is difficult to distinguish between soft and hard agglomerates. The difference in the density of materials prepared from ball milled and non-ball milled powders clearly demonstrates the importance of removing agglomerates from nano-crystalline powders to obtain high density. Furthermore, similar densification and densification rate curves as presented in Figure 6.4 has been reported [192-194], and the influence of agglomeration has been discussed. Two maxima in the densification rate has been reported both for In_2O_3 [194, 258] and for ITO [192-194]. These maxima have been attributed to different mechanisms caused by the agglomeration of nano-crystalline powders leading to a non-uniform particle size distribution. In the first mechanism of densification, the smaller pores inside the agglomerates are eliminated, while in the second, the larger inter-agglomerate pores are removed [192, 258]. In order to investigate this effect, the pore size distribution of the materials was measured by nitrogen adsorption. If the two maxima in the densification rate were caused by the elimination of pores of different sizes, the pore size distribution should be bi-modal at low temperatures, with the mode at the smallest pore size being removed as the first step of densification is progressing. Contrarily to this, the pore size distributions of the powders presented here were not bi-modal either at 600, 800 or 1000 °C (Figure 6.9). Even the non-ball milled samples, with more agglomerated powder, had uni-modal pore size distributions at

the same temperatures. Though it is evident that removal of hard agglomerates is important prior to sintering, our interpretation of these results is that the two maxima in the densification rate is not caused by agglomerates, but rather from a change in the rate determining mechanism for mass transport, as discussed here.

Final densities higher than 95 % were obtained both for In_2O_3 and ITO with 5 cat%Sn in this study. Even higher densities could possibly be obtained by increasing the uniaxial pressure from 200 MPa to 300 MPa, leading to better packing of the green body [192, 259]. The present findings clearly demonstrates that significant coarsening takes place at intermediate temperatures, especially in the case of ITO, and high heating rate during sintering is beneficial. However, too high heating rates have been reported to be undesirable due to so-called differential densification [191, 195]. Sintering in oxygen would also be beneficial regarding the final pore removal, as discussed above.

The preceding discussion on the sintering includes aspects which are relevant for the sintering of ITO thin films, as the constrained sintering of thin films basically occurs through the same mechanisms as in bulk materials [260]. Therefore, if the purpose of a heat treatment is to modify the microstructure of ITO thin films, the mass transport mechanisms discussed here must be taken into consideration. The present findings show that nano-crystalline ITO, not confined by any substrate, does not sinter in temperatures up to 1000 °C. The small amount of shrinkage that does occur is caused by grain boundary diffusion, which was demonstrated to be hindered by the tin doping, compared with pure In_2O_3. However, significant coarsening by surface diffusion was demonstrated to take place. In a thin film based on ITO nanoparticles coarsening will contribute to neck formation and improve the physical contact between the particles. This could substantially decrease the electrical resistivity of the film even though its density is not affected.

6.4. Conclusions

The sol-gel process can be used to prepare high quality nano-crystalline ITO powder. The powder was phase-pure, homogeneous and the tin doping amount could be readily controlled. The particle size of the prepared powder with 5 cat% tin was approximately 15 nm after heat treatment at 600 °C. The prepared powders were used to investigate the solid state sintering of In_2O_3 and ITO with 5 cat% Sn. The densification of In_2O_3 occurred in two temperature regions, the initial densification process starting at around 600 °C and the final above 1200 °C. These two processes were discussed in terms of grain boundary and bulk diffusion, respectively. Coarsening and particularly grain growth were demonstrated to

interfere with the densification of nano-crystalline In_2O_3 at intermediate temperatures. Coarsening at low temperatures was mainly due to surface diffusion mechanism, while coarsening by evaporation-condensation took place at higher temperatures. Pore coarsening due to grain growth reduced the density at temperatures above 1450 °C. SnO_2 doping was observed to inhibit sintering of ITO compared to In_2O_3 at intermediate temperatures. The reduced cation mobility in ITO relative to In_2O_3 was explained by the higher valence state of Sn^{4+} compared to In^{3+}. It was found that grain boundary diffusion and grain growth was hindered by the tin doping and ITO obtained a coarser microstructure at intermediate temperatures. This effect was enhanced by the precipitation of SnO_2(s), taking place in ITO below 1000 °C. SnO_2(s) was observed to re-dissolve in ITO above 1300 °C. At high temperature, evaporation of the oxides caused significant weight losses. This effect was more pronounced for ITO than for In_2O_3 due to the higher vapour pressure of SnO(g) relative to In_2O(g). Finally, it is pointed out that mainly surface diffusion can take place during processing of ITO thin films up to 1000 °C.

7. ITO thin films prepared by the aqueous sol-gel process

7.1. Deposition and characterisation of ITO thin films

The sol-gel process developed in Chapter 5 was applied by spin coating to prepare transparent and conducting ITO thin films. The total thickness of the films, and thereby also their functional properties, could be controlled by repeating the deposition process. It was demonstrated to be necessary to add PVA as a wetting agent [261, 262] to the solutions in order for thin films to be successfully formed. The thermogravimetrical analysis of the PVA modified sol is shown in Figure 5.4 (red curve, 1:1.5 AA + 1:1.5 EG + 3 wt % PVA). The total weight loss and the temperature where the decomposition is completed increased somewhat due to the addition of PVA, compared to the sols used for the preparation of ITO powder. Initial experiments demonstrated that the films prepared by the sol-gel process had an optimised conductivity with a tin doping concentration of 10 cat% [234]. The ITO films presented here all have this doping concentration, unless where otherwise is noted. The structural properties of the films were analysed by XRD and TEM while the functional properties were characterised by transmission spectroscopy, ellipsometry and electrical conductivity measurements. The films presented in Chapter 7.1 were prepared from Solution 1, as described in Chapter 4.2.

The presence of indium and tin in the films deposited on the glass substrates was confirmed by EDS, and a tin concentration of 9 ± 1 cat% was found. This confirms the nominal concentration in the sols and that the amount of possible SnO_2 precipitates, which were filtered away before spin coating, was small. No impurity elements from the substrate could be observed in the thin films. XRD of the heat treated films demonstrated that the films were nano-crystalline with the cubic In_2O_3 crystal structure with no preferred orientation, as shown for a film prepared by 10 depositions in Figure 7.1. Based on the line broadening in the XRD and the Scherrer equation, the crystallite size in the films was calculated to be 13 ± 3 nm. The lattice cell parameter of the films was 10.153 ± 0.004 Å, depicted in Figure 7.2, which is significantly higher than the lattice cell parameter of the nano-crystalline powders, suggesting a substantial lattice strain in the films (tensional strain).

TEM and SEM micrographs of selected films are given in Figure 7.3. Each deposited layer in the films could easily be distinguished, with a thickness of

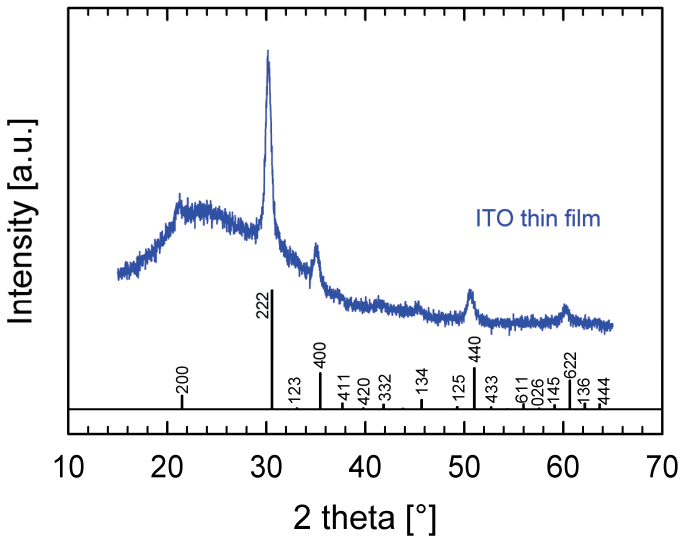

Figure 7.1. XRD of an ITO thin film with 10 cat% Sn prepared by 10 subsequent spin coating depositions. The reference pattern for the cubic In_2O_3 polymorph with space group $Ia\bar{3}$ is given at the bottom. The broad bump at around 25 ° is due to the amorphous substrate.

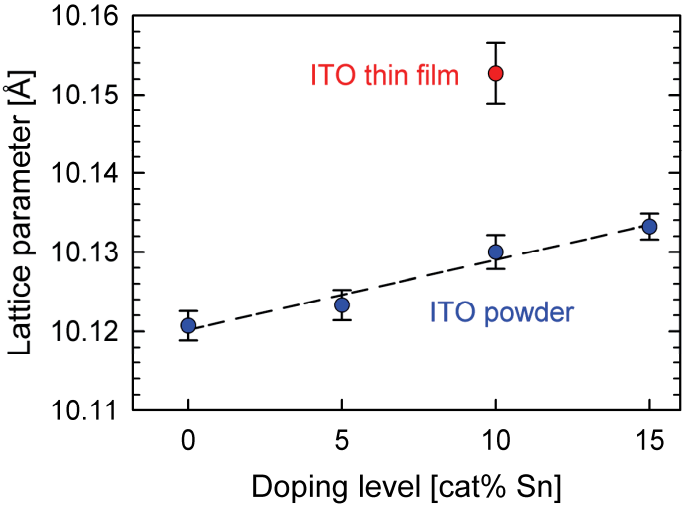

Figure 7.2. The cubic lattice parameter of an ITO thin film prepared by 10 subsequent depositions. The lattice parameters of ITO powders with different doping amounts, from Figure 6.1, are included as a reference.

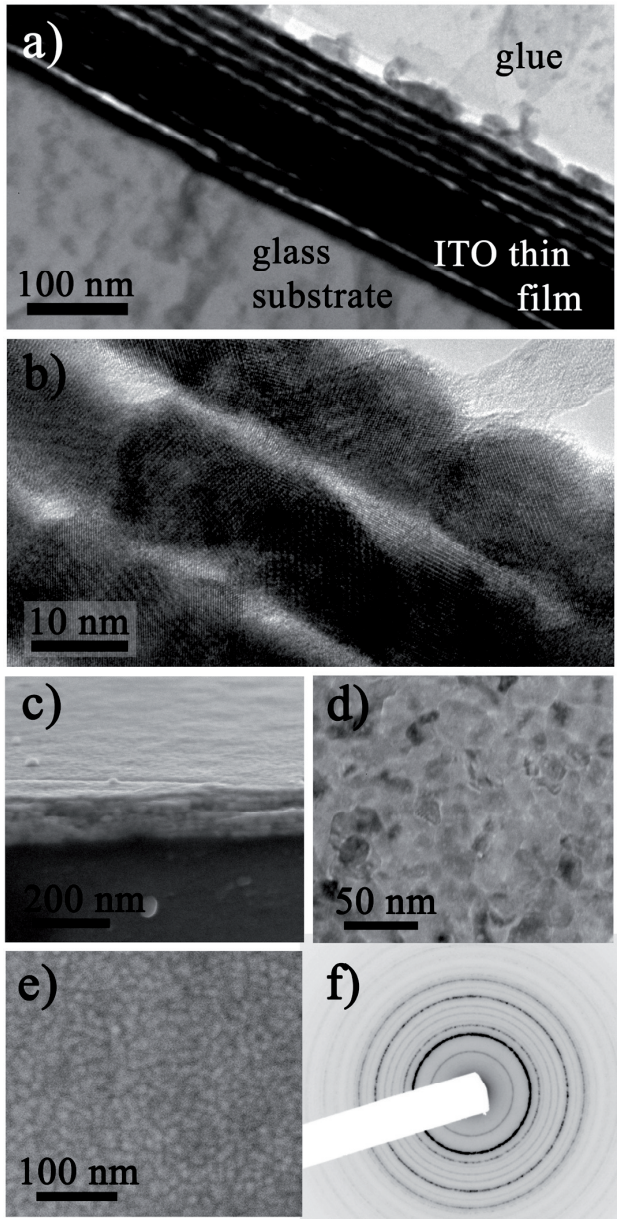

Figure 7.3. TEM image of the cross section of a film prepared by 10 subsequent depositions (a), HR-TEM image of a cross section (b), SEM image of the cross section of a film prepared by 7 subsequent depositions (c), TEM image of the top view of a film (d), SEM image of the top view of a film with only 1 deposited layer (e), diffraction pattern of a film with 10 layers (f).

17 ± 1 nm, as illustrated in Figure 7.3 (a). A single layer of grains was observed in each layer, Figure 7.3 (b), and no grains extending over multiple layers could be observed. The thickness of a film with 7 deposited layers, depicted in Figure 7.3 (c), was 121 ± 8 nm, which further indicates that the total thickness is approximately 17 nm times the number of depositions. TEM and SEM images of the top view of the films are given in Figure 7.3 (d) and (e), respectively. The TEM image shows how the grains are interconnected and that the grains appear to be approximately spherical with a grain size of 16 ± 3 nm. The film depicted in Figure 7.3 (e) was prepared by only 1 deposition, and demonstrates that the films were continuous and homogeneous without pin-holes even after the first deposition. Electron diffraction patterns from the thin films could be indexed to cubic In_2O_3 with no traces of other phases, in line with XRD (Figure 7.3 (f)). In some cases the relatively harsh mechanical treatment during the TEM sample preparation caused delamination between the layers in the film. The thickness of the films were also analysed by ellipsometri, and the thickness of films with different number of layers are given in Table 7.1. These results confirm that the total thickness of the films were ~ 17 nm times the number of depositions. The first deposited layers will be more affected by the properties of the substrate, and the data indicates that the first couple of layers are somewhat thicker than the rest, although this trend is rather weak.

Table 7.1. Thickness of ITO thin films prepared with different number of depositions based on ellipsometry measurements.

Number of depositions	Film thickness [nm]	Average thickness per deposition [nm]
1	18.1	18.1
3	52.4	17.5
5	82.9	16.6
7	116.3	16.6
10	168.8	16.9

The transmission spectra of ITO thin films prepared by varying number of depositions are given in Figure 7.4. The transmittance of the samples is 80 % or higher throughout the visible region, and remains high into the NIR region. The trasmittance of the pure glass substrate is shown for comparison. The UV-cut off is at approximately 300 nm, and is shifted to slightly higher wavelengths as the film becomes thicker. A similar trend was reported by Tahar et al., who claimed that

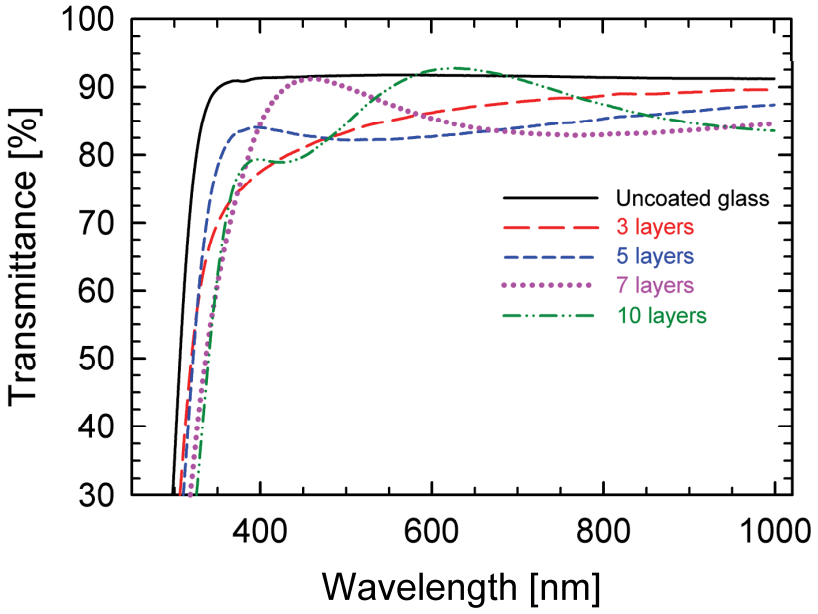

Figure 7.4. Transmittance of ITO thin films prepared by 3, 5, 7 or 10 subsequent depositions. Maxima and minima due to interference with the film thickness can be seen for the thicker films.

this observation was probably caused by a quantum effect [34]. The spectra of the thicker films appear to have maxima and minima indicating interference with thefilm thickness [140, 263]. This effect was not observed in films made by 3 or fewer layers (thinner than approximately 50 nm). The transmittance, including the maxima and minima due to interference, was highly reproducible for films made by the same number of depositions. The optical band gap for the films was found to be in the range of 3.7 to 3.9 eV, which is in good accordance with values reported for films prepared by various techniques [16]. No significant trend between the band gap and the thickness of the films could be observed. Transmittance spectra of thin films of pure In_2O_3 and ITO with 5 cat% Sn are given in Figure 7.5. Two interesting effects can be observed by comparing the two spectra, both of which are related to the increase of free electrons from the dopant. In the low-energy side, a decrease in the transmittance is observed for the tin-doped material, due to increased free-carrier absorption. On the high-energy side it can be seen that the UV-cut off is shifted towards higher energies for the doped sample caused by a Burstein-Moss shift.

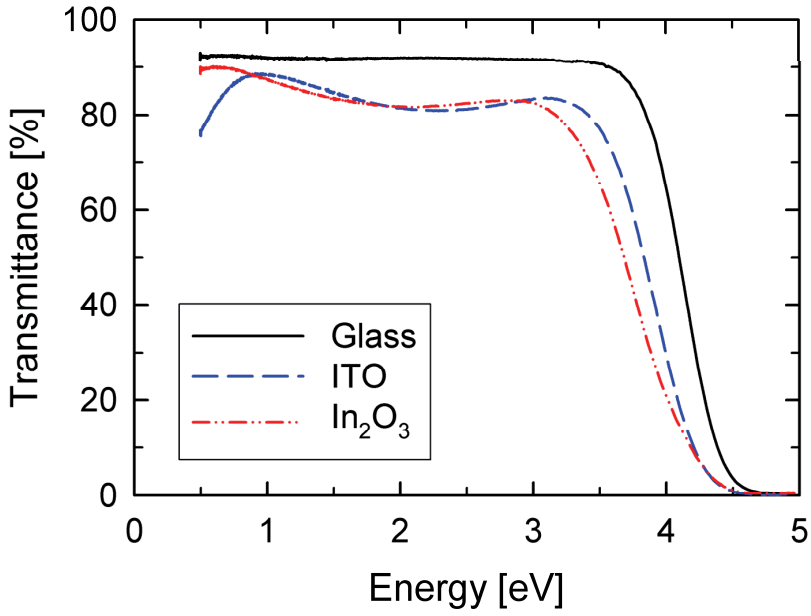

Figure 7.5. Transmittance of thin films of undoped In_2O_3 and ITO with 5 cat% Sn. The films were prepared by 5 depositions.

The complex dielectric function, $\tilde{\varepsilon}$, of the ITO thin films was obtained by ellipsometry and is given in Figure 7.6. The complex dielectric function consists of two parts, both of which are a function of wavelength or energy, according to Equation 7.1:

$$\tilde{\varepsilon}(\lambda) = \varepsilon_1(\lambda) + i\varepsilon_2(\lambda) \tag{7.1}$$

$\tilde{\varepsilon}(\lambda)$ is related to the refractive index, $\tilde{n}(\lambda)$, as described in Equation 7.2:

$$\tilde{\varepsilon}(\lambda) = \tilde{n}(\lambda)^2 \tag{7.2}$$

The first part of the complex dielectric function, ε_1, is related to the polarisability of the material, while to second, ε_2, is related to absorption [242, 263]. The dielectric function displayed in Figure 7.6 is typical for semiconductors, where ε_2 is zero below the band gap and increases as the energy is increased above the band gap. The visible part of the electromagnetic spectrum is from about 1.8 to 3.2 eV, and the ε_2-curve clearly demonstrates that the deposited ITO thin film is not absorbing in this region. At energies below about 1 eV a slight increase in ε_2 can be observed due to the contribution from the free electrons in the material.

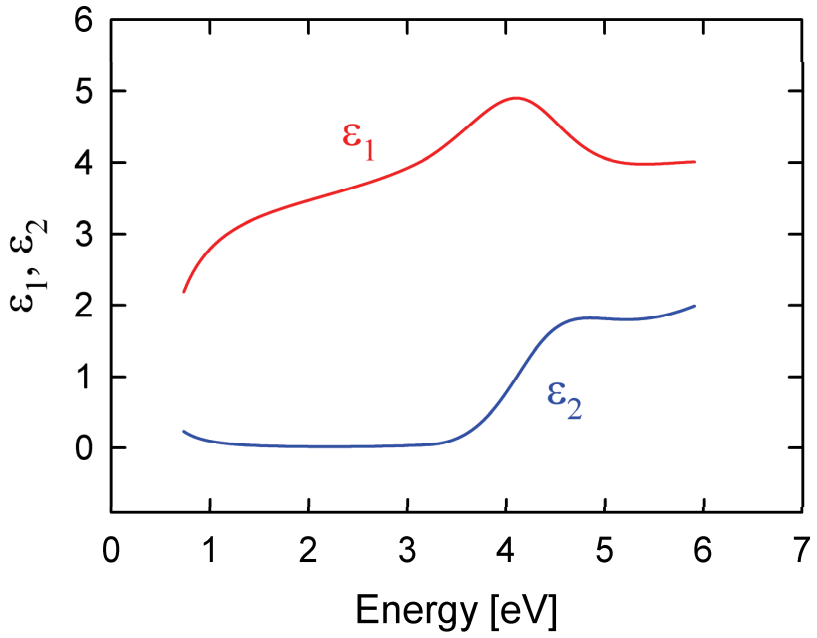

Figure 7.6. The two parts of the complex dielectric function as a function of energy for ITO thin films on glass substrates obtained by ellipsometry.

The sheet resistance of the films as a function of the number of deposited layers are given in Figure 7.7 (a). The sheet resistance was reproduced for two different samples for each thickness, and as the films became thicker the sheet resistancebecame almost equal for the two parallels pointing to good homogeneity of the films and reproducibility of the sol-gel spin coating depositon process. The reproducibility of the conductivity was also found to be good. The sheet resistance for the films with 10 deposited layers was 270 ± 3 Ω/square. The sheet resistance was fitted to a simple exponential function, $R_s = 2690 / \#^{0.99}$, where R_s is the sheet resistance and # is the number of deposited layers. The sheet resistance was, thus, close to inversely proportional to the number of depositions. As the sheet resistance is the specific resistance of the material divided by the thickness (Equation 4.2), this observation further verifies that the thickness of the film is proportional to the number of layers. The specific resistance of the films was calculated by assuming that the thickness was 17 nm times the number of deposited layers and is given in Figure 7.7 (b). The specific resistance is converging towards 4.59 ± 0.05 × 10^{-3} Ω·cm with increasing thickness of the films.

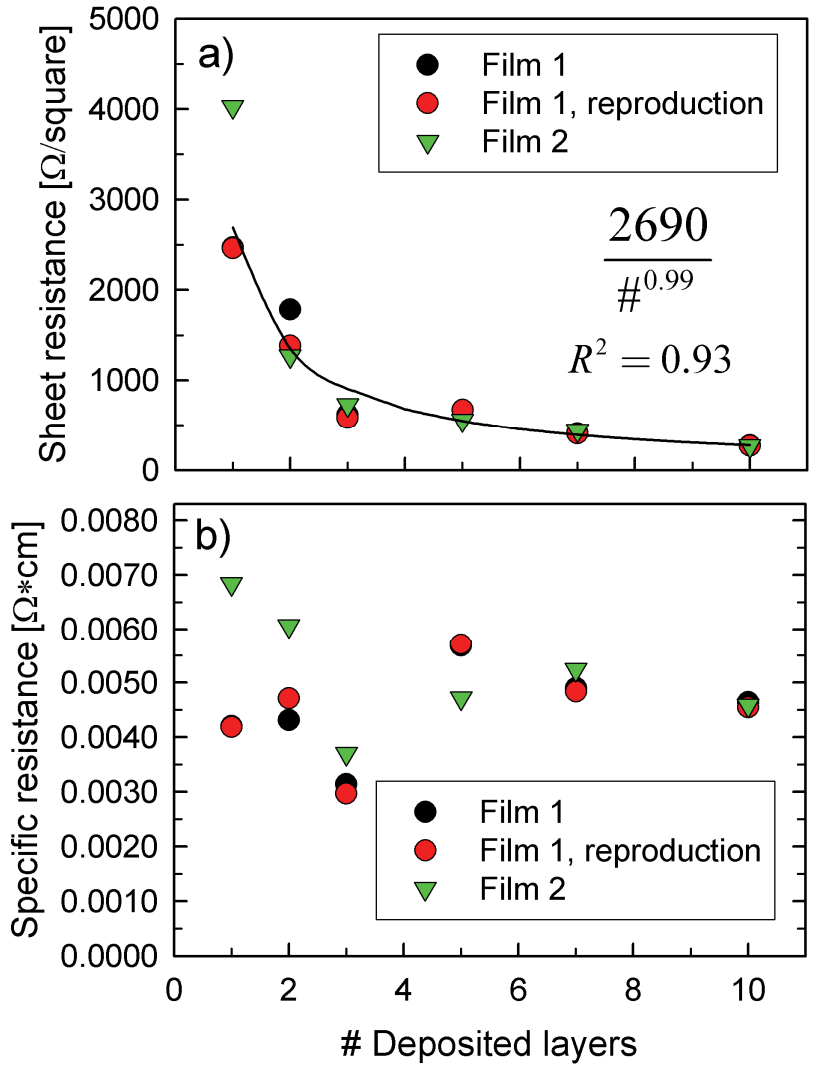

Figure 7.7. Sheet resistance of ITO thin films as a function of the number of deposited layers obtained by the van der Pauw method. The data was fitted to the formula $R_s = 2690 / \#^{0.99}$ ($R^2 = 0.93$) (a). Specific resistance calculated by assuming that the thickness of the films was 17 nm times the number of depositions (b). Two films were analysed for each number of depositions. Film 1 with two deposited layers was damaged during cutting, which is why the reproducability of the sheet resistance was poorer for this sample.

7.2. Modifications of the deposition process

For an industrial process it is a disadvantage that multiple depositions are required in order to get a film with sufficient thickness to achieve the desired conductivity. It therefore became desirable to modify the deposition process in an attempt to control the thickness of the deposited layers. An important parameter during spin coating is the viscosity of the solution [132, 264], and the measured viscosity of selected prepared solutions is summarised in Table 7.2. The solutions labelled Solution 3, 4 and 5 were solutions prepared by a 1:1 volume ratio mixing of one solution with the precursors and complexing agents and one with dissolved PVA, as described in Chapter 4.2. In this case the PVA content is the content of the PVA solution before the mixing, while the cation concentration is the final concentration after mixing. For the solutions labelled 3, 5 and 10 wt% PVA, on the other hand, the PVA content is the actual PVA content in the solutions.

Table 7.2. The viscosity of selected solutions with varying PVA content and cation concentration. The estimated uncertainty in the viscosity is ± 2 %.

Solution	PVA content [wt%]	Cation concentration [M]	Viscosity [$Pa \cdot s$]
Distilled water	0	0	9.06×10^{-4}
Solution 3	5	0.2	7.93×10^{-3}
Solution 4	5	0.5	9.49×10^{-3}
Solution 5	5	1.0	1.36×10^{-2}
3 wt %PVA	3	0	1.23×10^{-2}
5 wt % PVA	5	0	4.93×10^{-2}
10 wt % PVA	10	0	1.01

The viscosity of all the measured solutions was significantly higher than the viscosity of water. The difference in the viscosity between Solution 3, 4 and 5 is suggested not to be caused by the higher concentration of the cations themselves, but rather from the increasing concentration of the complexing agents that necessarily followed as the ratio between cations and complexing agents was kept at 1:1.5 for all solutions. The viscosity of the PVA solutions illustrates how drastically the viscosity is affected by increasing the PVA concentration. However, the difference between the viscosity of the 5 wt % PVA solution and the three mixed solutions show that the viscosity in the final mixed solutions is significantly reduced compared to the pure PVA solution.

All of the solutions demonstrated Newtonian behaviour, as illustrated in Figure 7.8 (a), except for the 10 wt % PVA solution which exhibited shear thinning properties, as shown in Figure 7.8 (b). In the first case the viscosity quickly reached a stable value as the shear rate was increased, whereas the viscosity was observed to be reduced as the shear rate increased in the latter.

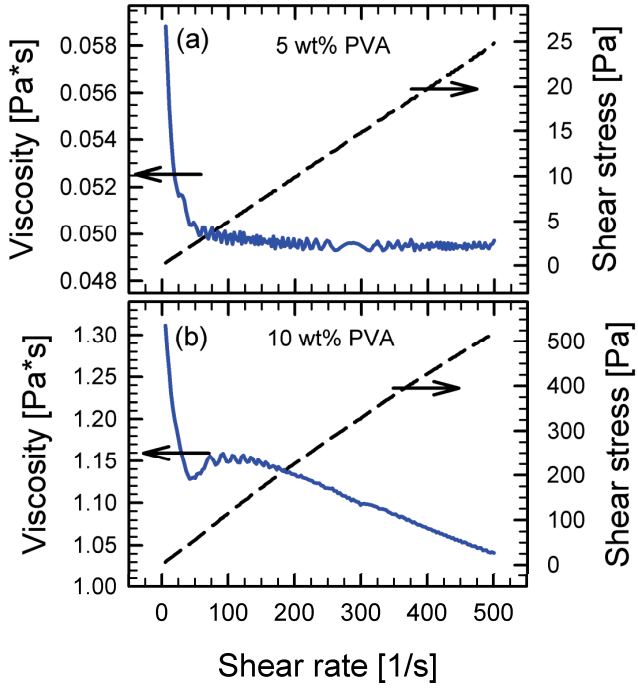

Figure 7.8. Viscosity (solid lines) and shear stress (broken lines) as a function of shear rate for solutions with 5 wt% (a) and 10 wt% PVA (b) dissolved in distillied water. The experiments were performed at 25 °C.

The variation in the parameters used during the deposition process, together with the obtained sheet resistances of the films, is presented in Table 7.3. Again, the cation concentration is the final cation concentration in the solution while the PVA content is the content in the original PVA solution before the 1:1 volume ratio mixing. Due to experimental problems, the thickness of the films presented in Chapter 7.2 was not measured. The effect of the modifications made to the deposition was therefore evaluated based on the sheet resistance of the films. All the films discussed in this chapter were prepared from three subsequent depositions, being a compromise between obtaining homogeneous films with a sufficient thickness and limiting the amount of time requiered to prepare the films.

Table 7.3. Film preparation parameters and sheet resistance of films prepared from solutions with different cation concentration and PVA content, spin coated at different rotation speeds and on different substrates. All films were prepared by three subsequent depositions and with heat treatment at either 530 or 600 °C after each deposition. The estimated uncertainty in the sheet resistance is ± 1 %.

Solution	Substrate	PVA content [wt%]	Cation concentration [M]	Rotation speed [rpm]	Heat treatment temperature [°C]	Sheet resistance [Ω/□]
Solution 1	Glass	3	0.2	1000	530	913
				2000	530	1062
				3000	530	803
				4000	530	1524
Solution 2	Glass	3	0.5	1000	530	213
				2000	530	186
				3000	530	300
				4000	530	351
Solution 3	Glass	5	0.2	1000	530	760
				2000	530	2510
				3000	530	3410
				4000	530	4330
Solution 3	Glass	5	0.2	2000	530	1216
Solution 4	Glass	5	0.5	2000	530	~6000
Solution 5	Glass	5	1.0	2000	530	806
Solution 1	Glass	3	0.2	3000	530	803
	Al_2O_3	3	0.2	3000	530	557
	YSZ	3	0.2	3000	530	630
Solution 1	Al_2O_3	3	0.2	2000	600	1191
Solution 2	Al_2O_3	3	0.5	2000	600	221
Solution 3	Al_2O_3	5	0.2	2000	600	248
Solution 4	Al_2O_3	5	0.5	2000	600	131

In the first series of experiments, Solution 1, 2 and 3 were used and the rotation speed during the spin coating was varied from 1000 to 4000 rpm. The sheet resistance of the films are given in Figure 7.9. The films spun at 4000 rpm had the highest sheet resistance for all three solutions. The difference between the films spun at 1000, 2000 and 3000 rpm was small for the films prepared from Solution 1 and 2, but for Solution 3 the sheet resistance decreased with decreasing rotation speed. Furthermore, increasing the cation concentration appeared to have a substantial effect on the sheet resistivity as the films prepared from Solution 2 had a lower sheet resistance than the ones prepared from Solution 1 for all rotation speeds. Increasing the PVA content, on the other hand, significantly increased the sheet resistance. However, in some of the films, especially the ones with increased PVA content, carbon residues could be observed.

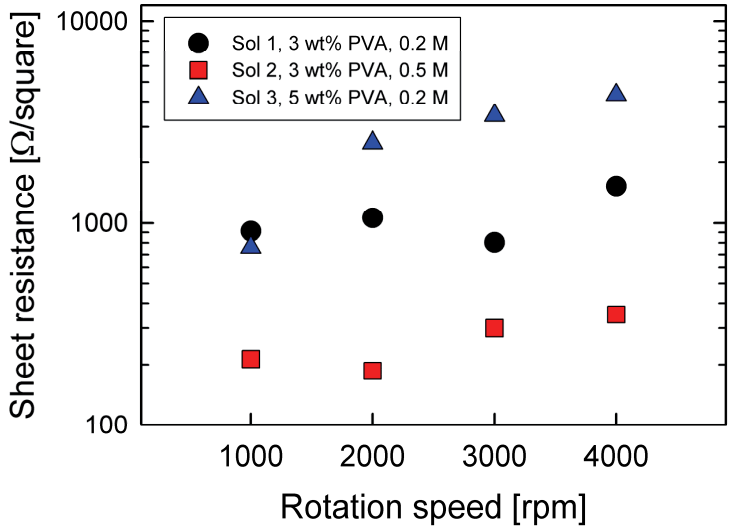

Figure 7.9. Sheet resistance of films prepared from spin coating of solutions with different cation concentration and PVA content and with varying rotation speed.

In the next series of experiments it was attempted to further increase the cation concentration. Films were prepared from Solution 3, 4 and 5 with a rotation speed of 2000 rpm, as described in Table 7.3. The films prepared from Solution 3 and 5 had sheet resitances of 1216 and 806 Ω/□, respectively, while the film prepared from Solution 4 was visually observed to be cracked and somewhat delaminated. This film had a significantly higher sheet resistance than the others and the sheet resistance was not reproducible when the conductivity measurement was repeated.

In order to be able to heat treat the films at higher temperatures it was attempted to deposit the films on more refractory substrates, YSZ, Al_2O_3 and MgO. The sheet resistance of films deposited on glass, YSZ and Al_2O_3 were 803, 630 and 558 Ω/□, respectively, while no film was formed on the MgO substrate. These films were prepared from Solution 1 and a rotation speed of 3000 rpm. Following this, thin films were deposited on Al_2O_3 substrates and heat treated at 600 °C in the last series of experiments. These films were prepared from Solution 1 to 4 and a rotation speed of 2000 rpm. The sheet resistances were 1191, 221, 248 and 131 Ω/□ for the films prepared from the respective solutions. On the three latter films, with the lowest sheet resistance, interference patterns were visible and certain inhomogeneities could be observed. These results, together with the sheet resistance of the films on different substrates, are presented in Figure 7.10.

The cubic lattice parameter of the four films is given in Table 7.4. The difference in the lattice parameter between the films prepared from Solution 1, 2 and 3 was small, while the film prepared from Solution 4 had a noticable smaller lattice parameter than the others.

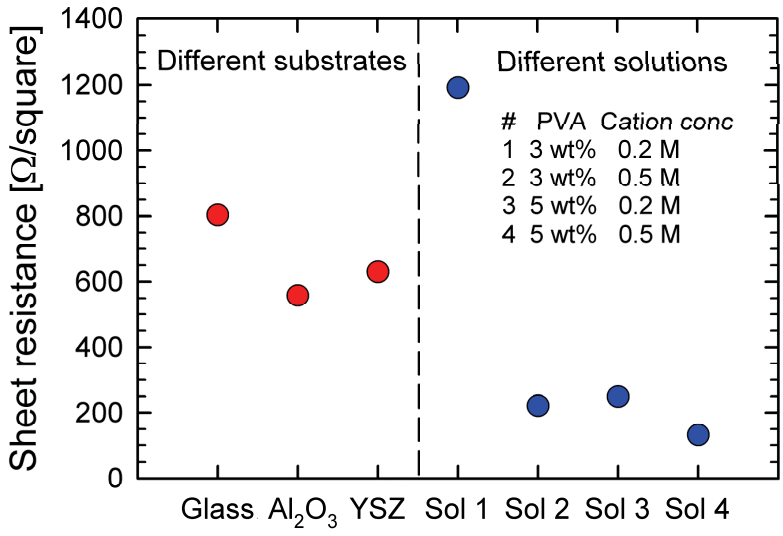

Figure 7.10. Sheet resistance of films prepared on different substrates and from different solutions. The three films to the left were prepared from Solution 1, a rotation speed of 3000 rpm and heat treated at 530 °C on glass, Al_2O_3 and YSZ respectively. The four films to the right were prepared from solution 1 to 4 with a rotation speed of 2000 rpm and heat treated at 600 °C. These four films were all deposited on Al_2O_3 substrates.

Table 7.4. Cubic lattice parameter of ITO films prepared from solutions with different cation concentration and PVA content. The estimated uncertainty in the lattice parameter is ± 0.002 Å.

Solution	PVA content [wt%]	Cation concentration [M]	Lattice parameter [Å]
Solution 1	3	0.2	10.139 ± 0.002
Solution 2	3	0.5	10.136 ± 0.002
Solution 3	5	0.2	10.138 ± 0.002
Solution 4	5	0.5	10.133 ± 0.002

Several of the films discussed in Chapter 7.2, prepared by only 3 depositions, have a lower sheet resistance than the one with 10 depositions in Figure 7.7. The sheet resistances to the right in Figure 7.10 clearly demonstrate that both an increase of the PVA content and the cation concentration reduced the sheet resistance. The thickness of the films was not established. However, as the four films were heat treated at the same temperature it it reasonable to assume that the specificic resistance of the films is similar, indicating that the significant improvement of the sheet resistance is related to thicker films. Thus, changing the properties of the spin coating solution can clearly be used to tailor the thickness of the deposited layers.

7.3. Optimisation of the conductivity

In order to improve the conductivity of the deposited ITO thin films, the heat treatment temperature and atmosphere was modified. In situ conductivity measurements were performed inside a sealed quartz tube in order to investigate the effect of post-annealing at different temperatures and in different atmospheres. The point defect chemistry of ITO dictates that annealing in different atmospheres should have a large impact on the conductivity. At high partial pressures of oxygen the tin dopants are compensated by interstitial oxygen atoms, causing a decrease in the conductivity. Annealing in reducing conditions will remove interstitial oxygen and activate the tin dopants, according to Equation 3.4, thereby increasing the conductivity. This oxidation or reduction requires oxygen diffusion through the film, a process which is thermally activated. A change in temperature or partial pressure of oxygen will move the system away from equilibrium, upon which a conductivity relaxation will occur. The conductivity will change, relax and reach a stable steady state value when the new equilibrium is reached. All of the films

investigated in Chapter 7.3 were deposited from Solution 1, spun at 3000 rpm and prepared by three depositions. These parameters were selected in order for the films to be comparable to the films presented in Chapter 7.1. The heat treatment of the films was performed under vacuum (10^{-2} mbar), corresponding to an estimated partial pressure of oxygen of about 10^{-6} bar.

Initial experiments were carried out in order to confirm the effect of the annealing atmosphere. These films were all prepared on glass substrates and heat treated at 530 °C. The in situ sheet conductivity of a film during annealing at 500 °C for 5 h in air is given in Figure 7.11. The conductivity initially increased due to the increasing temperature, but reached a maximum at about 270 °C and then rapidly decreased before stabilising at a significantly lower conductivity. The sheet resistance was 546 Ω/□ before the experiment, but increased to 4992 Ω/□ after the experiment, due to the oxidation. Another film was annealed for 5 h in nitrogen at 300 °C, and the in situ conductivity is given in Figure 7.12. The partial pressure of oxygen in the nitrogen gas during the post-annealing was estimated to be approximately 10^{-4}, i.e. higher than during the prior heat treatment in vacuum, indicating that the film will be oxidised. The same behaviour was observed as for the film annealed in air. However, in this case the decrease in conductivity was slower due to the lower temperature and lower driving force for oxidation and

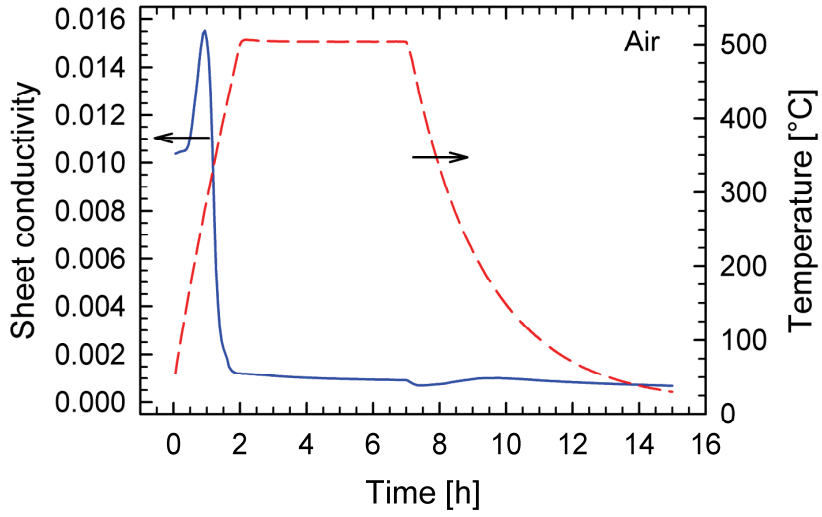

Figure 7.11. In situ condictivity of an ITO film during post-annealing at 500 °C in air for 5 h. The conductivity and temperature are given as a solid and broken line, respectively

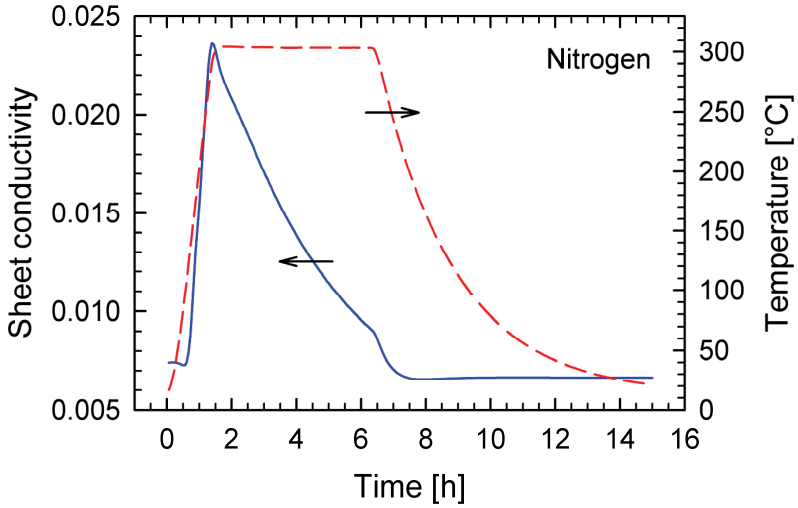

Figure 7.12. In situ conductivity of an ITO thin film during post-annealing at 300 °C in nitrogen for 5 h. The conductivity and temperature are given as a solid and broken line, respectively.

a steady state conductivity was not reached during the 5 hours at 300 °C. The conductivity before the annealing in nitrogen was 580 Ω/□, but increased to 862 after the experiment. In situ measurements of the conductivity were also conducted during annealing in 5 % hydrogen in argon. It was confirmed that the conductivity increased due to reduction, contrarily to the experiments in air and nitrogen. A steady state conductivity was not reached during annealing at 300 °C for 5 h in 5 % hydrogen in argon.

It was clearly established that post-anneling in different atmospheres had a significant effect on the conductivity, as predicted from the point defect chemistry of ITO (Chapter 3.2). However, it also became apparent during the initial experiments that it was impossible to anneal the films at high temperatures while measuring the in situ changes in the conductivity. When the temperature was elevated to above 500 °C, an abrupt drop in the conductivity was consistently observed, both for films deposited on glass and YSZ substrates. After the experiments the conductivity of these films was severely reduced or in some cases not possible to measure. This indicates that the drop was not caused by a loss of contact between the film and the electrodes, but rather from the films being damaged. The mechanical stress from the clamp which was pressing the film against the electrodes (Figure 4.2) may have caused damage to the films. The films were investigated by SEM, but it was not possible to observe possible cracks.

In order to observe the effect of an increased temperature on the conductivity of the films it was decided to do the high temperature heat treatment in the RTP furnace. These films were deposited on YSZ substrates in order to withstand the elevated temperatures. In situ changes in conductivity in reducing atmospheres were then performed separately at temperatures below the initial heat treatment temperature. The reduction was performed in 5 % hydrogen in argon for 10 h at 400 °C. The sheet resistance measured during different stages of this process is given in Table 7.5 and Figure 7.13. Two films were prepared for each RTP heat treatment temperature, but only one of these films was annealed. The sheet resistance of the two films prepared at the same temperature was within 5 % of each other. It was clear that increasing the heat treatment temperature after film deposition had a significant effect on the sheet resistance, as it decreased from 520 to 353 Ω/□ for the films heat treated at 530 and 800 °C. However, when the sheet resistance was measured again before the reduction, which was performed two weeks later, the sheet resistance was shown to decrease from 7 to 16 %, demonstrating an ageing effect. No trend could be observed between the size of this effect and the heat treatment temperature the films had been exposed to.

Table 7.5. The sheet resistance, R_s, after deposition, before the reduction, directly after reduction and a few days after the reduction for ITO thin films deposited on YSZ. The films were prepared by three depositions from Solution 1 on YSZ substrates, spun at 3000 rpm and heat treated at different temperatures after each deposition.

Heat treatment temperature [°C]	R_s after deposition [Ω/□]	R_s before reduction [Ω/□]	R_s directly after reduction [Ω/□]	R_s two days after reduction [Ω/□]
530	520	469	201	242
530	523			
600	399	365	154	197
600	424			
700	350	301	128	156
700	343			
800	353	295		128
800	354			

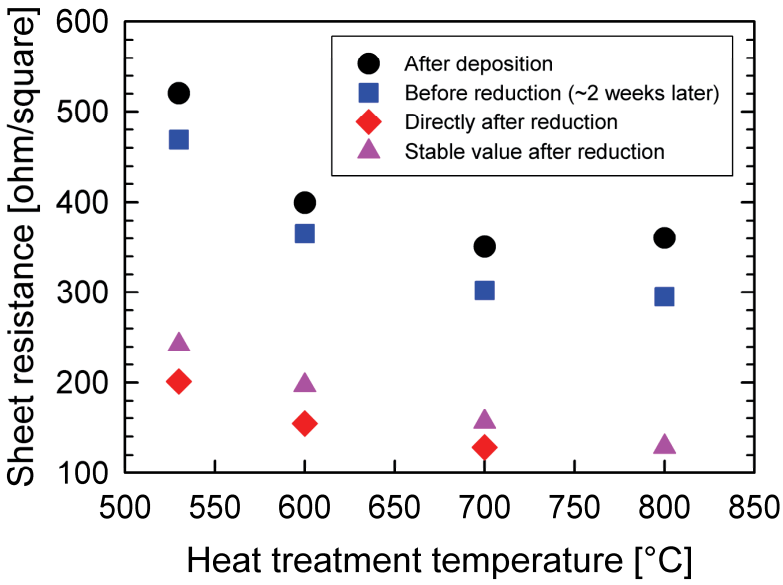

Figure 7.13. The sheet resistance after deposition, before the reduction about 2 weeks later, directly after reduction and a few days after the reduction for ITO thin films deposited on YSZ. The films were prepared by three depositions from Solution 1, spun at 3000 rpm and heat treated at different temperatures after each deposition.

The in situ conductivity for the four films measured during 10 h reduction at 400 °C in 5 % hydrogen in argon is given in Figure 7.14. The initial conductivity reflects that the conductivity was improved by increasing the RTP heat treatment temperature, as shown in Table 7.5 and Figure 7.13. The conductivity of all of the films increased with increasing temperature, but when the temperature reached about 400 °C the contact with platinum electrodes appeared to be damaged, causing noise. However, the conductivity stabilised during the 10 h reduction, indicating that equilibrium was reached. The conductivity was lowered during cooling after reduction, but stabilised at a level 55 to 64 % higher than the initial conductivity.

The conductivity of the films reached a stable value as the temperature was lowered down to room temperature after the reduction and was not affected by the removal of the gas flow of 5 % hydrogen in argon. However, when the quartz tube was removed, thereby exposing the film to ambient air, the conductivity started to decrease. The sheet resistances given in Table 7.5 and Figure 7.13 were measured directly after the removal of the quartz tube. The sheet resistance was then measured again at different times ranging from a couple of hours after the removal

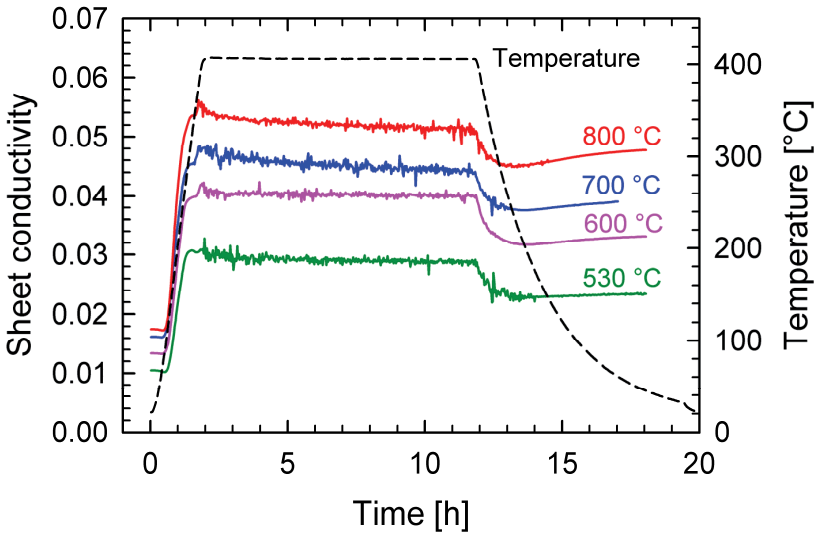

Figure 7.14. In situ conductivity of four ITO films during post-annealing at 400 °C for 10 h in 5% hydrogen in argon. The thin films were deposited on YSZ substrates, prepared by three depositions and were heat treated at temperatures ranging from 530 to 800 °C after each deposition. The conductivities and the temperature are given as a solid and broken line, respectively.

of the quartz tube to three weeks after the reduction. The consistent trend was that the sheet resistance stabilised at 18 to 27 % higher values after a couple of days and was not further increased when the measurement was repeated later. The sheet conductivity at room temperature of film after the post-annealing in hydrogen was measured for a couple of days after the removal of the quartz tube and is given in Figure 7.15. This film was heat treated at 530 °C, and it can be seen that the end value for such a film in Figure 7.14 matches the initial value in Figure 7.15. Initially, there is a drastic reduction of the conductivity. Already within the first minute the conductivity decreased with 2 %, and the conductivity was lowered by 5 and 10 % after about 6 and 24 minutes. After the first few hours the decrease in the conductivity became slower and it appeared to stabilise after some time. The variations in the conductivity after about 14 hours could be related to temperature fluctuations inside the room during the time the experiment was performed.

The lattice parameters of the films were measured by XRD before and after the reduction and are given in Table 7.6 and Figure 7.16. Two significant trends could be observed. First, a significant decrease was found in the lattice parameter as the heat treatment temperature was increased above 530 °C. Second, the lattice parameter increased with about 0.002 Å for all of the films after the reduction.

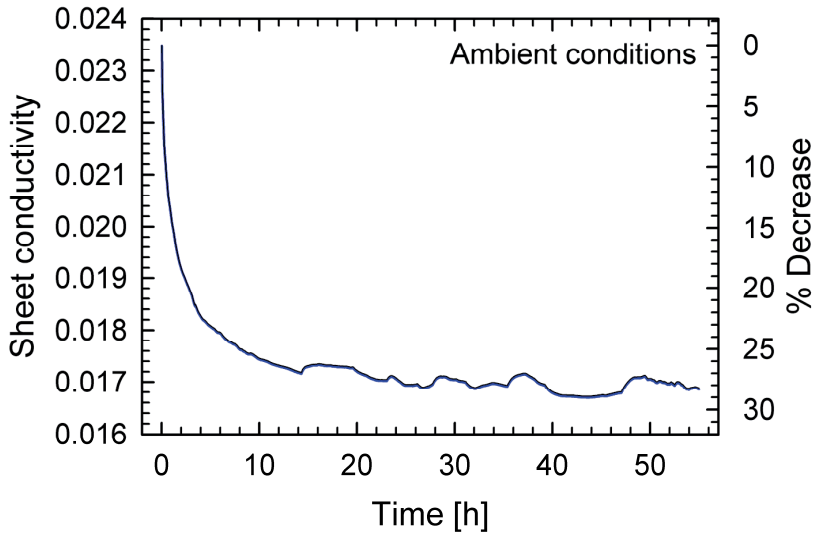

Figure 7.15. In situ conductivity at room temperature as a function of time for an ITO film after reduction measured directly after the film was exposed to ambient air.

Table 7.6. Cubic lattice parameter and crystallite size of films deposited on YSZ substrates and heat treated at different temperatures before and after reduction for 10 h at 400 °C in 5 % hydrogen in argon. The estimated uncertainty is ± 0.002 Å for the lattice parameter and ± 0.2 nm for the crystallite size.

Heat treatment temperature [°C]	Lattice parameter [Å]		Crystallite size [nm]	
	Before	After	Before	After
530	10.154	10.157	12.3	12.1
530	10.156		12.2	
600	10.143	10.144	13.0	12.7
600	10.138		12.7	
700	10.122	10.125	12.8	12.8
700	10.123		13.1	
800	10.126	10.128	13.3	13.3
800	10.127		13.5	

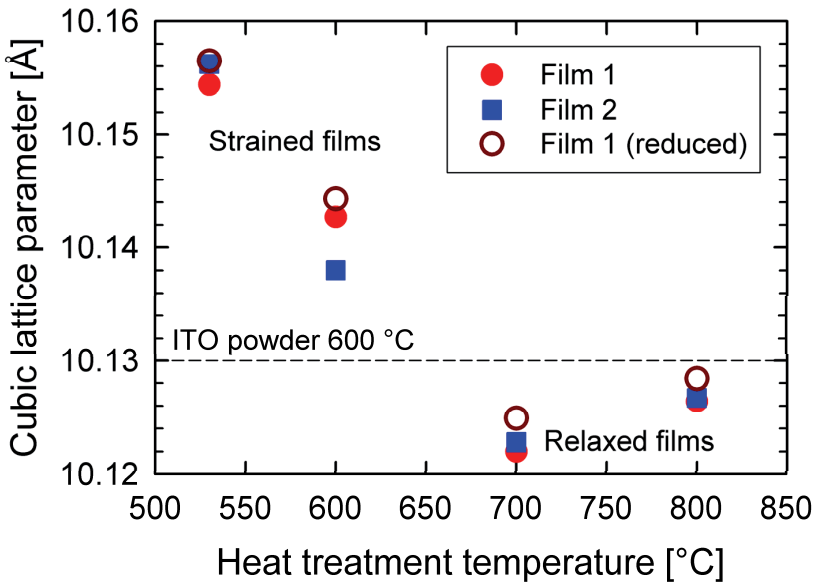

Figure 7.16. Cubic lattice parameter of ITO films deposited on YSZ and heat treated at different temperatures before and after reduction for 10 h at 400 °C in 5 % hydrogen in argon. The dashed line is the lattice parameter of ITO powder with 10 cat% Sn after annealing at 600 °C.

Though this increase is comparable in size with the estimated uncertainty, the increase was consistent and in good agreement with previous studies [84]. The lattice parameters of the two films heat treated at each temperature were in reasonable agreement. The crystallite size of the films was calculated from the diffractograms and is given in Table 7.6 and Figure 7.17. Increasing the annealing temperature did increase the crystallite size, in line with expectations. However, the effect was rather small as the crystallite size only increased from about 12.3 ± 0.2 to 13.4 ± 0.2 nm for the samples heat treated at 530 and 800 °C, respectively.

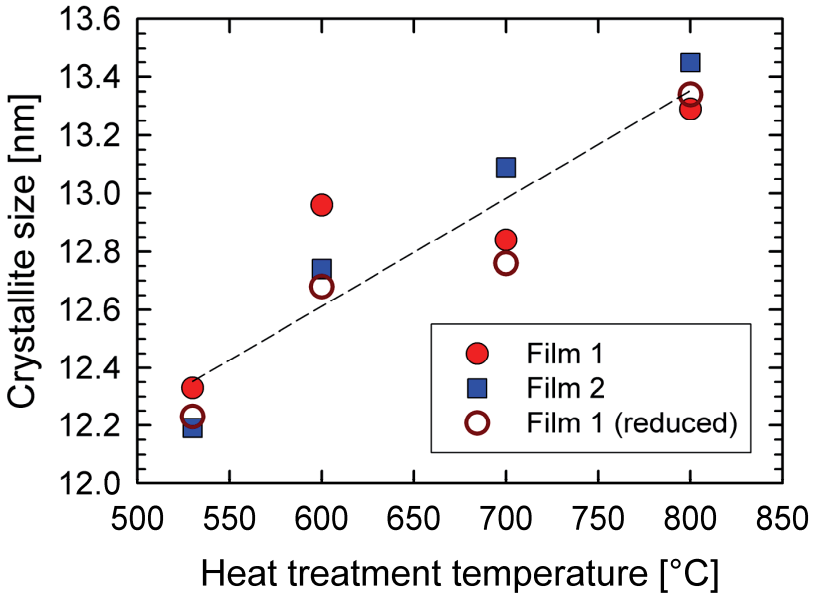

Figure 7.17. Crystallite size of ITO films deposited on YSZ and heat treated at different temperatures. The dashed line is a guide to the eye.

7.4. Discussion

7.4.1. Deposition of ITO thin films

The aqueous sol with PVA additions was succesfully applied by spin coating to prepare ITO thin films with very good functional properties. Diffraction patterns confirmed that the films were single phase and polycrystalline with no preferred crystal orientation. The electron micrographs confirmed the homogeneous nature of the microstructure and continuous films with no pin-holes, while the nominal elemental composition was confirmed by EDS. The films appeared homogeneous and transparent, and the optical characterisation demonstrated excellent properties such as a high transmittance in the visible region and band gap similar to reported values [16, 154]. The electric properties of the films are discussed in detail in Chapter 7.4.2. The reproducibility of the process was demonstrated to be very good. Films prepared by the same solution and with the same parameters had an excellent agreement in both optical and electrical properties. In some cases, films prepared by similar solutions but from separate batches had somewhat larger differences in the electrical properties, which were probably caused by the

difficulty of weighing and measuring out the exact same mass and volume of the chemicals from batch to batch.

The total thickness of the films, and thereby also their functional properties, could be controlled by the number of depositions. For films deposited on glass substrates the correlation between film thickness and number of depositions appear to be linear, although it is possible that the first couple of layers were slightly thicker. When the original recipe was used, referred to as Solution 1, it was established by electron microscopy and ellipsometry that each spin coating deposition added around 17 ± 1 nm to the total thickness of the film. The spherical grains in the film had an average size of 16 ± 3 nm, which demonstrates that the grain size reflects the thickness of each deposited layer. A significant grain growth would have caused the grains to grow between the layers, but these observations shows that each deposited layer is similar to a monolayer of particles, even after the final annealing step at 530 °C. It is possible that the microstructure caused by these subsequent depositions is the reason for the significant tensional strain in the films (Figure 7.2). Certain films were deposited on YSZ substrates and were heat treated at higher temperatures. The crystallite size in the films increased with increasing temperature (Figure 7.17), but the microstructure of these films was not investigated further. However, the lattice parameter of the films, shown in Figure 7.16, clearly demonstrated that the tensional strain in the films was released by heat treatment above ~ 650 °C.

In order to increase the thickness of the deposited layers it was decided to change the cation conentration and PVA content in the sol together with the rotation speed during spin coating. Increasing the PVA content of the solutions increased the viscosity thereby increasing the thickness of the liquid film formed during spinning [264]. Reducing the rotation speed will also have the same effect [135]. Increasing the cation concentration in the solution will theoretically not give thicker liquid films after spinning, but the thickness of the final oxide layer will increase linearly with the concentration [138]. For films deposited on Al_2O_3 and heat treated at 600 °C it was clearly demonstrated that an increase in both the cation concentration and the PVA content caused a significant decrease in the sheet resistance (Table 7.3 and Figure 7.9). The sheet resistance is a function of both the specific resistance and the thickness of the sample (Equation 4.2). It was attempted to analyse the thickness of the films by ellipsometry, however, it was difficult to obtain a model which produced reliable results. It was not attempted to measure the thickness by electron microscopy. The four films were heat treated at the same temperature and although the different amounts of organics and nitrates could cause an increase in the local temperature during oxidation, it is suggested that the specific resistance of the films should be fairly equal. Hence, even though the true thickness of the films

has not been confirmed, the significant effect on sheet resistance is proposed to be caused by differences in the films thickness.

For the films deposited on glass substrates and heat treated at 530 °C it was demonstrated that an increase in the cation concentration lowered the sheet resitance, but the effect of increasing the PVA content and changing the rotation speed are not evident. For some of these films carbon residues were observed after heat treatment. The original heat treatment program for 1 h at 530 °C was only optimised for the process based on Solution 1. Furthermore, TGA analyses demonstrated that the solutions with increased PVA content required a higher temperature in order to fully decompose to a pure oxide film. Thus, it is likely that this heat treatment was not sufficient to remove the organics when thicker films with more organic matter were prepared. By depositing the films on a refractory substrate and heat treating them at higher temperatures, the effect of the PVA content and rotation speed could probably have been verified, though this was not further investigated.

In some cases the films appeared to be cracked and delaminated from the substrate when a high PVA content and/or cation concentration was used. This could be caused by an increased amount of organics to be removed and also because films above a certain thickness are more prone to cracking [132]. Furthermore, a too high PVA concentration was demonstrated to give shear thinning solutions, of which it is difficult to obtain homogeneous film thickness after spinning [132]. In this regard, increasing the cation concentration of the solutions appears to be a better approach to increase the thickness of the films than increasing the PVA content above a critical concentration. For some of the presumably thicker films interference patterns and certain inhomogeneities were observed. However, it is not clear whether these films were actually more inhomogeneous or if this optical effect was simply easier to visually observe because the increased film thickness produced interference with visible light.

The films deposited on YSZ and Al_2O_3 substrates had slightly lower sheet resistance than a similar film deposited on glass. A possible explanation could be that the different substrates had different interactions with the solution, where differences in the surface tension could lead to changes in the film thickness after spinning. The fact that no film was formed on MgO, the substrate with the most basic properties, indicates that the interaction between the substrate and solution is important. It is proposed that this was caused by a poor wetting of the solution on the substrate caused by the surface tension. It is also possible that there was an epitaxial effect due to a favourable match between the lattice parameter of the film and the substrates. The lattice constants of the YSZ, Al_2O_3 and MgO single crystals with the specific orientation used in this work is 5.139, 4.785 and 4.212 Å

respectively, where twice the first value is close to the lattice constant of ITO. However, possible epitaxial effects can not explain why no film was formed on MgO.

7.4.2. Electrical properties

The electrical properties of the as-prepared films were demonstrated to be very good. The reproducability of the van der Pauw measurements was excellent, within a few percent. The specific resistance of the films presented in Chapter 7.1 was $4.59 \pm 0.05 \times 10^{-3}$ Ω·cm. As the specific resistance was demonstrated to be approximately equal also for the thinnest films, surface scattering does not appear to be a dominating loss mechanism. This value for the specific resistivity of the films is better than most reported values for ITO thin films prepared by aqueous sol-gel deposition processes, but is around an order of magnitude higher than the best reported values for sputtered ITO thin films [8]. Kanbara et al. achieved a conductivity of 1.3×10^{-3} Ω·cm for ITO thin films prepared by an aqueous process, however these films were fired at 900 °C and subsequently annealed in a N_2 atmosphere [149]. The importance of annealing at elevated temperatures and in reducing atmospheres in order to increase the conductivity of ITO thin films has been demonstrated in several reports [34, 149, 151, 154, 265]. Annealing at higher temperatures can improve the crystallinity of the films and it can also induce grain growth, which will limit the grain boundary scattering of the charge carriers. Furthermore, according to the point defect chemistry of ITO, oxygen interstitials in the lattice will compensate and trap some of the itinerant electrons from the n-type tin donor atoms [13, 84]. Annealing in reducing atmospheres can thereby increase the conductivity by removing these oxygen interstitials.

Both increasing the heat treatment temperature and annealing in reducing atmospheres were demonstrated to significantly improve the conductivity of the films. The thickness of the films presented in Chapter 7.3 was not confirmed by microscopy. However, apart from the different substrates, the process is equal to the original process used in Chapter 7.1, which yielded a thickness of 17 nm per deposition. If a thickness of 51 nm is assumed, the specific resistance after reduction of the film heat treated at 800 °C would be 6.58×10^{-4} Ω·cm. This value is excellent compared to other ITO thin films prepared by aqueous sol-gel methods and comparable to the best reported values for ITO.

The thin film heat treated at 800 °C possessed a sheet resistance between 32 and 47 % lower than the film heated at 530 °C after the different processing steps (Table 7.5). As the thickness of the films is most likely equal, it is proposed that the

decrease in the sheet resistance is caused by a lowering of the specific resistivity of the films. The microstructure of the films heat treated at 530 °C consisted of individual layers from each deposition. The sample preparation for the TEM investigation revealed that the adhesion between the layers was weaker than the bond between the grains in each layer. Annealing at higher temperatures could, thereby, increase the conductivity of the films by strengthening the physical contact between the layers. It was also established that the films heat treated at 530 °C had a significant amount of tensional strain, which was released by increasing the heat treatment temperature. This could also affect the conductivity. Furthermore, the crystallite size of the films increased somewhat with increasing annealing temperature, as shown in Figure 7.17. Tahar et al. have calculated a carrier mean free path of 1.6 nm for a doping level of 10 cat% Sn [250], which suggests that the grain sizes in the films are sufficiently large to avoid grain boundary scattering causing significant reduction of the mobility. However, this effect can not be ruled out and, and it is not clear which of the aforementioned effects is the most important regarding the improved conductivity of the films that were heat treated at higher temperatures. Regardless of the heat treatment temperature and the initial conductivity before reduction, all of the films experienced a decrease in the sheet resistance of about 50 % after the 10 h post-annealing in 5 % hydrogen in argon. This implies that the improvement of conductivity due to the increased temperature and the reducing atmosphere are two separate effects which can be utilised independently.

It was clearly demonstrated that the sheet resistance of the films which had been annealed for 10 h at 400 °C in reducing atmospheres increased when the films were exposed to air. The conductivity drastically decreased during the first couple of hours, but appeared to stabilise within a couple of days. This effect can probably be explained by oxygen incorporation from the air reducing the amount of free carriers. However, it is remarkable that this process would be so fast at room temperature (2 % decrease in the sheet conductivity within the first minute). This shows that oxygen anions have sufficient mobility in the fluorite type crystal structure of ITO, even at ambient temperatures. The exact density of the deposited ITO thin films could not be measured easily. Thus, it is not clear whether the oxygen diffusion is occurring through the solid films or if diffusion through nano-pores is also taking place. The same effect has been reported for thin films prepared by dispersion of nano-sized ITO particles [176, 179, 266]. Similar observations have also been reported in partly reduced $CeO_{2-\delta}$ with the fluorite crystal structure [267, 268].

It became apparent that the sheet resistance of the films decreased with 7 to 16 % within two weeks after their deposition and subsequent heat treatment in 10^{-2} mbar vacuum. It is possible that this is caused by some sort of ageing or relaxation of the

films. The sheet resistance measurements discussed in this chapter were generally performed within a few days after the films were prepared and when the measurements were reproduced it was generally perfomed on the same day. The reproducibility were always 1-2 %, though generally lower, which might also point to the same phenomenon. Further investigations would be necessary in order to conclude regarding the cause of this effect.

7.5. Conclusions

ITO thin films were successfully deposited by spin coating from the inexpensive and simple sol-gel process. The films were phase pure and homogeneous and the functional properties of the films were demonstrated to be very good. The thickness of the films could readily be modified by adjusting the deposition process. The electrical properties of the films were demonstrated to be significantly improved by increasing the heat treatment temperature and annealing in reducing atmosphere. In situ conductivity measurements were performed to confirm the effect of the atmosphere during annealing. It was demonstrated that oxidation of the films, leading to a decrease in the conductivity, occurred even at room temperature when the films were exposed to air after reduction.

8. REE-doped In_2O_3 and ITO

8.1. Synthesis

Phase-pure and nano-crystalline powders of REE-doped In_2O_3 and ITO were succesfully prepared when TA and EG were used as complexing agents. In initial investigations it was attempted to prepare REE-doped ITO powders with AA and EG as complexing agents, as this synthesis yielded phase-pure undoped ITO, as demonstrated in Chapter 5. A brief review of the results from the initial syntheses is given here.

The syntheses with AA and EG yielded amorphous gels, indicating no cation segregation. However, after calcination a relatively large fraction of the metastable rhombohedral In_2O_3 polymorph (space group $R\bar{3}c$) could be observed by XRD. The diffraction patterns of ITO with 1 and 5 cat% Nd prepared using these synthesis conditions are presented in Figure 8.1. The phase content of the syntheses with different dopants, doping concentration and calcination temperature is given in Table 8.1. The powders with 5 and 10 cat% REE generally had a significantly

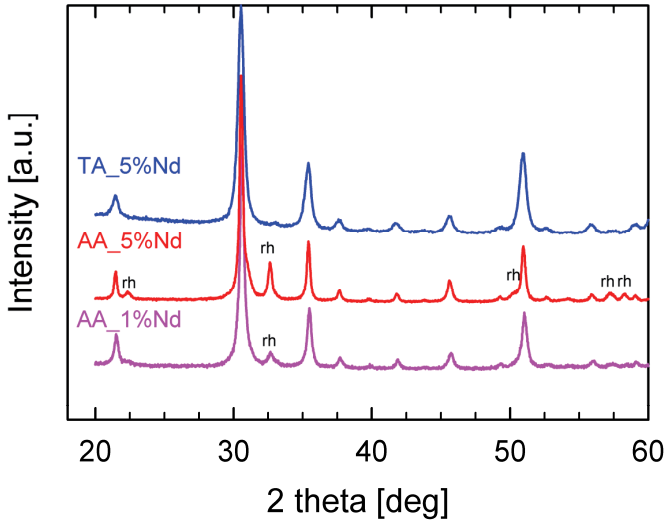

Figure 8.1. XRD patterns of ITO powder doped with 1 and 5 cat% Nd after calcination at 600 °C. The two bottommost powders were prepared with acetic acid (AA) as a complexing agent, while in the topmost tartaric acid (TA) was used. Some of the strongest reflections from rhombohedral In_2O_3 (space group $R\bar{3}c$) are marked with rh.

Table 8.1. Phase content of ITO powders doped with different amounts of REE after calcination at 400 and 600 °C. The powders were prepared with acetic acid and ethylene glycol as complexing agents. The estimated uncertainty in the phase content is ± 1 wt%.

Material	Calcination temperature [°C]	c-In_2O_3 [wt%]	rh-In_2O_3 [wt%]	Goodness of Rietveld fit [R_{wp}]
ITO:1%Nd	400	86.6	13.4	6.7
	600	87.1	12.9	6.8
ITO:5%Nd	400	71.9	28.1	8.7
	600	73.3	26.7	7.0
ITO:10%Nd	400	75.7	24.3	10.8
ITO:1%Eu	400	92.5	7.5	7.8
	600	95.6	4.4	7.6
ITO:5%Eu	400	83.7	16.3	7.1
	600	90.2	9.8	7.6
ITO:10%Eu	400	76.6	23.4	9.9
	600	91.8	8.2	8.2
ITO:1%Tb	400	95.5	4.5	8.5
	600	95.3	4.7	9.3
ITO:5%Tb	400	82.7	17.3	8.6

higher amount of the rhombohedral phase than the powders with only 1 cat% REE. The amount of the rhombohedral phase appears to be larger for Nd-doping than for Eu or Tb. Increasing the calcination temperature from 400 to 600 °C slightly reduced the amount of the rhombohedral In_2O_3 polymorph.

In order to prepare phase-pure powders it was decided to try to replace acetic acid with tartaric acid. When TA and EG were used as complexing agents phase-pure powders with the cubic In_2O_3 polymorph (space group $Ia\bar{3}$) were successfully obtained, as illustrated by the topmost diffractogram in Figure 8.1. The larger tartaric acid molecule was more difficult to remove by oxidation, so the calcination of these powders was performed at 600 °C for 15 h. All of the powders discussed in the rest of this chapter were prepared with TA and EG as complexing agents.

8.2. Solid solubility

The solid solubility of REEs in In_2O_3 and ITO was investigated by preparing materials with different REE doping concentrations, heat treating them at different temperatures and anlysing the products by XRD. For In_2O_3, materials with 5 different REE dopant concentrations, ranging from 0.5 to 10 cat% REE, were prepared in order to determine the solid solubility limit for the different dopants accurately. For ITO, on the other hand, fewer compositions were investigated, as it was determined that the materials were not phase pure after heat treatment at 1400 °C even with only 1 cat% REE-doping, as discussed further in Chapter 8.2.2. The In to Sn ratio in the doped ITO materials was kept constant at 95:5. A higher tin doping concentration could have improved the conductivity of the materials, but was still not desirable due to phase purity issues. When the term powder is used in this chapter it refers to the nano-crystalline powder after calcination at 600 °C, while bulk materials refers to samples after heat treatment at 1400 °C for 2 h.

8.2.1 Pure In_2O_3

Powders with pure In_2O_3 as host were prepared with 0.5, 1, 2, 5 and 10 cat% doping with Nd, Eu and Tb oxide. The powders were phase pure according to XRD, as shown for In_2O_3:10%Eu in Figure 8.2. Broad reflections were observed,

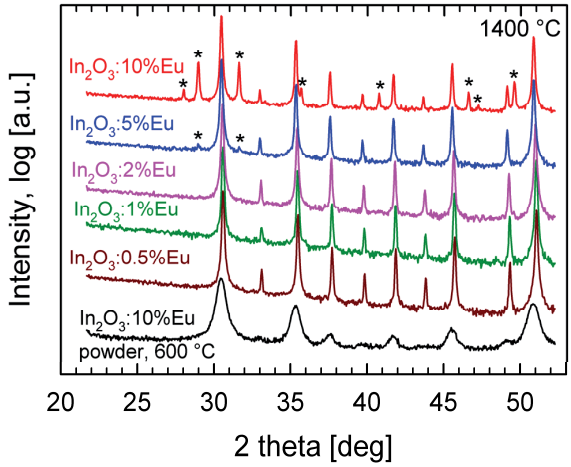

Figure 8.2. XRD of In_2O_3 doped with different amounts of Eu after heat treatment at 1400 °C. $EuInO_3$ diffraction lines, with space group $P6_3cm$, are denoted by *. The bottommost diffractogram is for In_2O_3:10%Eu powder after calcination at 600 °C.

demonstrating the nano-crystalline nature of the powders. XRD of bulk materials of In_2O_3 with different amounts of Eu-doping are also included in Figure 8.2. At low doping concentrations the materials were phase-pure, with a secondary phase appearing at higher doping concentrations. The diffraction lines due to the secondary phase could be ascribed to $EuInO_3$ and $TbInO_3$ with the hexagonal $YMnO_3$ crystal structure (space group *P6₃cm*) in case of Eu- and Tb-doped materials. $NdInO_3$, with the orthorhombic $GdFeO_3$ perovskite structure (space group *Pnma*) could be identified for the Nd-doped materials. The amount of doping that was required for the secondary phase to appear was different for the different dopants. The phase content of the different REE-doped In_2O_3 materials is given in Table 8.2.

Table 8.2. The phase content of In_2O_3 doped with different amounts of Nd, Eu and Tb oxide after heat treatment at 1400 °C obtained from Rietveld refinement. The estimated uncertainty in the phase content is ± 1 wt%.

Dopant	Doping amount [cat%]	c-In_2O_3 [wt%]	$REInO_3$ [wt%]	Goodness of Rietveld fit [R_{wp}]
Nd	0.5	100.0	-	12.5
	1	~100.0	traces	8.4
	2	97.4	2.6	7.6
	5	90.5	9.5	7.4
	10	79.0	21.0	6.4
Eu	0.5	100.0	-	8.1
	1	100.0	-	9.3
	2	100.0	-	8.1
	5	~100.0	traces	7.1
	10	93.1	6.9	7.0
Tb	0.5	100.0	-	8.1
	1	100.0	-	6.5
	2	100.0	-	7.8
	5	100.0	-	7.2
	10	~100.0	traces	5.7

The lattice parameters and crystallite size of the cubic In_2O_3 phase, determined for the powders and bulk materials, are summarised in Table 8.3 and Figure 8.3. Some general remarks can be made. For all materials the lattice parameter appears to follow Vegard's law [269] at lower doping levels, while the lattice parameter saturated at higher dopant concentrations. The inflection point corresponds to the solid solubility limit of RE_2O_3 in In_2O_3 and correlates with the appearance of secondary phases, as shown in Table 8.2. The determined lattice parameters for the powders followed the same trend, even though no secondary phases could be observed by XRD. Furthermore, the nano-crystalline powders seem to have larger lattice constants than the bulk materials. This difference was most noticable for the samples doped with Nd, where the lattice constant of the powder on average was

Table 8.3. Lattice parameter of cubic In_2O_3 doped with Nd, Eu and Tb oxide. The powders were calcined at 600 °C and the bulk materials heat treated at 1400 °C. The crystallite size is included for the nano-crystalline powders. The estimated uncertainty is ± 0.002 and ± 0.001 Å in the lattice parameter for the powders and bulk, respectively, and ± 3 nm for the crystallite size.

		600 °C		1400 °C
Dopant	Doping amount [cat%]	Lattice parameter [Å]	Crystallite size [nm]	Lattice parameter [Å]
Nd	0.5	10.133	22	10.122
	1	10.147	20	10.125
	2	10.143	18	10.125
	5	10.142	18	10.124
	10	10.145	18	10.126
Eu	0.5	10.133	22	10.121
	1	10.132	20	10.124
	2	10.144	18	10.134
	5	10.159	18	10.156
	10	10.161	17	10.155
Tb	0.5	10.132	23	10.120
	1	10.140	19	10.125
	2	10.136	20	10.129
	5	10.142	19	10.151
	10	10.155	18	10.185

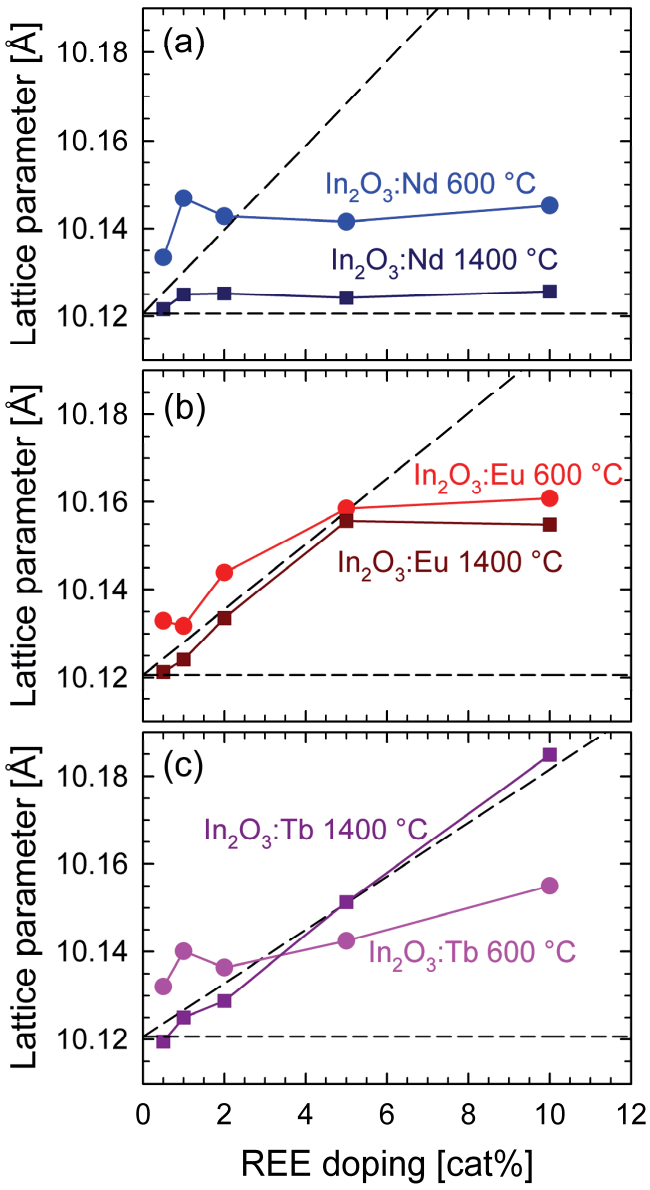

Figure 8.3. Lattice parameter of cubic In_2O_3 doped with Nd (a), Eu (b) and Tb (c) in nano-crystalline powders after calcination at 600 °C (●) and in bulk matetials after heat treatment at 1400 °C (■). The horizontal dashed lines are the lattice parameter of undoped In_2O_3 (10.1206 Å) while the diagonal dashed lines are the lattice parameter according to Vegard's law with end values of 11.0770, 10.8660 and 10.7300 Å for Nd_2O_3, Eu_2O_3 and Tb_2O_3, respectively [49].

about 0.018 Å larger than the bulk material, while for Eu the average difference was 0.008 Å. The Tb-doped powder had larger lattice constants at small doping concentrations, but did not increase according to Vegar's law, like observed for the bulk. The crystallite size appeared to decrease with increasing amount of REE-doping in the nano-crystalline powders.

8.2.2. ITO

XRD of the doped ITO powders did not indicate the presence of any secondary phases, as illustrated by the bottommost diffractogram in Figure 8.4. However, after heat treatment at 1400 °C several different phases were observed, illustrated by XRD of ITO with 1, 5 and 10 cat% Nd oxide, included in Figure 8.4. For the samples with 1 and 5 cat% Nd oxide, the secondary phase was found to be a

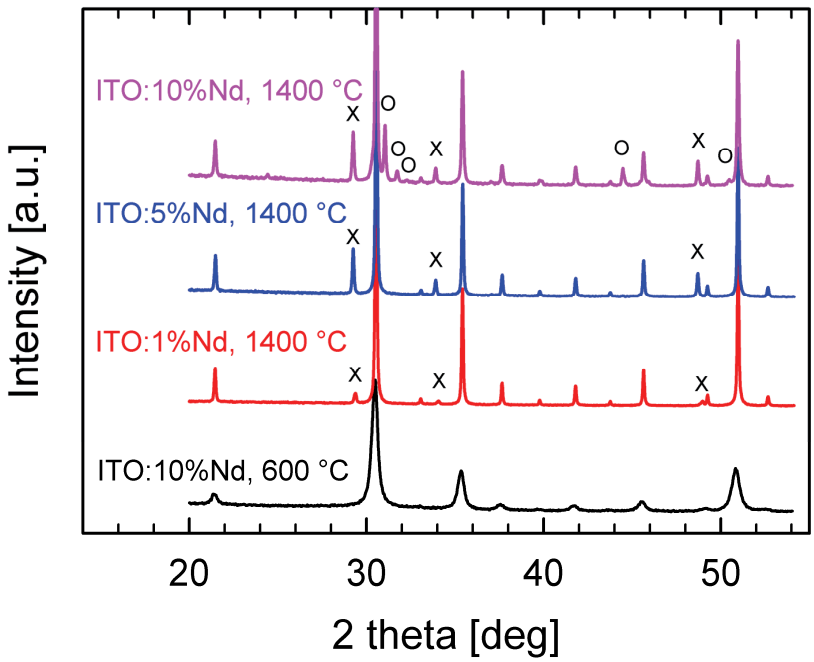

Figure 8.4. XRD of ITO with 5 cat% Sn doped with different amounts of Nd oxide after calcination at 600 °C and heat treatment at 1400 °C. Diffraction lines from $Nd_2Sn_2O_7$ with space group $Fd\bar{3}m$ are marked by X and from $NdInO_3$ with space group *Pnma* by O.

pyrochlore phase, $Nd_2Sn_2O_7$, with space group $Fd\bar{3}m$, while for the material with 10 cat% Nd oxide also the orthorhombic perovskite, $NdInO_3$, with space group *Pnma* was observed. Similar observations were made for the ITO:Eu and ITO:Tb systems, only with progressively smaller amounts of the $REInO_3$ phase for 10 cat% doping. The phase content in the ITO-based materials after heat treatment at 1400 °C, based on Rietveld refinement, is given in Table 8.4.

Table 8.4. The phase content of ITO with 5 cat% Sn doped with different amounts of Nd, Eu and Tb oxide after heat treatment at 1400 °C obtained from Rietveld refinement. The estimated uncertainty in the phase content is ± 1 wt%.

Dopant	Doping amount [cat%]	c-In_2O_3 [wt%]	$RE_2Sn_2O_7$ [wt%]	$REInO_3$ [wt%]	Goodness of Rietveld fit [R_{wp}]
Nd	1	96.9	3.1	-	7.2
	5	89.9	10.1	-	5.9
	10	78.7	8.7	12.6	5.8
Eu	1	97.2	2.8	-	7.2
	5	90.5	9.5	-	7.0
	10	87.5	9.9	2.6	7.7
Tb	1	97.9	2.1	-	10.4
	5	90.7	9.3	-	9.5
	10	~89.9	~10.1	traces	6.7

The lattice parameters and crystallite size of cubic In_2O_3 in nano-crystalline powders and bulk materials of ITO doped with 1, 5 and 10 cat% of Nd, Eu and Tb oxide are given in Table 8.5 and Figure 8.5. The ITO-based materials did not follow Vegar's law like the In_2O_3-based materials, which is reasonable due to a significant higher content of secondary phases and lower solid solubility. The bulk materials had approximately the same amount of the pyrochlore $RE_2Sn_2O_7$-phase at 1 and 5 cat% REE doping, and the lattice parameters for these materials are in close agreement. The lattice parameters of bulk samples with 10 cat% REE, on the other hand, was inversely proportional to the amount of the $REInO_3$-phase. The materials with 5 and 10 cat% REE had a higher lattice parameter than the ITO with 5 cat% Sn reference, suggesting that there is a certain solubility of REEs in ITO. On the other hand, for the bulk material with 1 cat% REE the lattice parameter was

lower than the ITO reference. The powders did not display a clear relationship between the lattice parameter and composition, but the highest lattice parameter for all three systems was observed for 10 cat% REE. The powders were all nano-crystalline with similar crystallite sizes.

Table 8.5. Lattice parameter of the cubic In_2O_3 phase in ITO with 5 cat% Sn doped with Nd, Eu and Tb oxide. The powders were calcined at 600 °C and the bulk materials heat treated at 1400 °C. The crystallite size is included for the powders. The estimated uncertainty is ± 0.002 and ± 0.001 Å in the lattice parameter for the powders and bulk, respectively, and ± 3 nm for the crystallite size.

		600 °C		1400 °C
Dopant	Doping amount [cat%]	Lattice parameter [Å]	Crystallite size [nm]	Lattice parameter [Å]
Nd	1	10.139	21	10.122
	5	10.138	18	10.128
	10	10.148	23	10.126
Eu	1	10.128	22	10.125
	5	10.141	23	10.131
	10	10.150	24	10.148
Tb	1	10.134	22	10.124
	5	10.130	23	10.132
	10	10.157	20	10.162

XRD of ITO:10%Eu oxide after heat treatment at different temperatures are given in Figure 8.6. No secondary phases could be observed at 600 and 800 °C. At 1000 °C and higher the presence of the secondary phases is evident and it appears that $EuInO_3$ forms at lower temperatures than the pyrochlore $Eu_2Sn_2O_7$. A similar observations was made for the ITO:10%Nd material

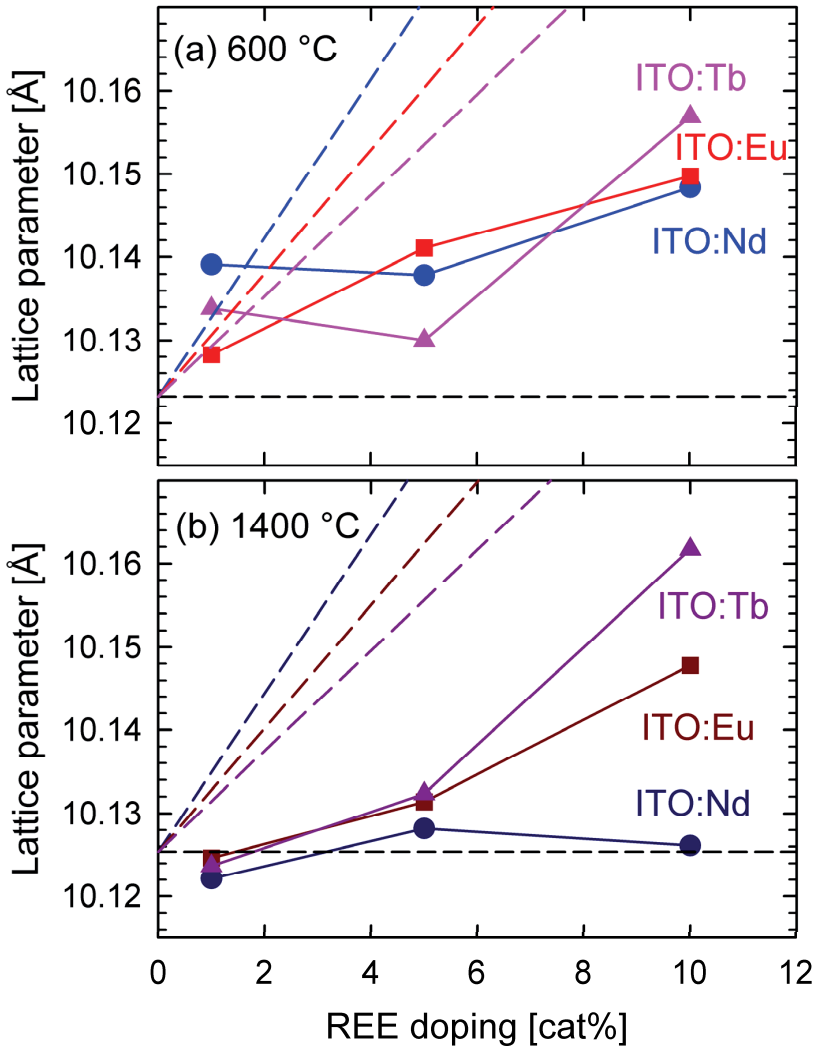

Figure 8.5. Lattice parameter of the cubic In_2O_3 phase in ITO with 5 cat% Sn doped with Nd (●), Eu (■) and Tb (▲).The nano-crystalline powders were calcined at 600 °C (a) and the bulk materials heat treated at 1400 °C (b). The horizontal dashed lines are the lattice parameter of ITO with 5 cat% Sn from Chapter 6 (10.1233 Å for the powder and 10.1254 Å for bulk) while the diagonal dashed lines are the lattice parameter according to Vegar's law with end values of 11.0770, 10.8660 and 10.7300 Å for Nd_2O_3, Eu_2O_3 and Tb_2O_3, respectively [49].

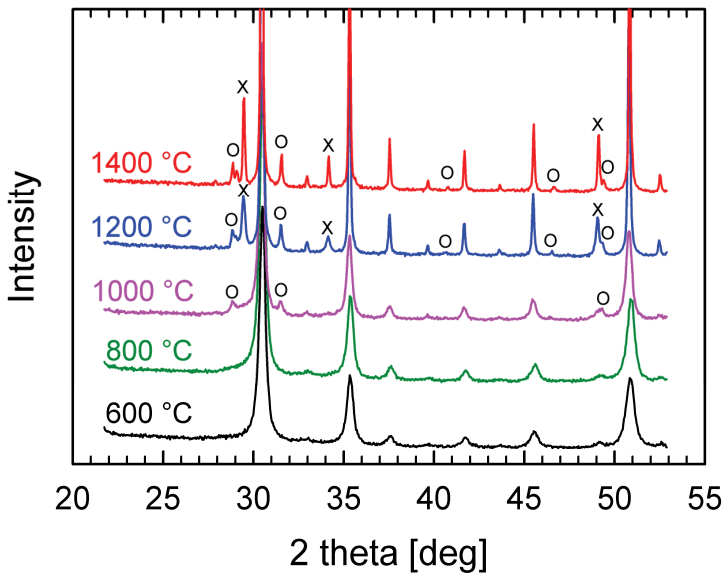

Figure 8.6. XRD of ITO:10%Eu after heat treatment at different temperatures. Diffraction lines from $Eu_2Sn_2O_7$ with space group $Fd\bar{3}m$ are marked by X and from $EuInO_3$ with space group $P6_3cm$ by O.

8.3. Functional properties of bulk materials

The functional properties of bulk materials of REE-doped In_2O_3 and ITO were investigated. The electrical properties of the materials were characterised by conductivity and thermopower measurements, while the optical properties by diffuse reflectance and photoluminescence spectroscopy. The focus of the electrical characterisation was to determine to which extent the REE-doping deteriorated the conductvity of the host, whereas the optical characterisation was performed in order to verify if the REE dopants could be optically active in the selected host materials.

8.3.1. Electrical properties

The electrical conductivity and thermopower of bulk materials of In_2O_3 and ITO doped with the REEs are given in Table 8.6 and Figures 8.7 and 8.8. The density of the materials after sintering at 1400 °C is also included in the table. The conducitivity of ITO with 5 cat% Sn was 6145 S/cm, while 130.8 S/cm for In_2O_3.

All of the REE-doped materials had a lower conductivity than their respective hosts. The In_2O_3-based materials had a drastic decrease in conductivity even at small doping concentrations. The conductivity of 1 cat% Nd-doped In_2O_3 was nearly four orders of magnitude lower than for pure In_2O_3. The decrease was progressively smaller for Eu- and Tb-doping, but also in the latter case the decrease in conductivity from pure In_2O_3 to the material with 2 cat% Tb-doping was more than one order of magnitude. The ITO:1%REE materials had conductivities between 4180 and 5375 S/cm. The 1 cat% doped materials were not phase pure, and it was not attempted to measure the conductivity on ITO-based materials with higher doping concentrations. The thermopower of ITO and In_2O_3 was -30.43 and -130.8 μV/K, respectively. The negative sign of the thermopower confirms the n-type conductivity in line with expectations. The REE-doping did not appear to affect the thermopower in the same way as the conductivity. The thermopower of

Table 8.6. Density, conductivity and thermopower of bulk materials of In_2O_3 and ITO doped with Nd, Eu and Tb. The estimated uncertainty is ± 2.5 % for the conductivity and thermopower and ± 0.2 % for the density.

Material	Doping amount [cat%]	Relative density [%]	Conductivity [S/cm]	Thermopower [μV/K]
ITO	0	92.3	6.15×10^3	-30.4
ITO:Nd	1	90.4	5.38×10^3	-30.0
ITO:Eu	1	85.4	4.18×10^3	-30.5
ITO:Tb	1	86.2	4.55×10^3	-31.3
In_2O_3	0	87.4	1.31×10^2	-230
In_2O_3:Nd	0.5	59.1	3.15×10^0	-222
	1	74.9	1.99×10^{-2}	-220
In_2O_3:Eu	0.5	82.0	5.54×10^1	-171
	1	64.6	1.76×10^0	-249
	2	59.4	1.20×10^1	-245
In_2O_3:Tb	0.5	84.3	1.49×10^2	-197
	1	85.5	4.89×10^1	-227
	2	58.5	1.00×10^1	-235

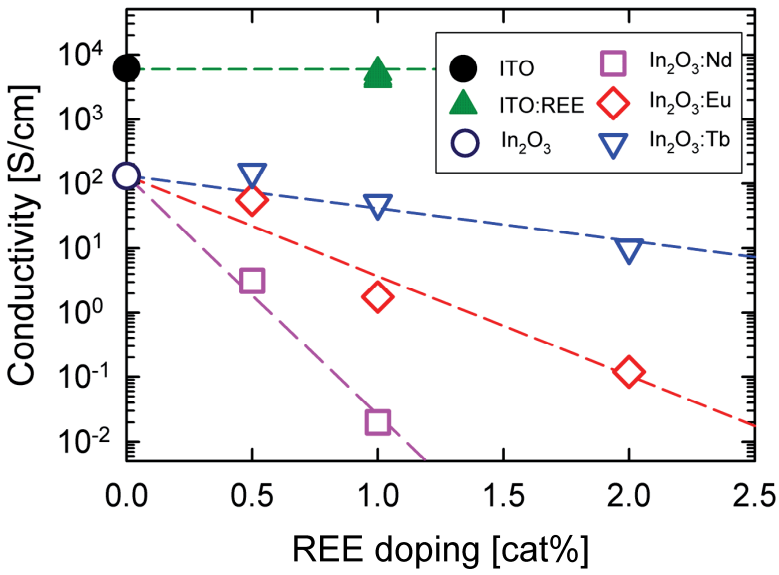

Figure 8.7. Conductivity of bulk samples of In_2O_3 and ITO doped with Nd, Eu and Tb measured by a four point linear configuration. The dashed lines are guides to the eye.

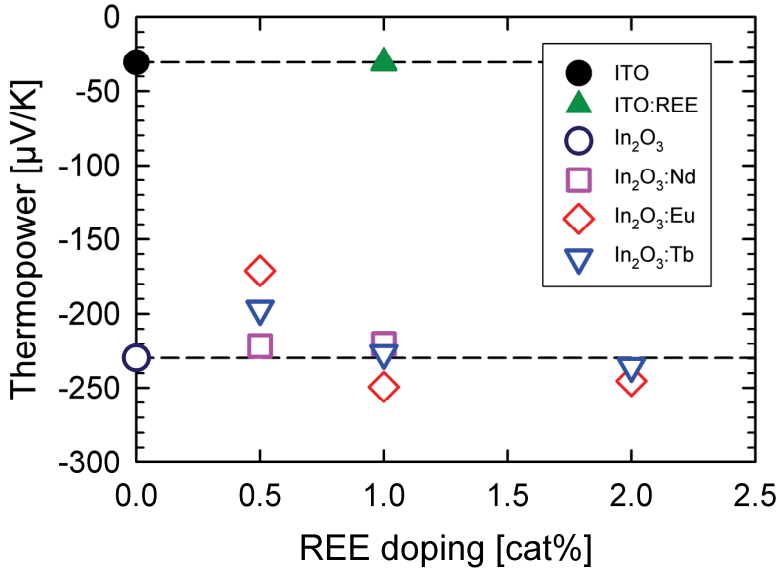

Figure 8.8. Thermopower of bulk samples of In_2O_3 and ITO doped with Nd, Eu and Tb. The dashed lines are guides to the eye.

the In_2O_3-based materials appeared to be quite stable up to 2 cat% REE-doping, although the In_2O_3:0.5%Eu and In_2O_3:0.5%Tb materials had a somewhat lower thermopower than the rest. Also the ITO-based materials had a thermopower roughly equal to the ITO host reference. Measurements were also performed on materials with higher doping amounts, but the experiments were either not successful, possibly because the conductivity was too low, or further efforts were not made since they were not phase pure.

8.3.2. Optical properties

Diffuse reflectance were measured and the data are given in Figure 8.9 to 8.11 for In_2O_3:Nd, In_2O_3:Eu and In_2O_3:Tb, respectively. The spectrum of In_2O_3 is given as a reference in all three figures. In_2O_3 exhibited typical semiconductor behaviour with the reflectance decreasing rapidly with decreasing wavelength due to absorptions across the band gap. The Nd-doped materials demonstrated strong absorption bands in the region from approximately 500 to 900 nm, which appeared to increase in intensity with increasing amount of doping. Outside of this region no differences

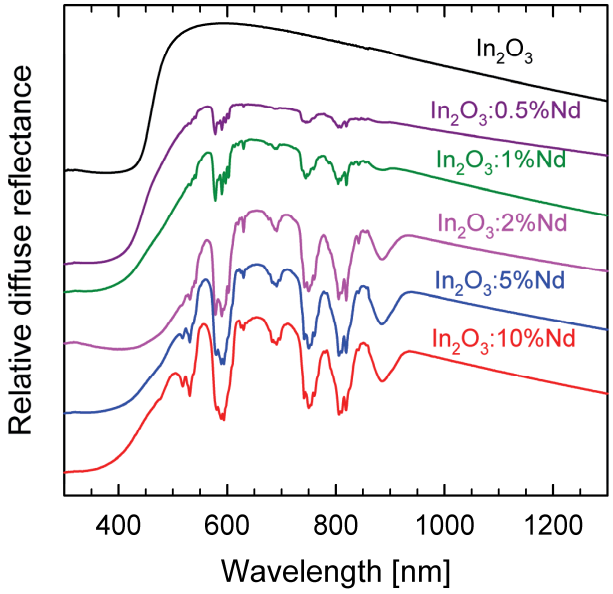

Figure 8.9. Diffuse reflectance of In_2O_3-based bulk materials with different amounts of Nd-doping.

were observed between the doped samples and the In_2O_3 reference. The Eu-doped materials exhibited absorption in the visible region, around 530 and 580 nm, and in the IR region, at approximately 1970, 2090 and 2180 nm (Figure 8.10). The absorptions in the visible region increased with increasing doping concentration, with the 530 nm absorption being observed for all concentrations. The absorptions in the IR-region could only be established for the In_2O_3:5%Eu material. All of the Tb-doped materials appeared to have a broad absorption from about 500 to 800 nm compared to pure In_2O_3, with increasing intensity with increasing doping concentration (Figure 8.11). Absorption lines could also be seen in the IR region for the samples with 5 and particularly 10 cat% Tb-doping.

The ITO-based materials demonstrated very low reflectance and are not reported here

.

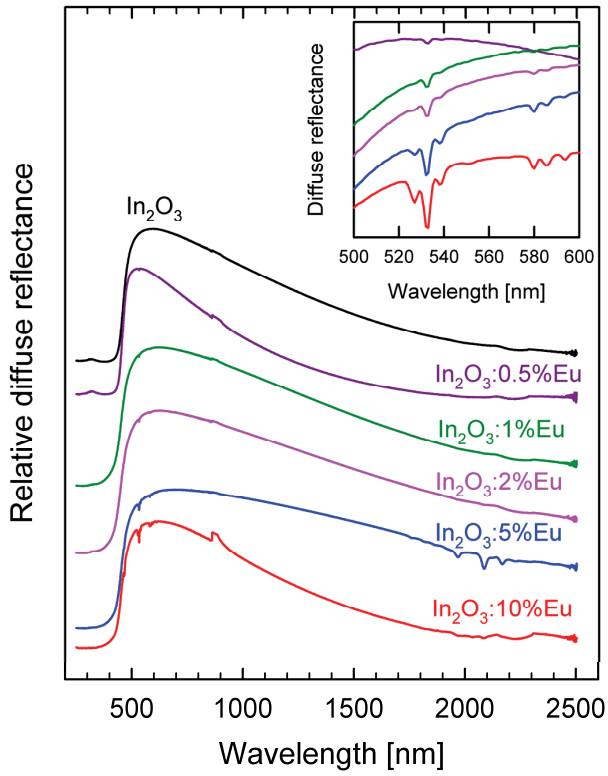

Figure 8.10. Diffuse reflectance of In_2O_3-based bulk materials with different amounts of Eu-doping. The inset shows a close-up of the absorptions around 530 and 580 nm for the same materials, with the topmost being In_2O_3:0.5%Eu and the bottommost In_2O_3:10%Eu. The anomaly at 860 nm is due to a change of detector.

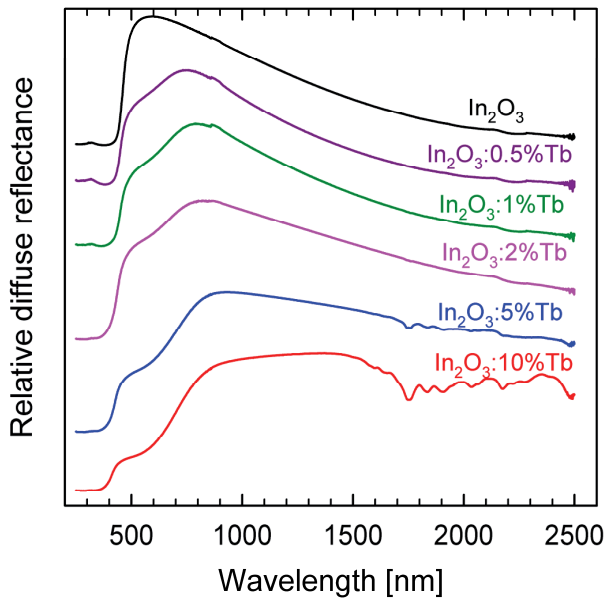

Figure 8.11. Diffuse reflectance of In_2O_3-based bulk materials with different amounts of Tb-doping.

Photoluminescence experiments were performed on the bulk materials. The excitation and emission spectra of In_2O_3:5%Eu are given in Figure 8.12. When monitoring the characteristic red emission of Eu^{3+} at around 611 nm [42, 270], two broad excitation peaks were observed centered around 465 and 530 nm, where the intensity was highest at 530 nm. This wavelength corresponded well with the absorption observed by diffuse reflectance. No excitations were found at lower wavelengths. The emission spectra after excitation at these two wavelengths clearly shows the emission centred around 611 nm. This emission was strongest for excitation at 530 nm, in line with the intensities in the excitation spectrum. Also emissions with lower intensity were observed at approximately 578, 584, 592, 597 and 629 nm, for both excitation wavelengths. The materials with 5 cat% Eu-doping exhibited the strongest emission, as shown in Figure 8.13. The emission at 611 nm was clearly observed also for the material with 10 cat% Eu, but with considerably lower intensity. The emission was also observed for doping concentrations as low as 1 cat% Eu.

Photoluminescence measurements were also performed on pressed porous powder samples. The powder materials also exhibited the emission at 611 nm upon excitation at 465 and 530 nm, but with significantly lower intensity than the corresponding bulk materials. The emission was only observed with 5 and 10 cat% Eu and not for lower doping concentrations in case of powder pellets.

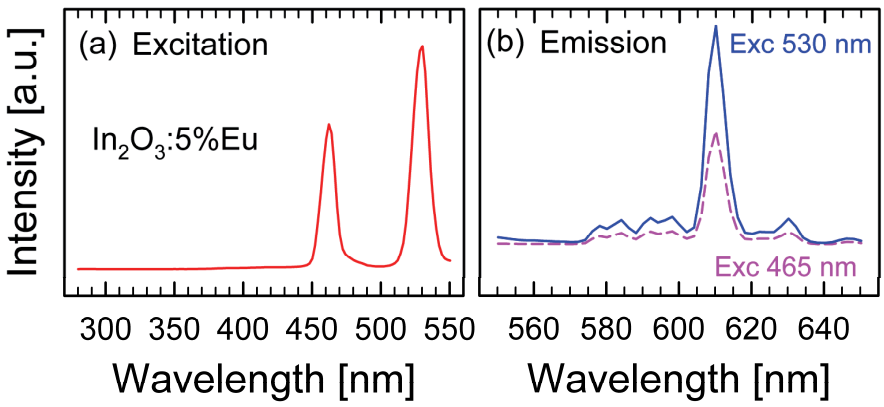

Figure 8.12. Excitation (a) and emission spectra (b) of In_2O_3 doped with 5 cat% Eu. The excitation spectrum was obtained by monitoring the emission at 611 nm, while the emission spectra were obtained after excitation at 530 (solid line) and 465 nm (broken line).

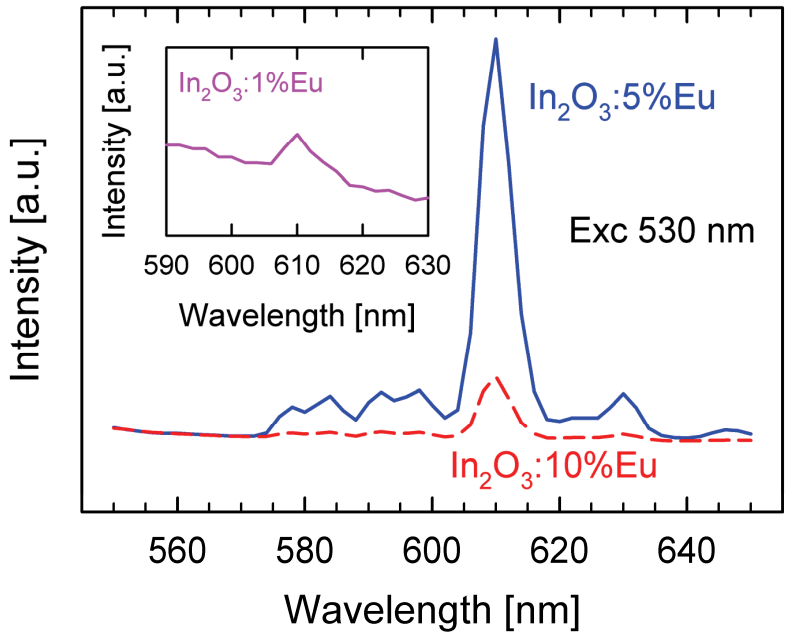

Figure 8.13. Emission spectra of In_2O_3 doped with 5 (solid line) and 10 cat% Eu (broken line) after excitation at 530 nm. The inset shows a similar emission spectrum for In_2O_3 doped with 1 cat% Eu.

Luminescence decay measurements were performed on the emission at 611 nm after excitation at 530 nm and the results, given in Figure 8.14, clearly demonstrates the different behaviour of the powder and bulk materials. The lifetime of bulk In_2O_3:10%Eu appears to be approximately twice that of the corresponding powder. The time decay of the bulk material appears to be close to a single exponential, as demonstrated by the nearly straight line in the logarithmic plot. On the other hand, the decay appears to be more complex for the powder sample. Similar observations were also observed for In_2O_3:5%Eu. The decay times of bulk and powder materials of In_2O_3 doped with 5 and 10 cat% Eu are summarised in Table 8.7. The average lifetime of the material, accounting for the relative strength of the contributions from the different decays, are given as the weighted average. The decay of the powder materials were fit by three exponential decays, while two decays were used for the bulk samples. The lifetimes corresponded well with the observed intensities in the emissions, as the materials with 5 cat% Eu had longer lifetimes than the materials with 10 cat% Eu, and that the powders had a shorter lifetime than the corresponding bulk material. The lifetime of bulk In_2O_3 doped with 5 and 10 cat% Eu was 0.867 and 0.782 ms,

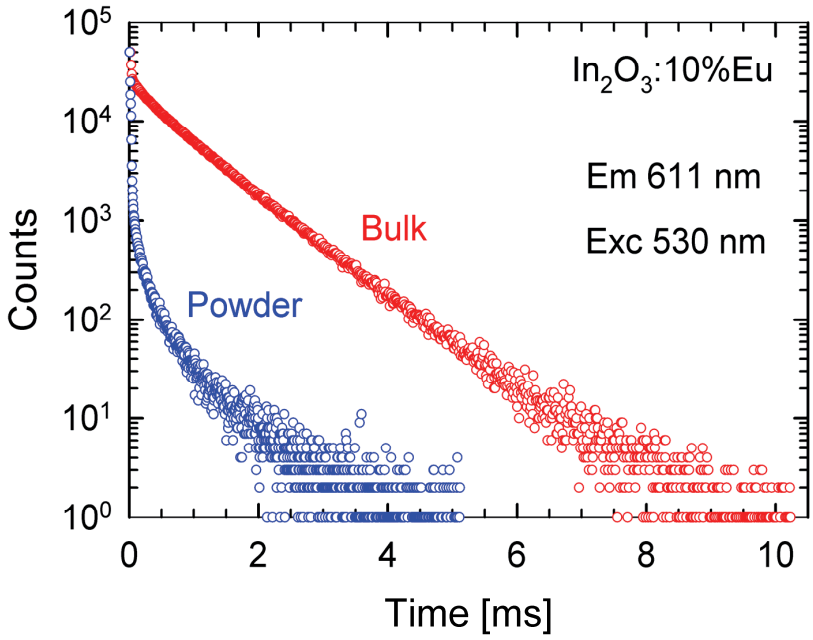

Figure 8.14. Luminescence decay curves of the 611 nm emission for bulk and powder In_2O_3 doped with 10 cat% Eu after excitation at 530 nm.

.**Table 8.7.** Decay times for emission at 611 nm after excitation for bulk and powder materials of In_2O_3 doped with 5 and 10 cat% Eu after excitation at 530 nm. The value in parenthesis behind the decay times is the relative weight for each component of the fit.

Material	State	Heat treatment temperature [°C]	Decay [ms]	Weighted average [ms]
In_2O_3:5%Eu	Powder	530	$\tau_1 = 0.20 \pm 0.01$ (53.0 %) $\tau_2 = 0.67 \pm 0.01$ (35.5 %) $\tau_3 = 0.041 \pm 0.002$ (11.7 %)	0.35
In_2O_3:10%Eu	Powder	530	$\tau_1 = 0.18 \pm 0.02$ (49.5 %) $\tau_2 = 0.62 \pm 0.02$ (30.9 %) $\tau_3 = 0.042 \pm 0.001$ (19.6 %)	0.29
In_2O_3:5%Eu	Bulk	1400	$\tau_1 = 0.84 \pm 0.01$ (92.7 %) $\tau_2 = 1.19 \pm 0.03$ (7.3 %)	0.87
In_2O_3:10%Eu	Bulk	1400	$\tau_1 = 0.24 \pm 0.01$ (8.7 %) $\tau_2 = 0.83 \pm 0.01$ (91.3 %)	0.78

respectively. When only a single exponential was used for the bulk materials the corresponding lifetimes were 0.863 and 0.756 ms. No emissions were observed for In_2O_3 doped with Nd or Tb, while no experiments were performed on ITO-based materials

The band gap of the materials was estimated from the diffuse reflectance spectra by the Kubelka-Munk method and is given in Figure 8.15. This method is known to underestimate the band gap [271], and the band gap of pure In_2O_3 was about 2.7 eV, somewhat lower than the reported value of 2.9 eV [126]. The band gaps appear to be slightly increasing with REE-doping, however the error is estimated to be in the order of ± 0.1 eV.

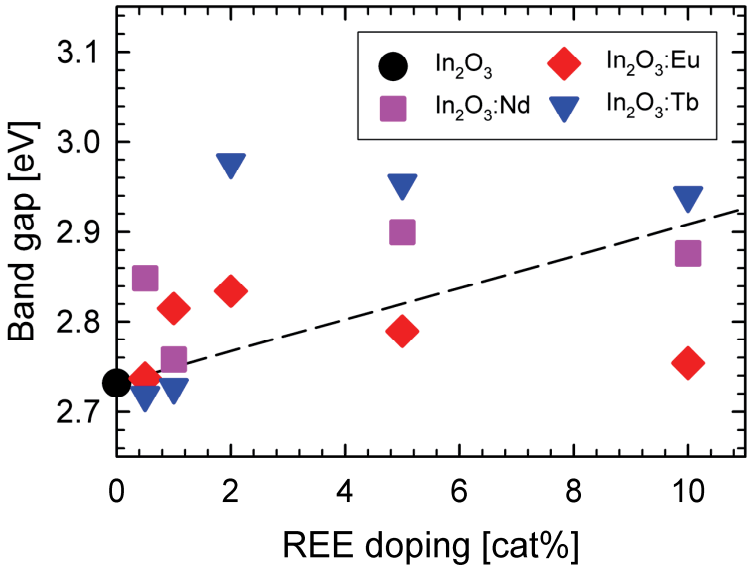

Figure 8.15. Band gap of REE-doped In_2O_3 materials estimated from diffuse reflectance spectra using the Kubelka-Munk method. The dashed line is a guide to the eye.

8.4. REE-doped thin films

Thin films of In_2O_3 and ITO doped with REEs were succesfully synthesised by the spin coating procedure described in Chapter 4.2. Five different doping concentrations of Eu were used, ranging from 0.5 to 10 cat%, both for In_2O_3 and ITO as hosts. Only three compositions were prepared for Nd- and Tb-doping, namely In_2O_3 doped with 0.5, 1 and 2 cat% REE. The focus on Eu was motivated by the successful photoluminescence experiments for bulk materials in Chapter 8.3.2. The structural properties if the films were investigated by XRD, while the functional properties were characterised by a combined conductivity and Hall effect measurements and transmission and reflectance spectroscopy. The characterisation of the properties focused on how the REE-doping affected the functional properties of the host. Due to time limitations the photoluminescence properties of the thin film materials were not investigated.

The REE-doped thin films appeared phase pure by XRD, similar to the diffractogram of an ITO thin film given in Figure 7.1. No secondary phases could be observed even at 10 cat% Eu-doping. The lattice parameter of the cubic In_2O_3 phase for the different films is given in Table 8.8 and Figure 8.16. The lattice

parameter of In_2O_3 and ITO with 5 cat% Sn was 10.126 and 10.137 Å, respectively. The lattice parameter of In_2O_3:Eu appeared to increase with increasing amount of doping. Also the lattice parameters of In_2O_3 doped with Nd and Tb appeared to be larger than the In_2O_3 reference thin film. The lattice parameter of ITO:Eu did not increase significantly at high doping concentrations. Both host materials experienced a small decrease in the lattice parameter at low Eu doping concentrations. The crystallite size of the thin films did not dependent on doping.

Table 8.8. Lattice parameter and crystallite size of the cubic In_2O_3 phase for films of ITO, ITO:Eu, In_2O_3, In_2O_3:Nd, In_2O_3:Eu and In_2O_3:Tb. The estimated uncertainty is ± 0.005 Å for the lattice parameter and ± 3 nm for the crystallite size.

Material	Doping amount [cat%]	Lattice parameter [Å]	Crystallite size [nm]
ITO	0	10.137	15
ITO:Eu	0.5	10.134	14
	1	10.129	14
	2	10.139	14
	5	10.136	15
	10	10.141	16
In_2O_3	0	10.126	14
In_2O_3:Nd	0.5	10.132	15
	1	10.135	14
	2	10.129	14
In_2O_3:Eu	0.5	10.123	14
	1	10.127	14
	2	10.131	14
	5	10.140	14
	10	10.157	14
In_2O_3:Tb	0.5	10.135	15
	1	10.128	14
	2	10.130	14

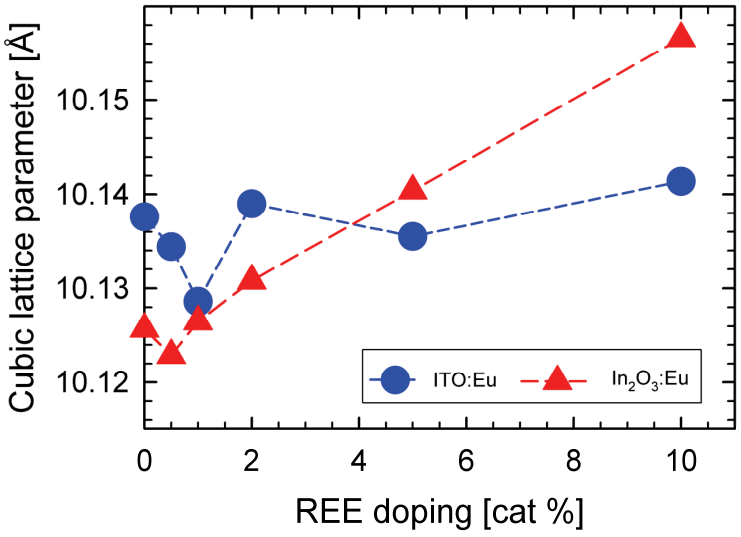

Figure 8.16. Cubic lattice parameter of the In_2O_3 phase for thin films of ITO:Eu (●) and In_2O_3:Eu (▲).

The sheet resistance of the films were measured and combined with a Hall effect measurement in order to find the mobility and carrier concentration, and the results are given in Table 8.9 and Figure 8.17. The mobility of the ITO-based films is largely unaffected by the REE-doping, but the sheet resistance and sheet carrier concentration appears to be deteriorated to some extent at 10 cat% Eu. Also for In_2O_3:Eu, the properties were not significantly affected at low doping concentrations, but at 5 and 10 cat% a large increase in sheet resistance and decrease in sheet carrier concentration were observed. The reproducability of the experiment was good, but some scattering is evident. This could indicate that there are other differences between the films apart from the nominal composition, such as thickness, homogeneity or possible cracks, which could influence their properties.

The transmittance of ITO:Eu thin films are given in Figure 8.18. The transmittance of the thin films was not significantly affected by the Eu-doping. Similar observations were made for the other material systems. Moreover, the REE-doping did not have a significant effect on the reflectivity of the films. The band gap of the films was estimated based on the transmittance and reflectance data, as depicted in Figure 8.19. The band gap is about 0.2 eV higher for ITO than for In_2O_3 due to the Burstein-Moss effect. For the In_2O_3-based films the band gap appears to increase slightly with increasing amount of REE-doping, while for the ITO-based films the trend appears to be opposite.

Table 8.9. Sheet resistance, mobility and sheet carrier concentration of REE-doped thin films. The estimated uncertainty is ± 1 % for the sheet resistance and the sheet carrier concentration and ± 0.05 $cm^2/V*s$ for the mobility.

Material	Doping amount [cat%]	Sheet resistance [Ω/□]	Mobility [$cm^2/V*s$]	Sheet carrier concentration [10^{14}]
ITO	0	844	9.15	8.85
ITO:Eu	0.5	452	12.00	11.6
	1	1620	8.57	4.63
	2	1140	9.64	6.12
	5	907	8.87	7.89
	10	2410	7.34	3.62
In_2O_3	0	5610	5.68	2.36
In_2O_3:Nd	0.5	4980	9.67	1.52
	1	782	17.50	4.65
	2	6850	8.68	1.18
In_2O_3:Eu	0.5	2320	12.00	2.63
	1	4900	10.70	1.20
	2	1160	15.50	3.54
	5	107000	4.78	0.164
	10	133000	3.41	0.139
In_2O_3:Tb	0.5	884	15.40	4.59
	1	1280	15.80	3.13
	2	3890	9.09	1.94

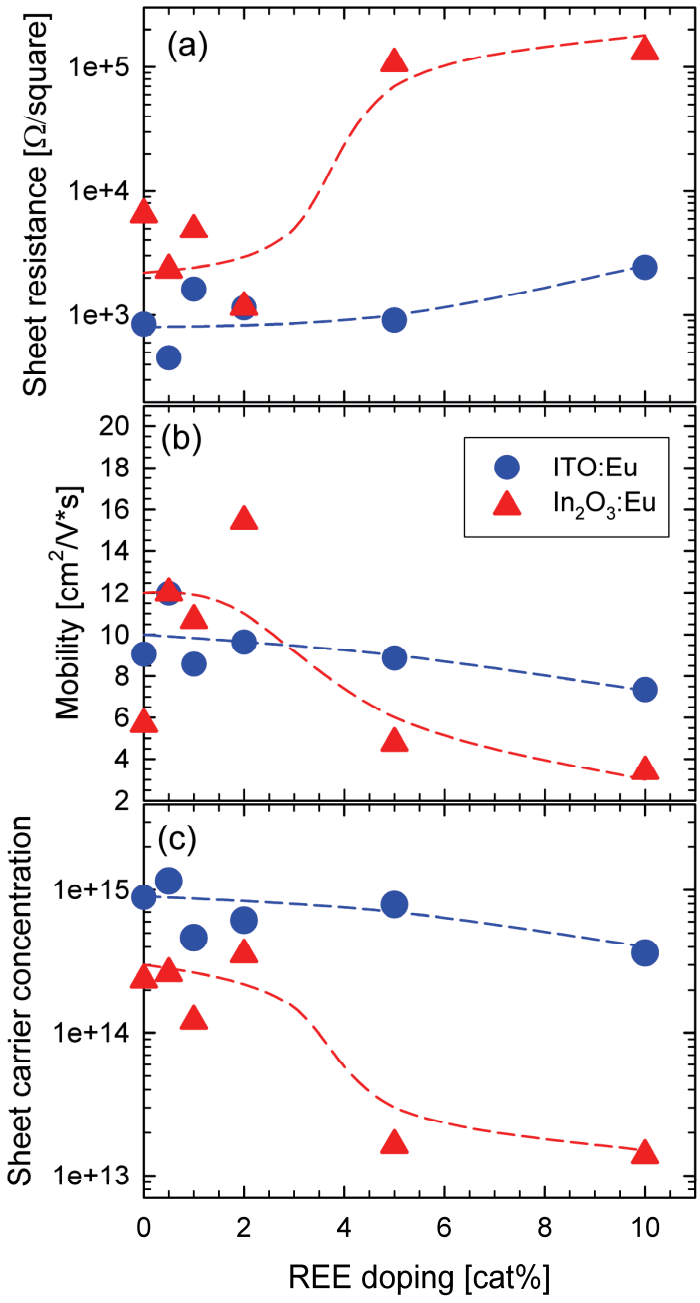

Figure 8.17. Sheet resistance (a), mobility (b) and sheet carrier concentration (c) of ITO:Eu (●) and In_2O_3:Eu (▲). The same labelling is used in the three figures. The dashed lines are guides to the eye.

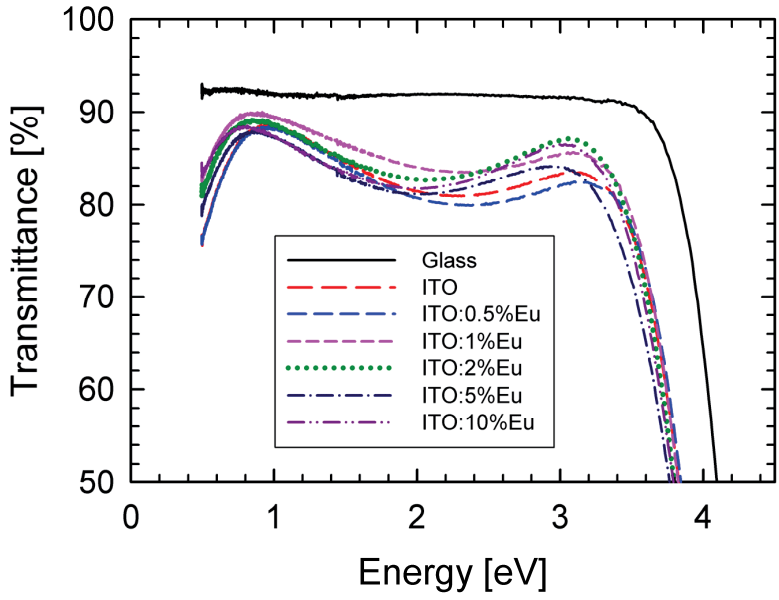

Figure 8.18. Transmittance of ITO:Eu thin films on glass substrates.

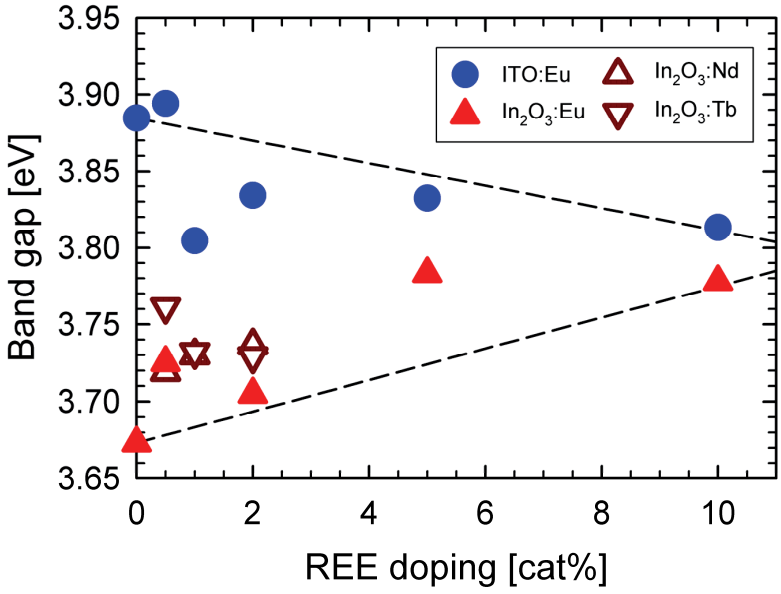

Figure 8.19. Band gap of REE-doped In_2O_3 and ITO thin films. The dashed lines are guides to the eye.

8.5. Discussion

8.5.1. Synthesis and solid solubility

It was demonstrated that the aqueous sol-gel process could be used to prepare phase-pure powders and thin films of In_2O_3 and ITO doped with REEs. The phase-pure materials were in a metastable state, as secondary phases could be observed to form during heat treatment at higher temperatures where sufficient cation mobility allow precipitation to occur. The metastabililty of the prepared materials indicates that doping with higher concentrations than the solibulity limit could be possible. The same phenomenon is well known for ITO where tin doping concentrations significantly higher than the solubility limit are commonly applied.

When acetic acid was used as a complexing agent, the REE-doping increased the amount of the metastable rhombohedral In_2O_3 polymorph (space group $R\bar{3}c$). The amount of this polymorph appeared to be higher with Nd, which is the largest of the three dopants. The cubic bixyite structure is the stable crystal structure for the RE_2O_3 compounds, as for In_2O_3. Yet, unlike for In_2O_3, the rhombohedral corrundum structure is not the stable structure at high pressures for the RE_2O_3 compounds [49, 67]. It is not clear why the REE-doping increases the amount of the rhombohedral phase, but it is probably related to the kinetics of the crystallisation when the gel is decomposing to the final oxide materials. However, the formation of this phase was avoided by using larger complexing agents, in line with the observations for the materials without REE-doping in Chapter 5.

The equilibrium solubility of REEs in In_2O_3 could be established after annealing at 1400 °C. The solid solubility at this temperature was observed to be about 1, 5 and 10 cat% for Nd, Eu and Tb, respectively. At higher doping concentrations a secondary $REInO_3$ phase was observed (space group *Pnma* for $NdInO_3$ and $P6_3cm$ for $EuInO_3$ and $TbInO_3$). All of the three dopants are most stable in their trivalent state, and the chemistry of the elements in the lanthanide group is known to be similar. The similar properties is caused by the additional electrons being added to the 4f orbitals, which are effectively shielded by the valence electrons in the outer 5s and 5p orbitals. The property of the dopants which is most important for their solid solubility is their size. The size of the different cations [79] together with their solid solubility in In_2O_3 is given in Table 8.10. All of the dopants are larger than In^{3+} and the larger the dopant and the size mismatch is, the smaller the solid solubility. The size of the cations decreases from left to right in the lanthanide group. Hence, it is proposed that the solid solubility of the cations to the left of Nd, such as La^{3+} and Pr^{3+}, would be very small. On the other hand, cations smaller than Tb^{3+}, like the technologically important Er^{3+} [207, 272] which could have good

Table 8.10. Ionic radius, size difference compared to In^{3+} and solid solubility of Nd, Eu and Tb in In_2O_3. The ionic radii were taken from [79].

Ion	Ionic radius [pm]	Size difference [%]	Solid solubility [cat%]
In^{3+}	80	-	-
Nd^{3+}	98	22.5	~1
Eu^{3+}	95	18.8	~5
Tb^{3+}	92	15.0	~10

upconversion properties [208], is suggested to be high. When ITO was used as a host, the solid solubility was reduced due to a strong tendency of the tin and REE codopants to form a pyrochlore $RE_2Sn_2O_7$ phase (space group $Fd\bar{3}m$).

A ternary phase diagram of the In_2O_3-SnO_2-RE_2O_3 system was constructed, given in Figure 8.20 (a). The phase diagram was derived from the phase compositions and solid solubility limits for the bulk materials described in Chapter 8.2. The phase diagram includes the phases $REInO_3$, $RE_2Sn_2O_7$ and $In_4Sn_3O_{12}$, where the two first have been observed in this work. The latter phase was not detected here, but is reported to be thermodynamically stable at 1400 °C [82]. It is the solid solubility in In_2O_3, marked with bold red lines in the bottom left corner of the phase diagram, which is of most importance. Based on mass balance and the lever rule, the composition of the cubic In_2O_3 phase could be estimated. It was assumed that there was no solid solubility in either $REInO_3$ or $RE_2Sn_2O_7$. The results are given in Table 8.11. Close-ups of the indium-rich side of the phase diagrams for the three different systems are given in Figure 8.20 (b), (c) and (d). The crosses in the figures represent the compositions from Table 8.11, together with the solid solubility of REEs in In_2O_3 from Table 8.10 and the solid solubility of Sn in In_2O_3. The latter value was 3 cat% based on the phase-diagrams of Gonzãles et al. [80] and Heward and Swenson [78]. The proposed solid solubility lines were drawn based on these points.

The most important difference between the phase diagrams in Figure 8.20 (b), (c) and (d) is the solubility of the REEs in In_2O_3, which was shown to be inversely proportional to the size difference between the RE^{3+} and In^{3+}. The two phase region between In_2O_3 and $RE_2Sn_2O_7$ increases with increasing solubility of RE in In_2O_3 at the expense of the three phase region where also $REInO_3$ is present. This correlates with the phase content of the 10 cat% REE-doped materials (Table 8.4). The

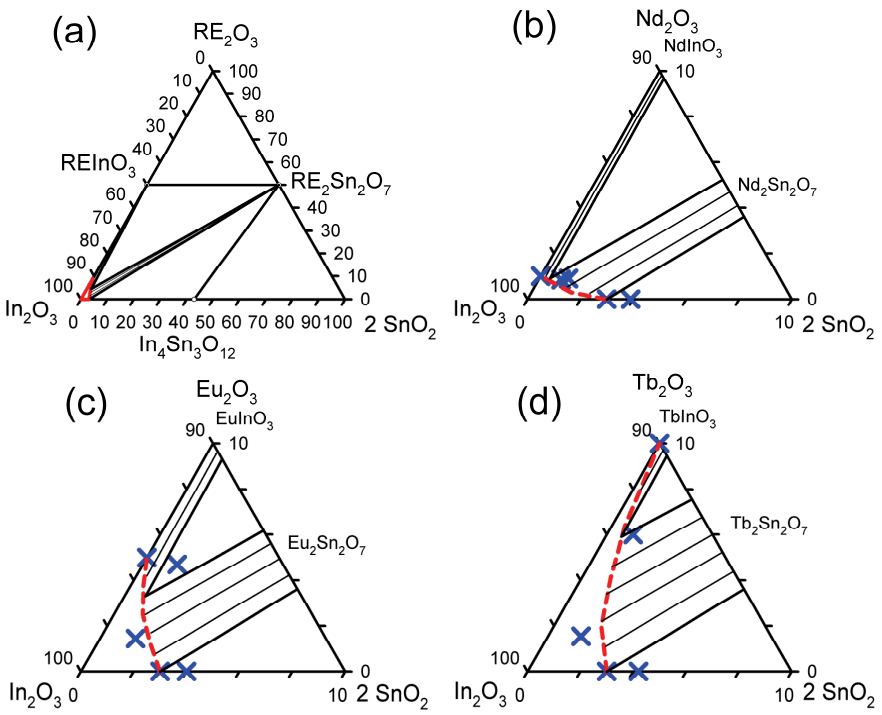

Figure 8.20. Ternary phase diagram of the system In_2O_3-SnO_2-RE_2O_3 at 1400 °C (a). The solid solubility region of the indium-rich phase in the bottom left corner is marked with bold red lines. Close up of the indium-rich side of the ternary phase diagrams of the systems In_2O_3-SnO_2-RE_2O_3 with RE_2O_3 = Nd_2O_3 (b), Eu_2O_3 (c) and Tb_2O_3 (d) at 1400 °C. The crosses marks the composition of the In_2O_3 phase in the ITO materials with 1, 5 and 10 cat% REE-doping, as given in Table 8.11, and the solid solubility of RE and Sn in In_2O_3. The proposed solid solubility region of In_2O_3 is marked with a broken line. The thinner lines represent two phase regions.

composition of the materials with 1 and 5 cat% REE was similar for the three dopants, due to the formation of the pyrochlore $RE_2Sn_2O_7$ phase and the fixed solubility of tin in In_2O_3.

The solid solutions of all In_2O_3-based materials appeared to follow Vegard's law, except for the Tb-doped powders. Also in this case the lattice parameter increased with the amount of doping, but less than expected from Vegard's law. For 5 and 10 cat% Tb the lattice parameter was notably smaller than for the bulk materials with the same composition. Terbium is, along with cerium and praseodymium, known to be stable also in a tetravalent state [49], forming TbO_2 for which the lattice parameter is smaller than the sesquioxide [273]. It is therefore proposed that a

Table 8.11. Estimated composition of the cubic In_2O_3 phase for ITO doped with Nd, Eu and Tb based mass balance and the lever rule.

Material	Nominal composition [cat%]			Composition of cubic In_2O_3 [cat%]		
	In	Sn	RE	In	Sn	RE
ITO:1%Nd	94.1	4.9	1.0	96.1	3.9	0.0
ITO:5%Nd	90.3	4.7	5.0	98.0	1.1	0.9
ITO:10%Nd	85.5	4.0	10.0	98.3	0.9	0.8
ITO:1%Eu	94.1	4.9	1.0	96.0	4.0	0.0
ITO:5%Eu	90.3	4.7	5.0	97.2	1.4	1.4
ITO:10%Eu	85.5	4.5	10.0	94.0	1.3	4.7
ITO:1%Tb	94.1	4.9	1.0	95.8	4.2	0.0
ITO:5%Tb	90.3	4.7	5.0	97.2	1.5	1.3
ITO:10%Tb	85.5	4.5	10.0	93.0	6.0	1.0

fraction of the terbium dopant being tetravalent is the cause of the relatively small lattice parameters. At small doping levels this effect was not observed, so it appears that the tetravalent fraction increased with increasing doping. After the materials were heat treated at 1400 °C this effect was not observed. It is common for oxide materials to become more stable in lower oxidation states with increasing temperatures [274]. Tetravalent cations have the possibility of functioning as n-type donors in In_2O_3. This opens up to the possibility of influencing the conductivity of the material by controlling the amount of tetravalent terbium. However, it is not known whether the luminescent ability of terbium will be retained in its tetravalent state. More work is needed to understand how Tb^{3+}/Tb^{4+} will effect directly on the free carrier concentration in ITO.

All of the prepared powders, including when ITO was used as host, appeared to be phase pure based on XRD. However, similarly as for the bulk materials, the In_2O_3-based powders had an inflection point in the lattice parameter with increasing doping, reaching saturation at higher amounts of doping. It is therefore inferred that also the nano-crystalline powders have secondary phases above this concentration, but with amounts and/or crystallite sizes too small to be observed by XRD. Furthermore, all of the nano-crystalline powders had a larger lattice parameter than their bulk counterparts, except for the powders with large amounts

of Tb, as discussed above. The increase in the lattice parameter is proposed to be caused by a finite size effect, due to the nano-scale of the powder. For the In_2O_3-based powders it appeared that the crystallite size decreased somewhat with increasing REE-doping, but this effect was not observed when ITO was used as the host. There was no significant difference in crystallite size between the In_2O_3- and ITO-based powders. The lattice parameters of the thin films had a slightly diffrerent trend regarding doping concentration than for the powders (Table 8.8). In this case there was an increase in the lattice parameter with increasing doping concentration with In_2O_3 as a host, while this trend appeared to be absent for the ITO-based materials. However, the results in Chapter 7 show that the thin films are subject to tensional strain, and it is possible that this effect will dominate the lattice parameter, thereby concealing trends regarding the composition. Both In_2O_3:Eu and ITO:Eu thin films experienced a small decrease in the lattice parameter at low doping concentrations. A similar trend has also been observed for Tb-doped ITO films with a 90:10 ratio between In and Sn, as shown in Figure 8.21 [275]. The same phenomenon has also been reported for ITO with low Sn doping concentrations [84].

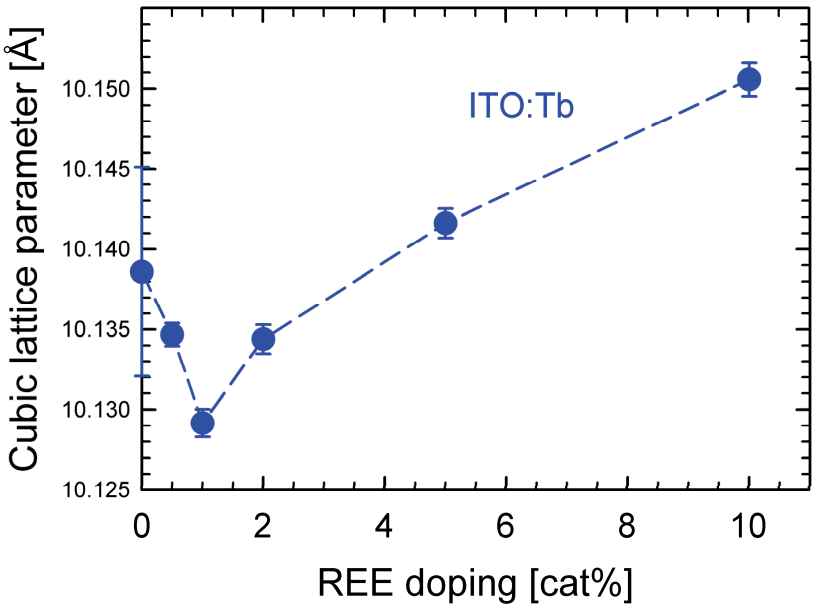

Figure 8.21. Cubic lattice parameter of the In_2O_3 phase for thin films of ITO with 10 cat% Sn doped with different concentrations of Tb oxide [275].

8.5.2. Functional properties

The effect of the REE-doping on the functional properties of the host was investigated. It was demonstrated that both the electrical conductivity and the optical transmittance was retained even with high doping concentrations in ITO. The electrical conductivity of ITO is caused by tetravalent tin dopants acting as n-type donors. Hence, it is reasonable that trivalent dopants, isovalent with In^{3+}, should not cause a severe decrease in conductivity. The sheet resistance and mobility was not deteriorated by low concentrations of REE-doping (Figure 8.17.) both for In_2O_3- and ITO-based thin films. At high doping concentrations the carrier concentration of In_2O_3:Eu was reduced, while the trend was significantly smaller for ITO:Eu. Oxygen vacancies act as the electrical charge donor for In_2O_3. It is possible that the REE-doping somehow affects the oxygen vacancy concentration, thereby affecting the carrier concentration more strongly for In_2O_3 than ITO.

The effect of the REE-doping on the conductivity was substantially different for bulk In_2O_3-based materials. A dramatic decrease in the conductivity with increasing REE-doping was demonstrated, even at low doping concentrations (Figure 8.7). The decrease was most significant for In_2O_3:Nd and progressively smaller for In_2O_3:Eu and In_2O_3:Tb. It appears to be a correlation between the size of the dopant and the decrease in the conductivity. The thermopower of the bulk materials, on the other hand, was not affected by the REE-doping (Figure 8.8). While the conductivity is a function of both charge mobility and carrier concentration, the thermopower only varies with carrier concentration [13]. Hence, the dramatic decrease in conductivity for In_2O_3 doped with REEs must be caused by a decrease in mobility, in line with the assumption that the isovalent REE-doping should not cause a dramatic decrease in the carrier concentration. The materials with low doping concentration were all phase pure (small traces of secondary phase was observed for In_2O_3:1%Nd), excluding that the decrease in mobility is caused by the presence of secondary phases. A possible explanation is that the exposure to high temperatures caused the dopants to segregate to the grain boundaries of the sample. The thin films were only exposed to 530 °C, so a possible segregation of the REEs to grain boundaries is not likely to occur. It was attempted to search for an increase in REE-concentration at grain boundaries by EDS and SEM, but the concentrations were too low to be conclusive. Electrical impedance spectroscopy of the materials was also performed, but the conductivity was too high to give any useful results. Both the conductivity and the thermopower of the ITO-based materials appeared to be largely unaffected by the REE-doping at low concentrations. However, the solid solubility was limited for these materials, and they were not phase pure.

The In_2O_3:Eu materials exhibited a broad emission centered around 611 nm upon excitation at 465 and 530 nm. The emission is attributed to the transition $^5D_0 \rightarrow {}^7F_2$, while the excitations corresponds to transitions from the ground state of Eu^{3+}, $^7F_0$, to the levels $^5D_2$ and $^5D_1$. A schematic illustration of these energy transitions is given in Figure 8.22. The emission was fairly broad, which has been attributed to the activator not being well incorporated into the host lattice. However, the lattice parameters clearly increased with increasing amount of doping, as shown in Figure 8.3, thereby demonstrating a good incorporation. The lower intensity emissions at approximately 578, 584, 592, 597 and 629 nm are ascribed to transitions from $^5D_0$ to $^7F_0$, $^7F_1$ and $^7F_2$ levels [43]. The absence of excitations at lower wavelengths indicates that host sensitisation was not possible and that emissions only occurred upon direct excitation of the 4f energy levels of Eu^{3+}. This is in line with the work of Xiao et al. where strong host sensitisation was only observed at temperatures below 200 K, while excitation over the band gap of the host was absent at room temperature [43]. The emission at 611 nm increased in intensity with increasing Eu-doping up to 5 cat% and was lower for 10 cat% Eu. It is known that doping above a certain limit can cause concentration quenching, due to non-radiative

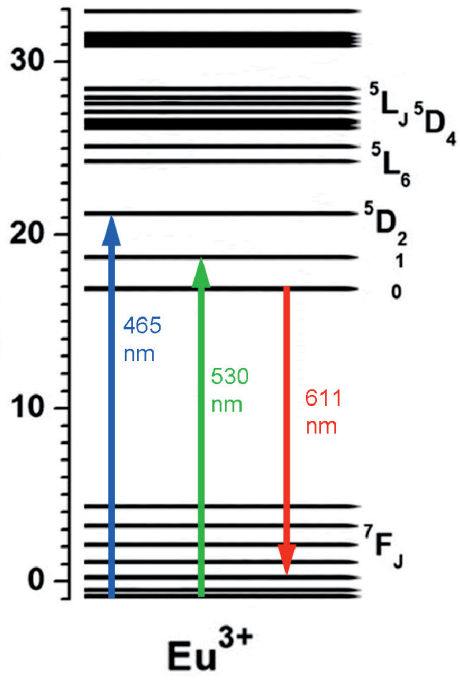

Figure 8.22. Illustration of the energy transitions within the 4f-levels of Eu^{3+} causing the observed emission at 611nm and excitations at 465 and 530 nm.

interactions between the REE activator ions [207]. However, the material with 10 cat% Eu contained a secondary phase, which also might affect the photoluminescence. The lifetime of the 611 nm emission after excitation at 530 nm for In_2O_3:5%Eu was 0.87 ms, which compares well with previously reported value of 0.81 ms [43]. The lifetime for In_2O_3:10%Eu was reduced to 0.78 ms, again illustrating the negative effect of increasing the doping concentration above a certain limit.

It was demonstrated that the bulk materials have longer lifetimes than their corresponding nano-crystalline powder materials (Table 8.7). The shape of the luminescence decay curves also indicated a more complicated behaviour for the powders. A significant amount of the previous works focuses on nano-particles or quantum dot hosts [41-43, 47, 224]. However, in this work it is obvious that the bulk samples had better luminescence properties than the nano-sized powder. It is not clear whether this was caused by finite size effects influencing the band structure of the powder. No host sensitisation was observed, which might indicate that the match between the energy levels of the host and activator was not the limitation. A possible explanation is a better incorporation of the dopants in the lattice for the bulk materials. The nano-sized powder also has a higher surface to volume ratio, which is known to cause more defects, and a higher possibility of remaining humidity from the synthesis, which will favour non-radiative decay.

The diffuse reflectance of In_2O_3 doped with Nd clearly demonstrated absorption bands around 518, 531, 594, 630, 691, 750, 806 and 885 nm. These absorptions are ascribed to energy transitions from the ground state of Nd^{3+}, being $^4I_{9/2}$, to $^2G_{9/2}$, $^4G_{7/2}$, $^2G_{7/2}$/$^4G_{5/2}$, $^2H_{11/2}$, $^4F_{9/2}$, $^4F_{7/2}$, $^4F_{5/2}$ and $^4F_{3/2}$, respectively [207, 276]. For convenience, the energy levels of Nd^{3+}, as given in Figure 3.20, are shown in Figure 8.23. However, even if the materials were demonstrated to have the absorptions corresponding to the characteristic energy transitions in Nd^{3+}, it was not possible to observe the distinct emission around 1064 nm. Nor was it possible to observe emission in Tb-doped materials. The cause of this absence is unclear, however it is possible that the band structure of the In_2O_3 host mathces more favourably with the energy levels of Eu^{3+} than Nd^{3+} and Tb^{3+}. In case of the Nd-doped materials the presence of the secondary phase could also have an effect.

The large band gaps of the materials, and therefore also their transmittance in the visible region, were retained also with high concentrations of REE-doping. The band gap appeared to increase slightly with increasing REE-doping when In_2O_3 was used as a host, both for bulk materials and thin films. Further investigations would be necessary in order to understand how the REE-doping affects the band structure of In_2O_3. It appears that the trend was opposite in Eu-doped ITO films,

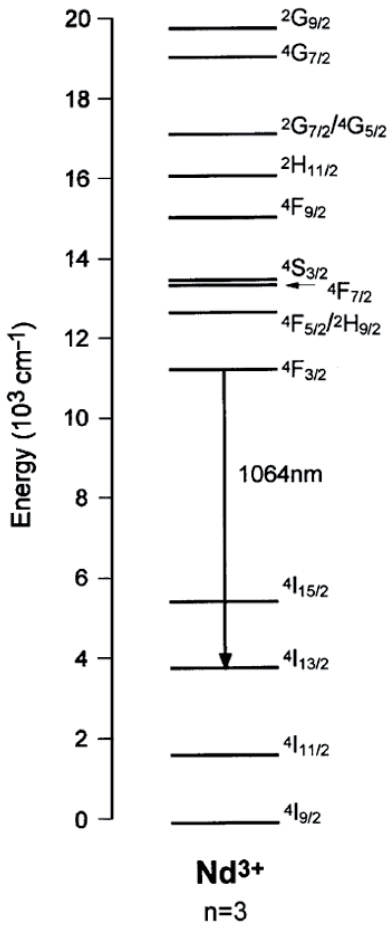

Figure 8.23. Energy levels of Nd^{3+}, as given in Figure 3.20.

with a slightly decreasing band gap with increasing amount of doping. It is possible that this is caused by a reduced amount of free carriers, thereby giving a smaller Burstein-Moss effect, which appears to correlate well with the carrier concentrations in Figure 8.17. Furthermore, the band gap of bulk In_2O_3 based on diffuse reflectance was around 2.7 eV, while approximately 3.7 eV based on transmission and reflectance of the thin films. The first value was obtained by the Kubelka-Munk method, which is known to slightly underestimate the band gap [271]. However, it has been demonstrated that the band gap of In_2O_3 is about 2.9 eV, but that the direct transition from the top of the valence band to the bottom of the conduction band is parity forbidden [126], as discussed in Chapter 3.2. The electrons must therefore be excited from about 0.8 eV below the maximum of the valence band in order for strong transitions to occur. It is possible that the diffuse

reflectance measurement of bulk samples can respond to the parity forbidden transition, while the spectroscopy of the thin films only is sensitive to the allowed transitions with about 0.8 eV higher energy.

The density of the prepared bulk samples was shown to range between 58 and 92 %. The conductivity was corrected for porosity, and the differences in conductivity were so large, ranging over several orders of magnitude, which is not likely to be caused by changes in density. The density of the samples did not follow a clear trend regarding the REE doping concentration and dense samples could be prepared from powders with high concentrations of REEs (the density of In_2O_3:10%Eu was 88 %). The different sintering characteristics of the powders could have been caused by other properties than the composition, such as different degrees of agglomeration from powder to powder.

The REE-doped thin films were all prepared from separate solutions, which were demonstrated to cause some differences from film to film. The films also had to be cut in order to perform the experiments, possibly damaging the films, which could explain the scatter in the electrical conductivity data (Figure 8.17).

8.6. Conclusions

Phase-pure materials of In_2O_3 and ITO doped with REEs were succesfully prepared in form of nano-crystalline powders and thin films. The equilibrium phase composition and solid solubility of Re in In_2O_3 and ITO at 1400 °C were determined. The solubility of the REEs in In_2O_3 was largely controlled by the size of the dopant. When ITO was used as a host the solid solubility was reduced due to a strong tendency of the tin and REE codopants to form a pyrochlore $RE_2Sn_2O_7$ phase. Phase diagrams at 1400 °C were constructed based on the findings. The metastable character of the materials demonstrates that it is possible to dope with higher concentrations of REEs than the solid solubility limit. The effect of the REE-doping on the functional properties of the host was investigated. Neither the conductivity nor the transparency of thin films was deteriorated by the REE-doping. The conductivity of bulk materials of REE-doped In_2O_3 was significantly reduced, even at low doping concentrations, due to a decrease in carrier mobility. ITO-based bulk materials did not experience the same decrease, although these materials were not phase pure. Finally, strong emissions at around 611 nm were observed for Eu-doped In_2O_3, demonstrating the possibility of obtaining photoluminescence in a TCO host material.

9. Conclusions

An aqueous sol-gel process for the synthesis of In_2O_3 and ITO has been developed. The process could successfully be applied to prepare phase-pure In_2O_3-based materials, both in the form of thin films, nano-crystalline powders as well as bulk materials. The thin films were demonstrated to have excellent functional properties and particles down to about 15 nm could be prepared by calcination of the decomposed gels. Excellent crystallinity was demonstrated both in case of the thin films and the powders. Preparation of phase-pure materials were also demonstrated when In_2O_3 or ITO was doped with REEs. The doping amount, both with regards to Sn and REEs, could readily be controlled. The sol-gel process enabled the synthesis of metastable solid solutions, thereby making doping levels higher than the equilibrium solid solubility in bulk materials possible.

The chemistry of the sol-gel process was studied, and an amorphous gel was formed after evaporation of the solvent, demonstrating the desired homogeneous distribution of the cations in the materials. The use of complexing agents with hydroxyl groups was found to be important with respect to complexing and immobilisation of the cations during the sol-gel process. Phase-pure materials, avoiding crystallisation or segregation of undesirable components, could also be prepared without the formation of a polymer network during the sol-gel transition. Upon calcination, the gel decomposed and crystallised to nano-crystalline materials with the In_2O_3 cubic crystal structure. The decomposition and crystallisation was demonstrated to take place simultaneously. Formation of the metastable rhombohedral In_2O_3-polymorph was shown to be controlled by the choice of the organic additives.

The nano-crystalline powders prepared by the sol-gel process were used to investigate the solid state sintering of In_2O_3 and ITO with 5 cat% Sn with a particular focus on the mass transport mechanisms. Materials with a relative density higher than 95 % could be prepared from the phase-pure, nano-crystalline powders. The removal of agglomerates by ball-milling prior to the sintering was demonstrated to be vital for the final density. Surface diffusion leading to coarsening was demonstrated to be detrimental for the densification of both In_2O_3 and ITO at low temperatures, while densification was initially promoted by grain boundary diffusion and further by bulk diffusion at higher temperatures. SnO_2 doping was observed to inhibit sintering of ITO compared to In_2O_3 at intermediate temperatures. This was discussed with respect to the higher valence state of Sn^{4+} compared to In^{3+}, and the Sn-doping was shown to hinder grain boundary diffusion and grain growth. The vapour pressures of In and Sn sub-oxides were calculated

and demonstrated to cause evaporation-condensation at high sintering temperatures, while pore coarsening due to grain growth reduced the density at temperatures above 1450 °C.

Poly-crystalline ITO thin films were prepared, and the functional properties of the deposited films were characterised. The optical properties were excellent, with a high transmittance in the visible region and band gaps similar to reported values. The electrical properties were demonstrated to be significantly improved by increasing the heat treatment and annealing in a reducing atmosphere. The specific resistance of the ITO films was significantly lower than corresponding data reported for films prepared by similar sol-gel processes. The electrical performance was in good accord with the best reported values obtained by physical deposition techniques. In situ conductivity measurements demonstrated that oxidation of the films due to a change in the oxidation state of Sn, leading to a decrease in the conductivity, occurred even down to room temperature when the films were exposed to air after reduction. The thickness of the deposited layers could be controlled by optimising the parameters of the process.

The equilibrium phase composition and solid solubility of neodymium, europium and terbium in In_2O_3 and ITO at 1400 °C were determined. The solubility of the REEs in In_2O_3 was largely controlled by the size of the dopant, while when ITO was used as a host the solid solubility was reduced due to a strong tendency of the tin and REE co-dopants to form a pyrochlore $RE_2Sn_2O_7$ phase. Isothermal sections of the ternary phase diagrams at 1400 °C were constructed based on the findings. Phase-pure materials of In_2O_3 and ITO doped with REEs were successfully prepared in form of nano-crystalline powders and thin films. In this form the solubility limit for the REEs could be circumvented by synthesis of metastable materials. The effect of the REE-doping on the functional properties of the host was investigated. Neither the conductivity nor the transparency of ITO thin films was deteriorated by the REE-doping. The conductivity of bulk materials of REE-doped In_2O_3 was significantly reduced, even at low doping concentrations, due to a decrease in mobility. Finally, strong emissions at around 611 nm were observed for Eu-doped In_2O_3, demonstrating the possibility of obtaining photoluminescence in a TCO host material.

10. Outlook

Indium tin oxide is recognised as the TCO with the superior combination of optical and electrical properties. Tremendous efforts have been made to find an alternative to ITO due to the high price and limited abundance of indium. However, so far no alternative TCO material has been developed with equal properties to ITO. The forecast is therefore that ITO will retain a significant market share for many applications also in the years to come. Furthermore, there is also a continuous desire to find new deposition techniques in order to overcome some of the limitations related to physical deposition techniques, such as sputtering. In this regard, the developed sol-gel route is proposed to have some merit, as the properties of the thin films prepared by this simple and inexpensive process was found to be close to the best reported values for ITO.

The sol-gel process developed in this work has close resemblances with several other Pechini-related processes, which have been applied to prepare a whole range of different complex oxide materials. Some of the present findings related to the sol-gel chemistry may be of generic relevance for the synthesis of other oxide materials. It was demonstrated that the choice of complexing agent was very important, especially regarding the number and type of their functional groups. More specifically, it was observed that the presence of hydroxylic groups was important regarding the phase purity of the prepared materials. It was also shown that phase-pure materials could be synthesised even when a cross-linked polymer network was not formed, as long as the cations were immobilised by the complexing agents. Additionally, it was demonstrated that the formation of the rhombohedral In_2O_3 phase could be controlled by the choice of complexing agent. This phase is metastable and in some cases undesirable. However, the potential of this phase as a TCO material is not fully established, and the ability to control its formation could have some value.

The sol-gel process was shown to be very well suited for the synthesis of phase-pure nano-crystalline ITO powders with excellent sintering properties. The comprehensive sintering study performed in this work has contributed to improve the understanding of this complex, challenging, yet industrially important process. Furthermore, the synthesis of nano-crystalline ITO powders has recently received a lot of attention in the literature, due to the possibility of depositing thin films from slurries containing nano-crystalline ITO particles. This is attractive both regarding the possibility of readily patterning of thin films and for potential deposition on flexible substrates.

The present sol-gel process was demonstrated to prepare ITO thin films with very good functional properties. An increase in the heat treatment temperature and annealing in reducing atmospheres was shown to significantly improve the conductivity of the ITO thin films. While the latter effect can be readily explained by the established point defect chemistry of ITO, the cause of the prior effect is not fully understood. It could be related to larger grain size, better crystallinity in the film, better contact between the deposited layers in the film or the removal of inherent lattice strain. Furthermore, the cause of the initial inherent strain itself was not established. It was also proposed that the thickness of the films could be controlled by changing certain parameters in the process. However, thickness measurements were not performed on these films, and a direct quantification of the effect of the different parameters was therefore not possible. Further optimisations of the process regarding the conductivity of the films and the thickness of each deposited layer are proposed to be possible topics for further investigations.

It was observed that the conductivity of the ITO thin films decreased when the films were exposed to air after reduction. This was proposed to be related to an oxidation process, which correlates well with the established point defect chemistry of Sn-doped In_2O_3. However, it is remarkable that this process, which requires oxygen anion mobility in the thin films, is taking place at considerable rate even at ambient temperature. Further investigations to gain an improved understanding of the kinetics of the red-ox process, possibly relating the effect to the crystal structure of the material, is very interesting. Thin oxide films are used in a large variety of applications, and the red-ox process related to the electronic conductivity of the materials could have implications also outside of the TCO community. An ageing or relaxation phenomenon was also observed in the films, which improved the conductivity of the as-prepared ITO films during storage in air. This phenomenon was not understood and could also be relevant for thin films prepared by other wet chemical methods.

It was demonstrated that it is possible to obtain luminescence from a REE activator in a TCO host and that the functional properties of the host could be retained even with relatively high concentrations of REE doping. However, further work is clearly necessary in order to establish the potential of these doped ITO materials as optically active materials. Particularly a good understanding of the possible host sensitisation and the effect of the crystallite size of the host on the luminescence appears to be lacking in the literature. The suitability of the different possible REE activators in In_2O_3-based hosts also remains unclear. Strong emissions were observed for Eu-doped materials, but not for Nd- or Tb-doping, despite the strong absorptions in In_2O_3:Nd indicating that this activator could be optically active in this host.

Several other aspects regarding REE-doping of ITO were not fully investigated in this work and could be a basis for further studies. It was demonstrated that the bulk materials had stronger luminescence than the nano-crystalline powders. However, thin films were not investigated. The effect of using ITO as a host, compared to In_2O_3, on the luminescence was also not established. Furthermore, the conductivity of bulk REE-doped In_2O_3 materials was demonstrated to be significantly decreased relative to the In_2O_3 host reference, due to a decrease in mobility of charge carriers. It was not concluded regarding the cause of this effect, though it was proposed that a segregation of the dopants to grain boundaries could be a possible explanation. Concerning the conductivity of the materials, it could also be of fundamental interest to experiment with the oxidation state of terbium in order to control the conductivity of the material. Finally, a major motivation for investigating REE-doped ITO was to obtain a luminescent material with good conductivity. A possible way of utilising such a combination of properties could be by electroluminescence, i.e. luminescence that is activated by an electric field or a current passing through the material. The potential of these materials for electroluminescent applications should be further investigated.

References

1. T. J. Coutts, D. L. Young and X. N. Li, "Characterization of transparent conducting oxides." *Mrs Bulletin,* **25** 8 (2000) p.58-65.
2. K. L. Chopra, S. Major and D. K. Pandya, "Transparent conductors - A status review." *Thin Solid Films,* **102** 1 (1983) p.1-46.
3. D. S. Ginley and C. Bright, "Transparent conducting oxides." *Mrs Bulletin,* **25** 8 (2000) p.15-18.
4. B. G. Lewis and D. C. Paine, "Applications and processing of transparent conducting oxides." *Mrs Bulletin,* **25** 8 (2000) p.22-27.
5. P. P. Edwards, A. Porch, M. O. Jones, D. V. Morgan and R. M. Perks, "Basic materials physics of transparent conducting oxides." *Dalton Transactions,* 19 (2004) p.2995-3002.
6. I. Hamberg and C. G. Granqvist, "Evaporated Sn-doped In_2O_3 films - Basic optical properties and applications to energy-efficient windows." *Journal of Applied Physics,* **60** 11 (1986) p.R123-R159.
7. D. Ginley, H. Hosono and D. C. Paine, eds., "Handbook of transparent conductors." 1st ed. (2011), Springer: New York.
8. C. G. Granqvist and A. Hultaker, "Transparent and conducting ITO films: new developments and applications." *Thin Solid Films,* **411** 1 (2002) p.1-5.
9. C. G. Granqvist, A. Azens, A. Hjelm, L. Kullman, G. A. Niklasson, D. Ronnow, M. S. Mattsson, M. Veszelei and G. Vaivars, "Recent advances in electrochromics for smart windows applications." *Solar Energy,* **63** 4 (1998) p.199-216.
10. G. A. Niklasson and C. G. Granqvist, "Electrochromics for smart windows: thin films of tungsten oxide and nickel oxide, and devices based on these." *Journal of Materials Chemistry,* **17** 2 (2007) p.127-156.
11. E. Fortunato, D. Ginley, H. Hosono and D. C. Paine, "Transparent conducting oxides for photovoltaics." *Mrs Bulletin,* **32** 3 (2007) p.242-247.
12. R. B. H. Tahar, T. Ban, Y. Ohya and Y. Takahashi, "Tin doped indium oxide thin films: Electrical properties." *Journal of Applied Physics,* **83** 5 (1998) p.2631-2645.
13. G. B. Gonzalez, T. O. Mason, J. P. Quintana, O. Warschkow, D. E. Ellis, J. H. Hwang, J. P. Hodges and J. D. Jorgensen, "Defect structure studies of bulk and nano-indium-tin oxide." *Journal of Applied Physics,* **96** 7 (2004) p.3912-3920.
14. D. S. Hecht and R. B. Kaner, "Solution-processed transparent electrodes." *Mrs Bulletin,* **36** 10 (2011) p.749-755.
15. R. G. Gordon, "Criteria for choosing transparent conductors." *Mrs Bulletin,* **25** 8 (2000) p.52-57.
16. E. N. Dattoli and W. Lu, "ITO nanowires and nanoparticles for transparent films." *Mrs Bulletin,* **36** 10 (2011) p.782-788.
17. J. H. W. De Wit, "Structural aspects and defect chemistry in In_2O_3." *Journal of Solid State Chemistry,* **20** 2 (1977) p.143-148.

18. T. Minami, "New n-type transparent conducting oxides." *Mrs Bulletin,* **25** 8 (2000) p.38-44.
19. A. J. Freeman, K. R. Poeppelmeier, T. O. Mason, R. P. H. Chang and T. J. Marks, "Chemical and thin-film strategies for new transparent conducting oxides." *Mrs Bulletin,* **25** 8 (2000) p.45-51.
20. "The future of ITO: Transparent conductor and ITO replacement markets." (2008). NanoMarkets
21. Y. Shigesato, S. Takaki and T. Haranoh, "Electrical and structural properties of low resistivity tin-doped indium oxide-films." *Journal of Applied Physics,* **71** 7 (1992) p.3356-3364.
22. Y. Shigesato and D. C. Paine, "A microstructural study of low-resistivity tin-doped indium oxide prepared by DC magnetron sputtering." *Thin Solid Films,* **238** 1 (1994) p.44-50.
23. D. B. Fraser and H. D. Cook, "Highly conductive, transparent films of sputtered $In_{2-x}Sn_xO_{3-y}$." *Journal of the Electrochemical Society,* **119** 10 (1972) p.1368.
24. Y. Sawada, C. Kobayashi, S. Seki and H. Funakubo, "Highly-conducting indium-tin-oxide transparent films fabricated by spray CVD using ethanol solution of indium (III) chloride and tin (II) chloride." *Thin Solid Films,* **409** 1 (2002) p.46-50.
25. L. A. Ryabova, V. S. Salun and I. A. Serbinov, "Transparent conductive films of In_2O_3-Sn by the pyrolysis method." *Thin Solid Films,* **92** 4 (1982) p.327-332.
26. J. Kane, H. P. Schweizer and W. Kern, "Chemical vapor-deposition of transparent electrically conducting layers of indium oxide doped with tin." *Thin Solid Films,* **29** 1 (1975) p.155-163.
27. I. Hamberg, A. Hjortsberg and C. G. Granqvist, "High-quality transparent heat reflectors of reactively evaporated Indium Tin Oxide." *Applied Physics Letters,* **40** 5 (1982) p.362-364.
28. T. Ishida, H. Kobayashi and Y. Nakato, "Structures and properties of electron-beam-evaporated indium tin oxide-films as studied by X-ray photoelectron-spectroscopy and work-function measurements." *Journal of Applied Physics,* **73** 9 (1993) p.4344-4350.
29. M. Mizuhashi, "Electrical properties of vacuum-deposited indium oxide and indium tin oxide-films." *Thin Solid Films,* **70** 1 (1980) p.91-100.
30. H. Kim, C. M. Gilmore, A. Pique, J. S. Horwitz, H. Mattoussi, H. Murata, Z. H. Kafafi and D. B. Chrisey, "Electrical, optical, and structural properties of indium-tin-oxide thin films for organic light-emitting devices." *Journal of Applied Physics,* **86** 11 (1999) p.6451-6461.
31. C. Coutal, A. Azema and J. C. Roustan, "Fabrication and characterization of ITO thin films deposited by excimer laser evaporation." *Thin Solid Films,* **288** 1-2 (1996) p.248-253.
32. H. Kim, J. S. Horwitz, G. P. Kushto, Z. H. Kafafi and D. B. Chrisey, "Indium tin oxide thin films grown on flexible plastic substrates by pulsed-laser deposition for organic light-emitting diodes." *Applied Physics Letters,* **79** 3 (2001) p.284-286.

33. N. J. Arfsten, "Sol-gel derived transparent IR-reflecting ITO semiconductor coatings and future applications." *Journal of Non-Crystalline Solids,* **63** 1-2 (1984) p.243-249.
34. R. B. H. Tahar, T. Ban, Y. Ohya and Y. Takahashi, "Optical, structural, and electrical properties of indium oxide thin films prepared by the sol-gel method." *Journal of Applied Physics,* **82** 2 (1997) p.865-870.
35. D. Gallagher, F. Scanlan, R. Houriet, H. J. Mathieu and T. A. Ring, "Indium Tin Oxide thin-films by metal-organic decomposition." *Journal of Materials Research,* **8** 12 (1993) p.3135-3144.
36. K. Nomura, H. Ohta, A. Takagi, T. Kamiya, M. Hirano and H. Hosono, "Room-temperature fabrication of transparent flexible thin-film transistors using amorphous oxide semiconductors." *Nature,* **432** 7016 (2004) p.488-492.
37. Y. S. Liu, W. Q. Luo, H. M. Zhu and X. Y. Chen, "Optical spectroscopy of lanthanides doped in wide band-gap semiconductor nanocrystals." *Journal of Luminescence,* **131** 3 (2011) p.415-422.
38. C. Ronda, ed. "Luminescence: From theory to applications." ed. (2008), Wiley-VCH Verlag:
39. J. C. G. Bunzli and C. Piguet, "Taking advantage of luminescent lanthanide ions." *Chemical Society Reviews,* **34** 12 (2005) p.1048-1077.
40. G. S. Yi, H. C. Lu, S. Y. Zhao, G. Yue, W. J. Yang, D. P. Chen and L. H. Guo, "Synthesis, characterization, and biological application of size-controlled nanocrystalline $NaYF_4$: Yb,Er infrared-to-visible up-conversion phosphors." *Nano Letters,* **4** 11 (2004) p.2191-2196.
41. Y. L. Yu, D. Q. Chen, Y. S. Wang, P. Huang, F. Y. Weng and M. T. Niu, "Enhanced photoluminescence of Eu^{3+} induced by energy transfer from In_2O_3 nano-crystals embedded in glassy matrix." *Physical Chemistry Chemical Physics,* **11** 39 (2009) p.8774-8778.
42. J. Vela, B. S. Prall, P. Rastogi, D. J. Werder, J. L. Casson, D. J. Williams, V. I. Klimov and J. A. Hollingsworth, "Sensitization and protection of lanthanide ion emission in In_2O_3:Eu nanocrystal quantum dots." *Journal of Physical Chemistry C,* **112** 51 (2008) p.20246-20250.
43. Q. B. Xiao, Y. S. Liu, L. Q. Liu, R. F. Li, W. Q. Luo and X. Y. Chen, "Eu^{3+}-doped In_2O_3 nanophosphors: Electronic structure and optical characterization." *Journal of Physical Chemistry C,* **114** 20 (2010) p.9314-9321.
44. J. Kido and Y. Okamoto, "Organo lanthanide metal complexes for electroluminescent materials." *Chemical Reviews,* **102** 6 (2002) p.2357-2368.
45. Y. G. Choi, S. M. Yu and W. J. Chung, "Local structural environment and photoluminescence of Er^{3+} ions doped in indium tin oxide nanopowder." *Chemical Physics Letters,* **461** 4-6 (2008) p.290-293.
46. J. K. Kim and Y. G. Choi, "Eu-doped indium tin oxide thin films fabricated by sol-gel technique." *Thin Solid Films,* **517** 17 (2009) p.5084-5086.
47. D. P. Dutta, V. Sudarsan, P. Srinivasu, A. Vinu and A. K. Tyagi, "Indium oxide and europium/dysprosium doped indium oxide nanoparticles:

Sonochemical synthesis, characterization, and photoluminescence studies." *Journal of Physical Chemistry C,* **112** 17 (2008) p.6781-6785.
48. M. Marezio, "Refinement of crystal structure of In_2O_3 at 2 wavelengths." *Acta Crystallographica,* **20** (1966) p.723.
49. G. Adachi and N. Imanaka, "The binary rare earth oxides." *Chemical Reviews,* **98** 4 (1998) p.1479-1514.
50. D. Kaczmarek, J. Domaradzki, A. Borkowska, A. Podhorodecki, J. Misiewicz and K. Sieradzka, "Optical emission from Eu, Tb, Nd luminescence centers in TiO_2 prepared by magnetron sputtering." *Optica Applicata,* **37** 4 (2007) p.433-438.
51. K. Bädeker, "Concerning the electricity conductibility and the thermoelectric energy of several heavy metal bonds." *Annalen Der Physik,* **22** 4 (1907) p.749-766.
52. G. Helwig, "Elektrische leitfahigkeit und struktur aufgestaubter kadmiumoxydschichten." *Zeitschrift für physik,* **132** 5 (1952) p.621-642.
53. L. Holland and G. Siddall, "The properties of some reactively sputtered metal oxide films." *Vacuum,* **3** 4 (1953) p.375-391.
54. R. Groth and E. Kauer, "Thermal insulation of sodium lamps." *Philips Technical Review,* **26** 4-6 (1965) p.105.
55. R. Groth, "Untersuchungen an halbleitenden indiumoxydschichten." *Physica Status Solidi,* **14** 1 (1966) p.69.
56. A. J. Leenheer, J. D. Perkins, M. Van Hest, J. J. Berry, R. P. O'hayre and D. S. Ginley, "General mobility and carrier concentration relationship in transparent amorphous indium zinc oxide films." *Physical Review B,* **77** 11 (2008) p.5.
57. H. Kawazoe, M. Yasukawa, H. Hyodo, M. Kurita, H. Yanagi and H. Hosono, "P-type electrical conduction in transparent thin films of $CuAlO_2$." *Nature,* **389** 6654 (1997) p.939-942.
58. E. Burstein, "Anomalous optical absorption limit in InSb." *Physical Review,* **93** 3 (1954) p.632-633.
59. I. Hamberg, C. G. Granqvist, K. F. Berggren, B. E. Sernelius and L. Engstrom, "Band-gap widening in heavily Sn-doped In_2O_3." *Physical Review B,* **30** 6 (1984) p.3240-3249.
60. J. Robertson and B. Falabretti, "Electronic Structure of Transparent Conducting Oxides." Ch. 2 in "Handbook of Transparent Conductors." (2011), Springer: New York.
61. Y. Shigesato, "In-based TCOs." Ch. 5 in "Handbook of Transparent Conductors." (2011), Springer: New York.
62. S. P. Harvey, T. O. Mason, C. Korber and A. Klein, "Bulk defect chemistry and surface electronic behavior of Zn,Sn codoped In_2O_3 transparent conducting oxides." *Physical Chemistry Chemical Physics,* **11** 17 (2009) p.3099-3104.
63. N. Nadaud, N. Lequeux, M. Nanot, J. Jove and T. Roisnel, "Structural studies of tin-doped indium oxide (ITO) and In4Sn3O12." *Journal of Solid State Chemistry,* **135** 1 (1998) p.140-148.

64. G. B. Gonzalez, J. B. Cohen, J. H. Hwang, T. O. Mason, J. P. Hodges and J. D. Jorgensen, "Neutron diffraction study on the defect structure of indium-tin-oxide." *Journal of Applied Physics,* **89** 5 (2001) p.2550-2555.
65. R. D. Shannon, "New high-pressure phases having corundum structure." *Solid State Communications,* **4** 12 (1966) p.629.
66. A. N. Christensen, N. C. Broch, O. V. Heidenstam and Å. Nilsson, "Hydrothermal investigation of systems In_2O_3-H_2O-Na_2O and In_2O_3-D_2O-Na_2O. Crystal structure of rhombohedral In_2O_3 and of $In(OH)_3$." *Acta Chemica Scandinavica,* **21** 4 (1967) p.1046.
67. C. T. Prewitt, R. D. Shannon, D. B. Rogers and A. W. Sleight, "C rare earth oxide-corundum transition and crystal chemistry of oxides having corundum structure." *Inorganic Chemistry,* **8** 9 (1969) p.1985.
68. A. Gurlo, P. Kroll and R. Riedel, "Metastability of corundum-type In_2O_3." *Chemistry-a European Journal,* **14** 11 (2008) p.3306-3310.
69. Y. G. Park, K. H. Seo, J. H. Lee, J. J. Kim, S. H. Cho, C. J. O'conner and J. S. Lee, "Phase transformation behavior of nanocrystalline ITO powders during heat-treatment: Oxygen partial pressure effect." *Journal of Electroceramics,* **13** 1-3 (2004) p.851-855.
70. A. Walsh, C. R. A. Catlow, A. A. Sokol and S. M. Woodley, "Physical properties, intrinsic defects, and phase stability of indium sesquioxide." *Chemistry of Materials,* **21** 20 (2009) p.4962-4969.
71. L. A. Dunlop, A. Kursumovic and J. L. Macmanus-Driscoll, "Highly Conducting, Transparent Rhombic/Cubic Indium Tin Oxide Nanocomposite Thin Films." *Crystal Growth & Design,* **10** 4 (2010) p.1730-1735.
72. S. S. Farvid, N. Dave and P. V. Radovanovic, "Phase-controlled synthesis of colloidal In_2O_3 nanocrystals via size-structure correlation." *Chemistry of Materials,* **22** 1 (2010) p.9-11.
73. S. Z. Karazhanov, P. Ravindran, P. Vajeeston, A. Ulyashin, T. G. Finstad and H. Fjellvag, "Phase stability, electronic structure, and optical properties of indium oxide polytypes." *Physical Review B,* **76** 7 (2007) p.13.
74. Z. B. Zhuang, Q. Peng, J. F. Liu, X. Wang and Y. D. Li, "Indium hydroxides, oxyhydroxides, and oxides nanocrystals series." *Inorganic Chemistry,* **46** 13 (2007) p.5179-5187.
75. Y. F. Hao, G. W. Meng, C. H. Ye and L. D. Zhang, "Controlled synthesis of In_2O_3 octahedrons and nanowires." *Crystal Growth & Design,* **5** 4 (2005) p.1617-1621.
76. C. H. Lee, M. Kim, T. Kim, A. Kim, J. Paek, J. W. Lee, S. Y. Choi, K. Kim, J. B. Park and K. Lee, "Ambient pressure syntheses of size-controlled corundum-type In_2O_3 nanocubes." *Journal of the American Chemical Society,* **128** 29 (2006) p.9326-9327.
77. M. Sorescu, L. Diamandescu, D. Tarabasanu-Mihaila and V. S. Teodorescu, "Nanocrystalline rhombohedral In_2O_3 synthesized by hydrothermal and postannealing pathways." *Journal of Materials Science,* **39** 2 (2004) p.675-677.

78. W. J. Heward and D. J. Swenson, "Phase equilibria in the pseudo-binary In2O3-SnO2 system." *Journal of Materials Science,* **42** 17 (2007) p.7135-7140.
79. R. D. Shannon, "REVISED EFFECTIVE IONIC-RADII AND SYSTEMATIC STUDIES OF INTERATOMIC DISTANCES IN HALIDES AND CHALCOGENIDES." *Acta Crystallographica Section A,* **32** SEP1 (1976) p.751-767.
80. G. B. Gonzalez, T. O. Mason, J. S. Okasinski, T. Buslaps and V. Honkimaki, "Determination of the Solubility of Tin in Indium Oxide Using In Situ and Ex Situ X-Ray Diffraction." *Journal of the American Ceramic Society,* **95** 2 (2012) p.809-815.
81. J. L. Bates, C. W. Griffin, D. D. Marchant and J. E. Garnier, "Electrical conductivity, Seebeck coefficient and structure of In_2O_3-SnO_2." *American Ceramic Society Bulletin,* **65** 4 (1986) p.673-678.
82. G. B. Gonzalez, J. S. Okasinski, T. O. Mason, T. Buslaps and V. Honkimaeki, "In situ studies on the kinetics of formation and crystal structure of $In_4Sn_3O_{12}$ using high-energy X-ray diffraction." *Journal of Applied Physics,* **104** 4 (2008)
83. T. Minami, Y. Takeda, S. Takata and T. Kakumu, "Preparation of transparent conducting $In_4Sn_3O_{12}$ thin films by DC magnetron sputtering." *Thin Solid Films,* **308** (1997) p.13-18.
84. G. Frank and H. Kostlin, "Electrical properties and defect model of tin-doped indium oxide layers." *Applied Physics a-Materials Science & Processing,* **27** 4 (1982) p.197-206.
85. O. Warschkow, D. E. Ellis, G. B. Gonzalez and T. O. Mason, "Defect structures of tin-doped indium oxide." *Journal of the American Ceramic Society,* **86** 10 (2003) p.1700-1706.
86. O. Warschkow, D. E. Ellis, G. B. Gonzalez and T. O. Mason, "Defect cluster aggregation and nonreducibility in tin-doped indium oxide." *Journal of the American Ceramic Society,* **86** 10 (2003) p.1707-1711.
87. J. H. Hwang, D. D. Edwards, D. R. Kammler and T. O. Mason, "Point defects and electrical properties of Sn-doped In-based transparent conducting oxides." *Solid State Ionics,* **129** 1-4 (2000) p.135-144.
88. M. J. H. W. De Wit, P. F. Elbers and M. Laheij, "Grain growth and sintering of In_2O_3." *Science of Ceramics, 9, Proc,* **9** (1977) p.143.
89. J. H. W. De Wit, "Electrical properties of In_2O_3." *Journal of Solid State Chemistry,* **8** 2 (1973) p.142-149.
90. J. H. W. De Wit, "High-temperature behaviour of In_2O_3." *Journal of Solid State Chemistry,* **13** 3 (1975) p.192-200.
91. J. H. W. Dewit, "STRUCTURAL ASPECTS AND DEFECT CHEMISTRY IN IN2O3." *Journal of Solid State Chemistry,* **20** 2 (1977) p.143-148.
92. P. Agoston, P. Erhart, A. Klein and K. Albe, "Geometry, electronic structure and thermodynamic stability of intrinsic point defects in indium oxide." *Journal of Physics-Condensed Matter,* **21** 45 (2009) p.11.
93. J. R. Bellingham, A. P. Mackenzie and W. A. Phillips, "Precise measurements of oxygen-content - Oxygen vacancies in transparent

conducting indium oxide-films." *Applied Physics Letters,* **58** 22 (1991) p.2506-2508.

94. C. Warmsingh, Y. Yoshida, D. W. Readey, C. W. Teplin, J. D. Perkins, P. A. Parilla, L. M. Gedvilas, B. M. Keyes and D. S. Ginley, "High-mobility transparent conducting Mo-doped In_2O_3 thin films by pulsed laser deposition." *Journal of Applied Physics,* **95** 7 (2004) p.3831-3833.
95. Y. Meng, X. L. Yang, H. X. Chen, J. Shen, Y. M. Jiang, Z. J. Zhang and Z. Y. Hua, "A new transparent conductive thin film In_2O_3 : Mo." *Thin Solid Films,* **394** 1-2 (2001) p.219-223.
96. H. Kim, J. S. Horwitz, G. P. Kushto, S. B. Qadri, Z. H. Kafafi and D. B. Chrisey, "Transparent conducting Zr-doped In_2O_3 thin films for organic light-emitting diodes." *Applied Physics Letters,* **78** 8 (2001) p.1050-1052.
97. J. N. Avaritsiotis and R. P. Howson, "Composition and conductivity of fluorine-doped conducting indium oxide films prepared by reactive ion plating." *Thin Solid Films,* **77** 4 (1981) p.351-357.
98. N. Yamada, I. Yasui, Y. Shigesato, H. L. Li, Y. Ujihira and K. Nomura, "Donor compensation and carrier-transport mechanisms in tin-doped In_2O_3 films studied by means of conversion electron Sn-119 Mossbauer spectroscopy and Hall effect measurements." *Japanese Journal of Applied Physics Part 1-Regular Papers Short Notes & Review Papers,* **39** 7A (2000) p.4158-4163.
99. H. Kostlin, R. Jost and W. Lems, "Optical and electrical properties of doped In_2O_3 films." *Physica Status Solidi a-Applied Research,* **29** 1 (1975) p.87-93.
100. N. Yamada, Y. Shigesato, I. Yasui, H. Li, Y. Ujihira and K. Nomura, "Estimation of chemical states and carrier density of Sn-doped In_2O_3 (ITO) by Mossbauer spectrometry." *Hyperfine Interactions,* **112** 1-4 (1998) p.213-216.
101. R. Chwang, B. J. Smith and C. R. Crowell, "Contact size effects on Van der Pauw method for resistivity and Hall-coefficient measurement." *Solid-State Electronics,* **17** 12 (1974) p.1217-1227.
102. P. Agoston, C. Korber, A. Klein, M. J. Puska, R. M. Nieminen and K. Albe, "Limits for n-type doping in In_2O_3 and SnO_2: A theoretical approach by first-principles calculations using hybrid-functional methodology." *Journal of Applied Physics,* **108** 5 (2010) p.6.
103. S. B. Adler, "Chemical expansivity of electrochemical ceramics." *Journal of the American Ceramic Society,* **84** 9 (2001) p.2117-2119.
104. X. Y. Chen, J. S. Yu and S. B. Adler, "Thermal and chemical expansion of Sr-doped lanthanum cobalt oxide ($La_{1-x}Sr_xCoO_{3-delta}$)." *Chemistry of Materials,* **17** 17 (2005) p.4537-4546.
105. A. Atkinson, "Chemically-induced stresses in gadolinium-doped ceria solid oxide fuel cell electrolytes." *Solid State Ionics,* **95** 3-4 (1997) p.249-258.
106. R. L. Weiher, "Electrical properties of single crystals of indium oxide." *Journal of Applied Physics,* **33** 9 (1962) p.2834.
107. J. C. C. Fan and J. B. Goodenough, "X-ray photoemission spectroscopy studies of Sn-doped indium-oxide films." *Journal of Applied Physics,* **48** 8 (1977) p.3524-3531.

108. H. Odaka, S. Iwata, N. Taga, S. Ohnishi, Y. Kaneta and Y. Shigesato, "Study on electronic structure and optoelectronic properties of indium oxide by first-principles calculations." *Japanese Journal of Applied Physics Part 1-Regular Papers Short Notes & Review Papers,* **36** 9A (1997) p.5551-5554.
109. Y. M. Mi, H. Odaka and S. Iwata, "Electronic structures and optical properties of ZnO, SnO_2 and In_2O_3." *Japanese Journal of Applied Physics Part 1-Regular Papers Short Notes & Review Papers,* **38** 6A (1999) p.3453-3458.
110. H. Odaka, Y. Shigesato, T. Murakami and S. Iwata, "Electronic structure analyses of Sn-doped In_2O_3." *Japanese Journal of Applied Physics Part 1-Regular Papers Short Notes & Review Papers,* **40** 5A (2001) p.3231-3235.
111. O. N. Mryasov and A. J. Freeman, "Electronic band structure of indium tin oxide and criteria for transparent conducting behavior." *Physical Review B,* **64** 23 (2001)
112. V. Christou, M. Etchells, O. Renault, P. J. Dobson, O. V. Salata, G. Beamson and R. G. Egdell, "High resolution x-ray photoemission study of plasma oxidation of indium-tin-oxide thin film surfaces." *Journal of Applied Physics,* **88** 9 (2000) p.5180-5187.
113. A. Klein, "Electronic properties of In_2O_3 surfaces." *Applied Physics Letters,* **77** 13 (2000) p.2009-2011.
114. H. Kawazoe, H. Yanagi, K. Ueda and H. Hosono, "Transparent p-type conducting oxides: Design and fabrication of p-n heterojunctions." *Mrs Bulletin,* **25** 8 (2000) p.28-36.
115. P. Erhart, K. Albe and A. Klein, "First-principles study of intrinsic point defects in ZnO: Role of band structure, volume relaxation, and finite-size effects." *Physical Review B,* **73** 20 (2006)
116. I. N. Yakovkin and P. A. Dowben, "The problem of the band gap in LDA calculations." *Surface Review and Letters,* **14** 3 (2007) p.481-487.
117. P. Agoston, K. Albe, R. M. Nieminen and M. J. Puska, "Intrinsic n-Type Behavior in Transparent Conducting Oxides: A Comparative Hybrid-Functional Study of In_2O_3, SnO_2, and ZnO." *Physical Review Letters,* **103** 24 (2009) p.4.
118. J. H. W. Dewit, G. Vanunen and M. Lahey, "Electron-concentration and mobility in In_2O_3." *Journal of Physics and Chemistry of Solids,* **38** 8 (1977) p.819-824.
119. S. Lany and A. Zunger, "Comment on "Intrinsic n-type Behavior in Transparent Conducting Oxides: A Comparative Hybrid-Functional Study of In_2O_3, SnO_2, and ZnO"." *Physical Review Letters,* **106** 6 (2011) p.1.
120. P. Agoston, K. Albe, R. M. Nieminen and M. J. Puska, "Comment on "Intrinsic n-type Behavior in Transparent Conducting Oxides: A Comparative Hybrid-Functional Study of In_2O_3, SnO_2, and ZnO" Reply." *Physical Review Letters,* **106** 6 (2011) p.1.
121. R. L. Weiher and R. P. Ley, "Optical properties of indium oxide." *Journal of Applied Physics,* **37** 1 (1966) p.299.

122. P. A. Cox, W. R. Flavell and R. G. Egdell, "Solid-state and surface chemistry of Sn-doped In_2O_3 ceramics." *Journal of Solid State Chemistry,* **68** 2 (1987) p.340-350.
123. A. Bourlange, D. J. Payne, R. G. Egdell, J. S. Foord, P. P. Edwards, M. O. Jones, A. Schertel, P. J. Dobson and J. L. Hutchison, "Growth of In_2O_3 (100) on Y-stabilized ZrO_2 (100) by O-plasma assisted molecular beam epitaxy." *Applied Physics Letters,* **92** 9 (2008) p.3.
124. L. F. J. Piper, A. Demasi, S. W. Cho, K. E. Smith, F. Fuchs, F. Bechstedt, C. Korber, A. Klein, D. J. Payne and R. G. Egdell, "Electronic structure of In_2O_3 from resonant x-ray emission spectroscopy." *Applied Physics Letters,* **94** 2 (2009) p.3.
125. P. Erhart, A. Klein, R. G. Egdell and K. Albe, "Band structure of indium oxide: Indirect versus direct band gap." *Physical Review B,* **75** 15 (2007) p.4.
126. A. Walsh, J. L. F. Da Silva, S. H. Wei, C. Korber, A. Klein, L. F. J. Piper, A. Demasi, K. E. Smith, G. Panaccione, P. Torelli, D. J. Payne, A. Bourlange and R. G. Egdell, "Nature of the band gap of In_2O_3 revealed by first-principles calculations and x-ray spectroscopy." *Physical Review Letters,* **100** 16 (2008) p.4.
127. K. Seshan, ed. "Handbook of thin-film deposition processes and techniques - Principles, methods, equipments and applications." 2nd ed. (2002), Noyes Publications: New York.
128. P. Sigmund, "Theory of sputtering. 1. Sputtering yield of amorphous and polycrystalline targets." *Physical Review,* **184** 2 (1969) p.383.
129. B. L. Gehman, S. Jonsson, T. Rudolph, M. Scherer, M. Weigert and R. Werner, "Influence of manufacturing process of Indium Tin Oxide sputtering targets on sputtering behavior." *Thin Solid Films,* **220** 1-2 (1992) p.333-336.
130. G. Falk, "Sintering of Transparent Conducting Oxides - From oxide ceramic powder to advanced optoelectronic devices." Ch. 26 in "Sintering of ceramics - New emerging techniques." (2012), InTech:
131. Schlott M, M. Kutzner, B. L. Gehman, N. Reger and F. J. Stadermann, "Nodule formation of indium-oxide tin-oxide sputtering targets." in *SID International Symposium, Santa Anna, CA, USA*, (1996).
132. C. J. Brinker, A. J. Hurd, P. R. Schunk, G. C. Frye and C. S. Ashley, "Review of sol-gel thin-film formation." in *6th International workshop on glasses and ceramics from gels*, Seville, Spain (1992).
133. C. J. Brinker, G. C. Frye, A. J. Hurd and C. S. Ashley, "Fundamentals of sol-gel dip coating." *Thin Solid Films,* **201** 1 (1991) p.97-108.
134. C. Legnani, S. A. M. Lima, H. H. S. Oliveira, W. G. Quirino, R. Machado, R. M. B. Santos, M. R. Davolos, C. A. Achete and M. Cremona, "Indium tin oxide films prepared via wet chemical route." *Thin Solid Films,* **516** 2-4 (2007) p.193-197.
135. O. Yamamoto, T. Sasamoto and M. Inagaki, "Indium tin oxide thin-films prepared by thermal decomposition of ethylene-glycol solution." *Journal of Materials Research,* **7** 9 (1992) p.2488-2491.

136. C. C. Perry, J. K. Mcgiveron and P. G. Harrison, "Aqueous sol-gel routes to conducting films of indium oxide and indium-tin-oxide." Ch. in "Sol-Gel Optics V." (2000), Spie-Int Soc Optical Engineering: Bellingham.
137. D. M. Mattox, "Sol-gel derived, air-baked indium and tin oxide-films." *Thin Solid Films,* **204** 1 (1991) p.25-32.
138. Q. Wei, H. X. Zheng and Y. H. Huang, "Direct patterning ITO transparent conductive coatings." *Solar Energy Materials and Solar Cells,* **68** 3-4 (2001) p.383-390.
139. Y. Aksu and M. Driess, "A Low-Temperature Molecular Approach to Highly Conductive Tin-Rich Indium Tin Oxide Thin Films with Durable Electro-Optical Performance." *Angewandte Chemie-International Edition,* **48** 42 (2009) p.7778-7782.
140. J. C. Manifacier, J. P. Fillard and J. M. Bind, "Deposition of In_2O_3-SnO_2 layers on glass substrate using a spraying method." *Thin Solid Films,* **77** 1-3 (1981) p.67-80.
141. K. S. Ramaiah, V. S. Raja, A. K. Bhatnagar, R. D. Tomlinson, R. D. Pilkington, A. E. Hill, S. J. Chang, Y. K. Su and F. S. Juang, "Optical, structural and electrical properties of tin doped indium oxide thin films prepared by spray-pyrolysis technique." *Semiconductor Science and Technology,* **15** 7 (2000) p.676-683.
142. J. Yu, S. Kang, J. Kim, J. Han, J. Yoo, S. Lee and Z. Ahn, "Nano-sized indium oxide powder synthesized by spray pyrolysis process." *Materials Transactions,* **47** 7 (2006) p.1838-1846.
143. S. M. Rozati and T. Ganj, "Transparent conductive Sn-doped indium oxide thin films deposited by spray pyrolysis technique." *Renewable Energy,* **29** 10 (2004) p.1671-1676.
144. A. M. E. Raj, K. C. Lalithambika, V. S. Vidhya, G. Rajagopal, A. Thayumanavan, M. Jayachandran and C. Sanjeeviraja, "Growth mechanism and optoelectronic properties of nanocrystalline In_2O_3 films prepared by chemical spray pyrolysis of metal-organic precursor." *Physica B-Condensed Matter,* **403** 4 (2008) p.544-554.
145. S. Kundu and P. K. Biswas, "Synthesis and photoluminescence property of nanostructured sol-gel indium tin oxide film on glass." *Chemical Physics Letters,* **414** 1-3 (2005) p.107-110.
146. J. Liu, E. Radlein and G. H. Frischat, "Preparation, nanostructure and properties of indium tin oxide (ITO) films on glass substrates. Part 1. Preparation and nanostructure." *Physics and Chemistry of Glasses,* **40** 5 (1999) p.277-281.
147. T. Maruyama and A. Kojima, "Indium-tin oxide thin-films prepared by thermal decomposition of metallic complex salts." *Japanese Journal of Applied Physics Part 2-Letters,* **27** 10 (1988) p.L1829-L1831.
148. K. Nishio, T. Sei and T. Tsuchiya, "Preparation and electrical properties of ITO thin films by dip-coating process." *Journal of Materials Science,* **31** 7 (1996) p.1761-1766.
149. T. Kanbara, M. Nagasaka and T. Yamamoto, "Preparation of electrically conducting indium tin oxide thin-films by heat-treatment of mixed-metal

hydroxide dispersion containing polymer binder." *Chemistry of Materials,* **2** 6 (1990) p.643-645.
150. M. J. Alam and D. C. Cameron, "Optical and electrical properties of transparent conductive ITO thin films deposited by sol-gel process." *Thin Solid Films,* **377** (2000) p.455-459.
151. Y. Takahashi, S. Okada, R. B. H. Tahar, K. Nakano, T. Ban and Y. Ohya, "Dip-coating of ITO films." *Journal of Non-Crystalline Solids,* **218** (1997) p.129-134.
152. X. A. Zhang, W. J. Wu, T. Tian, Y. H. Man and H. F. Wang, "Deposition of transparent conductive mesoporous indium tin oxide thin films by a dip coating process." *Materials Research Bulletin,* **43** 4 (2008) p.1016-1022.
153. K. Daoudi, B. Canut, M. G. Blanchin, C. S. Sandu, V. S. Teodorescu and J. A. Roger, "Densification of In_2O_3:Sn multilayered films elaborated by the dip-coating sol-gel route." *Thin Solid Films,* **445** 1 (2003) p.20-25.
154. S. S. Kim, S. Y. Choi, C. G. Park and H. W. Jin, "Transparent conductive ITO thin films through the sol-gel process using metal salts." *Thin Solid Films,* **347** 1-2 (1999) p.155-160.
155. M. Kakihana and M. Yoshimura, "Synthesis and characteristics of complex multicomponent oxides prepared by polymer complex method." *Bulletin of the Chemical Society of Japan,* **72** 7 (1999) p.1427-1443.
156. H. Tomonaga and T. Morimoto, "Indium-tin oxide coatings via chemical solution deposition." *Thin Solid Films,* **392** 2 (2001) p.243-248.
157. S. R. Ramanan, "Dip coated ITO thin-films through sol-gel process using metal salts." *Thin Solid Films,* **389** 1-2 (2001) p.207-212.
158. H. Dislich, P. Hinz, N. J. Arfsten and E. Hussmann, "Sol-gel yesterday, today and tomorrow." *Glastechnische Berichte-Glass Science and Technology,* **62** 2 (1989) p.46-51.
159. H. Dislich, "Glassy and crystalline systems from gels - Chemical basis and technical application." *Journal of Non-Crystalline Solids,* **57** 3 (1983) p.371-388.
160. M. Toki and M. Aizawa, "Sol-gel formation of ITO thin film from a sol including ITO powder." *Journal of Sol-Gel Science and Technology,* **8** 1-3 (1997) p.717-720.
161. D. Segal, "Chemical synthesis of ceramic materials." *Journal of Materials Chemistry,* **7** 8 (1997) p.1297-1305.
162. J. H. Ba, D. Fattakhova-Rohlfing, A. Feldhoff, T. Brezesinski, I. Djerdj, M. Wark and M. Niederberger, "Nonaqueous synthesis of uniform indium tin oxide nanocrystals and their electrical conductivity in dependence of the tin oxide concentration." *Chemistry of Materials,* **18** (2006) p.2848-2854.
163. M. G. Kim, M. G. Kanatzidis, A. Facchetti and T. J. Marks, "Low-temperature fabrication of high-performance metal oxide thin-film electronics via combustion processing." *Nature Materials,* **10** 5 (2011) p.382-388.
164. M. J. Alam and D. C. Cameron, "Investigation of annealing effects on sol-gel deposited indium tin oxide thin films in different atmospheres." *Thin Solid Films,* **420** (2002) p.76-82.

165. M. Epifani, R. Diaz, J. Arbiol, P. Siciliano and J. R. Morante, "Solution synthesis of thin films in the SnO_2-In_2O_3 system: A case study of the mixing of sol-gel and metal-organic solution processes." *Chemistry of Materials,* **18** 3 (2006) p.840-846.
166. T. Furusaki, K. Kodaira, M. Yamamoto, S. Shimada and T. Matsushita, "Preparation and properties of tin-doped indium oxide thin-films by thermal-decomposition of organometallic compounds." *Materials Research Bulletin,* **21** 7 (1986) p.803-806.
167. T. Furusaki, J. Takahashi and K. Kodaira, "Preparation of ITO thin-films by sol-gel method." *Nippon Seramikkusu Kyokai Gakujutsu Ronbunshi-Journal of the Ceramic Society of Japan,* **102** 2 (1994) p.200-205.
168. C. C. Addison and W. B. Simpsom, "Tin(IV) nitrate - Relation between structure and reactivity of metal nitrates." *Journal of the Chemical Society,* JAN (1965) p.598.
169. J. Donaldson and W. Moser, "Basic tin(II) nitrate." *Journal of the Chemical Society,* MAY (1961) p.1996.
170. M. Pechini, "Method of preparing lead and alkaline earth titanates and niobates and coating method using the same to form a capacitor." US Patent 3330697, 11th July (1967).
171. J. Lee, S. Lee, G. L. Li, M. A. Petruska, D. C. Paine and S. H. Sun, "A facile solution-phase approach to transparent and conducting ITO nanocrystal assemblies." *Journal of the American Chemical Society,* **134** 32 (2012) p.13410-13414.
172. K. Im, K. Cho, J. Kim and S. Kim, "Transparent heaters based on solution-processed indium tin oxide nanoparticles." *Thin Solid Films,* **518** 14 (2010) p.3960-3963.
173. G. Buhler, D. Tholmann and C. Feldmann, "One-pot synthesis of highly conductive indium tin oxide nanocrystals." *Advanced Materials,* **19** 17 (2007) p.2224.
174. N. Al-Dahoudi and M. A. Aegerter, "Comparative study of transparent conductive In_2O_3 : Sn (ITO) coatings made using a sol and a nanoparticle suspension." *Thin Solid Films,* **502** 1-2 (2006) p.193-197.
175. C. Goebbert, R. Nonninger, M. A. Aegerter and H. Schmidt, "Wet chemical deposition of ATO and ITO coatings using crystalline nanoparticles redispersable in solutions." *Thin Solid Films,* **351** 1-2 (1999) p.79-84.
176. J. Ederth, A. Hultaker, P. Heszler, G. A. Niklasson, C. G. Granqvist, A. Van Doorn, C. Van Haag, M. J. Jongerius and D. Burgard, "Electrical and optical properties of thin films prepared by spin coating a dispersion of nano-sized tin-doped indium oxide particles." *Smart Materials & Structures,* **11** 5 (2002) p.675-678.
177. R. A. Gilstrap, C. J. Capozzi, C. G. Carson, R. A. Gerhardt and C. J. Summers, "Synthesis of a nonagglomerated Indium Tin Oxide nanoparticle dispersion." *Advanced Materials,* **20** 21 (2008) p.4163.
178. T. Ogi, F. Iskandar, Y. Itoh and K. Okuyama, "Characterization of dip-coated ITO films derived from nanoparticles synthesized by low-pressure

spray pyrolysis." *Journal of Nanoparticle Research,* **8** 3-4 (2006) p.343-350.
179. M. Mahajeri, A. Schneider, M. Baum, T. Rechtenwald, M. Voigt, M. Schmidt and W. Peukert, "Production of dispersions with small particle size from commercial indium tin oxide powder for the deposition of highly conductive and transparent films." *Thin Solid Films,* **520** 17 (2012) p.5741-5745.
180. V. Zardetto, T. M. Brown, A. Reale and A. Di Carlo, "Substrates for flexible electronics: A practical investigation on the electrical, film flexibility, optical, temperature, and solvent resistance properties." *Journal of Polymer Science Part B-Polymer Physics,* **49** 9 (2011) p.638-648.
181. H. Hosono, "Transparent amorphous oxide semiconductors for flexible electronics." Ch. 13 in "Handbook of Transparent Conductors." (2011), Springer: New York.
182. J. Ederth, P. Johnsson, G. A. Niklasson, A. Hoel, A. Hultaker, P. Heszler, C. G. Granqvist, A. R. Van Doorn, M. J. Jongerius and D. Burgard, "Electrical and optical properties of thin films consisting of tin-doped indium oxide nanoparticles." *Physical Review B,* **68** 15 (2003) p.10.
183. J. Ederth, A. Hultaker, G. A. Niklasson, P. Heszler, A. R. Van Doorn, M. J. Jongerius, D. Burgard and C. G. Granqvist, "Thin porous indium tin oxide nanoparticle films: effects of annealing in vacuum and air." *Applied Physics a-Materials Science & Processing,* **81** 7 (2005) p.1363-1368.
184. I. J. Mccolm and N. J. Clark, "Forming, Shaping and Working of High-Performance Ceramics." 1st ed. (1988), Blackie: Glasgow.
185. R. M. German, "Sintering Theory and Practice." 1st ed. (1996), John Wiley & sons: New York.
186. D. W. Richerson, "Modern ceramic engineering." 3rd ed. (2006), Taylor & Francis:
187. K. Utsumi, O. Matsunaga and T. Takahata, "Low resistivity ITO film prepared using the ultra high density ITO target." *Thin Solid Films,* **334** 1-2 (1998) p.30-34.
188. R. K. Bordia and G. W. Scherer, "On constrained sintering: 1. Constitutive model for a sintering body." *Acta Metallurgica,* **36** 9 (1988) p.2393-2397.
189. T. Vojnovich and R. J. Bratton, "Impurity effects on sintering and electrical resistivity of indium oxide." *American Ceramic Society Bulletin,* **54** 2 (1975) p.216-217.
190. N. Nadaud, M. Nanot and P. Boch, "Sintering and electrical properties of titania-containing and zirconia-containing In_2O_3-SnO_2 (ITO) ceramics." *Journal of the American Ceramic Society,* **77** 3 (1994) p.843-846.
191. B. C. Kim, J. H. Lee, J. J. Kim, H. Y. Lee and J. S. Lee, "Densification of nanocrystalline ITO powders in fast firing: Effect of specimen mass and sintering atmosphere." *Materials Research Bulletin,* **40** 2 (2005) p.395-404.
192. B. C. Kim, J. H. Lee and J. J. Kim, "Effect of forming pressure on densification behavior of nanocrystalline ITO powder." *Journal of the European Ceramic Society,* **27** 2-3 (2007) p.807-812.

193. B. C. Kim, S. M. Kim, J. H. Lee and J. J. Kim, "Effect of phase transformation on the densification of coprecipitated nanocrystalline indium tin oxide powders." *Journal of the American Ceramic Society,* **85** 8 (2002) p.2083-2088.
194. S. M. Kim, K. H. Seo, J. H. Lee, J. J. Kim, H. Y. Lee and J. S. Lee, "Preparation and sintering of nanocrystalline ITO powders with different SnO2 content." *Journal of the European Ceramic Society,* **26** 1-2 (2006) p.73-80.
195. B. C. Kim, J. H. Lee, J. J. Kim and T. Ikegami, "Rapid rate sintering of nanocrystalline indium tin oxide ceramics: particle size effect." *Materials Letters,* **52** 1-2 (2002) p.114-119.
196. S. M. Kim, J. H. Lee and J. J. Kim, "Reaction-sintering behavior of nanocrystalline indium tin oxide with varying SnO2 content and particle size." *Scripta Materialia,* **56** 4 (2007) p.293-296.
197. C. P. Udawatte and K. Yanagisawa, "Sintering of additive free hydrothermally derived indium tin oxide powders in air." *Journal of Solid State Chemistry,* **154** 2 (2000) p.444-450.
198. X. H. Li, X. J. Xu, X. Yin, C. Z. Li and J. R. Zhang, "A sol-gel method to synthesize indium tin oxide nanoparticles." *Particuology,* **9** 5 (2011) p.471-474.
199. N. Nadaud and P. Boch, "Influence of TiO_2 additives on the microstructure of In_2O_3 ceramics." *Ceramics International,* **22** 3 (1996) p.207-209.
200. N. Nadaud, D. Y. Kim and P. Boch, "Titania as a sintering additive in indium oxide ceramics." *Journal of the American Ceramic Society,* **80** 5 (1997) p.1208-1212.
201. M. Suzuki, M. Muraoka, Y. Sawada and J. Matsushita, "Sintering of indium-tin-oxide with vanadium oxide additive." *Materials Science and Engineering B-Solid State Materials for Advanced Technology,* **54** 1-2 (1998) p.46-50.
202. M. Muraoka, M. Suzuki, Y. Sawada and J. Matsushita, "Sintering of tin-doped indium oxide (Indium-Tin-Oxide, ITO) with Bi_2O_3 additive." *Journal of Materials Science,* **33** 23 (1998) p.5621-5624.
203. E. Medvedovski, N. Alvarez, O. Yankov and M. K. Olsson, "Advanced indium-tin oxide ceramics for sputtering targets." *Ceramics International,* **34** 5 (2008) p.1173-1182.
204. G. S. Zhu, Z. P. Yang, L. Zhi, H. J. Yang, H. R. Xu and A. B. Yu, "Preparation and sintering behavior of the tin-doped indium oxide nanopowders." *Journal of the American Ceramic Society,* **93** 9 (2010) p.2511-2514.
205. E. N. Harvey, "A history of luminescence - From the earliest times until 1900." 1st ed. (1957), The American Philosophical Society: Philadelphia.
206. A. H. Kitai, ed. "Solid state luminescense - Theory, materials and devices." ed. (1993), Chapman & Hall: London.
207. A. J. Kenyon, "Recent developments in rare-earth doped materials for optoelectronics." *Progress in Quantum Electronics,* **26** 4-5 (2002) p.225-284.

208. F. Wang and X. G. Liu, "Recent advances in the chemistry of lanthanide-doped upconversion nanocrystals." *Chemical Society Reviews,* **38** 4 (2009) p.976-989.
209. R. Kudrawiec, A. Podhorodecki, N. Mirowska, J. Misiewicz, I. Molchan, N. V. Gaponenko, A. A. Lutich and S. V. Gaponenko, "Photoluminescence investigation of europium-doped alumina, titania and indium sol-gel-derived films in porous anodic alumina." *Materials Science and Engineering B-Solid State Materials for Advanced Technology,* **105** 1-3 (2003) p.53-56.
210. Y. S. Liu, W. Q. Luo, R. F. Li, H. M. Zhu and X. Y. Chen, "Near-infrared luminescence of Nd^{3+} and Tm^{3+} ions doped ZnO nanocrystals." *Optics Express,* **17** 12 (2009) p.9748-9753.
211. A. S. Pereira, M. Peres, M. J. Soares, E. Alves, A. Neves, T. Monteiro and T. Trindade, "Synthesis, surface modification and optical properties of Tb3+-doped ZnO nanocrystals." *Nanotechnology,* **17** 3 (2006) p.834-839.
212. Y. P. Du, Y. W. Zhang, L. D. Sun and C. H. Yan, "Efficient energy transfer in monodisperse Eu-doped ZnO nanocrystals synthesized from metal acetylacetonates in high-boiling solvents." *Journal of Physical Chemistry C,* **112** 32 (2008) p.12234-12241.
213. J. Bang, H. Yang and P. H. Holloway, "Enhanced luminescence of SiO_2 : Eu^{3+} by energy transfer from ZnO nanoparticles." *Journal of Chemical Physics,* **123** 8 (2005) p.5.
214. Y. S. Liu, W. Q. Luo, R. F. Li, G. K. Liu, M. R. Antonio and X. Y. Chen, "Optical spectroscopy of Eu^{3+} doped ZnO nanocrystals." *Journal of Physical Chemistry C,* **112** 3 (2008) p.686-694.
215. W. Q. Luo, R. F. Li, G. K. Liu, M. R. Antonio and X. Y. Chen, "Evidence of trivalent europium incorporated in anatase TiO_2 nanocrystals with multiple sites." *Journal of Physical Chemistry C,* **112** 28 (2008) p.10370-10377.
216. J. B. Yin, L. Q. Xiang and X. P. Zhao, "Monodisperse spherical mesoporous Eu-doped TiO_2 phosphor particles and the luminescence properties." *Applied Physics Letters,* **90** 11 (2007) p.3.
217. W. Q. Luo, R. F. Li and X. Y. Chen, "Host-sensitized luminescence of Nd^{3+} and Sm^{3+} ions incorporated in anatase titania nanocrystals." *Journal of Physical Chemistry C,* **113** 20 (2009) p.8772-8777.
218. Z. Assefa, R. G. Haire and P. E. Raison, "Photoluminescence and Raman studies of Sm^{3+} and Nd^{3+} ions in zirconia matrices: example of energy transfer and host-guest interactions." *Spectrochimica Acta Part a-Molecular and Biomolecular Spectroscopy,* **60** 1-2 (2004) p.89-95.
219. A. C. Yanes, J. Del Castillo, M. Torres, J. Peraza, V. D. Rodriguez and J. Mendez-Ramos, "Nanocrystal-size selective spectroscopy in SnO_2 : Eu^{3+} semiconductor quantum dots." *Applied Physics Letters,* **85** 12 (2004) p.2343-2345.
220. J. T. Kong, H. M. Zhu, R. F. Li, W. Q. Luo and X. Y. Chen, "Carrier-mediated 1.55 μm photoluminescence from single Er^{3+} center in SnO_2 nanocrystals." *Optics Letters,* **34** 12 (2009) p.1873-1875.

221. W. J. Miniscalco, "Erbium-doped glasses for fiber amplifiers at 1500 nm." *Journal of Lightwave Technology,* **9** 2 (1991) p.234-250.
222. C. C. Ting, C. H. Tsai, Y. C. Chien and C. T. Yu, "Enhanced red light photoluminescence of the europium and yttrium co-doped ITO powders." *Journal of the Electrochemical Society,* **159** 4 (2012) p.H400-H406.
223. A. Podhorodecki, R. Kudrawiec, J. Misiewicz, N. V. Gaponenko and D. A. Tsyrkunov, "1.54 μm photoluminescence from Er-doped sol-gel derived In_2O_3 films embedded in porous anodic alumina." *Optical Materials,* **28** 6-7 (2006) p.685-687.
224. N. Wan, J. Xu, T. Lin, X. G. Zhang and L. Xu, "Energy transfer and enhanced luminescence in metal oxide nanoparticle and rare earth codoped silica." *Applied Physics Letters,* **92** 20 (2008) p.3.
225. "ISO5017:1998(E)".
226. A. A. Coelho, "TOPAS Academic: General profile ans structure analysis software for powder diffraction data." 1st ed. (2004), Bruker AXS: Karlsruhe, Germany.
227. W. H. Baur, "Uber die verfeinerung der kristallstrukturbestimmung einiger vertreter des rutiltyps - TiO_2, SnO_2, GeO_2 und MgF_2." *Acta Crystallographica,* **9** 5 (1956) p.515-520.
228. C. G. Whinfrey, D. W. Eckart and A. Tauber, "Preparation and X-ray diffraction data for some rare earth stannates." *Journal of the American Chemical Society,* **82** 11 (1960) p.2695-2697.
229. B. J. Kennedy, B. A. Hunter and C. J. Howard, "Structural and bonding trends in tin pyrochlore oxides." *Journal of Solid State Chemistry,* **130** 1 (1997) p.58-65.
230. S. J. Schneider, R. S. Roth and J. L. Waring, "Solid state reactions involving oxides of trivalent cations." *Journal of Research of the National Bureau of Standards,* **A 65** 4 (1961) p.345.
231. D. M. Giaquinta and H. C. Zurloye, "Structural predictions in the ABO_3 phase-diagram." *Chemistry of Materials,* **6** 4 (1994) p.365-372.
232. R. D. Shannon, "Synthesis of some new perovskites containing indium and thallium." *Inorganic Chemistry,* **6** 8 (1967) p.1474.
233. C. Pistorius and G. J. Kruger, "Stability and structure of noncentrosymmetric hexagonal $LnInO_3$ (Ln=Eu, Gd, Tb, Dy, Ho, Y)." *Journal of Inorganic & Nuclear Chemistry,* **38** 8 (1976) p.1471-1475.
234. B. R. Otter, *Master thesis*, "Chemical solution deposition of transparent conducting oxide thin films." Department of Materials Science and Engineering, NTNU: Trondheim, (2011).
235. L. J. Van Der Pauw, "A method of measuring resistivity and Hall coefficient on lamellae of arbitrary shape." *Philips Technical Review,* **20** (1958) p.220 - 224.
236. F. M. Smits, "Measurement of sheet resistivities with the 4-point probe." *Bell System Technical Journal,* **37** 3 (1958) p.711-718.
237. D. S. Mclachlan, M. Blaszkiewicz and R. E. Newnham, "Electrical-resistivity of composites." *Journal of the American Ceramic Society,* **73** 8 (1990) p.2187-2203.

238. A. Trestmanmatts, S. E. Dorris and T. O. Mason, "Measurement and interpretation of thermopower in oxides." *Journal of the American Ceramic Society,* **66** 8 (1983) p.589-592.
239. B. S. Hong, S. J. Ford and T. O. Mason, "Equilibrium electrical property measurements in electroceramics." Ch. in "Electrical Properties of Oxide Materials." (1997), Trans Tech Publications Ltd: Stafa-Zurich.
240. M. Cesaria, A. P. Caricato and M. Martino, "Realistic absorption coefficient of ultrathin films." *Journal of Optics,* **14** 10 p.10.
241. P. Kubelka and F. Munk, "An article on optics of paint layers." *Z. Tech. Phys.,* **12** (1931) p.593-601.
242. H. Fujiwara, "Spectroscopic ellipsometry - Principles and applications." 1st ed. (2003), John Wiley & Sons: Tokyo.
243. H. E. Fossheim, *Master thesis*, "Development of optical active layers in solar cells." Department of Materials Science and Engineering, NTNU: Trondheim, (2010).
244. S. Yang, G. Li, S. Tian, F. Liao and J. Lin, "An open-framework three-dimensional indium oxalate: $[In(OH)(C_2O_4)(H_2O)]_3{\cdot}H2O$." *Journal of Solid State Chemistry,* **178** 12 (2005) p.3703-3707.
245. M. U. Pechini, "Method of Preparing Lead and Alkaline Earth Titanates and Niobates and Coating Method Using the Same to Form a Capacitor." *US Patent number 3330697,* (1967)
246. M. L. Fontaine, C. Laberty-Robert, A. Barnabe, F. Ansart and P. Tailhades, "Synthesis of $La_{2-x}NiO_{4+delta}$ oxides by polymeric route: Non-stoichoimetry control." *Ceramics International,* **30** 8 (2004) p.2087-2098.
247. M. A. Gulgun, M. H. Nguyen and W. M. Kriven, "Polymerized organic-inorganic synthesis of mixed oxides." *Journal of the American Ceramic Society,* **82** 3 (1999) p.556-560.
248. T. Liu, Y. B. Xu and J. Y. Zhao, "Low-temperature synthesis of $BiFeO_3$ via PVA sol-gel route." *Journal of the American Ceramic Society,* **93** 11 (2010) p.3637-3641.
249. H. T. Zhou, M. A. Einarsrud and F. Vullum-Bruer, "PVA-assisted combustion synthesis and characterization of porous nanocomposite Li_2FeSiO_4/C." *Solid State Ionics,* **225** (2012) p.585-589.
250. R. B. H. Tahar, T. Ban, Y. Ohya and Y. Takahashi, "Electronic transport in tin-doped indium oxide thin films prepared by sol-gel technique." *Journal of Applied Physics,* **83** 4 (1998) p.2139-2141.
251. X. Y. Kong and Z. L. Wang, "Structures of indium oxide nanobelts." *Solid State Communications,* **128** 1 (2003) p.1-4.
252. R. H. Lamoreaux, D. L. Hildenbrand and L. Brewer, "High-Temperature Vaporization of Oxides .2. Oxides of Be, Mg, Ca, Sr, Ba, B, Al, Ga, In, Tl, Si, Ge, Sn, Pb, Zn, Cd, and Hg." *Journal of Physical and Chemical Reference Data,* **16** 3 (1987) p.419-443.
253. I. Barin, "Thermochemical Data of Pure Substances." 1st ed. (1989), VCH: New York.
254. N. Nadaud, M. Nanot and P. Boch, "SINTERING AND ELECTRICAL-PROPERTIES OF TITANIA-CONTAINING AND ZIRCONIA-

CONTAINING IN2O3-SNO2 (ITO) CERAMICS." *Journal of the American Ceramic Society,* **77** 3 (1994) p.843-846.
255. J. H. W. De Wit, "HIGH-TEMPERATURE BEHAVIOR OF IN2O3." *Journal of Solid State Chemistry,* **13** 3 (1975) p.192-200.
256. G. Frank and H. Kostlin, "ELECTRICAL-PROPERTIES AND DEFECT MODEL OF TIN-DOPED INDIUM OXIDE LAYERS." *Applied Physics a-Materials Science & Processing,* **27** 4 (1982) p.197-206.
257. G. B. Gonzalez, J. S. Okasinski, T. O. Mason, T. Buslaps and V. Honkimaeki, "In situ studies on the kinetics of formation and crystal structure of In(4)Sn(3)O(12) using high-energy x-ray diffraction." *Journal of Applied Physics,* **104** 4 (2008)
258. J. W. Son, D. Y. Kim and P. Boch, "Enhanced densification of In2O3 ceramics by presintering with low pressure (5 MPa)." *Journal of the American Ceramic Society,* **81** 9 (1998) p.2489-2492.
259. C. Liu, J. X. Liu and Y. Wang, "Preparation of indium tin oxide targets with a high density and single phase structure by normal pressure sintering process." *Rare Metals,* **30** 2 (2011) p.126-130.
260. R. K. Bordia and G. W. Scherer, "ON CONSTRAINED SINTERING .1. CONSTITUTIVE MODEL FOR A SINTERING BODY." *Acta Metallurgica,* **36** 9 (1988) p.2393-2397.
261. O. N. Tretinnikov and Y. Ikada, "Dynamic wetting and contact-angle hysteresis of polymer surfaces studies with the modified Wilhelmy balance method." *Langmuir,* **10** 5 (1994) p.1606-1614.
262. B. J. Kim, J. Lee and J. B. Yoo, "Sol-gel derived (La,Sr)CoO_3 thin films on silica glass." *Thin Solid Films,* **341** 1-2 (1999) p.13-17.
263. O. Stenzel, "The physics of thin film optical spectra." 1st ed. (2005), Springer-Verlag:
264. D. E. Bornside, C. W. Macosko and L. E. Scriven, "Spin coating - One-dimensional model." *Journal of Applied Physics,* **66** 11 (1989) p.5185-5193.
265. R. Balasundaraprabhu, E. V. Monakhov, N. Muthukumarasamy, O. Nilsen and B. G. Svensson, "Effect of heat treatment on ITO film properties and ITO/p-Si interface." *Materials Chemistry and Physics,* **114** 1 (2009) p.425-429.
266. J. Puetz and M. A. Aegerter, "Direct gravure printing of indium tin oxide nanoparticle patterns on polymer foils." *Thin Solid Films,* **516** 14 (2008) p.4495-4501.
267. T. Mokkelbost, *PhD thesis*, "Synthesis and characterization of CeO_2 - and $LaNbO_4$ -based ionic conductors." Department of Materials Science and Engineering, NTNU: Trondheim, (2006).
268. A. Trovarelli, "Catalytic properties of ceria and CeO2-containing materials." *Catalysis Reviews-Science and Engineering,* **38** 4 (1996) p.439-520.
269. L. Vegard, "Die konstitution der mischkristalle und die raumfüllung der atome." *Zeitschrift für physik,* **5** 1 (1921) p.17-26.
270. E. Rauwel, O. Nilsen, A. Galeckas, J. C. Walmsley, E. Rytter and H. Fjellvag, "ALD applied to conformal coating of nanoporous gamma-

alumina: Spinel formation and luminescence induced by europium doping." Ch. in "Atomic Layer Deposition Applications 7." (2012),
271. W. C. Sheets, E. S. Stampler, M. I. Bertoni, M. Sasaki, T. J. Marks, T. O. Mason and K. R. Poeppelmeier, "Silver delafossite oxides." *Inorganic Chemistry,* **47** 7 (2008) p.2696-2705.
272. C. L. Heng, T. G. Finstad, P. Storas, Y. J. Li, A. E. Gunnaes and O. Nilsen, "The 1.54-mu m photoluminescence from an (Er, Ge) co-doped SiO_2 film deposited on Si by rf magnetron sputtering." *Applied Physics Letters,* **85** 19 (2004) p.4475-4477.
273. D. M. Gruen, W. C. Koehler and J. J. Katz, "Higher oxides of the lanthanide elements - Terbium dioxide." *Journal of the American Chemical Society,* **73** 4 (1951) p.1475-1479.
274. S. Stølen and T. Grande, "Chemical thermodynamics of materials." 1st ed. (2004), John Wiley & Sons: London.
275. S. H. Skjærvø, *Master thesis*, "Transparent and conducting rare earth metal doped ITO thin films prepared by spin coating of an aqueous precursor solution." Department of Materials Science and Engineering, NTNU: Trondheim, (2013).
276. P. W. France, M. G. Drexhage, J. M. Parker, M. W. Moore, S. F. Carter and J. V. Wright, "Fluoride glass optical fibres." 1st ed. (1990), Blackie: Glasqow.

Paper I

Journal of Materials Chemistry **22** (2012) 15740 - 15749
Transparent and conducting ITO thin films by spin coating of an aqueous precursor solution
Tor Olav Løveng Sunde, Edita Garskaite, Benjamin Otter, Helle Ervik Fossheim, Ragnhild Sæterli, Randi Holmestad, Mari-Ann Einarsrud and Tor Grande

Journal of Materials Chemistry

Cite this: *J. Mater. Chem.*, 2012, **22**, 15740

www.rsc.org/materials

PAPER

Transparent and conducting ITO thin films by spin coating of an aqueous precursor solution†

Tor Olav Løveng Sunde,[a] Edita Garskaite,‡[a] Benjamin Otter,§[a] Helle Ervik Fossheim,¶[a] Ragnhild Sæterli,[b] Randi Holmestad,[b] Mari-Ann Einarsrud[a] and Tor Grande*[a]

Received 30th March 2012, Accepted 18th June 2012
DOI: 10.1039/c2jm32000b

An environmentally friendly aqueous sol–gel process has been developed to fabricate thin films of indium tin oxide (ITO). A stable sol was prepared from indium nitrate and tin acetate precursors together with acetic acid and ethylene glycol. The sol transformed into an amorphous gel during heating, which decomposed and crystallized further to nano-crystalline ITO at ~300 °C. The nano-crystalline ITO powders prepared from the precursor gel were homogeneous and single phase with particle sizes around 15 nm. The aqueous sol was applied for spin coating of ITO films on glass substrates. The deposited thin films were homogeneous and continuous with no cracks or pin-holes and exhibited very good and reproducible optical transparency and electrical conductivity, with a specific resistance of 4.59×10^{-3} Ω cm, thereby demonstrating the potential of this Pechini related sol–gel process. Experiments to determine the robustness of the process with respect to the concentration of the precursors and substitution of the organic components with other alcohols or acids were also performed, and some important aspects of the chemistry of the sol–gel process are addressed.

Introduction

Transparent conducting oxides (TCOs) demonstrate the remarkable combination of near-metallic conductivity, high transmittance in the visible region and high reflectivity in the infrared region of light. Owing to their unique properties, TCOs are utilized in numerous technological applications such as flat panel displays, touch panels, energy efficient windows, photovoltaic devices, light emitting diodes, gas sensors, *etc.*[1,2] TCOs are typically wide bandgap oxide semiconductors such as In_2O_3, ZnO, SnO_2, CdO, or mixtures of these. Indium oxide doped with tin oxide, often referred to as indium tin oxide (ITO), is recognized as the TCO with the best performance and is therefore the prime candidate in most of these applications, with more than a 90% share of the transparent electrode market.[3–5]

ITO thin films can be deposited by a wide range of techniques, such as rf and dc sputtering, pulsed laser deposition, spray pyrolysis, chemical vapour deposition, vacuum evaporation and sol–gel methods.[1–5] Sputtering is the most widely used industrial process, but wet chemical methods to fabricate thin films have potentially many advantages compared to these physical methods. They are relatively simple and less expensive techniques, and the composition and homogeneity down to the molecular level can readily be controlled. It is also possible to use wet chemical methods to coat larger substrates and substrates with different geometries by utilizing spin or dip coating deposition techniques.[6,7] Although ITO is conventionally applied as thin films in most cases, ITO nano-particles have recently attracted a lot of interest since nano-particle suspensions can be used to fabricate thin films on flexible substrates. Deposition on such substrates by sputter-deposition is known to be difficult as the technique yields brittle films, making nano-particle suspensions an attractive alternative.[5] Phosphors based on nano-crystalline ITO particles doped with rare earth ions have also been reported recently.[8]

Precursor solutions for wet chemical deposition techniques of thin films can be sub-divided into two types depending on whether an organic solvent or water is used as the solvent. A disadvantage with the organic solvents is that they are often flammable, expensive or harmful to the environment. Aqueous solution processing is therefore potentially more environmentally friendly and suitable for industrial processes.[9] The majority

[a]*Department of Materials Science and Engineering, Norwegian University of Science and Technology, N-7491 Trondheim, Norway. E-mail: grande@ntnu.no*
[b]*Department of Physics, Norwegian University of Science and Technology, N-7491 Trondheim, Norway*

† Electronic supplementary information (ESI) available: XRD of the organometallic salts obtained from as-evaporated gels and powders calcinated at 400 °C in the syntheses with different complexing agents. See DOI: 10.1039/c2jm32000b

‡ Current address: Department of General and Inorganic Chemistry, Faculty of Chemistry, Vilnius University, Naugarduko 24 LT-03225, Vilnius, Lithuania.
§ Current address: University of Applied Sciences and Arts Northwestern Switzerland, Institute for Chemistry and Bioanalytics, Gründenstrasse 40, 4132 Muttenz, Switzerland.
¶ Current address: Metallkraft AS, Setesdalsveien 110, NO-4617 Kristiansand, Norway.

of the wet chemical methods reported for depositing ITO are based on organic solvents like ethylene glycol, ethanol or acetylacetone,[10–13] although some water based processes have been reported including work on related materials.[9,14–16] In several of these reports tin chloride has been used as a Sn precursor.

In this work we report on the development of an environmentally friendly aqueous sol–gel process applied to prepare nano-crystalline ITO particles as well as high quality ITO thin films by spin coating. The method is a modified Pechini process[17] using simple and relatively inexpensive precursors avoiding challenges with hydrolysis of tin chloride as a precursor. We report on the crystal structure, microstructure and properties of the nano-crystalline ITO powders as well as ITO thin films prepared by this method. Some aspects of the chemistry of the Pechini method are also addressed based on experimental findings using different alcohols and organic acids and different precursor concentrations in the sol–gel process.

Experimental

Preparation of nano-crystalline ITO powders

Indium(III) nitrate hydrate ($In(NO)_3 \cdot xH_2O$, 99.9%, Aldrich) and tin(II) acetate ($Sn(CH_3CO_2)_2$, 99.9%, Aldrich) were used as precursors for preparation of In_2O_3 and ITO. The stoichiometry of indium nitrate was determined by thermogravimetrical analysis prior to the synthesis. The amount of tin was varied between 0 and 15 cation% Sn (cation% Sn $= n_{Sn}/(n_{Sn} + n_{In})$). Acetic acid (AA) ($CH_3COOH$, p.a., Acros Organics) and ethylene glycol (EG) ($C_2H_4(OH)_2$, VWR) were used as a complexing agent and an esterification agent. The molar ratio between the cations in the solution and the organic additives was 1 : 1.5. Stoichiometric amounts of the precursors, AA and EG, were dissolved in deionised water and kept on a hot-plate with a magnetic stirrer overnight in order to evaporate the solvent and to transform the solution into a gel. Finally, the gel was ground in a mortar and calcinated for 3 hours at 400 and 600 °C in order to decompose the gel to a nano-crystalline oxide powder.

The powder synthesis was also conducted using ethanol (EtOH), tartaric acid (TA) (DL-tartaric acid, 99%, Sigma-Aldrich), succinic acid (SA) (ReagentPlus ≥ 99%, Sigma-Aldrich) and polyvinyl alcohol (PVA) (VWR, average $M_w \sim$ 88 000 g mol^{-1}) as complexing agents. The molar ratio between the cations and the complexing agents was 1 : 3 when only one type of complexing agent was used and 1 : 1.5 for each of the complexing agents when two were used in combination. A solution similar to the one used for spin coating (described in the next paragraph) was used in the synthesis using PVA, but without the addition of AA and EG as designated complexing agents. In the synthesis where these different complexing agents were used, the cation concentration was 0.5 M (0.04 mol cations and 80 mL solution) and the Sn concentration was 5 cation%, while all other experimental parameters were kept the same. After the synthesis the as-evaporated gels were ground in a mortar and calcinated for 3 hours at various temperatures.

Preparation of ITO thin films

The solution used in the spin coating was prepared from stoichiometric amounts of $In(NO_3)_3$, $Sn(CH_3CO_2)_2$, AA and EG as described in the previous section. The cation concentration was 0.4 M. This solution was then mixed in a 1 : 1 volume ratio with a solution of de-ionised water with 3 wt% PVA, so that the cation concentration of the final solution used for spin coating was 0.2 M. The concentration of Sn was 10 cation% for the reported films.

ITO thin films were deposited on square glass substrates (Menzel-Gläser, microscope slides) of 25 × 25 mm by spin coating (Laurell WS-400B-6NPP-Lite Spinner) in a clean room ISO7 (NTNU Nanolab). The substrates were cleaned with soap water, rinsed in distilled water and ethanol and dried with an airbrush prior to the film deposition. A syringe with a 0.2 μm filter was used to apply the solution to the substrate prior to the spinning. A sufficient amount of solution was used to completely cover the substrate, approximately 25 droplets. The substrates were then spun at 3000 rpm for 45 seconds. The films were calcinated under vacuum (10^{-2} mbar) in a rapid thermal process furnace (RTP, Jipelec JetFirst 200 Processor) at 530 °C for 1 hour. The chamber was purged with nitrogen gas before the onset of the vacuum. This procedure was repeated in order to make films with multiple depositions.

Characterization

The phase composition and crystal structure of the nano-crystalline ITO powders and ITO thin films were studied by X-ray diffraction (XRD, Bruker AXS, D8 Focus). The crystallite size of the powders was estimated by the line broadening of the (222) reflection using the Scherrer equation. Rietveld refinements of the diffractograms were performed (Topas software v 4.2) using the space groups $Ia\bar{3}$ [18] and $R\bar{3}c$.[19] The BET surface area of the powders was determined by nitrogen gas adsorption (Micromeritics, Tristar 3000). The average particle size was estimated from the surface area by assuming spherical particles. Thermogravimetrical analyses (TGAs, Netzsch, STA 449 C) of the gels were performed up to 1000 °C in air, with a heating rate of 2 K min^{-1} up to 400 °C and 10 K min^{-1} from 400 to 1000 °C. Fourier transform infrared spectroscopy (FTIR, Bruker IFS 66v, OPUS 6.5 software) was performed on the powders calcinated at different temperatures embedded in KBr pellets (0.5 wt%). Scanning electron microscopy (FEG-SEM, Zeiss Ultra 55 Limited Edition) was performed on the thin films. Some of the samples were cut in order to observe the cross-section of the films in the middle of the substrate. Transmission electron microscopy (TEM) specimens from the ITO powder with 5 cation% Sn after calcination at 600 °C were prepared by dispersing the powder in ethanol and dripping it onto a standard TEM Cu grid covered with holey C film. Additionally, specimens made from films with 10 subsequent depositions were prepared by Tripod wedge polishing using an Allied MultiPrep system. Plane-view specimens were prepared by polishing off the substrate using an angle of two degrees between the polishing plane and the film–substrate interface plane. Cross-section specimens were prepared by gluing two films together and polishing the material into a two degree wedge normal to the film–substrate plane, before Ar ion milling for a few minutes. TEM characterization was performed at 200 kV using a JEOL2010F. Both the electron microscopes were equipped with energy dispersive X-ray spectrometers (EDS) for elemental analysis.

Optical transmission spectroscopy was carried out on the thin films (Shimadzu, UV-1601PC) in the UV-VIS-NIR region. The

absorption coefficient was calculated by neglecting the reflectance and using the simple relation:

$$\alpha = \frac{1}{t}\ln(T) \quad (1)$$

where T is the transmittance, α is the absorption coefficient and t is the thickness of the sample. The band gap, E_g, was estimated by plotting $(\alpha h\nu)^2$ *versus* the photon energy, $h\nu$ according to the equation:

$$\alpha = \frac{A(h\nu - E_g)^{1/2}}{h\nu} \quad (2)$$

where A is a proportionality constant. Electrical conductivity was measured using an in-house built van der Pauw apparatus with platinum contacts under ambient conditions. Two different samples were tested for each film thickness. The substrates with the deposited thin films were cut into squares of approximately 13 × 13 mm from the center of the substrates, in order to remove possible edge effects from the spin coating. Eight different measurements, where the current and voltage drop were measured in different directions and along different sides of the film, were performed on each sample. The sheet resistance of the films (R_s) was calculated by the equation:[20]

$$R_s = \frac{\pi}{\ln 2} \times \frac{R_{horizontal} + R_{vertical}}{2} \times f \quad (3)$$

where $R_{horizontal}$ and $R_{vertical}$ were determined as the average of the first and last four measurements respectively and f is a correction factor. The sheet resistance is the specific resistance of the material, ρ, divided by the thickness of the film.

$$R_s = \frac{\rho}{t} \quad (4)$$

The correction factor can be obtained from the following equation:[20]

$$\frac{R_{horizontal} - R_{vertical}}{R_{horizontal} + R_{vertical}} = \frac{f}{\ln 2} \times \operatorname{arccosh} \frac{e^{\ln 2/f}}{2} \quad (5)$$

Results

Nano-crystalline ITO powders

Amorphous and homogeneous gels were obtained in the synthesis using AA and EG as shown by the X-ray diffraction pattern, see Fig. 1. After drying no Bragg reflections due to crystalline materials could be detected in the gels using the optimized recipe. Precipitation of crystalline In-salts before the sol–gel transition and/or formation of the metastable rhombohedral In_2O_3-phase were however observed when other organic components were used or if the concentrations of the cations in the solution were altered. The chemistry of these experiments is reported in detail further below.

The dried amorphous gel decomposed and crystallized to cubic In_2O_3 (space group $Ia\bar{3}$) during heating as evidenced by the diffractograms in Fig. 1 and 2. As seen from Fig. 2, the crystallization occurred between 250 and 300 °C. Thermogravimetrical analysis of the dry gel is shown in Fig. 3 (blue curve, 1 : 1.5 AA + 1 : 1.5 EG). A significant weight loss is initiated below 250 °C and the gel was completely decomposed to oxides a few degrees

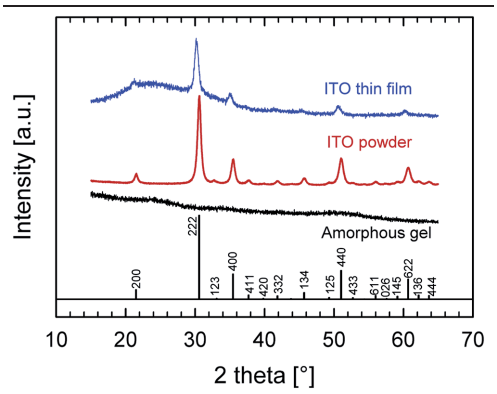

Fig. 1 XRD patterns of an amorphous ITO gel after evaporation of the solvent, ITO powder after calcination at 400 °C and an ITO thin film. The gel and the powder were prepared with acetic acid and ethylene glycol, an initial cation concentration of 0.125 M and 5 cation% Sn. The film with 10 cation% Sn was prepared by 10 subsequent depositions. The pattern for the powder and the film could be indexed to the cubic In_2O_3 with the space group $Ia\bar{3}$ given at the bottom. The broad bump at around 25° in the diffractogram of the ITO thin film is due to the amorphous glass substrate.

below 300 °C, which confirms the conclusions from XRD. FTIR spectra of the powders calcinated at different temperatures through the decomposition region are shown in Fig. 4. Evidence of residual nitrate groups and organics in the gels is seen up to 250 °C, while these characteristic bands are completely removed at 300 °C, confirming the conclusion from TGA and XRD. From combining these results it is concluded that the crystallization and decomposition of the gel occurred more or less

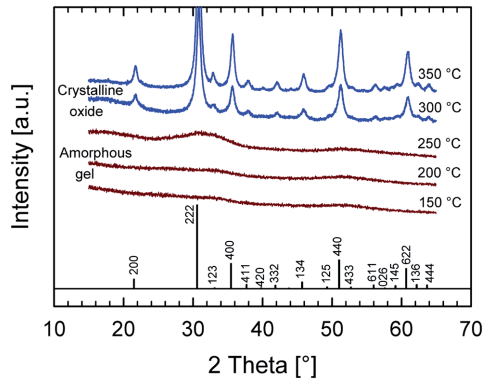

Fig. 2 XRD of ITO gels prepared with acetic acid and ethylene glycol, an initial cation concentration of 0.125 M and a doping amount of 5 cation% Sn after calcination at different temperatures. A reference pattern of the cubic In_2O_3 crystal structure (space group $Ia\bar{3}$) is given at the bottom.

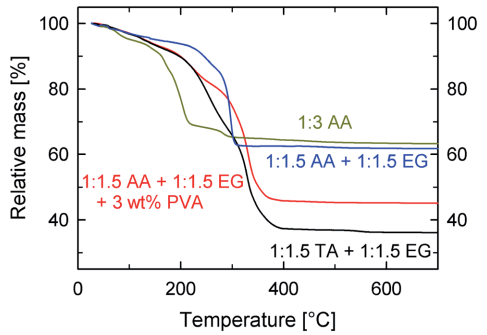

Fig. 3 Thermogravimetrical analyses of as-evaporated gels synthesized with different complexing agents: acetic acid (AA), ethylene glycol (EG), tartaric acid (TA) and polyvinyl alcohol (PVA). The molar ratio between the cations and the complexing agents in the solution is indicated.

simultaneously in the temperature interval between 250 and 300 °C. The nano-crystalline ITO obtained after calcination at 300 °C still contained some residual water from the solution, evidenced by the OH-stretching modes (Fig. 4). The OH-content continued to decrease by heat treatment at higher temperatures, and no indication of OH-stretching modes could be observed after calcination at 600 °C (Fig. 4).

The process was found to be robust with respect to the Sn-content in ITO as the amount of tin doping could be varied from 0 to 15 cation% without alternating the results significantly. The crystal structure, lattice parameter, crystallite size and particle size (calculated from the BET surface area) of powders with different Sn-concentrations after calcination at 400 and 600 °C are given in Table 1. The term crystallite size refers to the size calculated from the line broadening in XRD, which must be distinguished from particle size (for the powder) or grain size (for the films) determined by TEM. The particle size is also calculated from the BET surface area where this is noted. The diffractograms of the materials could be indexed to the cubic In_2O_3 crystal structure and were clearly nano-crystalline, with crystallite sizes ranging from 11 to 26 nm. As expected, the crystallite size of the powder increased with increasing calcination temperature. Moreover, it also seems to be slightly reduced with increasing Sn-content, as reported for other synthesis methods.[21,22] The cubic lattice parameter, depicted in Fig. 5, increased from 10.1206 ± 0.0018 to 10.1321 ± 0.0016 Å as the doping level increased from 0 to 15 cation% Sn, which is in good agreement with literature data.[23,24] There was no trend or significant difference between the lattice parameter of the powder calcinated at 400 and 600 °C.

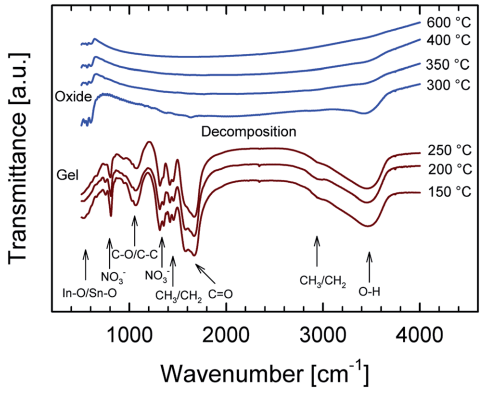

Fig. 4 FTIR spectra of ITO gels prepared with acetic acid and ethylene glycol, an initial cation concentration of 0.125 M and 5 cation% Sn after calcination at different temperatures. The most characteristic vibrational modes in the samples are assigned.

Representative TEM images of the ITO powder with 5 cation % Sn after calcination at 600 °C are shown in Fig. 6. Primary particles of approximately spherical shape and an average size of 15 ± 6 nm can be observed in the bright field image in Fig. 6a. The crystallite and particle size inferred from XRD and gas adsorption (Table 1) correspond well with the observed particle sizes from the TEM images. The diffraction pattern in Fig. 6b clearly demonstrates that the particles are crystalline. The pattern corresponds to the cubic In_2O_3 phase, and no reflections from any other crystalline phases were found, in agreement with XRD. The particles are single crystalline with little or no amorphous surface layer (Fig. 6c). The lattice fringes in the image corresponds to the [1$\bar{2}$2] zone axis, with plane spacings of $d_{0\bar{2}2}$ = 3.58 Å and $d_{41\bar{1}}$ = 2.38 Å, and the periodicity of the particle is clearly visualized in the FFT image. The concentration of tin, found by EDS (not shown here), was 5 ± 1 cation%, confirming the nominal composition.

Preparation of ITO thin films

PVA was added as a wetting agent to the solution used in the preparation of the films. This addition improved the wetting of the sol on the substrate and increased the viscosity of the solution, which is beneficial for the spin coating. The thermogravimetrical analysis of the PVA modified sol is shown in Fig. 3 (red curve, 1 : 1.5 AA + 1 : 1.5 EG + 3 wt% PVA). The total weight loss and the temperature where the decomposition is completed increased somewhat due to the addition of PVA.

Thin films with varying Sn concentrations were prepared in initial studies (not reported here), but only films with 10 cation% Sn are presented here since these gave the best performance with respect to the electrical conductivity. The presence of indium and tin in the films deposited on the glass substrates was confirmed by EDS, and a tin concentration of 9 ± 1 cation% was found. No impurity elements from the substrate could be observed. XRD of the heat treated films demonstrated that the films were nano-crystalline with the cubic In_2O_3 crystal structure with no preferred orientation (Fig. 1). The crystallite size in the films was 13 ± 3 nm and the lattice cell parameter of the films was 10.1527 ± 0.0039 Å, which is significantly higher than the lattice cell parameter of the nano-crystalline powders (Fig. 5 and Table 1), reflecting a substantial lattice strain in the films (tensional strain).

TEM and SEM micrographs of selected films are given in Fig. 7. Each deposited layer in the films could easily be distinguished, with a thickness of 17 ± 1 nm, as illustrated in Fig. 7a. A

Table 1 Crystal structure, lattice parameter, crystallite size and particle size of nano-crystalline ITO with different doping amounts and calcination temperatures

Doping amount (cation% Sn)	Crystal structure	Calcination temperature (°C)	Lattice parameter (Å)	Crystallite size (XRD) (nm)	Particle size (BET) (nm)	Goodness of Rietveld fit R_{wp}
ITO powder						
0	Cubic In_2O_3	400	10.1200 ± 0.0023	16 ± 3		5.4
		600	10.1207 ± 0.0014	26 ± 1	34 ± 1	5.5
5	Cubic In_2O_3	400	10.1231 ± 0.0020	11 ± 3		5.0
		600	10.1233 ± 0.0019	16 ± 2	21 ± 1	4.0
10	Cubic In_2O_3	400	10.1265 ± 0.0021	15 ± 1		3.8
		600	10.1300 ± 0.0023	18 ± 2		3.7
15	Cubic In_2O_3	400	10.1311 ± 0.0016	15 ± 3		4.5
		600	10.1332 ± 0.0018	17 ± 3		5.2
ITO thin film						
10	Cubic In_2O_3	530	10.1527 ± 0.0039	13 ± 5		

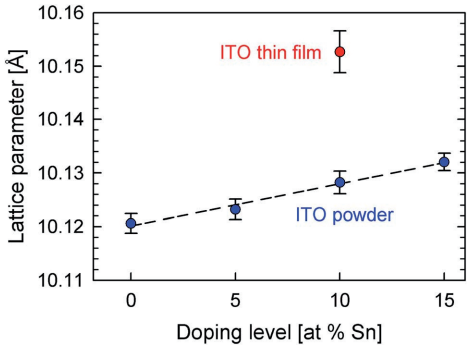

Fig. 5 Cubic lattice parameter of the ITO powders and ITO thin film as a function of composition. The powders were prepared using acetic acid and ethylene glycol and an initial cation concentration of 0.125 M. The film was prepared by 10 subsequent depositions.

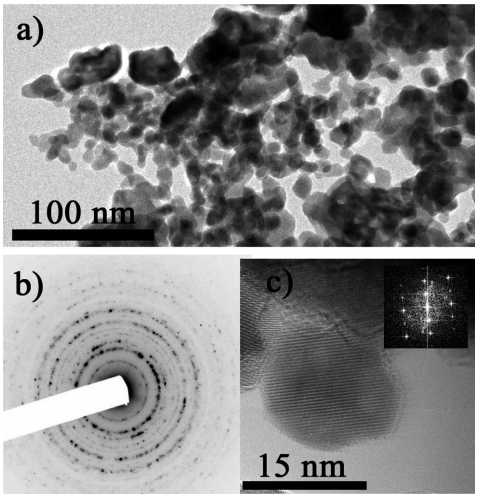

Fig. 6 TEM images of ITO powder prepared with acetic acid and ethylene glycol, an initial cation concentration of 0.125 M and 5 cation% Sn which has been calcinated at 600 °C, (a) bright field image, (b) diffraction pattern, and (c) high resolution image with FFT image as inset.

single layer of grains was observed in each layer (Fig. 7b), and no grains extending over multiple layers could be observed. The thickness of a film with 7 deposited layers, depicted in Fig. 7c, was 121 ± 8 nm, which confirms that the total thickness is approximately 17 nm times the number of depositions. TEM and SEM images of the top view of the films are given in Fig. 7d and e, respectively. The TEM image shows how the grains are interconnected and that the grains appear to be approximately spherical with a grain size of 16 ± 3 nm. The film depicted in Fig. 7e was prepared by only 1 deposition, and demonstrates that the films were continuous and homogeneous without pin-holes even after the first deposition. Electron diffraction patterns from the thin films could be indexed to cubic In_2O_3 with no traces of other phases, in line with XRD (Fig. 7f). In some cases the relatively harsh mechanical treatment during the TEM sample preparation caused delamination between the layers in the film.

The transmission spectra of ITO thin films prepared by varying the number of depositions are given in Fig. 8. The transmittance of the samples is 80% or higher throughout the visible region, and remains high into the NIR region. The transmittance of the pure glass substrate is shown for comparison. The UV-cutoff is at approximately 300 nm, and is shifted to slightly higher wavelengths as the film becomes thicker. A similar trend was reported by Tahar *et al.*, who claimed that this observation was probably caused by a quantum effect.[9] The spectra of the thicker films appear to have maxima and minima indicating interference with the film thickness.[25,26] This effect was not observed in films made by 3 or fewer layers (thinner than 50 nm). The transmittance, including the maxima and minima due to interference, was highly reproducible for films made by the same number of depositions. The optical band gap for the films was found to be in the range of 3.7 to 3.9 eV, which is in good accordance with values reported for films prepared by various techniques.[5] No significant trend between the band gap and the thickness of the films could be observed.

The sheet resistances as a function of the number of deposited layers are given in Fig. 9a. The sheet resistance was reproduced

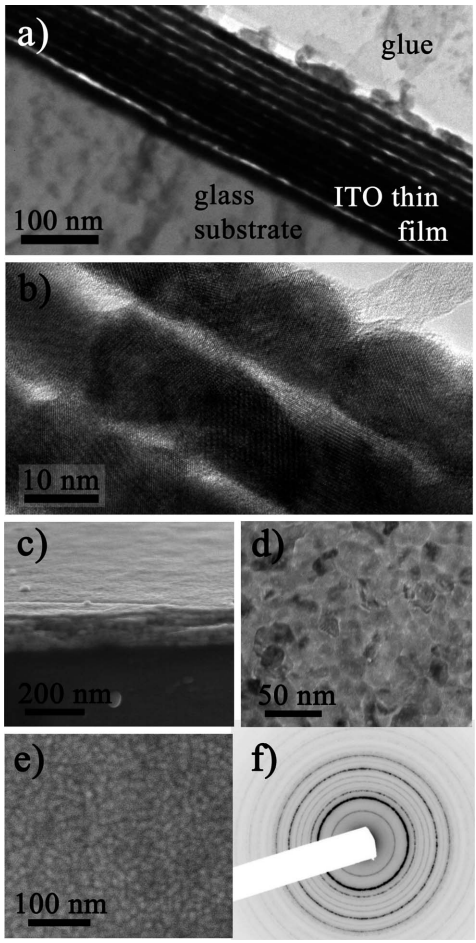

Fig. 7 (a) TEM image of the cross-section of a film prepared with 10 subsequent depositions. (b) HR TEM image of a cross-section. (c) SEM image of the cross-section of a film prepared with 7 subsequent depositions. (d) TEM image of the top view of a film. (e) SEM image of the top view of a film with only 1 deposited layer. (f) Diffraction pattern.

by two different samples for each thickness, and as the films became thicker, the sheet resistance became almost equal for the two parallels pointing to good homogeneity of the films. The sheet resistance for the films with 10 deposited layers was 270 ± 3 Ω per sq. The sheet resistance was fitted to a simple exponential function, $R_s = 2690/\#^{0.99}$, where R_s is the sheet resistance and # is the number of deposited layers. The specific resistance of the films was calculated by assuming that the thickness was 17 nm times the number of deposited layers and is given in Fig. 9b. The specific resistance is converging towards $4.59 \pm 0.05 \times 10^{-3}$ Ω cm with increasing thickness of the films.

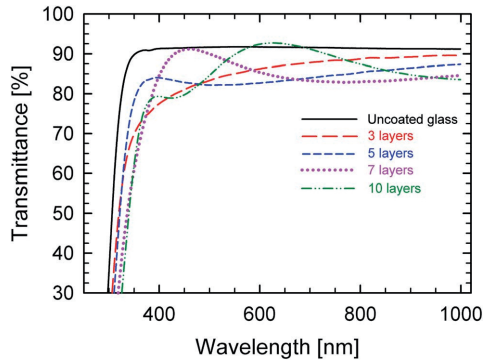

Fig. 8 Transmittance of ITO thin films prepared by 3, 5, 7 or 10 number of depositions. Maxima and minima due to interference with the film thickness can be seen for the thicker films.

Chemistry of the sol–gel process

When AA and EG were used as complexing agents, amorphous gels were obtained after evaporation of the solvent when the initial concentration of cations was 0.125 M or lower (Fig. 1).

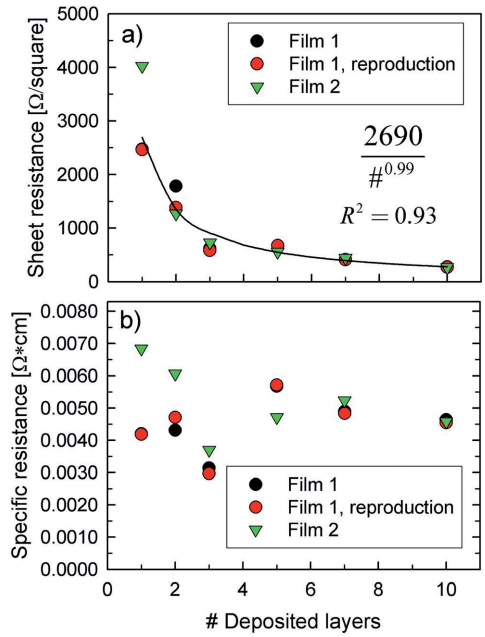

Fig. 9 (a) Sheet resistance of ITO thin films as a function of the number of deposited layers obtained from the van der Pauw method. The data were fitted to the formula $R_s = 2690/\#^{0.99}$ ($R^2 = 0.93$). (b) Specific resistance was calculated by assuming that the thickness of the films is 17 nm times the number of depositions.

However, when the concentration was 0.5 M or higher, precipitation of an In salt occurred during evaporation of the solvent (labelled In salt 5 in Table 2, XRD is given in the ESI†).

A series of experiments were carried out where the organic components in the recipe were alternated, all of which with an initial cation concentration of 0.5 M. The results from these experiments are summarized in Table 2. The synthesis resulted in homogeneous and amorphous gels only when EG and the combination EG + TA were used. In all the other cases either precipitation of salts or In_2O_3 occurred during drying or before a gel was formed. It was confirmed by XRD that none of the salts were nitrates or acetates, and that the same salt was observed in syntheses both with and without tin. It was therefore concluded that the salts are organometallic salts of indium and the respective organic additive. The salts are labelled In salt *X* according to their appearance in Table 2. XRD of the different products, with the same labelling, is given in ESI.† After calcination at 400 °C some of the samples were transformed into cubic In_2O_3 (space group $Ia\bar{3}$), however, in several of these materials rhombohedral In_2O_3 (space group $R\bar{3}c$) was found in addition to the cubic phase. The phase composition and the crystallite size of the phases after calcination are also included in Table 2. No systematic trend in the lattice parameters for the two polymorphs could be found. Furthermore, the completely decomposed gels were yellow, typical for indium oxide. However, in the case where larger organic molecules were used as complexing agents, the materials appeared black, which was due to carbon residues present in the materials. The carbon residual could be removed by oxidation during heat treatment at temperatures higher than 400 °C, thereby revealing the intrinsic yellow colour of the powder. TGAs of gels, which resulted in yellow and black powders after calcination at 400 °C, are given in Fig. 3 (yellow curve, 1 : 3 AA and black curve, 1 : 1.5 TA + 1 : 1.5 EG, respectively). The decomposition temperature interval is clearly dependent on the size of the organic complexing agent in the gels. After the TGA experiments the samples were yellow, in line with expectations.

In solutions stored for longer periods of time, oxidation of the divalent tin precursor resulted in precipitation of crystalline SnO_2. In order to prevent the oxidation of the precursor successful spin coatings were performed immediately after preparation of the sol. Also, the solution was filtered before spin coating in order to remove the possible SnO_2 precipitates in the sol. The nominal Sn content in the thin films was confirmed by EDS, as shown earlier, and both electron and X-ray diffraction indicated no traces of SnO_2 in either the powder or the thin films.

Discussion

Preparation of nano-crystalline ITO

The present work clearly demonstrated that homogeneous and nano-crystalline ITO can be prepared by the simple aqueous sol–gel process. The optimised precursor solution transformed into an amorphous gel during drying. The amorphous nature of the gel points to a homogenous distribution of the components and that segregation of In or Sn did not occur prior to the sol–gel transition. Moreover, the amorphous gel decomposed during calcination, which was accompanied by crystallization to a single

Table 2 Results from sol–gel syntheses with different complexing agents carried out with an initial cation concentration of 0.5 M

				Powder calcinated at 400 °C							
				Cubic In_2O_3		Rhombohedral In_2O_3					
Complexing agents	Cation : RCOOH ratio	Cation : ROH ratio	Gel/as evaporated	wt%	Crystallite size (nm)	wt%	Crystallite size (nm)	Other phase	Goodness of Rietveld fit R_{wp}	Colour
1 : 3 AA	1 : 3	—	c-In_2O_3 + In salt 1	85	19	15	43		10.9	Yellow
1 : 3 EtOH	—	1 : 3	c-In_2O_3 + rh-In_2O_3	55	26	45	45		10.5	Yellow
1 : 3 EG	—	1 : 6	Amorphous	90	21	10	13		7.0	Black
1 : 3 SA	1 : 6	—	In salt 2	—	—	—	—	In salt 3[a]	—	Black
1 : 3 TA	1 : 6	1 : 6	In salt 4	100	23	0	—		10.7	Black
1 : 1.5 AA + 1 : 1.5 EG	1 : 1.5	1 : 3	In salt 5	93	13	7	7		6.9	Yellow
1 : 1.5 EtOH + 1 : 1.5 SA	1 : 3	1 : 1.5	In salt 6	—	—	—	—	In salt 3[a]	—	Black
1 : 1.5 TA + 1 : 1.5 EG	1 : 3	1 : 6	Amorphous	100	15	0	—		9.9	Black
1 : 1.5 TA + 1 : 1.5 SA	1 : 6	1 : 3	In salt 7	100	12	0	—		10.6	Black
PVA	—	~1 : 0.7	In salt 8	90	11	10	12		10.3	Yellow

[a] An unknown organometallic salt was still present after the calcination at 400 °C of the sample prepared using SA and EtOH + SA, which made the Rietveld analysis of these samples difficult.

phase with the cubic In_2O_3 crystal structure. The decomposition and the crystallization were clearly demonstrated to take place between 250 and 300 °C, as evidenced by XRD, TGA and FTIR. These observations suggest that the decomposition and crystallisation occurred simultaneously and could not be separated. The mobility of the atoms is fairly limited at the temperature region where the crystallization takes place. However, the oxidation accompanying the decomposition of the gel is exothermic, and this reaction can thereby release sufficient heat to thermally induce crystallization of the amorphous oxide formed from the decomposed gel.

The average particle size of ITO powder with 5 cation% Sn was found to be 15 ± 6 nm after calcination at 600 °C, and the complementary data on the sizes from TEM, XRD and BET surface area were in very good agreement. The size coarsened with increasing calcination temperature and was somewhat smaller for the doped ITO powder compared to the undoped In_2O_3. The latter reflects that the cation mobility is reduced by doping In_2O_3 with a cation with a higher valance state. This is in line with similar information obtained by the investigation of sintering of nano-crystalline In_2O_3 and ITO.[27] Sintering studies of the nano-crystalline powders published elsewhere confirmed lower cation mobility with Sn-doping.[28]

The synthesized powders were highly crystalline as shown by both TEM and XRD. According to XRD the lattice parameter increased with increasing tin content, which is in line with previous reports.[23] Although Sn^{4+} is smaller than In^{3+} [29] it is known that the tin doping in ITO extends the lattice parameter due to interstitial oxygen atoms associated with the Sn-doping and incomplete shielding between the Sn^{4+}-ions.[24] The almost linear increase of the lattice parameter indicates that as much as 15 cation% Sn has been successfully incorporated into the host lattice, which is significantly higher than the equilibrium solubility limit.[30,31] The nano-crystalline ITO powders with high Sn-content are therefore metastable, and decomposition to ITO and SnO_2 occurs if the powders are heated above 800 °C, as confirmed and discussed further in a separate paper.[28]

Preparation of ITO thin films

The aqueous sol was applied by spin coating to prepare ITO thin films with very good optical and electrical properties. Good reproducibility of the functional properties of the films was demonstrated and the electrical conductivity improved with increasing the number of depositions in line with expectations and results from other deposition techniques.[9] The films appeared homogeneous and transparent, and the optical characterization demonstrated excellent properties such as a high transmittance in the visible region and band gap similar to reported values.[5,11] Diffraction patterns confirmed that the films were single phase and polycrystalline with no preferred crystal orientation, and the electron micrographs confirmed the homogeneous nature of the microstructure and continuous films with no pin-holes.

The total thickness of the films, and thereby also their functional properties, could be controlled by the number of depositions. The correlation between the film thickness and the number of depositions appears to be linear, with each deposition adding around 17 ± 1 nm to the total thickness. The spherical grains in the film had an average size of 16 ± 3 nm, which suggests that the grain size reflects the thickness of each deposited layer. A significant grain growth would have caused the grains to grow between the layers, but these observations show that each deposited layer is similar to a monolayer of particles, even after the final annealing step. It is possible that the microstructure caused by these subsequent depositions is the reason for the significant tensional strain in the films (Fig. 5). The occasional delamination during the TEM sample preparation could be due to the tensional strain present in the films.

The specific resistance of the films was $4.59 \pm 0.05 \times 10^{-3}$ Ω cm. This value is better than most reported values for ITO thin films prepared by aqueous sol–gel deposition processes, but is around an order of magnitude higher than the best reported values for ITO thin films.[3] Kanbara *et al.* achieved a conductivity of 1.3×10^{-3} Ω cm for ITO thin films prepared by an aqueous process, however these samples were fired at 900 °C and subsequently annealed in a N_2 atmosphere.[32] The importance of annealing at elevated temperatures and in reducing atmospheres in order to increase the conductivity of ITO thin films has been demonstrated in several reports.[9–11,32] Annealing at higher temperatures can improve the crystallinity of the films and it can also induce grain growth, which will limit the grain boundary scattering of the charge carriers. Furthermore, according to the defect chemistry of ITO, oxygen interstitials in the lattice will compensate and trap some of the itinerant electrons from the n-type tin donor atoms.[24,33] Annealing in reducing atmospheres can thereby increase the conductivity by removing these oxygen interstitials. In this work the annealing temperature was limited by the softening temperature of the glass substrate, and could not be increased above 530 °C. We propose that by using refractory substrates and optimizing the annealing process, the conductivity can be further increased, which is a subject of ongoing investigations. The microstructure of the films was demonstrated to be building up by individual layers from each deposition and the sample preparation for the TEM investigation revealed that the adhesion between the layers was weaker than the bond between the grains in each layer. Annealing at higher temperatures would increase the conductivity of the films by strengthening the physical contact between the layers, and presumably also relieve the observed tensional strain. Furthermore, it would also induce grain growth. However, Tahar *et al.* have calculated a carrier mean free path of 1.6 nm for a doping level of 10 cation% Sn,[21] which suggests that the grain sizes in the prepared films are sufficiently large to avoid grain boundary scattering causing a significant reduction of the mobility. Finally, annealing in reducing atmosphere and at higher temperature could also increase the conductivity by affecting the defect chemistry in the materials.

The sheet resistance was shown to be close to inversely proportional to the number of deposited layers. Because the sheet resistance is the specific resistance of the material divided by the thickness of the film (eqn (4)), this observation further demonstrates that the thickness of the film is proportional to the number of layers, and that the specific resistance of the deposited material is fairly constant regardless of the thickness of the film. Finally, surface scattering does not seem to be a dominating loss mechanism, even for the thinnest films, since the specific resistance was independent of the film thickness.

A simple calculation shows that the liquid film after spinning, given a cation concentration of 0.2 M, must be approximately 4 μm thick in order to form a 17 nm thick dense oxide film. For an industrial process it is a disadvantage that multiple depositions are required to obtain a sufficient conductivity. For thin film deposition by spin coating, the thickness of each deposition could be increased by optimizing parameters such as the viscosity of the solution, the cation concentration in the solution and the spinning parameters,[34,35] which were not optimized in this work.

Chemistry of the sol–gel process

The synthesis used here resembles the popular Pechini method.[17,36] In this process an α-hydroxycarboxylic acid, *i.e.* citric acid, is used as a complexing agent, which prevents segregation by complexing the cations, while a polyhydroxy alcohol, like ethylene glycol, is used as a polymerization agent. When the temperature is elevated, the acid and the alcohol will react and form esters according to the following esterification reaction:

$$\mathrm{ROOH + R'OH = ROOR' + H_2O} \quad (6)$$

A polymer network will be formed as the ester reaction continues to create new bonds between the acids and the alcohols. This rigid network will further limit the movement of the cations, which also contributes to maintain the local homogeneity, thereby preventing the formation of undesirable phases.

An amorphous gel was prepared using AA and EG when the initial cation concentration was 0.125 M or lower (Fig. 1), while a precipitation of an organometallic salt with indium occurred when the concentration was 0.5 M (labelled In salt 5 in Table 2; XRD is given in the ESI†). This observation can probably be explained by differences in the kinetics during the evaporation. If the initial cation concentration is higher, nucleation can occur before sufficient immobilization of the cations takes place. When the cation concentration is lower, on the other hand, it takes a longer time to reach supersaturation and the precipitation can be avoided by the complexing. A similar observation was made by Fontaine *et al.* in the synthesis of $La_{2-x}NiO_{4+\delta}$ with an aqueous modified Pechini process,[37] where phase pure materials were only obtained when the cation concentration was below 0.15 M.

In order to investigate the chemistry related to the process, a series of experiments were carried out where different organic molecules with varying numbers and types of functional groups were applied. A cation concentration of 0.5 M was used in all of these experiments, because experiments with AA and EG demonstrated that it was difficult to prevent precipitation under these conditions. Only the experiments with EG and TA + EG gave amorphous gels (Table 2). Hence, EG clearly has an important effect on the complexing of the cations. Both these experiments had a ratio between the cations and the ROH groups of 1 : 6, while the ratios between the cations and the RCOOH groups were 1 : 0 and 1 : 3, respectively (Table 2). Thus, it appears that for this material system the hydroxyl group is possibly more effective than the carboxyl group regarding the complexing of the cations, which is supported by the work of Kundu and Biswas, where PVA, and no carboxylic acids, was used to produce phase pure ITO thin films.[15] However, the steric hindrance of the cation mobility is perhaps more important than complexing when polymer chains like PVA are used.[38] Furthermore, for similar syntheses of $BiFeO_3$, Liu *et al.* observed that alcohol groups appeared to be vital, while the addition of carboxylic acid groups did not appear to be significant.[39] A possible explanation is that the ROH group is more important than the RCOOH group regarding complexing of the cations, In^{3+}, Sn^{4+} and Bi^{3+}, which all form amphoteric oxides, while the carboxylic acid group is more important for the complexation of cations, forming basic oxides.

The synthesis with TA and EG resembles the original Pechini process the most, with an α-hydroxycarboxylic acid and ethylene glycol, both with more than one functional group. The polyesterification will take place in the syntheses where these are used together. However, when only EG was used, the polyesterification reaction could not take place and a rigid polymer network could not be formed, though it is possible that some kind of bridging network was formed. When AA and EG were used in combination the ester reaction could occur. But as AA has only one functional group, a polymer network could not be formed again. However, also this synthesis route produced amorphous gels, when the solution was diluted (Fig. 1). This implies that the polymer network is not necessarily critical for maintaining the homogeneity as the solvent is evaporated, as long as the cations are immobilized by complexation.

Phase-pure cubic In_2O_3 was formed in the experiments where large organic molecules were used as complexing agents, such as TA, TA + EG and TA + SA. However, using smaller complexing agents such as AA, EtOH, EG and AA + EG, the metastable rhombohedral polymorph was also formed. Larger organic molecules, leading to a higher carbon to oxygen ratio, result in more reducing conditions during decomposition of the gel. Thus, it appears that crystallization of the rhombohedral polymorph is favoured kinetically by oxidizing conditions. The rhombohedral polymorph is metastable and will transform into the cubic upon heat treatment to above 700 °C,[40] and this phase transition has been observed to have a detrimental effect on densification.[41] However, DFT calculations have predicted that the rhombohedral polymorph should have good TCO properties,[42] and a composite film containing both rhombohedral and cubic In_2O_3 with good properties has recently been reported.[43]

Several parameters must be considered when choosing the optimum complexing agents. Most important is the homogeneity of the gel, where it appears that EG is important. To stabilize the cubic polymorph of In_2O_3 relatively large organic molecules are desirable, while smaller organic molecules promote the formation of rhombohedral In_2O_3. Furthermore, thermogravimetry (Fig. 3 and Table 2) demonstrated that the larger complexing agents require a higher temperature in order to fully decompose the gel. This might be undesirable, especially in cases where the substrate is temperature sensitive. A large amount of organic matter to be removed during the calcination might also cause problems during film formation, or even cause film cracking. However, the issue of film cracking is probably not important when the thickness of the deposited layers is as small as in this work.[6]

Conclusions

An environmentally friendly aqueous sol–gel process for the deposition of ITO thin films by spin coating has been developed.

The films prepared by this simple and inexpensive technique were homogeneous, phase pure and were continuous without any pinholes. The functional properties of the films were demonstrated to be good and reproducible with a specific resistance of 4.59×10^{-3} Ω cm, with the potential to be further increased by optimizing the heat treatment. The thickness of the films and thereby their functional properties could be controlled by the number of depositions. The sol–gel process can also be used for the synthesis of nanocrystalline ITO particles by evaporation of the solvent. The gel decomposed and crystallized to nanocrystalline particles with the cubic In_2O_3 structure at temperatures below 300 °C and the tin doping amount could readily be controlled. The particle size of the prepared powder with 5 cation% tin was 15 nm after heat treatment at 600 °C. The chemistry of the Pechini-related process was investigated and the functional groups of the organic additives, the size of the organic additives and the initial cation concentration in the solution were found to influence the homogeneity, phase composition and decomposition temperature of the prepared materials. The presence of hydroxyl groups in the process appears to be important regarding complexing and immobilization of the cations, and the possible formation of the metastable rhombohedral In_2O_3-phase could be controlled by the choice of the organic additives.

Acknowledgements

This work has been supported by NTNU and the strategic research area MATERIALS at NTNU. RS acknowledges the support from "The Norwegian Research Centre for Solar Cell Technology" (project number 193829), a Centre for Environment-friendly Energy Research co-sponsored by the Norwegian Research Council and research and industry partners in Norway. Dr Jerome Maria, Department of Physics, NTNU, is acknowledged for performing the transmittance experiments.

Notes and references

1 D. S. Ginley and C. Bright, *MRS Bull.*, 2000, **25**, 15–18.
2 K. L. Chopra, S. Major and D. K. Pandya, *Thin Solid Films*, 1983, **102**, 1–46.
3 C. G. Granqvist and A. Hultaker, *Thin Solid Films*, 2002, **411**, 1–5.
4 R. B. H. Tahar, T. Ban, Y. Ohya and Y. Takahashi, *J. Appl. Phys.*, 1998, **83**, 2631–2645.
5 E. N. Dattoli and W. Lu, *MRS Bull.*, 2011, **36**, 782–788.
6 C. J. Brinker, A. J. Hurd, P. R. Schunk, G. C. Frye and C. S. Ashley, *J. Non-Cryst. Solids*, 1992, **147–148**, 424–436.
7 D. S. Hecht and R. B. Kaner, *MRS Bull.*, 2011, **36**, 749–755.
8 Q. B. Xiao, Y. S. Liu, L. Q. Liu, R. F. Li, W. Q. Luo and X. Y. Chen, *J. Phys. Chem. C*, 2010, **114**, 9314–9321.
9 R. B. H. Tahar, T. Ban, Y. Ohya and Y. Takahashi, *J. Appl. Phys.*, 1997, **82**, 865–870.
10 Y. Takahashi, S. Okada, R. B. H. Tahar, K. Nakano, T. Ban and Y. Ohya, *J. Non-Cryst. Solids*, 1997, **218**, 129–134.
11 S. S. Kim, S. Y. Choi, C. G. Park and H. W. Jin, *Thin Solid Films*, 1999, **347**, 155–160.
12 K. Daoudi, B. Canut, M. G. Blanchin, C. S. Sandu, V. S. Teodorescu and J. A. Roger, *Thin Solid Films*, 2003, **445**, 20–25.
13 D. Gallagher, F. Scanlan, R. Houriet, H. J. Mathieu and T. A. Ring, *J. Mater. Res.*, 1993, **8**, 3135–3144.
14 C. Legnani, S. A. M. Lima, H. H. S. Oliveira, W. G. Quirino, R. Machado, R. M. B. Santos, M. R. Davolos, C. A. Achete and M. Cremona, *Thin Solid Films*, 2007, **516**, 193–197.
15 S. Kundu and P. K. Biswas, *Chem. Phys. Lett.*, 2005, **414**, 107–110.
16 B. Schumm, P. Wollmann, J. Fritsch, J. Grothe and S. Kaskel, *J. Mater. Chem.*, 2011, **21**, 10697–10704.
17 M. U. Pechini, *US Pat.*, 3330697, 1967.
18 M. Marezio, *Acta Crystallogr.*, 1966, **20**, 723–728.
19 A. N. Christensen, N. C. Broch, O. v. Heidenstam and Å. Nilsson, *Acta Chem. Scand.*, 1967, **21**, 1046–1056.
20 L. J. van der Pauw, *Philips Tech. Rev.*, 1958, **20**, 220–224.
21 R. B. H. Tahar, T. Ban, Y. Ohya and Y. Takahashi, *J. Appl. Phys.*, 1998, **83**, 2139–2141.
22 J. H. Ba, D. Fattakhova-Rohlfing, A. Feldhoff, T. Brezesinski, I. Djerdj, M. Wark and M. Niederberger, *Chem. Mater.*, 2006, **18**, 2848–2854.
23 N. Nadaud, N. Lequeux, M. Nanot, J. Jove and T. Roisnel, *J. Solid State Chem.*, 1998, **135**, 140–148.
24 G. B. Gonzalez, T. O. Mason, J. P. Quintana, O. Warschkow, D. E. Ellis, J. H. Hwang, J. P. Hodges and J. D. Jorgensen, *J. Appl. Phys.*, 2004, **96**, 3912–3920.
25 O. Stenzel, *The Physics of Thin Film Optical Spectra*, Springer-Verlag, 2005.
26 J. C. Manifacier, J. P. Fillard and J. M. Bind, *Thin Solid Films*, 1981, **77**, 67–80.
27 S. M. Kim, K. H. Seo, J. H. Lee, J. J. Kim, H. Y. Lee and J. S. Lee, *J. Eur. Ceram. Soc.*, 2006, **26**, 73–80.
28 T. O. L. Sunde, M.-A. Einarsrud and T. Grande, submitted.
29 R. D. Shannon, *Acta Crystallogr., Sect. A: Cryst. Phys., Diffr., Theor. Gen. Crystallogr.*, 1976, **32**, 751–767.
30 W. J. Heward and D. J. Swenson, *J. Mater. Sci.*, 2007, **42**, 7135–7140.
31 G. B. Gonzalez, T. O. Mason, J. S. Okasinski, T. Buslaps and V. Honkimaki, *J. Am. Ceram. Soc.*, 2012, **95**, 809–815.
32 T. Kanbara, M. Nagasaka and T. Yamamoto, *Chem. Mater.*, 1990, **2**, 643–645.
33 G. Frank and H. Kostlin, *Appl. Phys. A: Solids Surf.*, 1982, **27**, 197–206.
34 D. E. Bornside, C. W. Macosko and L. E. Scriven, *J. Appl. Phys.*, 1989, **66**, 5185–5193.
35 O. Yamamoto, T. Sasamoto and M. Inagaki, *J. Mater. Res.*, 1992, **7**, 2488–2491.
36 M. Kakihana and M. Yoshimura, *Bull. Chem. Soc. Jpn.*, 1999, **72**, 1427–1443.
37 M. L. Fontaine, C. Laberty-Robert, A. Barnabe, F. Ansart and P. Tailhades, *Ceram. Int.*, 2004, **30**, 2087–2098.
38 M. A. Gulgun, M. H. Nguyen and W. M. Kriven, *J. Am. Ceram. Soc.*, 1999, **82**, 556–560.
39 T. Liu, Y. B. Xu and J. Y. Zhao, *J. Am. Ceram. Soc.*, 2010, **93**, 3637–3641.
40 A. Gurlo, P. Kroll and R. Riedel, *Chem.–Eur. J.*, 2008, **14**, 3306–3310.
41 B. C. Kim, S. M. Kim, J. H. Lee and J. J. Kim, *J. Am. Ceram. Soc.*, 2002, **85**, 2083–2088.
42 S. Z. Karazhanov, P. Ravindran, P. Vajeeston, A. Ulyashin, T. G. Finstad and H. Fjellvag, *Phys. Rev. B: Condens. Matter Mater. Phys.*, 2007, **76**, 13.
43 L. A. Dunlop, A. Kursumovic and J. L. MacManus-Driscoll, *Cryst. Growth Des.*, 2010, **10**, 1730–1735.

Paper II

Journal of the European Ceramic Society, **33** (2013) 565 – 574
Solid state sintering of nano-crystalline indium tin oxide
Tor Olav Løveng Sunde, Mari-Ann Einarsrud and and Tor Grande

Available online at www.sciencedirect.com

SciVerse ScienceDirect

Journal of the European Ceramic Society 33 (2013) 565–574

www.elsevier.com/locate/jeurceramsoc

Solid state sintering of nano-crystalline indium tin oxide

Tor Olav Løveng Sunde, Mari-Ann Einarsrud, Tor Grande *

Department of Materials Science and Engineering, Norwegian University of Science and Technology, N-7491 Trondheim, Norway

Received 30 April 2012; received in revised form 14 September 2012; accepted 29 September 2012
Available online 23 October 2012

Abstract

The sintering of single phase nano-crystalline In_2O_3 and ITO ($In_{1.9}Sn_{0.1}O_{3.05}$) powders is reported and discussed with particular focus on the underlying mass transport mechanisms. The mass transport in the initial stage of sintering was surface diffusion, resulting in necking and coarsening, and grain boundary diffusion, accompanied by grain growth. Lattice diffusion caused significant densification at higher temperatures, leading to densities higher than 95%. The onset of densification and the maximum densification rate were shifted significantly to higher temperatures for ITO compared to In_2O_3. The reduced sintering rate of ITO was related to the higher valence state of Sn^{4+} relative to In^{3+}, and due to precipitation of SnO_2(s). The volatile sub-oxides In_2O(g) and SnO(g) caused significant weight losses at high temperatures, particularly in the case of ITO and inert conditions. The sintering at intermediate temperatures is discussed with focus on heat treatment of ITO thin films.

Keywords: In_2O_3; ITO; Solid state sintering; Nano-crystalline powder; Mass transport mechanisms

1. Introduction

Transparent conducting oxides (TCOs) demonstrate the remarkable combination of near-metallic conductivity, high transmittance in the visible region and high reflectivity in the infrared region of light. TCOs are typically wide bandgap oxide semiconductors such as, In_2O_3, ZnO, SnO_2, CdO, or mixtures of these.[1,2] Due to their unique functional properties TCOs are utilized in diverse applications such as flat panel displays, energy efficient windows, photovoltaic devices, light emitting diodes and gas sensors. Indium oxide doped with tin oxide, often referred to as indium tin oxide (ITO), is recognized as the TCO with the best performance and is therefore the prime candidate in most cases.[3–5] Thin films of ITO can be deposited using a wide range of techniques, such as rf and dc sputtering, spray pyrolysis, chemical vapour deposition, vacuum evaporation and sol–gel methods.[1–5] Sputtering is the most frequent industrial deposition technique used to fabricate ITO thin films, and the importance of using highly dense ITO targets has been pointed out,[3,6,7] making the sintering of bulk ITO industrially relevant, even though ITO is applied as thin films in most of the applications. Reports on the sintering of dense ITO targets have recently appeared in the literature.[8,9] There has also been a growing interest in depositing thin films from suspensions containing ITO nanoparticles in the recent years, which is believed to give less brittle films than sputtering.[10] A subsequent heat treatment step is necessary in order to obtain sufficient conductivity. This heat treatment is carried out at considerably lower temperatures than the sintering of ITO targets due to the temperature sensitivity of the substrates.

In order to control the microstructure of ceramic materials the knowledge of the mass transport mechanisms during sintering is vital. It has been known for decades that it is difficult to fabricate polycrystalline In_2O_3 and ITO with high density.[11–13] The challenges with the densification have caused considerable interest in nano-crystalline In_2O_3 and ITO powders with enhanced sintering properties due to the increased surface area.[14–22] In most of these studies nano-crystalline In_2O_3 and ITO was prepared by co-precipitation methods.[14–18,20,21] Single phase SnO_2-doped In_2O_3 can however not be prepared by co-precipitation due to simultaneous precipitation of both In and Sn hydroxides, resulting in heterogeneous cation distribution.[17,21]

Recently we have developed an aqueous sol–gel route to synthesize single phase nano-crystalline ITO powders,[23] which overcome the problems related to the co-precipitation route. Here we report on a detailed study of the sintering process of the single phase nano-crystalline In_2O_3 and ITO powders[23] with particular focus on the mass transport mechanisms during

* Corresponding author. Tel.: +47 73594084; fax: +47 73550203.
E-mail address: grande@ntnu.no (T. Grande).

0955-2219/$ – see front matter © 2012 Elsevier Ltd. All rights reserved.
http://dx.doi.org/10.1016/j.jeurceramsoc.2012.09.023

sintering and the effect of the tin doping during the sintering process. The mass transport mechanisms are discussed with particular focus on the effect of partial pressure of oxygen at high temperatures. The sintering of ITO during intermediate temperatures, i.e. lower than 1200 °C, which has received very little attention in the literature, is also emphasized. The present findings are compared to corresponding studies of nano-crystalline powders prepared by co-precipitation[14,15,17,18,20] or mixtures of nano-crystalline In_2O_3 and SnO_2.[19] Finally, the importance of ball-milling to remove agglomerates in nano-crystalline materials is illustrated.

2. Experimental

Pure In_2O_3 and ITO with 5 cation % Sn (ITO, $In_{1.9}Sn_{0.1}O_{3.05}$) were prepared by an aqueous sol–gel route using indium (III) nitrate hydrate ($In(NO)_3{\cdot}xH_2O$, 99.9%, Aldrich) and tin (II) acetate ($Sn(CH_3CO_2)_2$, 99.9%, Aldrich) as precursors. Due to the hygroscopic nature of indium nitrate, the In-content in the nitrate was determined by thermogravimetrical analysis. Stoichiometric amount of the precursors were dissolved in deionised water and heated to 80 °C on a hotplate with a magnetic stirrer. Acetic acid (CH_3COOH, p.a. Acros Organics) and ethylene glycol ($C_2H_4(OH)_2$, VWR) were added to the solution as complexing agents, in a molar ratio between the cations in the solution and each of the organics of 1:1.5. The sol was left on the hot plate overnight in order to evaporate the solvent and form a xerogel. The synthesis is described in detail elsewhere.[23] The as-prepared gel was ground and calcined at 400 and 600 °C. The calcined oxide powder was then ball milled with 5 mm YSZ balls in absolute ethanol for 24 h. After the evaporation of the solvent the powder was sieved through a 250 μm mesh and finally re-calcined at 400 °C.

Pellets of the ball milled powders with 5 mm diameter and about 2.5 mm height were pressed in a uniaxial press at <50 MPa, followed by subsequent cold isostatic pressing at 200 MPa. Green pellets were also prepared from un-milled powders to investigate the effect of ball milling on the final density. Stearic acid was used as a lubricant during the pressing of the pellets. The In_2O_3 powder compacted slightly better and reached relative green densities of 53 ± 2%, while the ITO powder compacted to 48 ± 2%. For the samples pressed from powder that was not ball milled the green densities were 48 ± 2% and 46 ± 2%, respectively. The sintering properties were investigated by conventional sintering for 2 h in air at temperatures ranging from 600 to 1600 °C and by dilatometry (Netzsch, Dil 402C) in different atmospheres. The heating and cooling rate was 200 K/h for the conventional sintering. The dilatometry was carried out in pure oxygen, air and nitrogen atmospheres with a heating rate of 2 K/min. The densities of the sintered samples were determined by Archimedes tests carried out in accordance with ISO 5017.

The phase composition of the sintered ITO materials was studied by X-ray powder diffraction (XRD, Bruker AXS, D8 Focus). The XRD data was refined using Topas v4.2 refinement software, and the crystallite sizes were estimated by the line broadening using the Scherrer equation. Scanning electron microscopy (FEG-SEM, Zeiss Ultra 55 Limited Edition) was performed on fracture surfaces of the sintered pellets. Based on the SEM-images, an average grain size was calculated from the average of 50 grains. Transmission electron microscopy (TEM) was performed at 200 kV using a JEOL2010F. Both electron microscopes were equipped with a energy dispersive X-ray spectrometer (EDS) for elemental analysis. Nitrogen gas adsorption was carried out on the as-prepared powder and on samples after sintering at 600, 800 and 1000 °C (Micromeritics, Tristar 3000) to calculate the BET surface area and the BJH pore size distribution.

3. Results

The XRD patterns of the powders after calcination at 600 °C confirmed that both powders were single phase with the cubic In_2O_3 crystal structure (JCPDS card 06-0416). The phase purity was particularly important with respect to previous studies of nano-crystalline ITO materials.[14–21] The crystallite sizes of the In_2O_3 and the ITO powders, calculated by the Scherrer equation, was found to be 26 ± 1 nm and 16 ± 2 nm respectively. The BET surface areas of the powders were 24.9 ± 0.8 and 39.4 ± 1.3 m^2/g, giving an average particle size of 34 ± 1 nm for In_2O_3 and 21 ± 1 nm for ITO. The relevant data of the powders are summarized in Table 1. The phase purity and morphology of the powder was confirmed by TEM/EDS, and a representative TEM-micrograph of the ITO powder is shown in Fig. 1.

The linear shrinkage and differential linear shrinkage (densification rate) of In_2O_3 and ITO in air, measured by dilatometry, are shown in Fig. 2. The green density and final density of the samples studied by dilatometry are summarized in Table 2. It is clear that tin doping deteriorates the densification of In_2O_3 at intermediate temperatures, which correlates well with previous reports.[17,19] The onset of densification and the maximum densification rate for ITO were shifted towards higher temperatures relative to pure In_2O_3. However, above approximately 1200 °C the densification rate is higher for ITO, and the ITO samples actually obtained higher final densities in the dilatometer

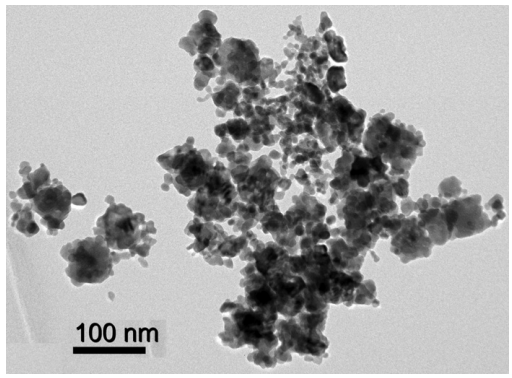

Fig. 1. Representative TEM micrograph of the ITO powder used for the sintering experiments.

Table 1
Crystal structure, BET surface area, crystallite size and particle size of the two materials after calcination at 600 °C.

Material	Doping amount (cation % Sn)	Crystal structure	BET surface area (m^2/g)	Crystallite size (XRD) (nm)	Particle size (BET) (nm)
In_2O_3	0	Cubic In_2O_3	24.9 ± 0.8	26 ± 1	34 ± 1
ITO	5	Cubic In_2O_3	39.4 ± 1.3	16 ± 2	21 ± 1

Table 2
Final density and weight loss measured after dilatometry with different atmospheres.

Composition	Atmosphere	Green density (%)	Density (%)	Weight loss (%)
In_2O_3	Oxygen	52.6	88.9	2.1
In_2O_3	Synthetic air	53.1	92.9	2.0
In_2O_3	Nitrogen	53.0	68.9	2.2
ITO	Oxygen	47.4	95.5	2.5
ITO	Synthetic air	47.0	95.3	2.3
ITO	Nitrogen	48.9	71.5	3.9

experiments. Similar conclusions could be drawn from the density of the pellets sintered for 2 h at isothermal conditions, shown in Fig. 3. Pure In_2O_3 achieved higher densities at intermediate temperatures, while the density was approximately equal for the two materials at 1300 °C and higher. Both materials reached densities above 95% after sintering at 1400 and 1450 °C, while the density decreased when the temperature was raised to 1500 and 1600 °C. The difference in density between the two materials after sintering at 600 and 800 °C is largely caused by the difference in green density. The ball milling procedure of the powder prior to the sintering was found to have a large impact on the sintering at high temperatures. For the samples prepared from non-ball milled powder the highest obtained density was approximately 88% for In_2O_3 and only 70% for ITO. Removal of hard agglomerates in the powders prior to the compaction was, thus, vital in order to obtain the high densities presented in Fig. 3. The lower density of the ITO samples could be explained by the smaller crystallites giving a higher degree of agglomeration.

The weight loss observed after the isothermal sintering experiments is also included in Fig. 3. It increased almost exponentially with sintering temperature above about 1300 °C, and the weight loss was notably higher for ITO compared to In_2O_3. The large weight losses at higher temperatures were found to be almost linearly proportional to the surface to volume ratio of the samples when pellets of different geometries were sintered. This shows that the weight loss could probably be significantly reduced by sintering in a suitable powder bed, though this was not further investigated. The observed weight loss below 1300 °C was attributed to the decomposition/evaporation of stearic acid, which was used as lubricant in the uniaxial pressing.

SEM micrographs of In_2O_3 and ITO after isothermal sintering at different temperatures are shown in Fig. 4. The microstructure and the grain size are quite similar for both compositions after the heat treatment at 600 °C. The micrographs of the materials sintered at 1000 °C, on the other hand, demonstrated the significant difference in the microstructure of the In_2O_3 and ITO materials. A significant coarsening and grain growth have accompanied the densification of In_2O_3, while the microstructure of ITO demonstrates almost only coarsening in line with the observed lack of densification below 1000 °C

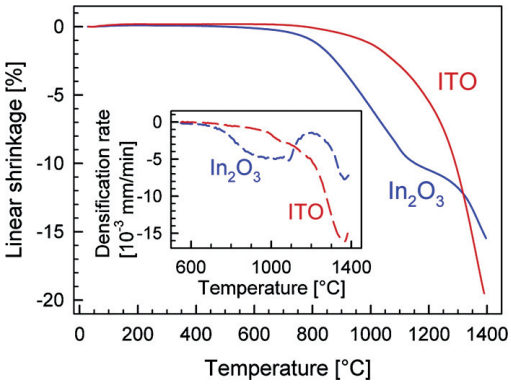

Fig. 2. Linear shrinkage of In_2O_3 and ITO in air with a heating rate of 2 K/min (solid lines). Inset: densification rate of the samples (dashed lines).

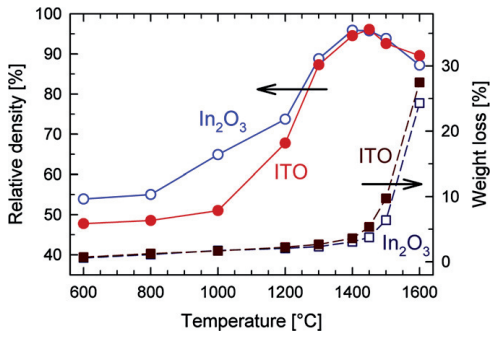

Fig. 3. Final density of In_2O_3 (○) and ITO (●) (left axis, solid lines) and weight loss of In_2O_3 (□) and ITO (■) (right axis, dashed lines) after isothermal sintering at different temperatures for 2 h.

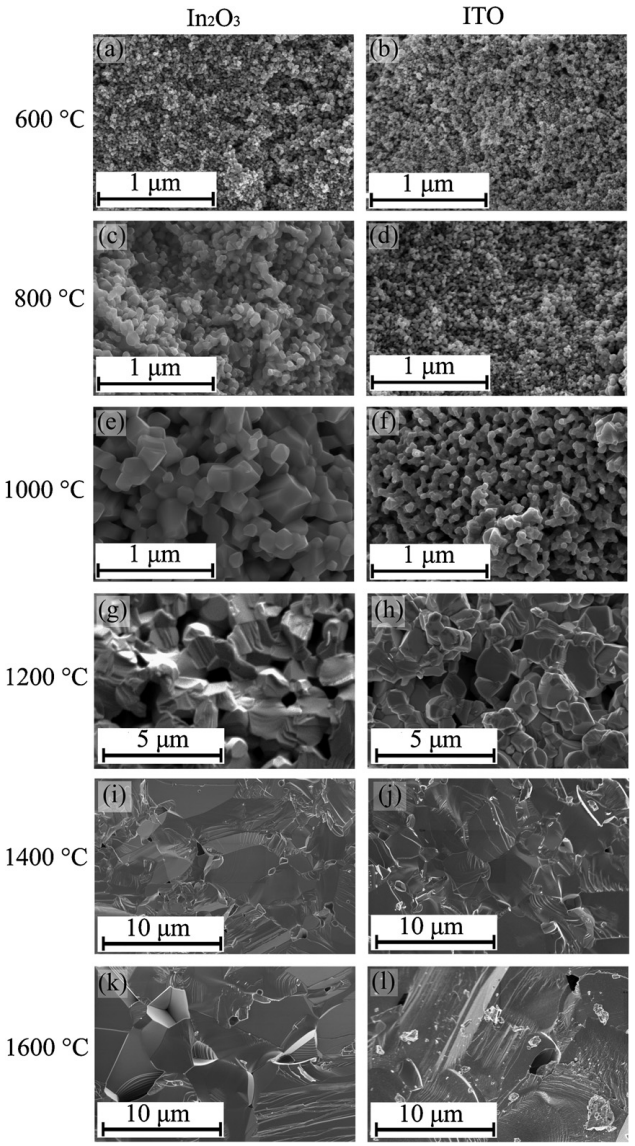

Fig. 4. Microstructure of In_2O_3 and ITO after sintering at various temperatures. (a) In_2O_3 600 °C, (b) ITO 600 °C, (c) In_2O_3 800 °C, (d) ITO 800 °C, (e) In_2O_3 1000 °C, (f) ITO 1000 °C, (g) In_2O_3 1200 °C, (h) ITO 1200 °C, (i) In_2O_3 1400 °C, (j) ITO 1400 °C, (k) In_2O_3 1600 °C and (l) ITO 1600 °C.

(Figs. 2 and 3). The BET surface area, relative density and grain size of the two materials sintered at intermediate temperatures are given in Fig. 5, while the pore size distributions calculated from nitrogen gas adsorption are shown in Fig. 6. These results confirm the conclusions drawn from the micrographs in Fig. 4. Both materials experience a substantial reduction of the surface area from 600 to 1000 °C, but the densification and the grain growth are significantly higher for In_2O_3 than for ITO. The pore size distribution is similar at 600 °C, but at 800 and 1000 °C the pore size is shifted towards larger pores for In_2O_3

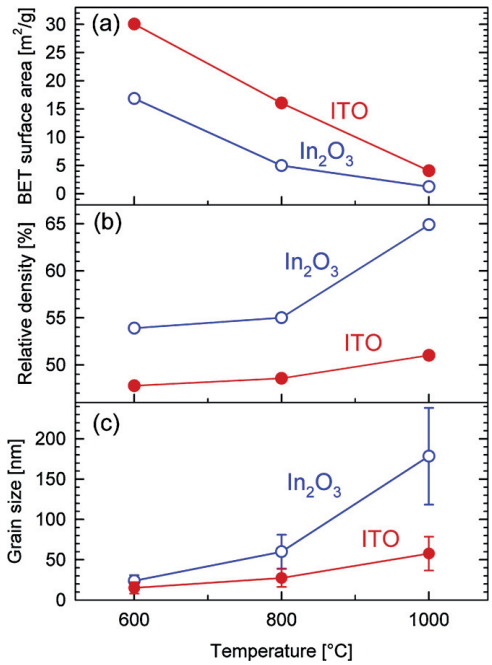

Fig. 5. BET surface area (a), relative density (b) and grain size (c) of In_2O_3 (○) and ITO (●) as a function of temperature after isothermal sintering at 2 h at intermediate temperatures.

and the total volume of pores is smaller for In_2O_3 compared to ITO. Both materials had densified considerably after sintering at 1200 °C, Fig. 4(g and h), though considerable porosity still remain. The grains had grown substantially for both compositions, but the grains of undoped In_2O_3 still appear to be larger than for their ITO counterpart. The microstructures after sintering at higher temperatures, Fig. 4(i–l), are similar for both materials and clearly reflects the densities presented in Fig. 3. At 1400 °C the microstructures are almost completely dense with only a few submicron pores, while larger pores are clearly seen

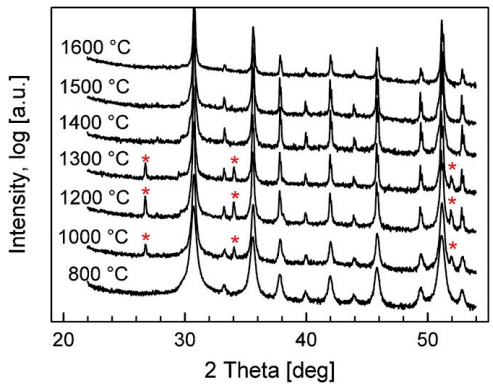

Fig. 7. XRD patterns of ITO samples after isothermal sintering. Diffraction lines due to SnO_2 at 27°, 34° and 52° are denoted by *.

at 1600 °C. The pores are mainly located at the grain boundaries and not within grains.

The XRD patterns of ITO after sintering at different temperatures are given in Fig. 7. The materials sintered at 800, 1400, 1500 and 1600 °C were single phase materials with only diffraction lines assigned to cubic indium oxide (In_2O_3, JCPDS card 06-0416). On the other hand, for the materials sintered at 1000, 1200 and 1300 °C, three extra Bragg reflections were evident (marked * at 27°, 34° and 52°). These reflections could be indexed to SnO_2 (JCPDS card 72-1147). The lattice parameter for the cubic In_2O_3 phase in ITO, determined by the Rietveld refinement of the diffractograms, is shown as a function of the sintering temperature in Fig. 8. The lattice parameter decreased from 800 to 1000 °C, followed by an increase with increasing sintering temperature, before it eventually saturated at about 10.1260 Å, which is close to the lattice parameter previously reported for bulk ITO with 5 cation % Sn.[24,25] The undoped In_2O_3 samples were phase pure and cubic throughout the sintering, without any reactions or phase transitions, and had a lattice parameter of 10.1195 Å.

The sintering kinetics was further investigated by dilatometry in three different atmospheres, synthetic air, oxygen and nitrogen, and the linear densification and the densification rate for the

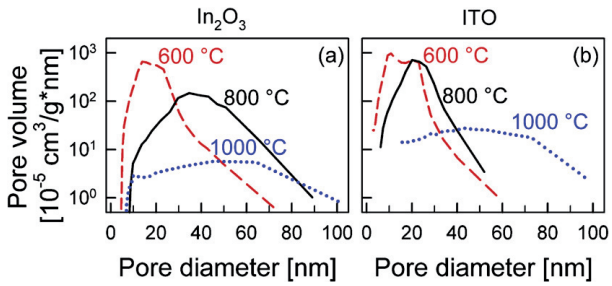

Fig. 6. Pore size distributions for (a) In_2O_3 and (b) ITO after isothermal sintering at different temperatures obtained by nitrogen adsorption analysis.

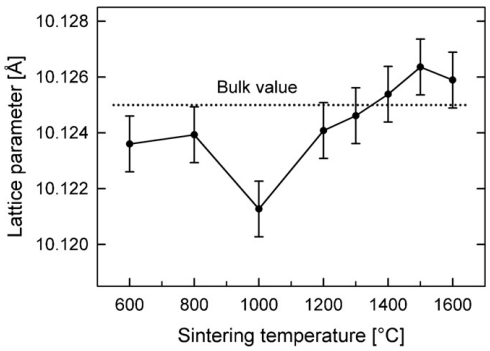

Fig. 8. Cubic lattice parameter of In_2O_3 phase in the ITO material sintered at different temperatures. The data were obtained by Rietveld refinement of XRD patterns in Fig. 7. The error was estimated to be 0.002 Å, including the statistical error obtained from the Rietveld refinement. The reference value for bulk ITO with 5 cation % Sn is taken from.[24]

two materials are shown in Fig. 9. The density and the weight loss observed after these experiments are given in Table 2. It has been noted in several reports that it is advantageous to sinter ITO in oxygen.[13–15,20] The difference in sintering behaviour in synthetic air and oxygen was minor, while there was a significant difference between the two oxygen-rich atmospheres and nitrogen (with an estimated oxygen partial pressure of 10^{-4}–10^{-5}). Below approximately 900 °C the sintering kinetics is not influenced by the atmosphere. Above this temperature, on the other hand, the densification is significantly retarded in nitrogen, and the final densities were almost 25% lower than in air or oxygen. The weight loss also appears to be significantly higher in nitrogen, especially in the case of ITO.

4. Discussion

4.1. Sintering of In_2O_3

It is clear from the dilatometer data that the nano-crystalline In_2O_3 powder started to densify already at temperatures as low as 600–700 °C in good agreement with previous reports.[17,19] Solid state sintering (densification) can occur by either grain boundary diffusion or bulk (lattice) diffusion from the grain boundary. The mass transport mechanism in the initial stage of densification of nano-crystalline In_2O_3 is proposed to be grain boundary diffusion due to the high melting point of In_2O_3 (2183 K).[26] In order for this mechanism to be active, grain boundaries must therefore have been formed by necking during heating to 600 °C. It is difficult to observe significant coarsening in the SEM-image of In_2O_3 at 600 °C (Fig. 4a), but there is a substantial drop in surface area from the powder to the sample sintered at 600 °C, showing that coarsening and neck formation has taken place. Surface diffusion contributes to the initial mass transport during heating of almost all systems,[27] and is the only possible mass transport mechanism that may lead to coarsening at these low temperatures.

The densification rate of In_2O_3 increases from 700 to 1000 °C, where it goes through a maximum, and then decreases again as the temperature is further increased. It is common for many ceramic systems to go through regimes where surface diffusion, leading to coarsening, grain boundary diffusion, causing densification, and grain growth dominates sequentially as the

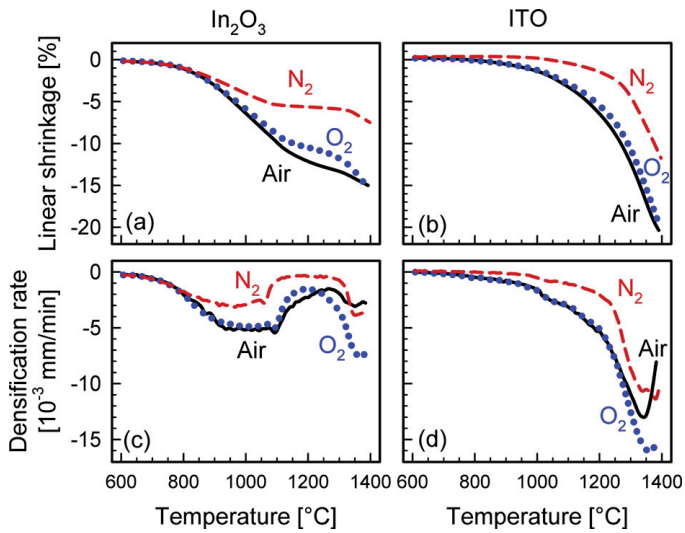

Fig. 9. Linear shrinkage and densification rate of In_2O_3 and ITO in different atmospheres, synthetic air (solid lines), oxygen (dotted lines) and nitrogen (broken lines). (a) Linear shrinkage of In_2O_3, (b) linear shrinkage of ITO, (c) densification rate of In_2O_3 and (d) densification rate of ITO.

temperature is elevated.[28] It was observed that the grain size of In_2O_3 began to increase substantially from about 800 and 1000 °C (Figs. 4 and 5). A substantial amount of the driving force for densification is, thus, removed by the considerable grain growth and coarsening.

The densification rate of In_2O_3 was observed to increase again above 1200 °C (Fig. 2) and the densities after isothermal sintering increased significantly from 1200 to 1400 °C (Fig. 3). Densification due to grain boundary diffusion is proposed to take place already at 700 °C, and it is unlikely that the same mass transport mechanism causes this re-entrance of densification at a temperature more than 500 °C higher. On the other hand, lattice diffusion will take place at a considerable rate at some point as the temperature is increased. We therefore propose that lattice diffusion causes the re-entrance of a higher densification rate from about 1200 °C, accompanied by grain growth and pore removal. An increasing weight loss is also starting to manifest itself in the same temperature region. This is an indication that evaporation–condensation, which is a mass transport mechanism leading to coarsening, is starting to take place at a significant rate. There will be a competition between lattice diffusion and evaporation–condensation regarding the use of the remaining driving force for sintering at high temperatures. However, the decreasing density above 1450 °C cannot solely be explained by an increasing influence of evaporation–condensation. In the dense microstructure of In_2O_3 obtained after sintering at 1400 °C for 2 h, no necks are present (Fig. 4i). The large weight loss demonstrates that significant evaporation from the sample is occurring, but at this stage the microstructure can no longer be influenced by evaporation–condensation, as there are no necks or areas with different curvature where the condensation can preferably occur. On the other hand, a significant grain growth accompanied by pore growth and coarsening is observed when comparing the microstructure of the In_2O_3 material sintered at 1400 and 1600 °C. It is known that the coalescence and growth of gas filled pores due to grain growth can cause a decrease in density during prolonged sintering when an inert gas like nitrogen is filling the pores.[27]

The sintering atmosphere starts to influence the sintering already below 900 °C (Fig. 9). The effect of the atmosphere has been documented previously,[14,20] but the thermodynamics of the sublimation of these oxides has not been discussed regarding the sintering and will be presented here. According to thermodynamic data,[29] the sublimation of In_2O_3 will mainly occur through the following reaction:

$$In_2O_3(s) \rightarrow In_2O(g) + O_2(g) \quad (1)$$

Decreasing the partial pressure of oxygen would, therefore, enhance evaporation, which can explain why the sample sintered in nitrogen achieved a lower density (Table 2). The calculated partial pressure of In_2O (g) as a function of T and partial pressure of O_2 is shown in Fig. 10a. The thermodynamic data for reaction (1) was taken from.[30] It has been shown by thermogravimetrical analyses that the sublimation of In_2O_3 start to occur at noticeable rates at around 1200 °C,[13,31] which is in reasonably good agreement with the results in this work. At these high temperatures the oxygen partial pressure will obviously influence on the sintering by affecting mass transport by evaporation–condensation. However, at 900 °C the vapour pressure of In_2O (g) is only about 10^{-15} bar even in the nitrogen atmosphere. Though the nano-size of the grains gives small diffusion lengths and large curvatures (driving force for mass transport), these very low vapour pressure suggests that mass transport by evaporation–condensation is not significant in this temperature region. Thus, it is likely that the partial pressure of oxygen may affect other mass transport mechanisms than evaporation–condensation, by introducing and removing oxygen vacancies and interstitials, either in bulk, at surfaces or grain boundaries as discussed further in the next chapter. Finally, though it is clear that the In_2O (g) sub-oxide has a significantly higher partial pressure in nitrogen than in air or oxygen, the difference between the two oxidizing atmospheres is small. This is also illustrated in both the dilatometer curves (Fig. 9) and in the densities and weight losses (Table 2). In a work by Kim et al. somewhat larger differences between samples sintered in air and oxygen was observed.[14] They argued that the effect was caused by reduced evaporation and also that in the final stage of sintering, where the porosity is mostly closed, the solubility of the gas in the solid lattice is vital for the elimination of the remaining pores. At this stage it is obvious that an oxygen atmosphere is a significant advantage, as air contains mostly nitrogen, which has a lower solubility. Our results indicate that the advantage of choosing an oxygen atmosphere over air is mostly because of the final pore removal, while the reduction of the evaporation is less important in the final stage of sintering. However, in earlier stages of sintering, when concave curvature still remains in the microstructure, evaporation–condensation will contribute significantly to retard densification. A higher heating rate was used for the dilatometer experiments performed by Kim et al.,[14] which could explain the higher influence from the oxygen atmosphere.

4.2. Sintering of ITO

It is evident from the present findings and previous reports[17,19] that doping In_2O_3 with SnO_2 degrades the sintering properties at intermediate temperatures, even in the case of nano-sized powders. The poor sinterability of ITO compared to In_2O_3 can partly be explained by the higher valence of Sn^{4+} compared to In^{3+}. The cation with higher valence will cause a more covalent bond with oxygen and, thus, reduce the mobility of the cations in ITO. It is also known that Sn^{4+} is compensated by oxygen interstitials forming defect clusters,[32] which also might influence on the bulk diffusion of cations. Furthermore, the fact that SnO_2 doping strongly influences the sintering denotes that the rate limiting step for the sintering process is cation diffusion. Reducing oxygen partial pressure would decrease the concentration of oxygen interstitials and expand the lattice, which suggest enhanced bulk diffusion of cations. The lower sintering rate in nitrogen (Fig. 9) can therefore not be related to bulk diffusion of cations. This is also in line with the conclusion that the initial sintering is caused by grain boundary diffusion. To reveal

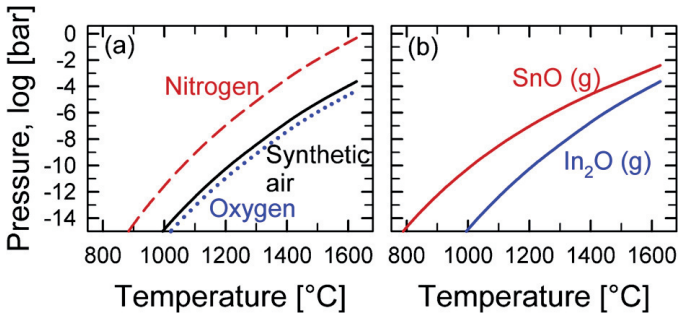

Fig. 10. The partial pressure of the suboxides In_2O and SnO as a function of temperature in different atmospheres. (a) Partial pressure of In_2O in nitrogen (dashed line), air (solid line) and oxygen (dotted line). Oxygen partial pressures of 10^{-4}, 0.2 and 1 were used for the respective atmospheres. (b) Comparison between the partial pressure of SnO and In_2O in air.

the mechanism for the strong retardation of sintering under inert conditions further investigations are needed.

Only minor shrinkage was observed for ITO up to 1000 °C (Figs. 2 and 3). The initial densification around 1000 °C, though significantly retarded compared to pure In_2O_3, can be ascribed to grain boundary diffusion due to the relatively moderate temperatures compared to the melting point of In_2O_3, as discussed above. The grain growth in ITO was also substantially lower than for In_2O_3 below 1000 °C. However, the significant reduction of surface area of the ITO material from 600 to 1000 °C clearly illustrates that coarsening has taken place (Fig. 5). A highly porous and coarse microstructure, where the particles have grown together without significant densification, is evident in the SEM image of ITO after sintering at 1000 °C (Fig. 4f). Thus, it appears that the tin doping is hindering both grain boundary diffusion and grain growth, thereby opening for more coarsening in the ITO material compared to In_2O_3.

A secondary SnO_2-phase precipitated from the ITO solid solution between 800 and 1000 °C (Fig. 7). The solid solution with 5 cation % Sn, prepared by the sol–gel route, is in a metastable state since 5 cation % Sn is significantly higher than the solubility limit of SnO_2 in ITO at 800 °C.[33] At low temperatures the cation mobility is not sufficient to acquire the stable two-phase equilibrium, but between 800 and 1000 °C the stable two phase mixture appeared, as shown by XRD. This exsolution of excess tin is in very good agreement with recent work by González et al.[25] SnO_2(s) are most likely nucleated at the grain boundaries. This precipitation will, thus, lead to a temporarily higher concentration of Sn^{4+} at the grain boundaries, which can explain that grain boundary diffusion and grain growth are hindered in ITO compared to In_2O_3 at these temperatures. The particle size of SnO_2 has been reported to be particularly important during sintering of initial mixtures of nano-crystalline In_2O_3 and SnO_2.[19] The lattice parameter of cubic In_2O_3 is reported to increase with increasing amount of tin doping.[24,25] Precipitation of SnO_2 reduced the tin content in the solid solution, which explains the observed reduction in the lattice parameter from 800 to 1000 °C. As the temperature was further increased the solubility of SnO_2 in In_2O_3 increases,[25,33] and SnO_2 re-dissolved in the ITO solid solution. The lattice parameter was observed to increase until it becomes close to constant (10.1260 Å) when the SnO_2-phase disappeared. This value is in good agreement with the previously reported lattice parameter for ITO with 5 cation % Sn.[24,25]

Other secondary phases in the In_2O_3–SnO_2 system, such as In_2SnO_5 and $In_4Sn_3O_{12}$, have also been reported to influence on the sintering of ITO.[17,19] The presence of In_2SnO_5 has been reported to have a negative effect on the sintering, while the presence of $In_4Sn_3O_{12}$ has been reported to have a positive effect by hindering abnormal grain growth in the final stages of sintering. In_2SnO_5 is a metastable phase that appears when tin-doped $In(OH)_3$ prepared by co-precipitation decomposes,[17] and was not observed in this work. $In_4Sn_3O_{12}$ is formed by In_2O_3 and SnO_2 at temperatures above 1345 °C.[34] According to the phase diagram[25,33] this phase should appear when a tin doping amount of 5 cation % is used, but it was not possible to establish its presence in the ITO material used in this work. Small concentrations of this phase is difficult to detect by XRD because its strongest peaks have similar d-spacings to that of the cubic In_2O_3 bixbyite structure, as both of them are fluorite derived structures.[34] The weight loss of the samples shows that the Sn content could have been somewhat reduced by evaporation, however the lattice parameters give evidence that the actual tin content in the bulk remains at about 5 cation % even at higher temperatures (mainly loss from surface). Though the presence of secondary phases appears to be important,[17] the difference between the sintering of In_2O_3 and ITO cannot exclusively be explained by this factor. There is a significant difference between the densification of ITO and In_2O_3 before the appearance of SnO_2, and at 1300 °C the shrinkage rate of ITO is significantly higher than for In_2O_3, even though SnO_2 is still present (Figs. 2 and 5). This indicates that the effect of other factors, such as the higher valency of Sn, should not be underestimated.

The densification rate of ITO increased significantly above 1100–1200 °C, which is also reflected in the SEM micrograph in Fig. 4h. Densification in this temperature region is dominated by lattice diffusion based on the observations for pure In_2O_3. At higher temperatures than 1300 °C the weight loss observed for ITO becomes noticeable, and mass transport due to evaporation–condensation must take place. SnO_2 has a

relatively high vapour pressure and evaporates mainly through to the following reaction [29]

$$2SnO_2(s) \rightarrow 2SnO(g) + O_2(g) \quad (2)$$

The calculated partial pressure of SnO (g) is significantly higher than for In_2O (g), as illustrated in Fig. 10b, which explains the higher weight loss of ITO compared to In_2O_3 (Fig. 3 and Table 2). However, though the partial pressure of SnO (g) is high, it is only about 10^{-10} bar at 1000 °C. This partial pressure is not high enough to give a significant contribution from evaporation–condensation. This implies that the mass transport mechanism leading to the considerable coarsening of ITO at intermediate temperatures most likely is surface diffusion (lattice diffusion from surface may also contribute to coarsening, but is not considered in this case). At temperatures above 1400 °C there was a significant pore coarsening due to grain growth, also for ITO (Fig. 4j and l). This effect can explain the reduced density at higher temperatures, probably in combination with a higher influence from evaporation–condensation.

The presence of agglomerates has been reported to be important regarding the sintering of nano-crystalline ITO.[15,35] The powder used in the present sintering study was prepared by a sol–gel method, and such Pechini-related syntheses are known to yield a certain degree of particle agglomeration.[36] Agglomerates can be seen in Fig. 1, though it is difficult to distinguish between soft and hard agglomerates. The difference in the density of materials prepared from ball milled and non-ball milled powders clearly demonstrates the importance of removing agglomerates from nano-crystalline powders to obtain high density. Furthermore, similar densification and densification rate curves as presented in Fig. 2 has been reported,[15–17] and the influence of agglomeration has been discussed. Two maxima in the densification rate, which has been reported both for In_2O_3[17,35] and for ITO,[15–17] has been attributed to agglomeration of nano-crystalline powders causing a non-uniform particle size distribution. In the first step of densification, the smaller pores inside the agglomerates are eliminated, while in the second step, the larger inter-agglomerate pores are removed.[15,35] In order to investigate this effect, the pore size distribution of the materials was measured by nitrogen adsorption. If the two stages were caused by the elimination of pores of different sizes, the pore size distribution should be bi-modal at low temperatures, with the mode at the smallest pore size being removed as the first step of densification is progressing. Contrarily to this, the pore size distributions of the powders presented here were not bi-modal either at 600, 800 or 1000 °C (Fig. 6). Even the non-ball milled samples, with agglomerated powder, had uni-modal pore size distributions at the same temperatures. Though it is evident that removal of hard agglomerates is important prior to sintering, our interpretation of these results is that the two steps of densification is not caused by agglomerates, but rather from a change in the rate determining mechanism for mass transport as discussed here.

Final density higher than 95% was obtained in this study. Even higher densities could possibly be obtained by increasing the uniaxial pressure from 200 MPa to 300 MPa, leading to better packing of the green body.[15,37] The present findings clearly demonstrates that significant coarsening takes place at intermediate temperatures, especially in the case of ITO, and high heating rate during sintering is beneficial. However, too high heating rates have been reported to be undesirable due to so-called differential densification.[14,18] Sintering in oxygen would also be beneficial regarding the final pore removal, as discussed above.

The preceding discussion on the sintering includes aspects which are relevant for the sintering of ITO thin films, as the constrained sintering of thin films basically occurs through the same mechanisms as in bulk materials.[38] Therefore, if the purpose of a heat treatment is to modify the microstructure of ITO thin films, the mass transport mechanisms discussed here must be taken into consideration. The present findings show that nano-crystalline ITO, not confined by any substrate, does not sinter in temperatures up to 1000 °C. The small amount of shrinkage that does occur is caused by grain boundary diffusion, which was demonstrated to be hindered by the tin doping, compared with pure In_2O_3. However, significant coarsening by surface diffusion was demonstrated to take place. In a thin film based on ITO nanoparticles coarsening will contribute to neck formation and improve the physical contact between the particles. This could substantially decrease the electrical resistivity of the film even though its density is not affected.

5. Conclusion

Solid state sintering of phase-pure nano-crystalline In_2O_3 and ITO with 5 cation % Sn has been investigated. The densification of In_2O_3 occurred in two stages, the initial densification of In_2O_3, starting at around 600 °C and a final stage above 1200 °C. The two stages were discussed in terms of grain boundary and bulk diffusion respectively. Coarsening and particularly grain growth were demonstrated to interfere with the densification of nano-crystalline In_2O_3 at intermediate temperatures. Coarsening at low temperatures was mainly due to surface diffusion mechanism, while coarsening by evaporation–condensation took place at higher temperatures. Pore coarsening due to grain growth reduced the density at temperatures above 1450 °C. SnO_2 doping was observed to inhibit sintering of ITO compared to In_2O_3 at intermediate temperatures, in line with previous reports. The reduced cation mobility in ITO relative to In_2O_3 was explained by the higher valence state of Sn^{4+} compared to In^{3+}. It was found that grain boundary diffusion and grain growth was hindered by the tin doping and ITO obtained a coarser microstructure at intermediate temperatures. This effect was enhanced by the precipitation of SnO_2(s), taking place in ITO below 1000 °C. SnO_2(s) was observed to re-dissolve in ITO above 1300 °C. At high temperature evaporation of the oxides caused significant weight losses. This effect was more pronounced for ITO than for In_2O_3 due to the higher vapour pressure of SnO(g) relative to In_2O(g). Finally, it is pointed out that mainly surface diffusion can take place during processing of ITO thin films up to 1000 °C.

Acknowledgement

This work has been supported by NTNU and the strategic research area MATERIALS at NTNU. Dr. Ragnild Sæterlie, Department of Physics, NTNU, is acknowledged for performing the TEM measurements.

References

1. Chopra KL, Major S, Pandya DK. Transparent conductors – a status review. *Thin Solid Films* 1983;**102**:1–46.
2. Ginley DS, Bright C. Transparent conducting oxides. *MRS Bull* 2000;**25**:15–8.
3. Tahar RBH, Ban T, Ohya Y, Takahashi Y. Tin doped indium oxide thin films: electrical properties. *J Appl Phys* 1998;**83**:2631–45.
4. Granqvist CG, Hultaker A. Transparent and conducting ITO films: new developments and applications. *Thin Solid Films* 2002;**411**:1–5.
5. Hecht DS, Kaner RB. Solution-processed transparent electrodes. *MRS Bull* 2011;**36**:749–55.
6. Utsumi K, Matsunaga O, Takahata T. Low resistivity ITO film prepared using the ultra high density ITO target. *Thin Solid Films* 1998;**334**:30–4.
7. Gehman BL, Jonsson S, Rudolph T, Scherer M, Weigert M, Werner R. Influence of manufacturing process of indium tin oxide sputtering targets on sputtering behavior. *Thin Solid Films* 1992;**220**:333–6.
8. Zhu GS, Yang ZP, Zhi L, Yang HJ, Xu HR, Yu AB. Preparation and sintering behavior of the tin-doped indium oxide nanopowders. *J Am Ceram Soc* 2010;**93**:2511–4.
9. Medvedovski E, Alvarez N, Yankov O, Olsson MK. Advanced indium-tin oxide ceramics for sputtering targets. *Ceram Int* 2008;**34**:1173–82.
10. Dattoli EN, Lu W. ITO nanowires and nanoparticles for transparent films. *MRS Bull* 2011;**36**:782–8.
11. Vojnovich T, Bratton RJ. Impurity effects on sintering and electrical-resistivity of indium oxide. *Am Ceram Soc Bull* 1975;**54**:216–7.
12. De Wit MJHW, Elbers PF, Laheij M. Grain growth and sintering of In_2O_3. *Sci Ceram, 9, Proc* 1977;**9**:143.
13. Nadaud N, Nanot M, Boch P. Sintering and electrical-properties of titania-containing and zirconia-containing In_2O_3–SnO_2 (ITO) ceramics. *J Am Ceram Soc* 1994;**77**:843–6.
14. Kim BC, Lee JH, Kim JJ, Lee HY, Lee JS. Densification of nanocrystalline ITO powders in fast firing: effect of specimen mass and sintering atmosphere. *Mater Res Bull* 2005;**40**:395–404.
15. Kim BC, Lee JH, Kim JJ. Effect of forming pressure on densification behavior of nanocrystalline ITO powder. *J Eur Ceram Soc* 2007;**27**:807–12.
16. Kim BC, Kim SM, Lee JH, Kim JJ. Effect of phase transformation on the densification of coprecipitated nanocrystalline indium tin oxide powders. *J Am Ceram Soc* 2002;**85**:2083–8.
17. Kim SM, Seo KH, Lee JH, Kim JJ, Lee HY, Lee JS. Preparation and sintering of nanocrystalline ITO powders with different SnO_2 content. *J Eur Ceram Soc* 2006;**26**:73–80.
18. Kim BC, Lee JH, Kim JJ, Ikegami T. Rapid rate sintering of nanocrystalline indium tin oxide ceramics: particle size effect. *Mater Lett* 2002;**52**:114–9.
19. Kim SM, Lee JH, Kim JJ. Reaction-sintering behavior of nanocrystalline indium tin oxide with varying SnO_2 content and particle size. *Scripta Mater* 2007;**56**:293–6.
20. Park YG, Seo KH, Lee JH, Kim JJ, Cho SH, O'Conner CJ, et al. Phase transformation behavior of nanocrystalline ITO powders during heat-treatment: oxygen partial pressure effect. *J Electroceram* 2004;**13**:851–5.
21. Udawatte CP, Yanagisawa K. Sintering of additive free hydrothermally derived indium tin oxide powders in air. *J Solid State Chem* 2000;**154**:444–50.
22. Li XH, Xu XJ, Yin X, Li CZ, Zhang JR. A sol–gel method to synthesize indium tin oxide nanoparticles. *Particuology* 2011;**9**:471–4.
23. Sunde TOL, Garskaite E, Otter B, Fossheim HE, Sæterli R, Holmestad R, et al. Transparent and conducting ITO thin films by spin coating of an aqueous precursor solution. *J Mater Chem* 2012;**22**:15740–9.
24. Nadaud N, Lequeux N, Nanot M, Jove J, Roisnel T. Structural studies of tin-doped indium oxide (ITO) and $In_4Sn_3O_{12}$. *J Solid State Chem* 1998;**135**:140–8.
25. González GB, Mason TO, Okasinski JS, Buslaps T, Honkimaki V. Determination of the solubility of tin in indium oxide using in situ and ex situ X-ray diffraction. *J Am Ceram Soc* 2012;**95**:809–15.
26. Kong XY, Wang ZL. Structures of indium oxide nanobelts. *Solid State Commun* 2003;**128**:1–4.
27. German RM. *Sintering theory and practice*. 1st ed. New York: John Wiley & sons; 1996.
28. McColm IJ, Clark NJ. *Forming, shaping and working of high-performance ceramics*. 1st ed. Glasgow: Blackie; 1988.
29. Lamoreaux RH, Hildenbrand DL, Brewer L. High-temperature vaporization of oxides. 2. Oxides of Be, Mg, Ca, Sr, Ba, B, Al, Ga, In, Tl, Si, Ge, Sn, Pb, Zn, Cd, and Hg. *J Phys Chem Ref Data* 1987;**16**:419–43.
30. Barin I. *Thermochemical data of pure substances*. 1st ed. New York: VCH; 1989.
31. De Wit JHW. High-temperature behavior of In_2O_3. *J Solid State Chem* 1975;**13**:192–200.
32. Frank G, Kostlin H. Electrical-properties and defect model of tin-doped indium oxide layers. *Appl Phys A-Mater Sci Process* 1982;**27**: 197–206.
33. Heward WJ, Swenson DJ. Phase equilibria in the pseudo-binary In_2O_3–SnO_2 system. *J Mater Sci* 2007;**42**:7135–40.
34. Gonzalez GB, Okasinski JS, Mason TO, Buslaps T, Honkimaeki V. In situ studies on the kinetics of formation and crystal structure of $In_4Sn_3O_{12}$ using high-energy X-ray diffraction. *J Appl Phys* 2008:104.
35. Son JW, Kim DY, Boch P. Enhanced densification of In_2O_3 ceramics by presintering with low pressure (5 MPa). *J Am Ceram Soc* 1998;**81**: 2489–92.
36. Kakihana M, Yoshimura M. Synthesis and characteristics of complex multicomponent oxides prepared by polymer complex method. *Bull Chem Soc Jpn* 1999;**72**:1427–43.
37. Liu C, Liu JX, Wang Y. Preparation of indium tin oxide targets with a high density and single phase structure by normal pressure sintering process. *Rare Metals* 2011;**30**:126–30.
38. Bordia RK, Scherer GW. On constrained sintering. 1. Constitutive model for a sintering body. *Acta Metall* 1988;**36**:2393–7.